Institute of Sustainable Energy Technology

Department of Architecture and Built Environment

Faculty of Engineering

A Heat Pipe Internally-cooled Membrane-based Liquid Desiccant Dehumidification System

Thesis by

Yuhao Wang, BEng, MSc.

30th March 2023

Thesis submitted to the University of Nottingham

For the Degree of Doctor of Philosophy in Building Technology

Table of Contents

List of Figures

List of Tables

Abstract

In recent years, membrane-based liquid desiccant dehumidification has emerged as an efficient approach for air humidity control in building air conditioning process, in which the internally-cooled liquid desiccant dehumidifier is regarded as an energy-efficient device with high dehumidification effectiveness and cooling performance.

This research project aims at investigating the dehumidification and cooling performance of a heat pipe internally-cooled liquid membrane-based desiccant dehumidification (HP-ICMLDD) system and its application in multi-family terraced houses under subtropical and humid Mediterranean climate conditions. The project also develops an integrated liquid desiccant air-conditioning (ILDAC) system by combining the HP-ICMLDD system with an air-water heat pump (AWHP), photovoltaics-thermal (PVT), and hot water storage.

An innovative HP-ICMLDD system is established by integrating the heat pipe internal cooling method with the dehumidification system, where experimental investigation is conducted. Moreover, the energy simulation of the building with the ILDAC system has been conducted via the IES VE and EnergyPro software using the reference buildings (RBs) in Spain, Italy and Greece.

The research output indicates that the dehumidification performance is influenced by the heat pipe's internal cooling effect, which is significantly improved by reducing the cold water temperature and increasing the cold water flow rate. The optimal operating conditions for the complete LDD system have been determined. For the dehumidifier in the HP-ICMLDD system, the optimal inlet cold water temperature, mass flow rate, solution temperature and solution concentration are 18 ℃, 0.017 kg/s, 18℃, 32%, respectively; For the regenerator in the system, the optimal solution temperature is 55 ℃. The correlations of thermal, electrical, total COP, air temperature and relative humidity at the dehumidifier outlet with the inlet air conditions have been generated using the linear regression method. It is found that the ILDAC system COP rises with the increasing inlet air temperature and relative humidity.

By comparing the energy consumption of the residential building without and with the ILDAC system in three different locations, the building energy consumption is reduced by 77.6%, 74.8% and 78.8% in Barcelona, Rome and Methoni, and the corresponding carbon reduction rate is 88.8%, 84.3% and 76.9%. The ILDAC system could achieve higher COP of 6.41, 8.14 and 7.52 in Barcelona, Rome and Methoni, which are significantly higher than those of the complete LDD and AWHP systems. The discounted payback period varies between 7 and 9 years, with the annual return on investment ranging from 8.40% to 11.90%. Moreover, it is appropriate to invest in the ILDAC system in Spain, Italy and Greece when the inflation rates fall between -6.80% and 12.20%, -6.90% and 12.20%, and -5.40% and 8.70%, respectively.

Acknowledgements

I would like to express my deep appreciation to my supervisors Dr Jie Zhu and

Dr Shenyi Wu for their help and inspiration throughout this thesis and project, where their enthusiasms towards the project were contagious, and their guidance was invaluable. Besides, this research would not have been possible without the technical support from the Marmont Laboratory, the Department of Architecture and Built Environment, where special mention goes to Tony Gospel and Carson Cheng for their professional and enthusiastic help and support with my experimental work. Special thanks also go to my dear colleagues, especially Dr Xiangjie Chen, Dr Tianhong Zheng, Dr Hongyu Bai, Ms Jiarui Sun, Mr Lingze Lin, Ms Luo Man, Mr Yuhan Zhang and Mr Yinrui Li for discussing problems I encountered during my research. I also want to thank my internal examiner Dr Guohui Gan and external examiner Dr Liben Jiang for their valuable advice. Also, I also want to give my sincere thank to Prof Saffa Riffat for his help to offer me working opportunites. I am also grateful to my cherished friend Dr Ke Qu, who helped me throughout my PhD research by being extremely patient and generous and inspiring me with many innovative ideas, where I give my utmost respect and thanks to him.

Most importantly, I would like to thank and appreciate my dear family members, my mom Ms Yongmei Yu, my dad Mr E Wang and my grandparents for supporting me spiritually and financially throughout the PhD study and my routine life. Finally, thanks again to the people I mentioned above. Thank you all for giving me tremendous trust, support and inspiration.

Publication Lists
Journal Publications

1. Qu K, Barreto G, Iten M, Wang Y, Riffat S. Energy and thermal performance of optimised hollow fibre liquid desiccant cooling and dehumidification systems in mediterranean regions: Modelling, validation and case study. Energy, Volume 263, Part C, 2023, DOI: https://doi.org/10.1016/j.energy.2022.125852.

2. Barreto G, Qu K, Wang Y, Iten M, Riffat S. An innovative window heat recovery (WHR) system with heat pipe technology: Analytical, CFD, experimental analysis and building retrofit performance. Energy Reports (2022), 8, pp. 3289 – 3305. DOI: https://doi.org/10.1016/j.egyr.2022.02.126.

3. Wang Y, Qu K, Chen X, Zhang X, Riffat S. A novel Energy-Flow based Ensemble Calibration model for rapid and accurate energy-economic performance prediction of deep energy retrofit in single-family houses. Energy Conversion and Management (2022), 258, DOI: https://doi.org/10.1016/j.enconman.2022.115507.

4. Wang Y, Qu K, Chen X, Gan G, Riffat S. An innovative retrofit Motivation-Objective-Criteria (MOC) approach integrating homeowners' engagement to unlocking low-energy retrofit in residential buildings. Energy and Buildings (2022), 259. DOI: https://doi.org/10.1016/j.enbuild.2022.111834.

5. Wang Y, Qu K, Chen X, Zhang X, Riffat S. Holistic electrification vs deep energy retrofits for optimal decarbonisation pathways of UK dwellings: A case study of the 1940s' British post-war masonry house. Energy (2022), 241. DOI: https://doi.org/10.1016/j.energy.2021.122935.

6. Emmanuel Tapia-Brito, James Riffat, Yixin Wang, Yuhao Wang, Amir M. Ghaemmaghami, Christopher M. Coleman, Mehmet T. Erdinç, Saffa Riffat. Experimental study of the purification performance of a MopFan-based photocatalytic air cleaning system. Building and Environment, Volume 240, 2023,110422, ISSN 0360-1323, https://doi.org/10.1016/j.buildenv.2023.110422.

International Conference Papers

1. Qu K, Wang Y, Barreto G, Iten M, Wang Y, Kosonen R, Riffat S. Energy performance Enhancement of Solar Assisted Heat Pump and building integrated PV/thermal storage system (PV-SAHP-TS) under different climate contexts. 19th International Conference on Sustainable Energy Technologies (SET 2019),

Istanbul, Turkey https://set2022.org/wp-content/uploads/2023/01/DRAFT%20proceedings%20SET2022%20Vol1.pdf .

2. Wang Y, Zheng T, Qu K, Luo M, Riffat S. Deep energy retrofit of historic residential buildings with the integration of prefabricated transparent insulation facades (TIF). 19th International Conference on Sustainable Energy Technologies (SET 2019), Istanbul, Turkey https://set2022.org/wp-content/uploads/2023/01/DRAFT%20proceedings%20SET2022%20Vol1.pdf.

3. Qu K, Wang Y, Chen X, Dodo A.M, Zheng T, Cimini V, Riffat S. An inclusive decision-making approach for selection of comprehensive energy-retrofit combinations in a typical Italian 1960s' multifamily house. (2021) ECOS 2021 - 34th International Conference on Efficency, Cost, Optimization, Simulation and Environmental Impact of Energy Systems, pp. 632 - 643. https://www.scopus.com/inward/record.uri?eid=2-s2.0-85134407776&partnerID=40&md5=f918fdc3bb73aaa02d5b59d95da23915

4. Qu K, Wang Y, Dodo A.M, Chen X, Pedro A.S, Riffat S. A data-driven based validation and calibration approach to building energy simulation model for accurate pre-retrofit design predictions. (2021) ECOS 2021 - 34th International Conference on Efficency, Cost, Optimization, Simulation and Environmental Impact of Energy Systems, pp. 827 – 838. https://www.scopus.com/inward/record.uri?eid=2-s2.0-85134400108&partnerID=40&md5=110ebaa9007e1942fd335fd6bf42bf07

Nomenclature

A	surface area (m^2)
ACH	air change per hour (h^{-1})
AH	absolute humidity (kg/m^3)
$AILMDD$	adjacently internally-cooled plate membrane liquid desiccant dehumidifier
$AROI$	annual return on investment (%)
$AWHP$	air-water heat pump
b	molality of electrolyte
C	concentration (%); constant number
CA	cellulose acetate
CHP	conventional heat pipe
$CMDR$	coefficient of moisture diffusive resistance
$CNPV$	cumulative discounted net present value
COP	coefficient of performance
c_p	specific heat capacity (J/kgK)
Cr	thermal capacity (W/K)
CRR	carbon reduction rate (%)
D	mass diffusivity (m^2/s)
DEG	diethylene glycol
d_h	hydraulic diameter of the fluid channel (m)
DPG	di-propylene glycol
DPP	discounted payback period (year)
$EPBD$	European performance building directive
ERR	energy reduction rate (%)
FIT	feed-in tariff (€)
F_R	heat extraction factor
$(fRe)_m$	mean Reynolds number
h	convective heat transfer coefficient (W/m^{2}K); operating factor
H	height of the membrane unit(m)
h_{fg}	water condensation heat (J/kg)
$HPHE$	heat pipe heat exchanger
$HP-ICMLDD$	heat pipe internally-cooled membrane-based liquid desiccant dehumidification
HX	heat exchanger
I	ionic strength (mol/kg)
$IHPMC$	internally-cooled hexagonal parallel-plate membrane channel
II	initial investment (€)
IL	ionic liquid
$ILDAC$	integrated liquid desiccant air-conditioning
$IMLDD$	internally-cooled plate membrane liquid desiccant dehumidifier
k	thermal conductivity (W/mK)

L	length of the dehumidifier and cooling box (m)
$LAMEE$	liquid-to-air membrane-based energy exchanger
$LCEC$	lifecycle energy cost (€)
LDD	liquid desiccant dehumidification
$LiCl$	lithium chloride
m	constant number
M	molecular weight (kg/mol)
$\dot{m}$	mass flow rate (kg/s)
MFR	moisture flux rate
MRR	moisture removal rate (kg/s)
NPV	net present value
$NTRL$	non-random two-liquid
NTU	number of heat transfer units
NTU_m	number of mass transfer units
NTU_w	number of heat transfer units of water
Nu	Nusselt number
OHP	oscillating heat pipe
P	pressure (Pa)
p	price (€)
Pe	Peclet number
PES	polyethersulfone
PG	propylene glycol
$P-H$	pressure-enthalpy
PHE	plate heat exchanger
Pr	Prandtl number
Pr_s	Prandtl number calculated by the heat pipe surface temperature
PV	photovoltaics
PVA	polyvinylalcohol
$PV-CDI$	photovoltaics-capacitive deionization
$PV-ED$	photovoltaics-electrodialysis
PVT	photovoltaics-thermal
Q	energy power (kW); volumetric flow rate (m³/s)
$QCPMCC$	quasi-counter flow parallel-plate membrane channels with cooling tubes
$QFPMC$	quasi-counter flow parallel-plate membrane contactor
r	heat pipe radius (m)
R	thermal resistance (m²K/W); bank interest rate (%)
RB	reference building
R_d	discount rate (%)
Re	Reynolds number
RH	relative humidity (%)
R_i	inflation rate (%)
ROI	return on investment (%)
R_r	real discount rate (%)
$RROR$	real rate of return (%)
Sc	Schmidt number

SEM	scanning electron micrograph
Sh	Sherwood number
T	temperature (℃)
TDR	temperature decrease rate
TEG	triethylene glycol
TH	solar thermal
$TPCT$	two-phase closed thermosyphon
$T-S$	temperature-entropy
U	the overall heat transfer coefficient (W/m^{2}K)
u	mean fluid velocity (m/s)
$UARS$	ultrasonic atomization liquid desiccant dehumidification/regeneration
U_m	the overall mass transfer coefficient (kg/m^{2}s)
U_x	variable uncertainty of measurement
U_y	variable uncertainty
W	humidity ratio (kg/kgdryair); power consumption (kW); width (m)
x_i	variable of measurement
X_{sol}	solution mass fraction (%)
Z	valence of electrolyte

Greek letters

ρ	density (kg/m^3)
δ	thickness (m)
ε	effectiveness
υ	kinematic viscosity (m^2/s)
α	fluid thermal diffusivity (m^2/s); constant number
γ	cooling box-to-dehumidifier height ratio
χ	closest approach parameter of the Pitzer-Debye-Huckel equation
η	efficiency
σ	energy consumption (kWh/m^2)
λ	carbon emission (kgCO$_2$/m^2)
ϕ	initial investment (€)

Subscripts

air	air flow
atm	atmosphere
c	cold fluid
C	cooling coil; cooling
cb	cooling box
d	duct
deh	dehumidifier
$desi$	desiccant
ele	electrical
exp	experimental
$exported$	PVT exported electricity to the grid (kWh)

fan	fan
$float$	float state
gas	natural gas
$grid - ele$	grid electricity
h	hot fluid
H	heating
hp	heat pipe
hp, a	heat pipe adiabatic section
hp, c	heat pipe condenser section
hp, e	heat pipe evaporator section
ic	internal cooling
in	inlet
lat	latent
lo	lower
max	maximum
mem	membrane
min	minimum
$moisture$	moisture of mass transfer
num	numerical
out	outlet
$pump$	pump
reg	regenerator
s	solvent
sen	sensible
sol	solution flow
th	thermal
tot	total
$upper$	upper
w	water flow

Superscripts

$*$	dimensionless

Chapter 1 Introduction

Chapter 1 is structured in the following sections: **section 1.1** gives a brief introduction to the background of this research; **section 1.2** states the existing research gaps of the liquid desiccant dehumidification systems; **section 1.3** provides with aims and objectives of this research; **section 1.4** presents the research novelties; **section 1.5** clarifies the detailed research methodology, and **section 1.6** summarises the thesis structure with the thesis structure flowchart.

1.1 Research background

Buildings consume around 40% of primary energy in the European Union [1], among them, 26% is used for air-conditioning [2]. Moreover, global warming has led to an average increase rate of 4% in space cooling demand since 2000, resulting in more energy requirements to maintain occupants' comfort level [3].

In the European Union (EU-28), while residential space cooling currently forms a minor share of sectoral final energy use (0.6% in 2015), it was the fastest-growing household end-use during 2000-2015, recording an average consumption growth rate of 6.3% per year [4], as shown in Fig 1-1.
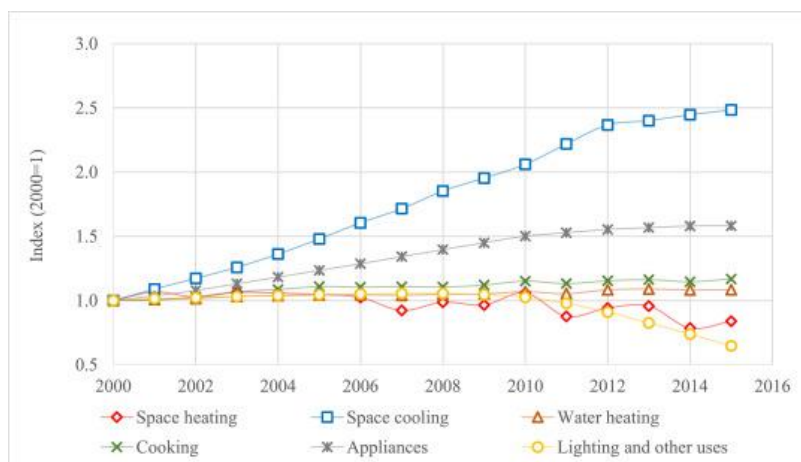
Fig 1-1 The average consumption growth rate in EU-28 countries [4]

Residential air-conditioning also has enormous future growth potential in the EU-28 as less than 10% of household floor area is currently cooled [5]. Since space cooling in EU-28 households is usually supplied through electric room air-conditioners (RACs [6]), the expected growth of residential AC markets across Europe will intensify pressure on national electricity sectors [7]. This translates into a need for additional off-site PV or wind electricity generation and more energy-efficient cooling systems, as well as humidity issues which are already evident in Mediterranean EU-28 countries [8].

Even evaluating only the warmest countries in Europe, cooling consumption is still considerably lower than heating. This is not because buildings are in good condition (35% of the buildings are older than 50 years, and more than 75% are considered inefficient [9]) but the general standards of comfort are not met in most dwellings. This is the case in hidden energy poverty, where households cannot guarantee comfort during the summer season. In addition, climate change has led to a 1.5-2 °C increase in global temperature compared to a pre-industrial scenario [10], making climates more extreme and endangering the most disadvantaged groups, particularly in cities where the "urban heat island" effect is added. Combined with only 0.4–1.2% of buildings being renovated yearly, these phenomena create a challenging problem that worsens yearly [10].

ASHRAE standard 55–2017 [11] states that 40%–60% of relative humidity must be maintained to meet human comfort requirements. With a traditional air-conditioner, the sensible heat can be removed successfully with dew-point cooling coils, however, latent heat removal brings the challenge to it [12]. Dehumidification using the cooling coils is the most common approach to removing the ambient air's excessive moisture content, consuming up to 50% of

total energy consumption [13, 14] with relative humidity and temperature at 70% and 30 °C or above [15]. Applying the dew-point cooling coils requires low-temperature cooling sources of approximately 5–10 °C, however, it could bring forward overcooling and reheating issues to the suppliers, leading to comfort cautions [16, 17] and low-energy efficiency [18, 19] simultaneously. Hence, adopting high-efficient dehumidification solutions for air-conditioning energy savings in hot and humid regions is urgent.

In addition, people spend around 90% of their time indoors [20]. Thus, the thermal comfort and health of humans can be considerably influenced by interior environmental characteristics such as temperature, humidity level, and air quality [21]. As a result of poor indoor air quality, it is stated that the productivity of office workers could fall by 6 to 9% [22].

Hence, improving air dehumidification efficiency plays a crucial role in the space cooling system [23, 12]. Conventionally, the dehumidification process of the air is accomplished by cooling the air below the dew point temperature to lower the moisture content in the cooling coil system. However, the overcooled air must be re-heated before being provided to the conditioned areas, which increases energy consumption [24-26].

In recent years, liquid desiccant dehumidification (LDD) has emerged as an efficient approach for air humidity control in the air conditioning process, which could deal with the latent load with desiccant absorption, regarded as an energy-saving and environmental-friendly alternative, where the LDD has the advantage of feasibility, highly efficient, cost-effective and has no liquid water condensation problem. The system can be regenerated by low-grade energy, such

as solar energy, and the regenerated solution can be used as an energy storage medium [27]. Typically, a liquid desiccant dehumidifier is used in conjunction with a sensible cooler to lower its temperature. Moreover, it could significantly increase the Coefficient of Performance (COP) of the combined refrigeration system with a vapour compression chiller [28], and it utilises liquid desiccant solution to absorb moisture from process air to reduce the latent cooling load.

Therefore, in order to solve the above-mentioned cooling and dehumidification issues in Mediterranean EU countries, it is urgent to adopt more energy-efficient cooling systems and integrate them with renewable technologies to supply building space cooling demand in Mediterranean EU countries.

1.2 Statement of the problems

Among different LDD structures, previous research focused on membrane-based liquid desiccant dehumidification systems to prevent carry-over issues [29], created by combining semi-permeable membranes with liquid desiccant dehumidification systems. Besides, the *LDD* can be classified as the adiabatic and internally-cooled types [30]. In the adiabatic type, the condensation heat generated increases the solution temperature during the water vapour absorbing process, which would largely deteriorate the dehumidification performances, as proved in literatures [31] [32] [33]. By contrast, the internally-cooled type is more energy-efficient than the adiabatic type, regarding 1) improving the dehumidification effectiveness [34], 2) enhancing the air cooling performance due to the solution temperature drop [35], and 3) reducing the circulating solution flow rate and pump power [30]. Experimental and numerical modelling analyses have been carried out on different internally-cooled dehumidifier types in the previous research [36-38].

4

However, although internal cooling methods are adopted by the traditional packed tower dehumidifier, the heat and mass transfer ability do not increase significantly compared with the internal cooling methods for flat-membrane dehumidifiers. Therefore, the internally-cooled flat membrane dehumidifier with higher heat transfer density and compactness should be focused on to enhance the heat and mass transfer performance. Using cooling channels adjacent to solution channels and cooling tubes within solution channels are two cooling approaches applicable to the internally-cooled type, both of which are simple to fabricate due to their simple structure. According to the aforementioned literature, even though the traditionally packed tower dehumidifier uses internal cooling methods, the heat and mass transfer capabilities do not increase significantly compared to the internal cooling methods for flat membrane dehumidifiers. The flat membrane dehumidifier with increased heat transfer density and compactness should be prioritised to improve the heat and mass transfer performance.

As a highly efficient heat recovery device, heat pipe heat exchanger ($HPHE$) has been widely employed in air conditioning and conventional cooling-based dehumidification systems. Studies show excellent performance in enhancing the energy efficiency in cooling-based dehumidification systems [39-42]. Long life and little required maintenance are inherent with heat pipes due to simplifying the design and construction of strong and durable materials without moving components [43]. However, few studies investigated the heat pipe internal cooling method in the membrane-based liquid desiccant dehumidification system. Besides, there is a lack of modelling of heat pipe internal cooling

application in the dehumidifier, as well as comprehensive parametric analysis of the operation control with the heat pipe internal cooling method.

Most research focused on theoretical and experimental studies, however, few studies investigated the operating energy performances in real building applications. In literature [26] [44] [45], the authors have applied the desiccant cooling and dehumidification system in real buildings with dynamic input air conditions where the system's COP is calculated under complex modelling methods. Without simplified COP correlations, the calculation results are irreplicable for practical implications in other retrofit projects. Besides, it is figured out that the system COP correlations are crucial for rapid and accurate post-retrofit building energy performance prediction considering the ambient conditions, especially in combinations with different building retrofit technologies, which have been proved by [39, 46-48].

In conclusion, several limitations exist in previous research regarding the internal cooling methods in membrane-based liquid desiccant dehumidification systems and their related building applications, which can be summarized in the following perspectives:

1) Lack of the heat pipe internal cooling method in the liquid desiccant dehumidification system;

2) Lack of system performance analysis of the heat pipe internally-cooled membraned-based liquid desiccant dehumidification system under various inlet and operating conditions;

3) Lack of correlations of system thermal and electrical COP and supply air temperature/relative humidity with variations of inlet air conditions;

4) Limited effort has been made to investigate the building energy performance in real buildings with a liquid desiccant dehumidification system under subtropical and humid Mediterranean climate conditions.

1.3 Research aim and objectives

Based on research background and current challenges, this PhD research aims at investigating a heat pipe internally-cooled liquid membrane-based desiccant dehumidification (HP-ICMLDD) system for multi-family terraced houses in subtropical and humid Mediterranean climate regions, which will be integrated with the air-water heat pump (AWHP), photovoltaics-thermal (PVT), and hot water storage systems as an integrated liquid desiccant air-conditioning (ILDAC) system.

In achieving this aim, several specific objectives have been carried out as below:

1) Evaluating the literature review on the liquid desiccant dehumidification system to give a comprehensive background and highlight the research gaps in the internal cooling structures, materials, modelling methods, effectiveness and energy performances of the membrane-based liquid desiccant dehumidification system;

2) Experimental analysis, validation and performance evaluation of the dehumidifier, regenerator and complete LDD systems under various conditions based on the experimental results;

3) Parametric analysis and optimization of the system operation strategy based on the thermal and energy efficiency of the complete LDD system;

4) Evaluating the energy, carbon and economic performances of the ILDAC system applied in three reference buildings under subtropical and humid Mediterranean climate regions.

1.4 Research novelties

The research novelties of this PhD study are:

1) Evaluating the performance of a heat pipe internally-cooled membraned-based liquid desiccant dehumidification system under various operation conditions and revealing the impact of cooling water temperature and flow rate on dehumidification effectiveness;

2) The system operation strategy is optimized based on the parametric analysis of the thermal and energy efficiency for the complete LDD system;

3) Deriving the thermal and electrical COP correlations of the complete LDD system, as well as the inlet and outlet air temperature and humidity correlations;

4) Simulating and assessing the energy, carbon and economic performances of the ILDAC system under subtropical and humid Mediterranean climate regions.

1.5 Research methodology

In this thesis, the methodology is mainly based on the following stages:

1) **Background investigation and literature review**: The increasingly building cooling and dehumidification demand due to climate change and the challenges of existing cooling and dehumidification systems have been studied and compared. Besides, the building overheating issue in subtropical and humid Mediterranean climate regions has been discussed with the proposed research gaps and solution methods;

2) **Model establishing and experimental validation**: A complete liquid desiccant dehumidification (LDD) system is established by integrating the dehumidifier and regenerator, combining the heat pipe internal cooling method with the membrane-based liquid desiccant dehumidification and regeneration process. Moreover, the ILDAC system simulation model is established via the IES VE and EnergyPro software;

3) **Performance evaluation of the complete LDD system**: The system effectiveness and energy performances of the dehumidifier, regenerator and complete LDD systems are evaluated under different parametric analyses. Besides, the optimal operating conditions of the complete LDD system are discussed with the derived thermal and electrical COP correlations and the inlet and outlet air temperature and humidity correlations;

4) **Techno-economic analysis of the ILDAC system in reference buildings**: The energy, carbon and economic performances of the ILDAC system are analysed in Spain, Italy and Greece reference buildings under subtropical and humid Mediterranean climate conditions. Meanwhile, sensitivity analyses are carried out under different economic parameters.

1.6 Thesis structure

This thesis is mainly organized into seven chapters and seven additional appendices to address the thesis aim and objectives, with the thesis structure flowchart presented in Fig 1-2:

Chapter 1 concisely introduces the thesis by outlining the research background, problem statement, aim and objectives, research novelties, research methodology and thesis structure;

Chapter 2 provides an in-depth systematic evaluation of the available literature on liquid desiccant dehumidification system-related technologies and internal cooling methods. The research gaps between published literatures and ongoing research are identified in this chapter;

Chapter 3 presents the experimental method for a heat pipe membrane-based liquid desiccant dehumidifier (HP-ICMLDD), membrane-based regenerator, complete liquid desiccant dehumidification (LDD) and the modelling of integrated liquid desiccant air-conditioning (ILDAC) systems;

Chapter 4 introduces the experimental set-up for the HP-ICMLDD, membrane-based regenerator and the complete LDD system, including the physical properties of the membrane, the air, desiccant solution and water transportation properties, the specifications of the experimental equipment and the primary measurement instruments with their corresponding accuracies;

Chapter 5 investigates the effectiveness and energy performances of the HP-ICMLDD, membrane-based regenerator and complete LDD systems under various inlet and operation conditions. Moreover, the system's optimal operating conditions are determined with the derived correlations of thermal and electrical COP and the inlet and outlet air temperature and humidity;

Chapter 6 evaluates the application of the ILDAC system in multi-family terraced houses in subtropical and humid Mediterranean climate regions with three reference building models in Spain, Italy and Greece. The building energy, carbon and economic performances applying the ILDAC system are discussed. The sensitivity analysis is carried out under different economic parameters (bank

interest rate, inflation rate and imported grid electricity and exported PV electricity tariff increasing rates);

Chapter 7 concludes the thesis by providing a summary of the principal conclusions and recommendations for future research.

Last but not least, the **Appendices** contain supplemental information such as the example calculations for components/system performance from original input data to final indicators, the reference building specifications and sensitivity analysis results.
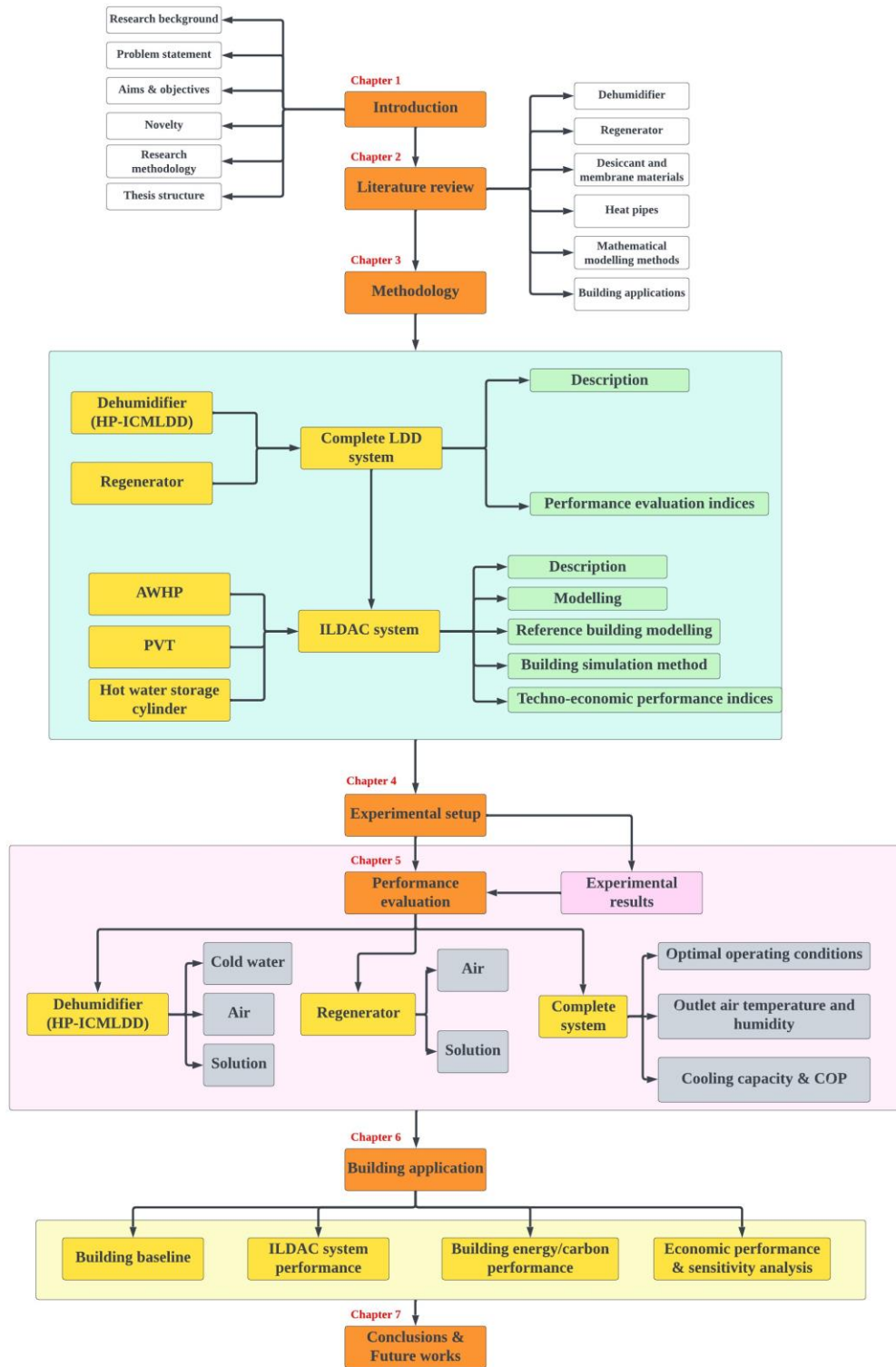
Fig 1-2 Thesis structure flowchart

Chapter 2 Literature Review

2.1 Introduction

This chapter provides a thorough literature evaluation of technologies linked to the liquid desiccant dehumidification system. The following subjects have been extensively discussed in critical literature:

Dehumidifier in **section 2.2**, including direct contact and membrane-based type, which are further categorised into hollow-fibre type, the adiabatic and internally-cooled membrane-based dehumidifier;

Regenerator in **section 2.3**, including direct contact and membrane-based type;

Materials of liquid desiccant and membranes in **section 2.4**;

Reviews of the heat pipe in **section 2.5**, including its structure, types and practical application in liquid desiccant dehumidification systems;

The different mathematical methods for the numerical modelling in **section 2.6**;

The applications of liquid desiccant dehumidification system in **section 2.7**;

The main findings and identified research gaps from the literature review are in **section 2.8**.

The objectives of the literature review are as follows: 1) to offer a full overview and evaluation of currently available literature on the issue; 2) to outline the research methodology; and 3) to identify the research gaps between published literatures and current research. To achieve these objectives, exhaustive reviews are conducted from various disciplines, including the components of the total liquid desiccant dehumidification system, the materials used for liquid desiccant and membrane, and the various mathematical methods developed for numerical

modelling. A concise description of the key results and research gaps between previous studies and the current study is presented in **section 2.8**.

2.2 Dehumidifier

In a liquid desiccant dehumidification system, the dehumidifier is the most important component. Liquid desiccant absorbs water vapour from humid air in the dehumidifier. Therefore, the literature review begins with the various types of dehumidifiers. In general, they can be separated into two distinct categories: direct contact and membrane-based.

2.2.1 The direct-contact type dehumidifier

In conventional liquid desiccant dehumidification systems, packed beds/columns are commonly used as dehumidifiers for heat and mass transfer. There are two primary varieties of direct contact dehumidifiers: adiabatic and internally cooled. The distinction between these types is whether the liquid desiccant's internal heat source is cooled within the dehumidifier. The adiabatic and internally-cooled dehumidifiers will be discussed in **sections 2.2.1.1** and **2.2.1.2**, respectively, where the latter will be emphasized and discussed thoroughly.

2.2.1.1 The adiabatic dehumidifier

Dehumidifiers of the adiabatic type are widely utilised in industrial and residential applications due to the following benefits:

1) Typically, the contact area between air and liquid desiccant is very large, resulting in relatively efficient heat and moisture transfer [49].

2) The geometry of the adiabatic dehumidifier is typically simple, resulting in generally low maintenance requirements [49].

Due to the lack of additional cooling for the liquid desiccant, during the dehumidification process in the dehumidifier, the temperature of the liquid desiccant would increase due to the release of latent heat, which would have a negative impact on the dehumidifier's performance. Moisture and temperature control of the processed air is consequently compromised. In addition, adiabatic dehumidifiers have the disadvantage of imposing a large pressure drop on the dehumidified air [49]. Moreover, the condensation heat generated in the solution side will make the solution temperature be increased during the water vapour absorbing process that transferred from the air across the membranes into the solution, which would largely deteriorate the dehumidification performances, as proven by literatures (Abdel-Salam et al. [31], Woods et al. [32], and Huang et al. [33]).

The structure of the adiabatic dehumidifier can be classified into spray tower and packed beds/columns types. In the spray tower type, the nozzle in the spray chamber breaks the liquid desiccant into small droplets, thereby increasing the contact area between air and liquid desiccant. The benefits of this type are its simple geometry and relatively low air pressure drop. However, its dehumidification efficiency is low, and the pressure drop on the solution side is significant [50]. Moreover, the spray tower types have been designed with finned coils, flat plate heat exchangers, and heat pipes to provide simultaneous cooling [51, 52]. The most common types of adiabatic direct contact dehumidifiers are packed beds/columns. They have numerous benefits, including high compactness, a large liquid-air contact area, a long liquid-air contact air, and high dehumidification effectiveness [50].

Numerous studies on packed beds and packed columns have been conducted. Zurigat et al. [53] conducted an experiment to determine the effectiveness of an air dehumidifier containing triethylene glycol (TEG) as a desiccant. Applying a packed bed column (dehumidifier) with a low packing density ($77m^2/m^3$) allowed for direct contact between the air and the TEG. Wood and aluminium are both utilised as structural packaging materials. The effectiveness of the column was found to be enhanced by increasing the TEG mass flow rate and TEG inlet temperature for both wood and aluminium packings. Babakhani and Soleymani et al. [54] proposed an analytical solution for air dehumidification by liquid desiccant in an adiabatic packed column based on a constant equilibrium humidity level at the interface. They compared their analytical solution to experimental data and found a high level of concordance. Factor and Grossman [55] used a randomly packed bed with liquid desiccant for solar air conditioning with a theoretical model developed to predict the performance of packed beds. They discovered that the packed bed performs well as a dehumidifier and that pressure drop can be reduced by using suitable packing. Patnaik. et al. [56] conducted experimental research on a solar open-cycle liquid desiccant dehumidification system employing a randomly packed column as the dehumidifier. The dehumidifier achieved a total cooling capacity of 3.5-14.0 kW (1.0-4.0 refrigeration tonnes). For randomly packed types, however, the required desiccant solution mass flow rate for good wetting and air side pressure drop is typically quite high. Elsarrag [57] utilised a packed column dehumidifier for the liquid desiccant dehumidification system. They noted that structured packed columns represent the most recent advancement in high efficiency and high packing capacity for heat and moisture transfer in comparison to randomly

packed columns. Additionally, they developed two mass transfer correlations for normal and high solution flows and predicted the mass transfer coefficient to be within 15%. Pietruschka et al. [58] used structured packed columns to present a new liquid desiccant dehumidification system for residential mechanical ventilation systems. A system-specific theoretical model was developed and compared to experimental data. According to their findings, the system can provide inlet air conditions with a temperature below 20 ℃ under the summer design conditions of 32 ℃ and 40% air relative humidity and generate a total of 886 W of cooling power when the air volume flow rate is 200 m^3/h.

In conclusion, all research on adiabatic type direct contact dehumidifiers focused primarily on structure optimization. In reality, the performance improvement is limited by the solution temperature increase of the dehumidifier caused by the latent heat release during the dehumidification process. A dehumidifier of the internally cooled type is an alternative to the adiabatic type, which will be discussed in the following section.

2.2.1.2 The internally-cooled dehumidifier

By contrast, the internally-cooled type is more energy-efficient than the adiabatic type, regarding 1) improving the dehumidification effectiveness [34], 2) enhancing the air cooling performance due to the solution temperature drop [35], and 3) reducing the circulating solution flow rate and pump power [30]. Experimental and numerical modelling analyses have been carried out on different internally-cooled dehumidifier types in the previous research [36-38]. Unlike the adiabatic type, the internally cooled type employs a cooling coil in the liquid side to remove the latent heat produced during dehumidification. The most important unit for this type is the cooling pipes installed in the liquid

desiccant; they must be kept strictly separate from the liquid desiccant. The structure of the dehumidifier unit is the focal point of this type. The internally-cooled dehumidifiers can be classified into two types: 1) packed tower with cooling tubes [30] [59], 2) parallel-plate dehumidifier [60, 38] and 3) fin-coil dehumidifier [61, 62]. The internally-cooled packed tower dehumidifier is widely used with finned tubes, Liu et al. [63] adopted an analytic solution to study the heat and mass transfer process in an internally cooled liquid desiccant dehumidifier using refrigerant as the cooling medium and found that the efficiency of the device is primarily influenced by three inlet parameters (dimensionless air enthalpy, dimensionless air humidity ratios, dimensionless solution humidity ratios), one operating parameter (thermal capacity ratio m^*), and two device parameters (mass transfer numbers of unit NTU_m and dimensionless transfer area ratio NTU_R). Similarly, Li et al. [64] investigated the internal cooling effect with cooling tubes in the liquid desiccant solution channel, where the cold water flows through the cooling tubes and cools the desiccant solution during the dehumidification process. The moisture removal rate and sensible and total cooling capacity gradually increase slowly with the mass flow ratio of cooling water to the air from 1 to 5. Besides, in such a dehumidifier, air flow and solution flow can be arranged as cross flow, parallel flow, or counter flow. A layer of exterior insulation is applied to the dehumidifier to prevent external heat gain. Both cold water and refrigerant are investigated as cooling mediums of the packed tower with finned tubes, where the solution heat is removed in sensible and latent heat, respectively. The packed-bed with cooling coils is the most common type of dehumidifier with both water and refrigerants as the cooling medium, which has been investigated in many types of research.

Fig 2-1 depicts a typical packed column with a cooling pipe in which embedded cooling coils remove latent heat [65, 66].
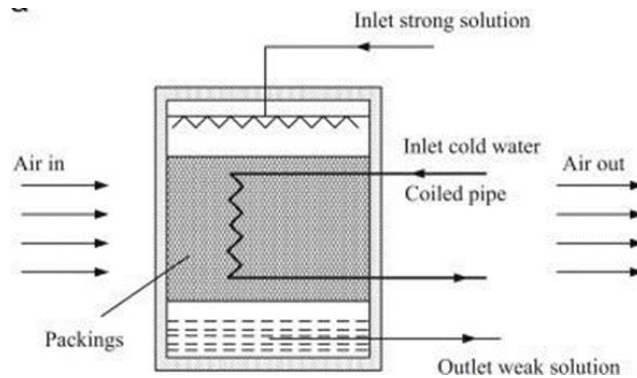
Fig 2-1 Schematic diagram of a packed column with cooling pipe dehumidifier [65, 66]

Bansal et al. [67] studied an internally cooled structured packed-bed dehumidifier that employs rigid media pads with cooling water flowing through tubes embedded in the packing. LiCl was utilised as the liquid desiccant, which flows by gravity, whereas air flows in a cross-flow configuration. Comparing the moisture removal rate and dehumidifier effectiveness of an adiabatic dehumidifier and an internally cooled dehumidifier, they discovered that the maximum effectiveness of an internally cooled dehumidifier ranges from 0.55 to 0.71, whereas it ranges from 0.38 to 0.55 for an adiabatic dehumidifier.

The parallel-plate structure is the second type of dehumidifier with internal cooling. Yin et al. [68] conducted experiments on an internally cooled parallel-plate type dehumidifier, as depicted in Fig 2-2.
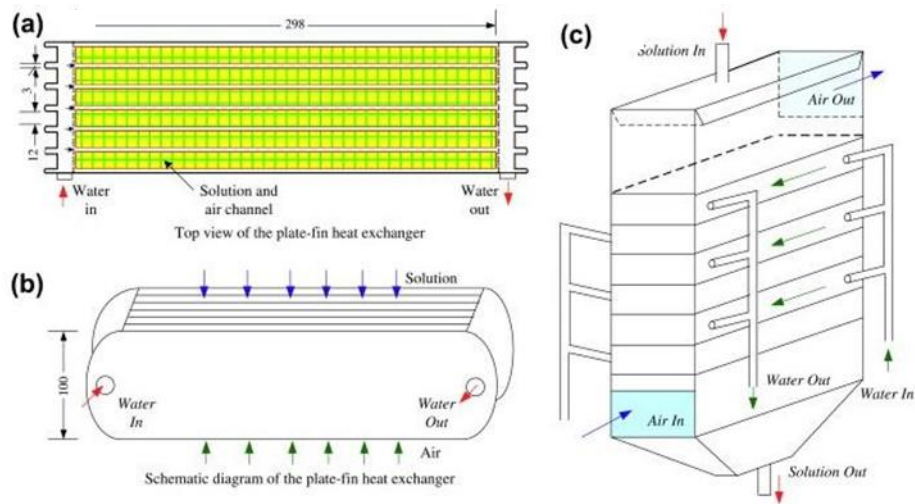
Fig 2-2 Schematic of parallel-plate internally cooled dehumidifier [68]

The desiccant solution is sprayed from the top of the dehumidifier to the bottom, driven by gravity, while humid air is blown from the bottom of the dehumidifier in a counter-flow configuration. Inside the plate, cooling water is pumped through cooling pipes to remove phase change heat. It is concluded that the desiccant with the lowest temperature possesses a greater mass transfer coefficient. As a result, a desiccant with a lower temperature and a desiccant with an internal cooling system can provide a more effective dehumidification effect. Kessling et al. [69] developed and experimentally tested a dehumidifier with an internally cool plastic plate structure. The plate is 0.46m tall, 0.98m wide, and 5.5mm thick. The distance between adjacent parallel plates in this dehumidifier is 5.5mm, and the plate's heat transfer coefficient is approximately 170 W/m^{2}K. In horizontal channels within the double plates, cooling water was circulated. A numerical model was created to simulate the performance of a dehumidifier, and a good agreement between numerical and experimental results was achieved. Due to the relatively small thickness of the plate, the dehumidifier demonstrated satisfactory heat transfer between liquid desiccant and cooling water, and the

dehumidification performance was satisfactory even with a low desiccant flow rate. Yoon et al. [70] created a new internally water-cooled vertical plate absorber. In their design, the spaces between vertical plates were uniform. Liquid desiccant flows under the influence of gravity down each vertical plate along both sides, and the solution in the falling film can be cooled by water flowing in a counter-flow configuration. They also developed a numerical model for analysis, and the results demonstrated effective dehumidification because the latent heat released in the solution channel can be effectively removed by cooling water in an adjacent channel.

Fin-coil dehumidifiers are another internally cooled dehumidifier in which cooling water flows within the coil to cool the liquid desiccant that flows from the top of the unit. The air can then be blown either from the front or the bottom of the fin coil. Liu et al. [27] experimentally examined a thermoconductive plastic fin-coil dehumidifier with an internal cooling system. Their dehumidifier is an eight-row heat exchanger with eight parallel channels in each row. As a result of the installation of tubes with fins in the dehumidifier to increase the unit's contact area, the moisture transfer between solution and air is significantly enhanced. The cooling water from a water separator enters the dehumidifier from the bottom and is collected at the top of the unit. Experimental and simulation analyses concluded that the moisture removal rate m_w increases with the solution flow rate, indicating that an increase in the solution flow rate would significantly increase the heat and mass transfer coefficient. Zhang et al. [71] designed a dehumidifier with stainless steel fins to enhance the heat and mass transfer coefficients by increasing the contact area. The fin is 0.127 mm thick,

and the distance between adjacent fins is 2.2 mm. Fig 2-3 is a diagrammatic representation of a dehumidifier of this type.
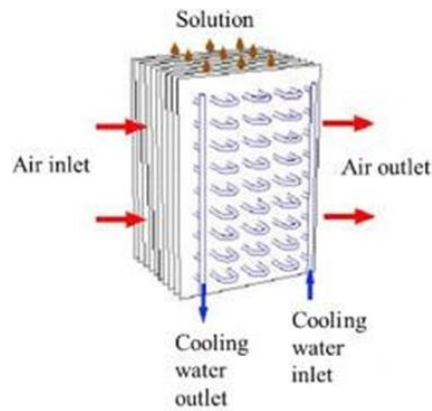
Fig 2-3 Schematic diagram of fin-coil type internally cooled dehumidifier [71]

The dehumidifier has eight rows with 22 cooling water channels per row. The distance between the centres of two adjacent pipes measures 25.4 mm. The lithium bromide was used as a liquid desiccant to conduct experiments under various conditions. For the prediction of this dehumidifier, an experimentally validated numerical model was used. According to their findings, the system coefficient of performance (COP) ranges between 4.2 and 6.5, and it increases as the processed air's relative humidity decreases. Furthermore, Liu et al. conducted [60] detailed quantitative comparisons of three common types of internally-cooled direct contact dehumidifiers (packed column, parallel plate, and fin-coil). Among the three types, the packed column with internal cooling tubes performed most similarly to an adiabatic type, and its dehumidification effect was inferior to those of the other two types. In contrast, the performance of the fin-coil type dehumidifier is superior under a variety of inlet conditions. The primary distinction between these three types is their ability to transfer mass;

therefore, more effort should be devoted to enhancing the mass transfer between air and desiccant solution.

In conclusion, internally-cooled dehumidifiers are more energy-efficient than adiabatic dehumidifiers, as they can improve the dehumidification effectiveness, enhance the air cooling performance due to the solution temperature drop, and reduce the circulating solution flow rate and pump power. In previous research, experimental and numerical modelling analyses have been carried out on different internally-cooled dehumidifier types to optimize their performance.

2.2.2 The membrane-based type dehumidifier

Concerning the structure of membranes, such types of dehumidifiers can be further divided into adiabatic and internally-cooled membrane-based dehumidifiers, with hollow-fibre and flat-membrane types. The hollow-fibre type is normally formed by layers of flat membranes being stacked together in a plastic shell. In the hollow-fibre type dehumidifier, the solution flows inside numerous hollow fibre tubes, and air flows in the shell side, similar to a tube-and-shell heat exchanger. They are contained within a rectangular or circular shell to create a complete hollow-fibre dehumidifier. As its name implies, flat-plate dehumidifiers typically comprise stacked layers of flat membranes and lack internal cooling sources. Differ from the adiabatic membrane-based dehumidifiers, more attention has been paid to investigating the internal cooling solutions for flat plate membrane-based heat and mass transfer, which could be divided into two types: 1) adjacent plate to the solution channel and 2) cooling tubes inside the solution channels. The adiabatic and internally-cooled membraned-based dehumidifiers will be discussed in **sections 2.2.2.1** and **2.2.2.2,** respectively.

2.2.2.1 The adiabatic membrane-based dehumidifiers

The adiabatic membrane-based dehumidifiers mainly contain two types regarding their different structures, where the first one is the flat-plate type, and the other is the hollow-fibre type.

Flat-plate type:

The flat-plate dehumidifier has numerous benefits. Firstly, the pressure losses in the solution and air channels are relatively low, necessitating less pump or fan power. Secondly, the structure of the flat-plate type is straightforward, which facilitates the construction and maintenance of the system [49]. Operating a system with a flat-plate dehumidifier is more dependable, and sealing desiccant solution is significantly simpler for flat-plate structures than other structures [72, 73]. As depicted in Fig 2-4, Zhang et al. [74] developed a cross-flow enthalpy exchanger, where the intake air and exhaust air flow in two adjacent channels in a cross-flow configuration with a membrane thickness of 100 μm. The CFD modelling was used to calculate the fully developed Nusselt number Nu_C and the Nusselt number under uniform heat flux boundary condition Nu_H, where the former is generally found to be less than that of the latter one, and Nu_C is greater than the Nusselt number under the constant temperature boundary condition Nu_T for large aspect ratios but 37% less than Nu_T for small aspect ratios.
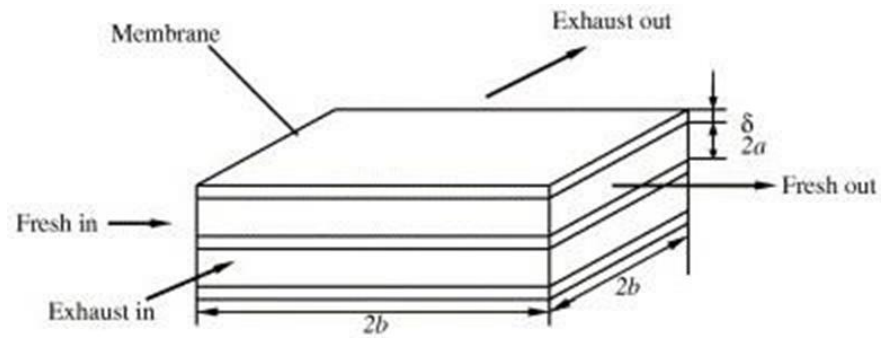
Fig 2-4 Schematic diagram of flat-plate air-to-air heat and mass exchanger [74]

Niu and Zhang [75] numerically investigated the effects of dimensionless parameters, membrane material, and moisture resistance clarification. According to their research, the membrane material with a linear sorption curve performed better than other materials. A new Coefficient of Moisture Diffusive Resistance (CMDR) was introduced to improve the performance prediction of the enthalpy exchanger. Abdel-Salam et al. [76] investigated the performance of a counter-flow membrane liquid desiccant air-conditioning system through experimentation. The dehumidifier unit has a height of 1 m, a length of 2 m, and a total of 250 solution channels. Each solution channel has a thickness of 3.17 mm, while the air channel has a thickness of 6.35 mm. The membrane is composed of polyethylene and has a thickness of 0.54 mm. They evaluated the effects of various parameters, such as the number of heat transfer units NTU, solution inlet temperature, and thermal capacity ratio Cr^*, to investigate the system's performance experimentally. The results indicated that the solution inlet temperature should be set between 15 °C and 20 °C for optimal dehumidification performance. The ideal NTU and Cr^* values are 5-10 and 3-5, respectively. Fan et al. [77] invented a cross-flow plate heat and mass exchanger in which the solution and air flow are arranged in a cross-flow configuration. A two-

dimensional steady-state numerical model was utilised to simulate heat and mass transfer in a dehumidification system employing LiCl as a liquid desiccant. It has been demonstrated that up to 70% of overall effectiveness can be attained if the correct dehumidifier size and operating conditions are chosen. Besides, the mathematical model for a cross-flow membrane enthalpy exchanger was developed by Min and Su [78], and the effects of membrane parameters on the effectiveness of the exchanger were investigated. Due to the fact that membrane resistance accounts for a small portion of total resistance, their findings demonstrate that membrane parameters have little effect on sensible effectiveness. In the meantime, the latent effectiveness varies significantly more with membrane parameters as the membrane's resistance to moisture decreases dramatically. Namvar et al. [79] compared the steady-state and transient performance of a counter-cross-flow membrane energy exchanger using experimental tests conducted in the summer and winter. The sensible and latent effectiveness of the dehumidifier increased during the dehumidifier's transient period before reaching a steady-state value. Huang et al. [80] investigated a dehumidifier with a similar structure, the so-called quasi-counter flow parallel-plate membrane contractor (QFPMC). The solution flows along an S-shaped path line in solution channels, configuring between counter and cross flow. According to their research, the sensible and latent efficacy of these QFPMCs decrease by 5%-29% and 2%-13% compared to a cross-flow parallel-plate membrane contractor. The pressure drop on the solution side is increased by approximately 0.15 to 4.84 times.

Hollow-fibre type:

The construction of hollow-fibre membrane heat exchangers resembles that of parallel tube-and-shell heat exchangers. Air can theoretically flow either inside (tube side) or outside (shell side) the fibres for a liquid-to-air hollow fibre membrane contractor. However, in the majority of applications, air flows outside the fibres while desiccant solution flows inside. The reason for this structure is that air flows into the shell side with significantly lower pressure drops, resulting in improved performance [81]. Regarding the flow pattern within the hollow-fibre membrane module, solution and air flow may be parallel (longitudinal) or cross. For parallel flow, solution and air flow parallel to one another on opposite sides of hollow fibres, with co-current or counter-current flows possible [81]. Zhang et al. [72, 73] studied analytically and numerically the heat and mass transfer in a dehumidification module containing a counter-flow hollow-fibre membrane. Fig 2-5 depicts the structure of the hollow fibre membrane module with counter-flow.
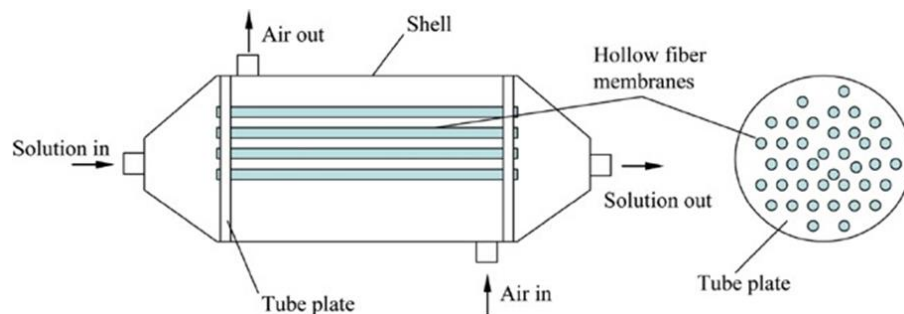
Fig 2-5 Structure of the counter-flow hollow fibre membrane module [72, 73]

200 hollow fibres were installed in a circular shell to form a complete module. The outer diameter of hollow fibres is 750 μm, and the inner diameter is 600 μm. After proposing a relatively simple analytical solution, the conjugate heat and mass transfer problem was solved using the free surface method. Using the finite volume method, the conjugate heat and mass transfer problems were solved, and

the velocity, temperature, and concentration distributions for air flow, solution flow, and membranes were determined, as well as the local and mean Nusselt number and Sherwood number. As depicted in Fig 2-6, Huang et al. [82] developed a cross-flow hollow-fibre membrane contractor.
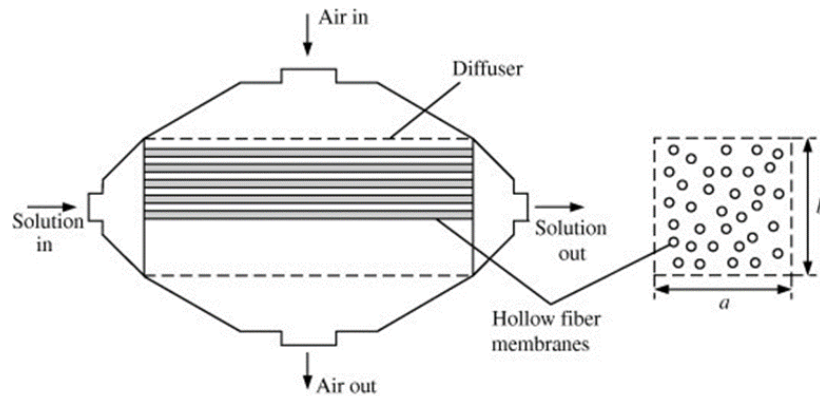
Fig 2-6 Structure of the cross-flow hollow fibre membrane module [82]

In contrast to a counter-flow contractor, a cross-flow contractor has a rectangular section through which both solution and air flow in a cross-pattern. The rectangular shell box was outfitted with 600 fibres in total. The outer and inner diameters of hollow fibres are identical to those of counter-flow contractors. Under the assumption of laminar air flow across the fibre bank, the conjugate heat and mass transfer was initially analysed using the free surface method. Subsequently, a more realistic and intricate scenario was considered by assuming that the air flow across the fibre bank tends to be turbulent. Air flow turbulence was modelled using a low-Re $k - \varepsilon$ turbulence model, whereas solution flow was modelled using a laminar model. Using experimental data, friction factors and the Nusselt and Sherwood numbers were determined and validated for both scenarios.

In conclusion, hollow-fibre membrane contractors offer higher performance and greater packing density than flat-plate. They can be classified according to their structure as parallel-flow, cross-flow, and coil types. The investigation of more realistic scenarios, such as asymmetrical flow and elliptical fibre shapes, has occurred. However, relatively high pressure drop on the tube side and a complex structure are two of the largest drawbacks for applications of this type. Consequently, flat-plate type membrane contractors are utilised far more frequently in practice than hollow-fiber type membrane contractors.

Previous research has determined that all membrane-based dehumidifiers are adiabatic, so the solution is heated by absorption heat released on the solution side. Consequently, the dehumidification effect may be diminished if the solution temperature rises. Similar to internally-cooled direct contact dehumidifiers, internally cooled membrane-based dehumidifiers have been created and studied in the following section.

2.2.2.2 The internally-cooled membrane-based dehumidifiers

Recently, more attention has been paid to investigating the internal cooling solutions for flat plate membrane-based heat and mass transfer, which could be divided into two types: 1) adjacent plate to the solution channel and 2) cooling tubes inside the solution channels. Huang et al. [34] proposed an adjacently internally-cooled plate membrane liquid desiccant dehumidifier (AIMLDD). The solution streams absorb the heat and water vapour moisture from the feed air through the plate membrane, while the absorption heat generated in the solution can be taken away by the water in the neighbouring channel. Cooling effectiveness, dehumidification effectiveness and dehumidification rate are calculated through an analytical solution and experimentally validated. The

performances of the AIMLDD are compared with those of an internally-cooled plate membrane liquid desiccant dehumidifier with cooling tubes inside the solution channels (IMLDD). The performances of the AIMLDD are about 3.3–9.1% higher than those of the IMLDD. Huang et al. [83] also constructed an IMLDD with a cross-flow configuration to enhance dehumidification, as depicted in Fig 2-7.
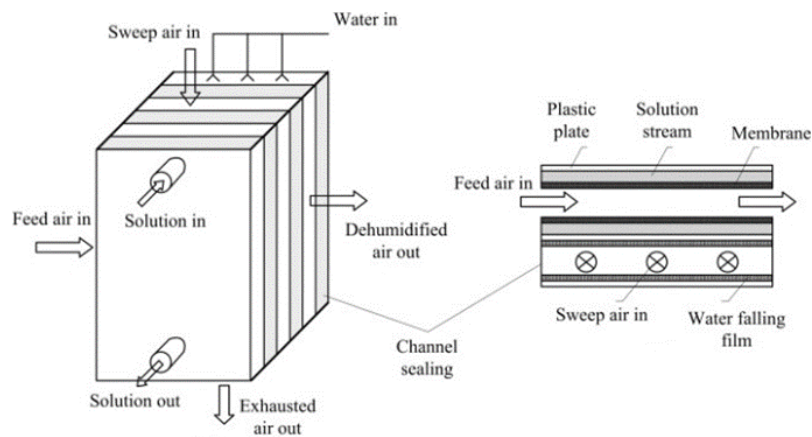
Fig 2-7 The structure of a cross-flow IMLDD [83]

Channels are constructed by stacking membranes and plastic plates, where the cross-flow configuration separates the feed air (process air) and liquid desiccant using membranes. The cooling water flows vertically along the plastic plates so water-falling films can form in the water channel. Next to water channels are solution channels that are separated by plastic plates. In a cocurrent configuration, the sweep air flows over falling water films. When heat is released into the solution channel, it is absorbed by falling water through plastic plates and extracted by sweeping air via evaporation. Numerical modelling and experimental tests reveal that the fully developed Nusselt and Sherwood numbers of cross-flow IMLDD in feed air and solution channels are 2 to 3% less than those of an adiabatic-type dehumidifier. Yang et al. [84] investigated the

performance of an internally cooled dehumidifier with cooling tubes inside the solution channel. In the dehumidifier, the air and the solution flow in the adjacent channels with a cross-flow configuration, while the cooling water in the tubes flows counter with the solution. Therefore, the increased sensible heat inside the solution could be taken away by the cooling water, where the outdoor air is cooled and dehumidified in the dehumidifier and then supplied to the indoors. Cooling water can effectively reduce the temperature and humidity ratio of the supply air. However, the effect on the system performance decreases with the rise of the water flow rate. Besides, it is found that changing the cooling water temperature is an effective means of regulating supply air conditions. Liu et al. [60] compared three typical internal cooling methods inside the dehumidifier, including parallel plate, fin coil and cooling tubes. The results indicate that the internally-cooled dehumidifier with the fin-coil structure adjacent to the solution channel has superior performance compared to the other two systems due to the highest heat transfer coefficients. Moreover, the packed tower with cooling tubes behaves much more like an adiabatic device, and its dehumidification performance showed apparent disadvantages compared to the other two types. Besides, Saman and Alizadeh [85] proposed another type of internally-cooled dehumidifier, as shown in Fig 2-8.
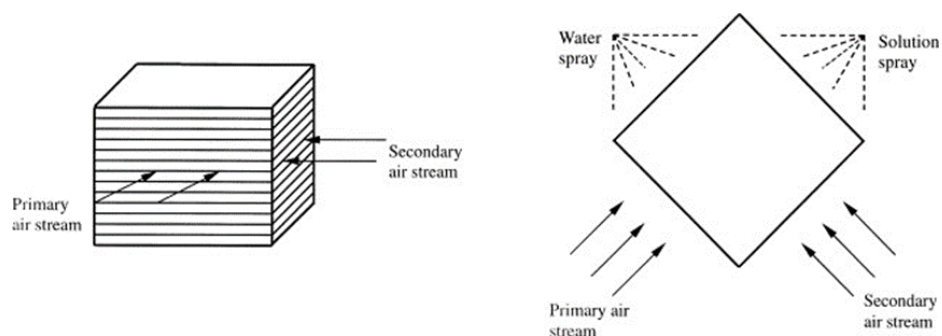
Fig 2-8 Schematic of an internally-cooled cross-flow type dehumidifier [85]

As seen, any two adjacent flow channels are separated by a flat plate that cools and dehumidifies the primary air. On one side of the plate, humid and warm primary air directly interacts with the liquid desiccant. On the opposite side of the plate, a secondary air, often returned air from air-conditioned rooms, is brought into contact with cooling water so that the phase change heat emitted by the primary air can be absorbed by the secondary air concurrently. Given that the room return air has a lower relative humidity than the external air, it can be exploited to enhance the performance of the secondary air side, so aiding in the maintenance of a nearly isothermal operation in each dehumidifier channel. According to their experimental findings, the mass transfer coefficient of a dehumidifier increases with primary air mass flow rate, temperature, and humidity level. In addition, the dehumidification efficiency can be enhanced by raising the angle of the plate heat exchanger (PHE). As indicated in Fig 2-9, Huang et al. [86] created the quasi-counter flow parallel-plate membrane channels with cooling tubes (QCPMCC).
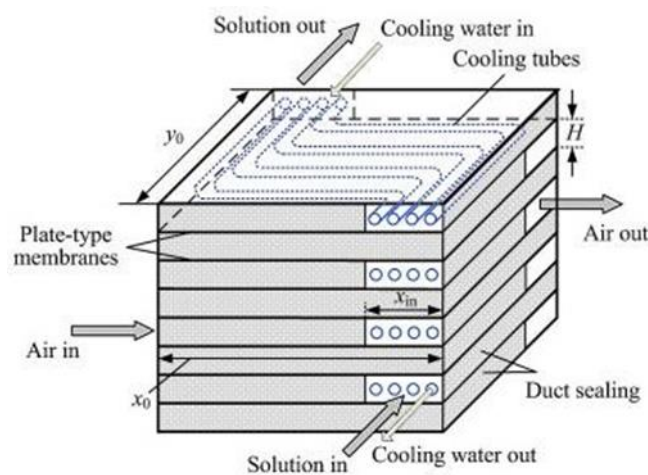
Fig 2-9 The structure of a quasi-counter flow parallel-plate membrane contractor with cooling tubes [86]

As illustrated in Fig 2-9, the solution flows into and out of the contractor through side ports, and solution and air flows are configured in a quasi-counterflow manner. Multiple Z-shaped cooling tubes containing cooling water are put in solution channels to remove absorption heat. Each channel is 0.1m in length and 0.1m in width and four cooling tubes with an outside diameter of 0.003 mm are installed. The focus of the study was primarily on the effects of channel structural features on friction factors and Nusselt numbers. Under an outer tube diameter of 0.003 m, it was observed that the mean Reynolds number $(fRe)_m$ grows with the tube number N_{tube}, whereas the mean Nusselt number Nu_m decreases with N_{tube}. When the number of tubes remains constant (4 in their instance), the $(fRe)_m$ increases with the tube's outer diameter, while the Nu_m declines. Moreover, Huang et al. [33] proposed an analytical solution for a desiccant plate membrane dehumidifier with a similar structure to QCPMCC. Nonetheless, the cooling tubes inserted in solution channels are not S-shaped but straight. The solution and air fluxes are in a counter-flow configuration. Their analytical solution implied that the dehumidifier's performance could be enhanced by controlling the solution's inlet temperature to be comparatively low. Abdel-Salam et al. [87] designed and studied a novel three-fluid liquid-to-air membrane-based energy exchanger (three-fluid LAMEE), as depicted in Fig 2-10.

(a)   (b)

(c)
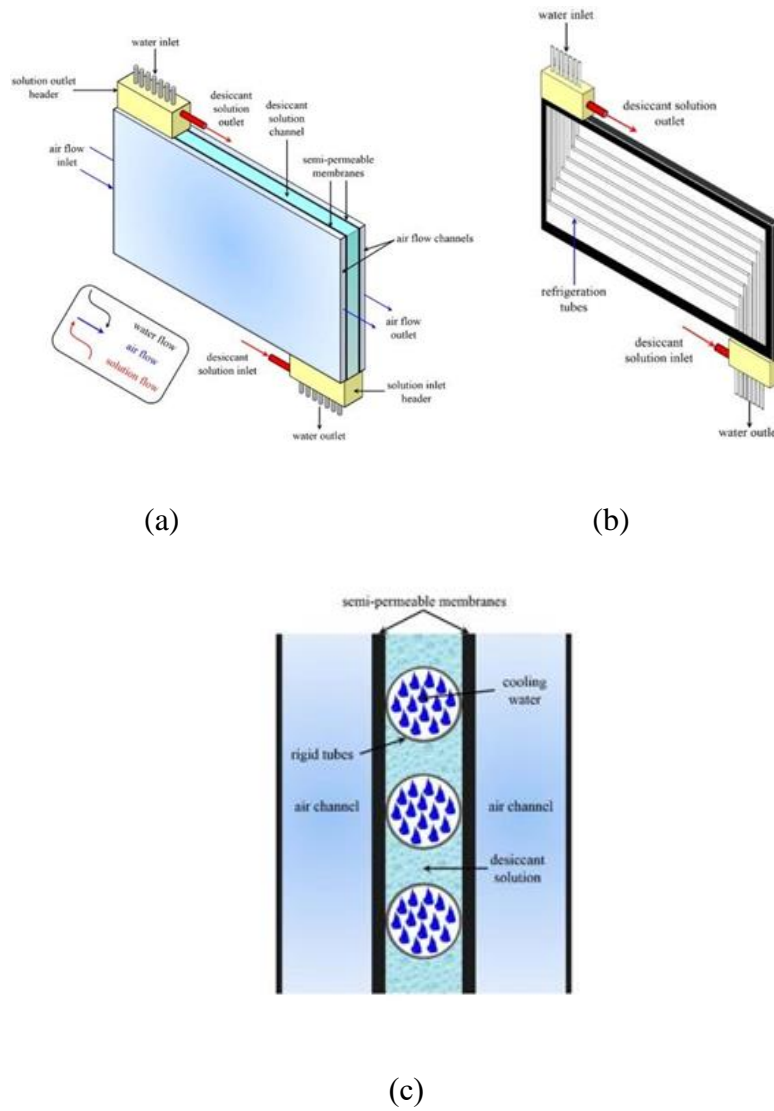
Fig 2-10 Schematic diagram of 3-fluid LAMEE; (a) prototype of 3-fluid

LAMEE; (b) solution channel with cooling tubes and (c) cross-section view

[87]

In such three-fluid LAMEE, solution and air flow in a counter-cross

configuration, whilst solution and refrigeration (water) flow in a counter

arrangement. The length and height of the device are 470 mm and 100 mm,

respectively. The membrane thickness is 0.3 mm. The solution channel contains

a total of seven Titanium refrigeration tubes with an inner diameter of 2.362 mm

and an outside diameter of 3.175 mm, in which water is utilised as the refrigerant.

The performance of the three-fluid LAMEE is superior to that of the two-fluid LAMEE introduced previously (adiabatic LAMEE), as the same effectiveness can be reached with lower NTU and Cr^*. As a result, the size of such LAMEE can be drastically decreased if the three-fluid design is implemented. Qiu et al. [88] designed a novel internally-cooled hexagonal parallel-plate membrane channel (IHPMC) for dehumidifying air, as depicted in Fig 2-11.

(a)   (b)

(c)
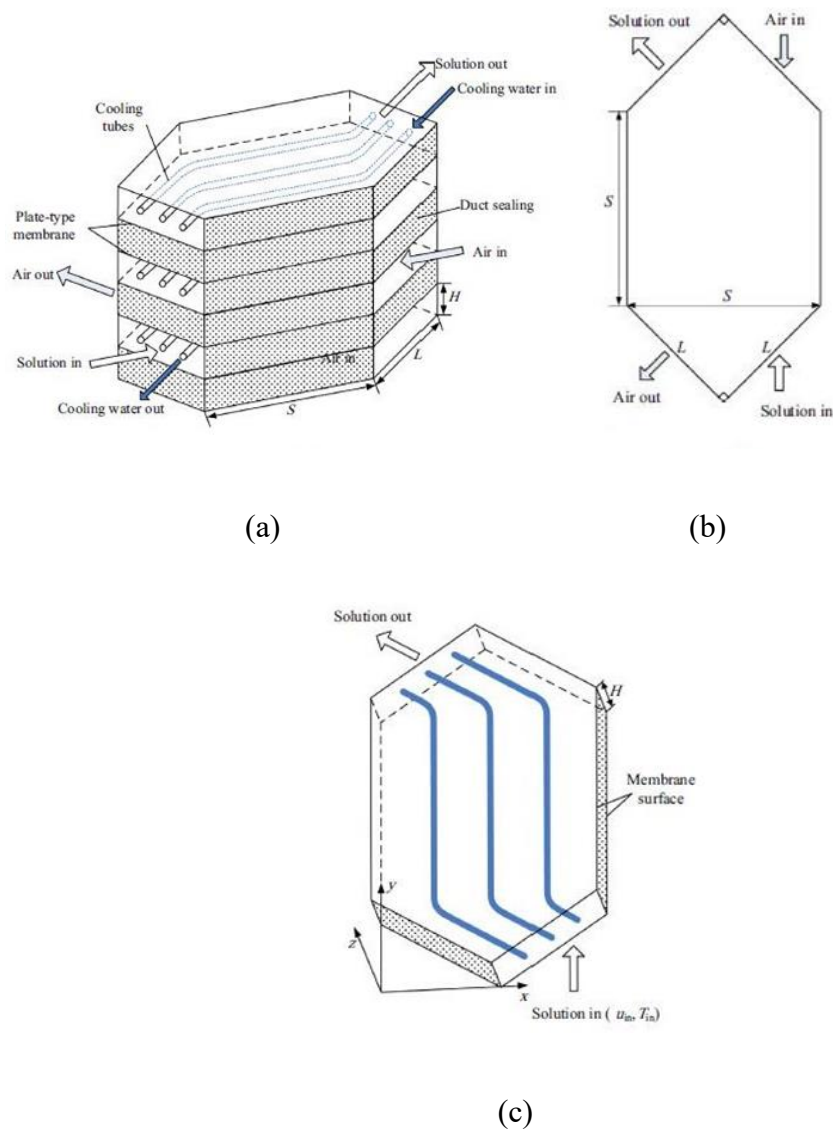
Fig 2-11 (a) schematic of IHPMC; (b) 3-D structure plan view and (c) calculation domain [88]

Another quasi-counter flow membrane channel type is the hexagonal configuration (side-in and side-out structure). Compared to side-in and side-out structures, hexagonal structures experience less pressure drop [89]. Layers of internally-cooled hexagonal parallel-plate membrane channels (IHPMC) and HPMC are compressed to form the module. Air and solution enter the contractor through its right inlets and exit through its left inlets, arranged in a quasi-counterflow configuration. Three cooling tubes containing water as the refrigerant are installed in HPMC to form IHPMC, and solution and cooling water are configured in counter-flow. The fluid flow and heat transfer in IHPMC were studied through the finite volume approach, which was solved by the CFD software. They calculated the fundamental numbers of the mean $(fRe)_m$ and mean Nusselt number Nu_m and they found that under the fixed cooling tube outer diameter of 0.002m, the $(fRe)_m$ increases and Nu_m decreases with the total tube number. By contrast, under the fixed total tube number of 3, the $(fRe)_m$ increases and Nu_m decreases with the tube's outer diameter.

In conclusion, numerous studies on flat-plate membrane-based dehumidifiers have been conducted on various topics. Depending on the flow arrangement, they can be parallel-flow, cross-flow, counter-cross-flow, or quasi-counter-flow. Based on their structure, they can be classified as either adiabatic or internally-cooled. Using cooling channels adjacent to solution channels and cooling tubes within solution channels are two cooling approaches applicable to the internally-cooled type, both of which are simple to fabricate due to their simple structure. According to the aforementioned literature, even though the traditionally packed tower dehumidifier uses internal cooling methods, the heat and mass transfer capabilities do not increase significantly compared to the internal cooling

methods for flat membrane dehumidifiers. The flat membrane dehumidifier with increased heat transfer density and compactness should be prioritised to improve the heat and mass transfer performance.

2.3 Regenerator

For a complete liquid desiccant dehumidification system, regeneration is one of the most important processes, as the diluted solution generated by the dehumidifier must be re-concentrated to recycle the solution. Similar to dehumidifiers, regenerators can be divided into direct contact and membrane-based types based on the module structure, which will be discussed respectively in **sections 2.3.1** and **2.3.2**.

2.3.1 Direct-contact type regenerator

Similar to direct contact dehumidifiers, the primary structure of direct contact regenerators consists of packed beds or columns. Regarding their flow patterns, liquid desiccant and air can be classified as either counter or cross flow. Nada et al. [90] investigated air regeneration numerically by a liquid desiccant falling over a rectangular finned-tube heat exchanger with three alternative air flow arrangements: parallel flow, counter flow, and cross flow. According to their design, the desiccant solution falls on a vertical rectangular fin surface while air travels through the spaces between neighbouring fins. The air flow and film solution flow may be configured in a variety of ways, including parallel flow (same direction), counter flow (opposite direction), and cross-flow (perpendicular direction). Kim et al. [91] formulated a simplified first-order empirical model for a cross-flow packed-bed tower regenerator employing LiCl as the working fluid. As the regenerator in the investigation, a honeycomb-structured packed tower was utilised. The regenerator had an internal diameter of 0.01 m and a volume of 0.31 m^2 using wood fibre structured packing with a

specific surface area of 223 m^2/m^3. The desiccant solution was sprayed from the top of the regenerator and distributed equally throughout the packing. The inlet air made direct contact with the solution, resulting in the transfer of thermal mass, where such a model can be used to determine the optimal regeneration temperature or desiccant mass flow rate in order to reduce the operating energy consumption. Yang et al. [92] created an ultrasonic atomization liquid desiccant dehumidification/regeneration (UARS) system, as presented in Fig 2-12. The mass transfer performance in such a system is significantly improved by atomizing the desiccant solution into multiple tiny droplets with a diameter of about 50 m.
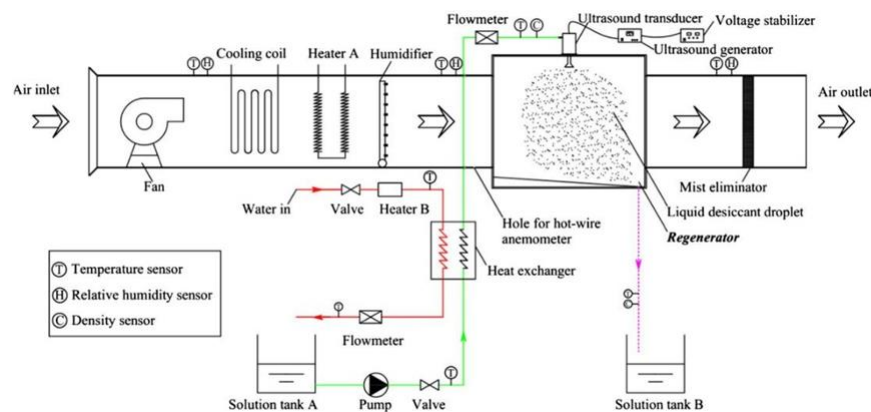
Fig 2-12 Schematic diagram of an ultrasonic atomization liquid desiccant regeneration system (UARS) [92]

The most important component of the system is the ultrasonic atomization system, which includes an ultrasonic generator, an ultrasonic transducer, and a voltage stabiliser. The ultrasonic generator may generate ultrasonic signals, which can then be transferred to the ultrasonic transducer, where high-frequency vibrations can be produced. The vibrations and cavitation action permit the atomization of desiccant solution into microscopic droplets. As little as 50 μm

in diameter, the droplets can be found. The results demonstrated that the UARS is superior to conventional packed bed regenerators. For regenerating a unit mass flow of desiccant solution, the required regeneration temperature can be decreased by 4.4 ℃, and the potential power savings can reach up to 23.4%. The results demonstrated that the UARS is superior to conventional packed bed regenerators. For regenerating a unit mass flow of desiccant solution, the required regeneration temperature can be decreased by 4.4 ℃, and the potential power savings can reach up to 23.4%.

2.3.2 Membrane-based type regenerator

The membrane-based regenerator is an alternative to the direct-contact regenerator to overcome the desiccant droplet carry-over issue. In addition, it conserves liquid desiccant since significant desiccant is lost owing to the carryover issue. Duong et al. [93] explored the regeneration of LiCl solution for air conditioning by membrane distillation. The regenerator was a plate-and-frame module comprised of PTFE membranes from Porous Membrane Technology. The membranes employed had a thickness of 60 μm, a nominal pore size of 0.2 μm, a porosity of 80%, and a total active surface area of 138 cm^2. To evaluate the regeneration performance, the regeneration capacity ΔC and thermal energy consumption α were utilised. The results demonstrated that when the feed temperature is 65 °C, the system is capable of increasing the solution concentration by up to 29% without considerable desiccant solution loss. Increasing the temperature of the feed would increase ΔC and decrease α.

Moghaddam et al. [29] established the solution side efficacy to evaluate regenerators, as the main focus in regenerators is on the desiccant solution side as opposed to the air side. In their experimental results, it was shown that the

solution-side latent effectiveness was sensitive to the solution inlet concentrations, however, the difference between the air-side and solution-side latent effectiveness was minimal. In contrast, solution-side sensible and total effectiveness should be utilised in the majority of circumstances when evaluating regenerators.

In conclusion, the regenerator, as one of the most important components of a liquid desiccant dehumidification system, has been extensively investigated in the past. In addition, they can be categorised based on their structure into direct contact type regenerators and membrane-based type regenerators. The most prevalent forms of direct-contact regenerators are packed beds or packed columns. Regarding the flow pattern, both counter-flow and cross-flow configurations have been devised, and each has advantages and disadvantages. The solution can be regenerated with low-grade energy sources such as solar thermal (TH), photovoltaic-electrodialysis ($PV - ED$), and photovoltaic capacitive deionization ($PV - CDI$). Reduced desiccant loss and elimination of carryover concerns are advantages of membrane-based regenerators over direct-type ones. Compared to the direct-contact type, membrane-based regenerators have been the subject of fewer studies.

2.4 Desiccant and membrane materials
The strength of a desiccant material can be determined by its equilibrium surface vapour pressure, which rises with increasing desiccant temperature and desiccant solution water content. In addition to surface vapour pressure, several other properties influence the efficacy of liquid desiccant, including regeneration temperature, energy storage density, crystallisation point, solubility, availability, cost, etc. [94]. In addition, the semi-permeable membrane is regarded as the most

important component of a membrane-based liquid desiccant dehumidification system. The features of membranes may greatly affect the performance of the system. Thus, this section will introduce and compare several liquid desiccant and membrane materials.

2.4.1 Liquid desiccants

There are three main categories of liquid desiccants used in dehumidification systems: organic desiccants, inorganic desiccants and mixed type desiccants. Recently, the frequently used inorganic liquid desiccants are halide salt solutions, such as lithium bromide (LiBr), lithium chloride (LiCl), calcium chloride ($CaCl_2$), and magnesium chloride ($MgCl_2$). In contrast, the organic solutions include triethylene glycol (TEG), diethylene glycol (DEG), di-propylene glycol (DPG) and propylene glycol (PG). Besides, mixed or composite desiccants are used since their high price is one of the issues limiting wide application. Under this situation, mixing different salts seems to be the auspicious method to reduce the solution cost with less performance deterioration, although LiCl has excellent properties for dehumidification [95]. Among all three types of desiccants, halide salt solutions are emphasized in the literature because of their widespread usage and high dehumidification capability.

LiCl solution is the most widely used due to its odourless and not vaporizing features. Chen et al. [96] analyzed the desiccant cooling system driven by a heat pump using low-temperature LiCl and found that the average COP of the system is about 4.0 when the temperature and humidity are controlled at 5.2-7.4°C and 47.9-63.6 kg/h respectively. Leboeuf and Lof [97] studied a cooling system driven by solar thermal energy with LiCl solution as the working fluid and

discovered that the desiccant temperature is in the range of 40-55℃. In terms of the application of the LiBr solution, several experimental tests have been carried out. Lazzarin et al. [98] compared the mass transfer rates of $CaCl_2$ and LiBr solutions statistically and concluded that the LiBr solution achieves exceptional performance compared with the $CaCl_2$ solution. Moreover, although it is feasible to control the pH value of the desiccant, the bromide ion can be readily ionized, causing odour issues. Liu et al. [99] tested an air conditioner with LiBr and LiCl solutions and found that the COPs in different desiccant systems are similar, whereas the LiBr solution outperforms regeneration progress. Conde [100] introduced the interpolating equations for describing the vapour pressure, surface tension, and other properties of LiCl and $CaCl_2$ solutions and stated that the proposed equations could produce accurate data to reflect the liquid desiccant properties. Kornnaki et al. [101] built a mathematical model for a counter-flow dehumidifier using three different solutions (LiCl, $CaCl_2$, and LiBr) and discovered that the LiCl system shows better performance than the others under the same circumstance. Furthermore, the LiCl system is of high stability under a high humidity ratio. Dai et al. [102] carried out an experimental test on a crossflow dehumidifier with a 40% concentration of $CaCl_2$ and discovered that the simulated Nusselt numbers for liquid and air sides are 2.84 and 6.54, respectively, while the experimental Nusselt numbers are higher than the simulated results.

Although halide salts are widely used in the LDD system, their disadvantages are apparent, for example, corrosion is a severe issue. Therefore, organic acids have been regarded as alternative materials, such as potassium (HCO_2K) and sodium formate (HCO_2Na). Atkinson [103] stated that the viscosity of potassium

formate is 0.01 Pa/s at 20℃ with 70% concentration, and its performance is near that of LiCl solution with 27% concentration. They also found that potassium formate could dry air below 30% relative humidity. Elmer et al. [104] investigated an integrated desiccant air conditioning system using potassium formate ($CHKO_2$) desiccant and claimed that when the inlet temperature, relative humidity, and moisture removal rate are set as 30-35℃, 51-70% and 0.15-0.4 g/s respectively, the system COP is around 0.72. In brief, although organic acids such as potassium formate and acetate have low dehumidification performance compared with halide salts, they are still the alternatives due to their low price and corrosion properties.

Other liquid desiccants, so-called ionic liquids (ILs), are formed of inorganic anions and organic cations. The ILs have incorporated salts in the liquid phase at room temperature, which have the advantages of low temperature, no corrosion, no crystallization characters, and excellent thermal stability [105]. In general, the satisfactory criteria of mixed desiccants are high boiling temperature and diluted heat, low vapour pressure, crystallization point and viscosity [106]. Meanwhile, the mixing ratio of two desiccants is one of the crucial criteria. Furthermore, Ertas et al. [107] studied the properties of LiCl and $CaCl_2$ mixture at 26.5-65.4 ℃ and their results show that the mixture solution EVP approaches the actual value of LiCl when the mass fraction is increased. Ge et al. [108] studied the mixture of LiCl and $MgCl_2$ and stated that the mixture equilibrium relative humidity is lower than that of a single $MgCl_2$ solution, and the mixture's relative humidity is inversely proportional to the ratio of LiCl. In recent research, Zhao et al. [109] investigated the performances of several composite desiccants, including LiCl-$CaCl_2$, LiBr-$CaCl_2$, LiCl-$MgCl_2$, LiCl-$CaCl_2$-$MgCl_2$, and LiCl-

CaCl$_2$-methanol solution. Their results show that the COP of the LiBr-CaCl2 solution is higher than the others, where the non-random two-liquid (NTRL) equation has been utilized to calculate the mixture surface vapour pressure.

In conclusion, the LDC system's performance with organic acids is inferior to that with halide salt. Nonetheless, their low corrosivity and absence of toxicity make them a good substitute. In terms of composite desiccants, they have the advantages of low cost and great dehumidification capability compared with other current desiccants.

2.4.2 Membrane materials

The membrane used in the dehumidification system is the type of semi-permeable layer. Based on this, the membrane could be used to remove moisture from the humid air. Hydrophobic microporous and nonporous membranes are the two fundamental forms of polymer membranes. Zhang et al. [110] created a microporous cellulose acetate (CA) membrane to recover heat and moisture. The membranes were produced in a single step using the direct wet phase inversion method and a cheap and abundant raw material, cellulose acetate. Additionally, the ecologically friendly solvent acetic acid and deionized water were utilised. Concurrently, a porous support layer and a dense skin layer were created with the solvent and coagulant medium exchange. Zhang et al. [111] fabricated a vapour-permeable composite membrane using a porous polyethersulfone (PES) support layer and a dense polyvinylalcohol (PVA) active separating layer. LiCl was added to the PVA solution during manufacturing to facilitate moisture permeability. The investigation results revealed that membranes containing 2.3% LiCl have the maximum moisture permeability rate, which is 70% higher than membranes without LiCl addition. The scanning electron micrograph (SEM)

photographs demonstrated that microporous membrane has a fractal structure with multiple macro or micro pores in varied diameters in the through-plane direction. Such membrane microstructure is typically disordered and exceedingly complex [112]. The microporous membranes are susceptible to desiccant solution infiltration. The higher the surface tension, the lower the probability of pore-wetting. Hence, halide salts were added to the organic absorbents during membrane production to boost surface tension [49]. In addition to surface tension, many other factors can cause leakage, such as the adhesion potential of hydrophobic materials and adsorption caused by electrostatic interactions [113].

Consequently, the operating conditions for microporous membranes could be severely constrained. Using impermeable membrane materials will solve this issue. In addition, Gabelman and Hwang [114] developed a hollow fibre membrane using nonporous polyolefin fibres woven into a fabric and wrapped around a central core. Zhang et al. [115] numerically analysed the heat and mass transfer in an enthalpy exchanger employing a novel membrane material called a hydrophobic-hydrophilic composite membrane. This substance comprised a hydrophobic porous support layer and a hydrophilic dense active layer. The support layer exhibited the greatest moisture resistance in the composite membrane, while the support and active layers exhibited negligible heat resistance.

In conclusion, there are currently two membrane materials: hydrophobic microporous and nonporous membranes. The former has the potential risk of pore-wetting by desiccant solution, which can be avoided by employing impermeable membranes. In conclusion, a good membrane material should

possess the following characteristics: high porosity, high selectivity, low resistance to vapour transfer, high strength and flexibility, high fouling resistance, high corrosion resistance, simple fabrication, and low cost.

2.5 Heat pipes

A heat pipe has high heat transfer ability and a simple structure [116], with its thermal conductivity reaching 8532W/mK to 18294W/mK [117], which is 21-45 times higher than that of copper [118]. In recent years, heat pipe has been widely used as a heat transfer component for thermal energy management in various applications, such as the battery, computer, pharmaceutical, food processing, biotechnology, chemical and medical industries [119]. Among them, the most commonly used heat pipe is a straight gravitational type, which has the advantages of a simple structure and easy-to-operate [120]. Due to high pressure in the evaporator section as the heat pipe is heated, the vapour flows into the condenser section, where it is cooled down and condensed, with a detailed configuration shown in Fig 2-13 [121]. The condensed liquid then flows back to the evaporator section to complete the internal cycle [122, 123]. Zhao et al. [124] investigated the performance of a direct-expansion terminal integrated with a gravitational heat pipe and found that a 24% cooling capacity improvement was achieved, and the indoor humidity was reduced from 82% to 60% within 30 minutes.
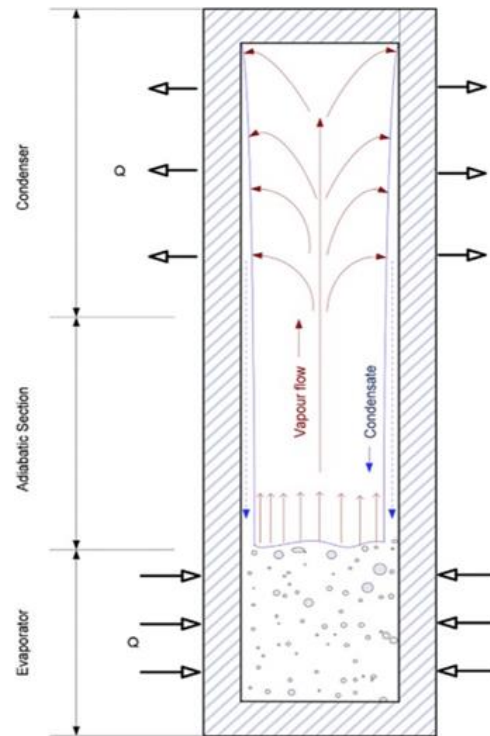
Fig 2-13 The gravitational heat pipe configuration and working principle [121]

John et al. [40] compared the conventional evaporative cooling system with the heat pipe-assisted cooling system, where water and ethanol are used as the working fluid in heat pipes. It is found that the air temperature could be reduced by 12-15K using the proposed cooling system, indicating that the heat pipes could provide a continuous and efficient cooling loop within the channel geometry as the heat transfer device. As a highly efficient heat recovery device, heat pipe heat exchanger (HPHE) has been widely employed in air conditioning and conventional cooling-based dehumidification systems. Studies show excellent performance in enhancing the energy efficiency in cooling-based dehumidification systems [39-42]. Srimuang et al. [42] presented a literature review of the applications of different HPHEs, including conventional heat pipe (CHP), two-phase closed thermosyphon (TPCT) and oscillating heat pipe (OHP) for heat recovery and their energy performances. It is summarized that the

TPCTs, without the wick structure, have relatively higher effectiveness since the wicks in the heat pipes increase the resistance to the flow of condense.

Moreover, Mostafa et al. [125] investigated the HPHE in heat recovery applications to cool the incoming fresh air in air conditioning applications and found that the effectiveness of evaporator and condenser sections increased by about 48% when the inlet fresh air temperature is set to 40 °C. Wu et al. [126] investigated the energy performance of TPCT in the air-conditioning system and found that the cooling capability for the system could be enhanced by 32.7% with the air mass flow rate ranging from 300 kg/h to 500 kg/h compared with the conventional system, resulting in energy-saving and little external energy needed. Yau et al. [127] studied the experimental performance of HVAC systems for tropical climates equipped with 8-row TPCTs and found that the sensible effectiveness could be reduced by 13.3% (i.e. 0.75 to 0.65) to 18.8% (i.e. 0.85 to 0.69) respectively, due to the use of the wickless heat pipes for relatively low air temperature and humidity (20℃ and 50%).

Long life and little required maintenance are inherent with heat pipes due to simplifying the design and construction of robust and durable materials without moving components [43]. Ahmad et al. [128] tested the feasibility of a liquid-desiccant-enhanced heat-pipe thermal recovery unit for preconditioning ventilation air, as shown in Fig 2-14 (a). During the test, the concentrated liquid desiccant is sprayed on the bank of heat-pipe fins on the supply side to dehumidify the air with the other heat pipe end in the exhaust air stream with water evaporative cooling, where the solution absorbed heat released during dehumidification is rejected to the exhaust side through the heat-pipe tubes. Results reveal that the heat pipe's cooling performance with lithium chloride

increased 40% more than the system without desiccants. Besides, it is found that only about 40% to 50% of the dehumidification potential of liquid desiccants is being used, attributed to the that packed tower type has poor mass transfer rates and insufficient contact area. Ou et al. [128] proposed a heat pipe enhanced internally-heated liquid desiccant regenerator, as shown in Fig 2-14 (b), where the HPHE and its temperature rise preheat the ambient air while humidity stays the same.

(a) Ahmad et al. [128]   (b) Ou et al. [129]
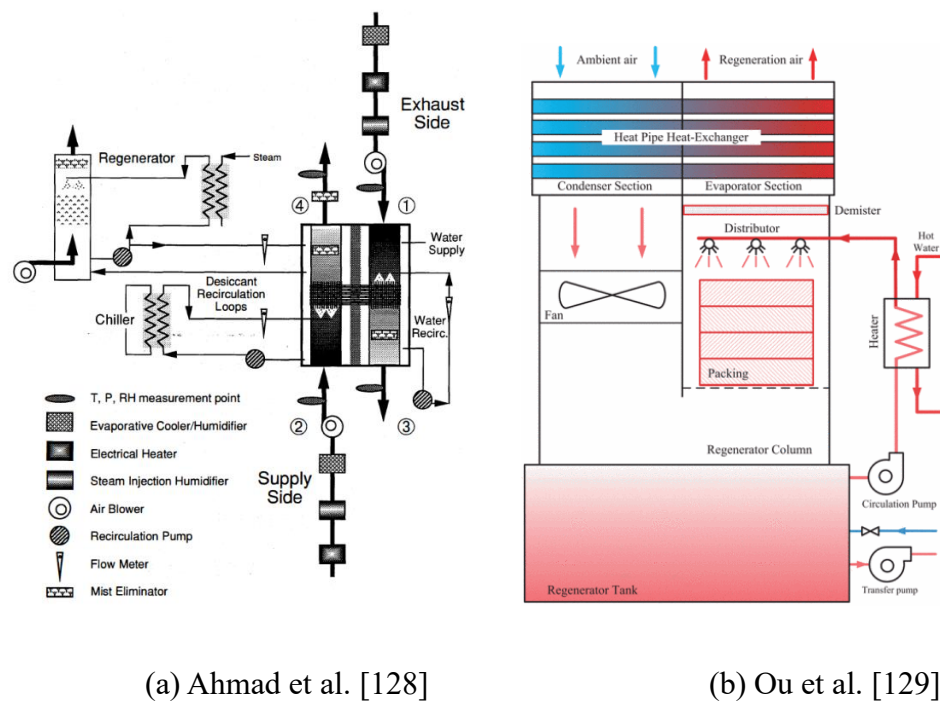
Fig 2-14 The heat pipe enhanced internally-heated liquid desiccant regenerator [128] [129]

As a result, the moisture absorptive capacity of process air is enhanced. Therefore, it is figured out that a heat pipe is an efficient heat transfer method in improving the system performance of the liquid desiccant with high-density heat flux within compact space, which may have a significant impact on internal cooling/heating of the desiccant solution in the dehumidifier side to maintain a

relatively low temperature. Results indicated that the ambient air temperature gradually promotes about 10 ℃ while its relative humidity reduces by about 30 %, leading to the energy saving to increase the inlet solution temperature of the condenser and regeneration enhancement, respectively. Moreover, Shen et al. [130] investigated a liquid desiccant regenerator with a heat recovery heat pipe system using LiCl as the desiccant solution. The regenerator used in the system is a direct contact regenerator tower, which is given in Fig 2-15.
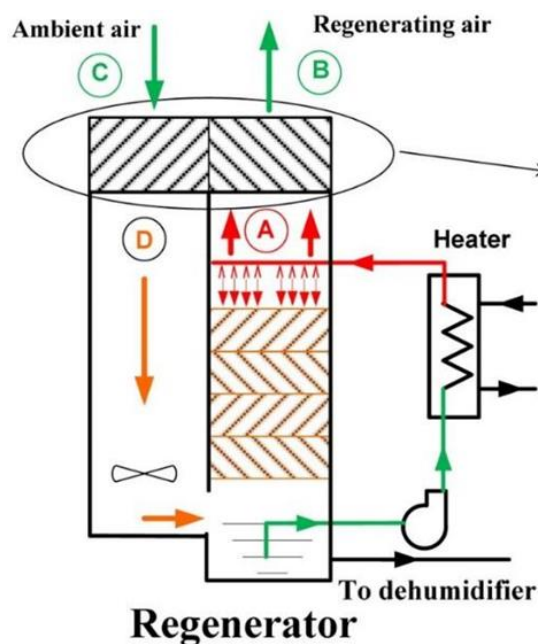
Fig 2-15 Schematic diagram of direct-contact regenerator tower [130]

In the regenerator tower, the upwind air flow and liquid desiccant are in direct contact with the surface of the structured packing in a counter-flow configuration, with simultaneous heat mass transfer between the air and solution flows. This is accomplished through the preheating of entering air by reusing the water heat from exhausted regenerated air. After this preheating procedure, the temperature difference between the regenerating air and solution in the regenerator is diminished, allowing the solution to maintain a relatively higher

temperature and vapour pressure. Results indicated that the existence of HPHE increases the temperature and reduces the relative humidity of incoming air, which implies higher moisture absorption capability, where the regenerating rate of the regenerator with 4 and 8 rows HPHE is increased by 11.51 % and 17.12 % maximally compared with regenerator without HPHE. Besides, it is also found that nearly 14-19 % of the regenerator's total energy consumption is recovered by the HPHE.

Therefore, from the above-mentioned literatures, it is figured out that heat pipe can be used in the liquid desiccant system to improve the system performance with high heat transfer ability for internal cooling and compact size. However, there is a lack of experiments of heat pipe internal cooling application in the dehumidifier, as well as comprehensive parametric analysis of the operation control with the heat pipe internal cooling method.

2.6 Mathematical modelling methods

In this section, various mathematical modelling methods are introduced. For the modelling of the liquid desiccant dehumidification system, there are primarily four distinct approaches: the Simplified method (**section 2.6.1**), the Effectiveness NTU ($\varepsilon - NTU$) method (**section 2.6.2**), and the Finite difference method (**section 2.6.3**), as well as the conjugate heat and mass transfer method (**section 2.6.4**).

2.6.1 The Simplified method

Liu et al. [131] proposed empirical correlations for cross-flow and counter-flow dehumidifiers with packed media. Due to the complexity of the model, the amount of time required for computer modelling is typically burdensome for differential element-based models to be feasible in practice. On the basis of

corresponding experiments, empirical correlations for enthalpy and moisture-effectiveness were proposed to develop a simplified method. Results showed that the cross-flow and counter-flow dehumidifiers had maximum average differences in moisture removal efficiency of 7.9% and 13.8%, respectively, compared to empirical relationships and previously published experimental data. For cross-flow and counter-flow dehumidifiers, the maximum average differences in enthalpy effectiveness were 6.3% and 10.8%, respectively. Liu et al. [132] created an analytical solution for a cross-flow, direct contact, packed bed liquid desiccant dehumidifier. In their study, for the sake of calculation simplicity, it was assumed that the liquid desiccant mass flow rate and concentration within the dehumidifier are constant, as the moisture content absorbed by the desiccant solution during the dehumidification process is negligible in comparison to the desiccant mass flow rate. On the basis of the similarity between the cross-flow dehumidifier and the cross-flow heat exchanger, analytical solutions to air and solution parameters, enthalpy and moisture efficiencies were proposed. Results were compared to numerical and experimental results, and the average absolute deviation was less than 8%. Khan and Ball [133] developed a simplified mathematical model to assess the performance of packed-type liquid desiccant dehumidifiers and regenerators. The model was a straightforward algebraic derivation based on simulation outcomes. 1700 groups of data from the finite difference model were analysed to create the simplified algebraic. It was determined that the model could successfully evaluate the hourly performance of eACAA component and predict the heating and cooling demand, but it may not be applicable to other conditions for which the model's fitting was not performed.

In conclusion, the simplified methods can simulate the annual performance of a liquid desiccant system without requiring a significant amount of calculation time. These analytical models were developed based on several assumptions that may restrict their applicability, and the analytical solution accuracy was generally low.

2.6.2 The Effectiveness NTU ($\varepsilon - NTU$) method

Stevens et al. [134] described a computationally efficient liquid desiccant packed-bed heat and mass exchanger model. The model was derived from a model of a cooling tower's effectiveness. Throughout the derivation, it was assumed that the water loss for the energy balance of the solution could be omitted. In addition, a linear relationship was postulated between the saturation enthalpy and temperature. In their study, they first obtained the number of heat transfer units (NTU):

$$NTU = \frac{\alpha_D AV}{G'_a} \tag{2-1}$$

The effectiveness of a counter-current flow dehumidifier was then determined by:

$$\varepsilon = \frac{1 - e^{-NTU(1-m^*)}}{1 - m^* e^{-NTU(1-m^*)}} \tag{2-2}$$

Where m^* was the capacitance ratio and defined as:

$$m^* = \frac{G'_a C_{sat}}{G'_{s,i} C_{p,s}} \tag{2-3}$$

Where C_{sat} was the saturated specific heat (J/kgK); G' was the specific mass flow rate (kg/s). On the basis of these correlations, all outlet parameters, including air temperature, humidity ratio, and enthalpy, were determined. Good

correlations have been established between the results and experimental and numerical results.

Besides, the above-mentioned method focused on heat and mass transfer for direct-contact type contractors or traditional flat-plate heat exchangers. As for membrane-based liquid desiccant heat and mass exchangers, Zhang and Niu [75] presented effectiveness correlations for a flat plate exchanger with membrane cores. In order to construct governing equations for their research, they made the following assumptions: no lateral mixing of the two fluids, no heat conduction and vapour diffusion in the fluids, constant heat conductivity and water diffusivity in the membrane, and one-dimensional heat and mass transfer across the membrane. The correlations between sensible and latent effectiveness were developed as follows:

$$\varepsilon_{sen} = 1 - exp\left[\frac{\exp(-NTU^{0.78}R_1)-1}{NTU^{-0.22}R_1}\right] \tag{2-4}$$

$$\varepsilon_{lat} = 1 - exp\left[\frac{\exp(-NTU_{lat}{}^{0.78}R_1)-1}{NTU_{lat}{}^{-0.22}R_1}\right] \tag{2-5}$$

$$R_1 = \frac{(\dot{m}c_{pa})_{min}}{(\dot{m}c_{pa})_{max}} \tag{2-6}$$

$$R_2 = \frac{\dot{m}_{min}}{\dot{m}_{max}} \tag{2-7}$$

Where NTU_{lat} is the total number of the transfer units for moisture which is calculated by:

$$NTU_{lat} = \beta \cdot NTU \tag{2-8}$$

$$\beta = \frac{1}{1+\alpha} \tag{2-9}$$

$$\alpha = \frac{\gamma_m}{\gamma_c} \tag{2-10}$$

$$\gamma_c = \frac{2}{k_s} \qquad\qquad (2\text{-}11)$$

Where γ_c is the convective moisture transfer resistance, α is the ratio of diffusive resistance to convective membrane resistance. The empirical correlations were compared with experimentally obtained data, and it was determined that they accurately predicted the performance of membrane-based heat mass exchangers. Moreover, Zhang's analytical solution was extended by assuming that the desiccant solution's mass flow rate and concentration remain constant, considering that the moisture contents absorbed/desorbed by the solution were insignificant compared to the desiccant mass flow rate [135]. A flat-plate counter-cross-flow LAMEE was utilised in the literature [135]. The solution characteristics and its equilibrium humidity ratio were only associated with the solution temperature and the slope (E_T) was only related to the iterated solution temperature. Zhang's analytical approach, in which E_T was connected to the temperature and concentration of the iterated solution, utilised a different method for calculating the slope.

In conclusion, compared to the simple method, the $\varepsilon - NTU$ method demonstrated more precision and applicability. Some iteration was necessary, but overall it is time-saving and predicts the performance of heat mass exchangers quite well.

2.6.3 The Finite difference method
Factor and Grossman [55] created a mathematical model for a packed-bed dehumidifier/regenerator employing liquid desiccant. The numerical model was based on the model for adiabatic gas absorption and utilised the finite difference approach. The adiabatic dehumidifier/regenerator height was divided into n differential elements, and the air and solution parameters were considered

constant across all differential elements. The differential governing equations for air temperature and humidity were created and solved using numerical integration along the unit height and boundary conditions. The experimental findings validated the numerical results. Oberg and Goswami employed a finite difference model similar to that of Factor and Grossman to simulate the performance of a packed bed liquid desiccant dehumidifier. Liu et al. [136] investigated heat and mass transfer for a cross-flow direct-contact liquid desiccant dehumidifier/regenerator. The desiccant flowed with air in a cross arrangement and was distributed by gravity over the packing. To solve the governing equations of heat and mass flow in air and solution sides, the dehumidifier/regenerator was divided into an unlimited number of differential elements, each with a volume of dV, and the computational domain was discretized into $M \times N$ meshes, as depicted in Fig 2-16.
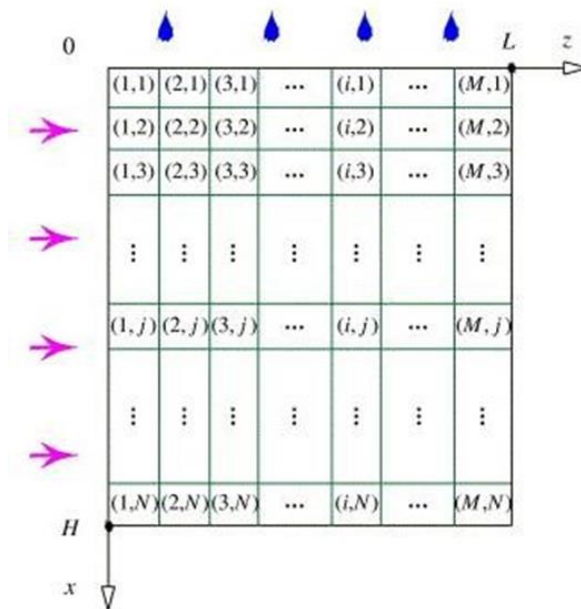
Fig 2-16 Two-dimensional schematic of the computational domain [136]

According to their findings, the average absolute discrepancies between numerical results and 284 groups of experimental data for dehumidifier enthalpy and moisture efficacy were 7.9% and 8.5%, respectively, while for regenerator, they were 5.8% and 6.6% under 82 groups of tests. Zhang et al. [137] conducted a comprehensive parameter study using the finite difference model to investigate a counter-crossflow indirect evaporative cooling-assisted liquid desiccant dehumidification system. They focused on operating parameters, such as air temperature, velocity, humidity, solution inlet temperature, solution concentration, the ratio of the secondary air to the primary air, and device parameters: *NTU* and channel gap. Compared to the traditional dehumidifier, the dehumidification efficiency of this developed system can be increased by 16 % from 35.0 % to 40.6% with the inlet air and solution of 30 ℃ and 25 ℃, respectively. Their simulation results show that auxiliary indirective cooling alleviates the solution temperature rise of 2.07 °C. Numerous research have also employed membrane-based contractors. By computationally modelling the coupled heat and mass transfer in the air, the solution flows, and the membrane of a counter-flow LAMEE, Moghaddam et al. [138] analysed the steady-state performance of the LAMEE. In order to simplify numerical modelling, the following assumptions were made in the developed module: well-insulated exchanger, steady state, fully developed flows, constant thermal properties and convective heat and mass transfer coefficients, uniform velocity and temperature at inlets, absence of axial conduction, and phase change heat gain or loss occurs only on the solution side. The solution and air side heat mass conservation governing equations were solved using the finite difference approach. Using experimental data to validate the model, excellent agreement was obtained under

summer operating circumstances. However, during winter operating conditions, the numerical model anticipated greater sensible effectiveness than the actual data, with a 10% difference.

In conclusion, the finite difference technique offers more precise modelling than the simplified method and the $\varepsilon - NTU$ method; its governing equations are discretized using the finite difference method and solved using the iteration method. The heat and mass transfer coefficients are generated using correlations of basic data such as the Nusselt and Sherwood values. However, these data were collected under uniform temperature (heat flow) or concentration (mass flux) boundary conditions, which cannot accurately represent the actual heat and mass transfer parameters in the membrane module. In order to tackle this issue, the conjugate heat and mass transfer modelling method will be presented in the following section.

2.6.4 The Conjugate heat and mass transfer method

As previously indicated, the drawback of finite difference modelling can be overcome by employing the conjugate heat and mass transfer modelling method. Huang and Zhang [139] developed a mathematical model for a cross-flow flat plate membrane module. The calculating unit cell comprises one membrane and two adjacent flow channels. In this model, certain assumptions were made, including laminar flow mode for both air and liquid solution, the Newtonian fluids with constant thermophysical properties, hydrodynamically developed while developing thermally and in concentration for both flows and absence of heat and mass diffusion along the main flow direction. The membrane surface's governing equations differed from those of prior models, and the membrane's real heat and mass boundary conditions were determined numerically by

58

simultaneously solving momentum, energy, and concentration equations for air and solution. The governing equations and their related boundary conditions were solved using the finite difference method, and iterative techniques were utilised. The numerical results were validated by comparing them to experimental data, and the discrepancies were less than 6%. In general, this model accurately anticipated heat and mass transfer. Liu et al. [140] applied the conjugate heat and mass transfer model to compare the performance between an internally-cooled dehumidifier and adiabatic dehumidifiers with various flow patterns. They focused on the air, solution and water inlet temperature and the non-dimensional heat and mass parameter (NTU and NTU_m) and indicated that an internally-cooled dehumidifier has better mass transfer performance than the adiabatic dehumidifier. The moisture removal rate is improved by 30% from 5 g/s to 6.5 g/s compared with the adiabatic type where NTU,inlet temperatures of the air, solution and cooling water are 2, 30℃, 30℃ and 25℃, respectively. Li et al. [64] combined the conjugate heat and mass transfer model and the finite difference model to investigate a dehumidifier performance based on the average temperature and air humidity differences for various flow types of cooling tubes. It is discovered that the cross-flow between air and solution and the counter-flow between air and cooling water are the best flow patterns. Moreover, a step forward to investigate the effects of the developing entrances on the fluid flow and the conjugate heat and mass transfer in a cross-flow flat plate membrane module was made by Huang et al. [141], where the membrane module structure in this study was the same as that in literature [139]. Taking into account the influences of the developing flow, heat, and mass transfer entrances, more accurate governing equations were established and solved directly. The

governing equations and conjugate heat and mass transfer boundary conditions were solved using the finite volume method. Iterative methods were also used to solve interactive problems. The model was validated by comparing it to experimental data, and the maximum difference between calculated values and experimental data was 4%, indicating that this model was able to predict heat and mass transfer for the flat plate membrane module with cross-flow. In addition, an internally-cooled membrane-based liquid desiccant dehumidifier (IMLDD) was studied by Huang et al. [83], which consisted of feed air, solution, cooling water and sweep air. In this modelling, the interface between the water film and the sweep air was in a state of thermodynamic equilibrium, and the velocity of the sweep air at the interface was equal to that of the water flow. In addition, the gravitational force of the feed air was disregarded, while only the gravitational force of the falling water was considered. The governing equations for the feed air, solution, water falling film, and sweep air were formulated and solved using a finite volume numerical method. Due to the difficulty of measuring parameters within the contractor, only the outlet parameters of the feed air, solution, water-falling film, and sweep air were measured in order to validate the numerical model. The maximum deviation between numerical and experimental results was less than 8%, indicating that the numerical model can accurately predict IMLDD performance.

In conclusion, compared to the simplified, the $\varepsilon - NTU$ and the finite difference methods, the conjugate heat and mass transfer method provides the most precise modelling. From the conjugate heat and mass transfer governing equations, fundamental heat and mass transport data could be derived directly. However, the disadvantage of this method is that extensive iterations were required for

solving governing equations, which renders it inappropriate for efficient performance prediction or annual assessment of the dehumidification system. In the end, a detailed comparison of four different modelling methods is summarized in Table 2-1.

Table 2-1 Comparison of different modelling methods for the liquid desiccant dehumidification system

References	Modelling method	System type	Flow pattern	Solutions to solve governing equations	Experimental validation	Characteristics
[131]	Simplified method	Direct-contact	Cross and counter	Analytical	≤ 7.9% (cross) ≤ 13.8% (counter)	Pros: No iteration; Rapid calculation Cons: Inaccurate; Limited application
[132]			Cross		≤ 8.0%	
[142]			Counter		Good agreements	
[143]			Counter		Good agreements	
[134]	$\varepsilon - NTU$ method	Direct-contact	-	Analytical	Good agreements	Pros: Simplified iteration; Time-saving Cons: Inaccurate
[144]			-		Good agreements	
[145]		Flat-plate membrane	Cross		≤ 7.3% (sensible) ≤ 8.6% (latent)	
[135]			Counter-cross		≤ 10.0%	
[55]			Cross		-	

[146]	Finite difference method	Direct-contact	Counter	Finite difference	-	Pros: Simplified iteration; Accurate; Suitable for dehumidifier performance evaluation Cons: Unsuitable for heat and mass transfer analysis
[138]		Flat-plate membrane	Counter		≤ 10.0%	
[77]			Cross		Good agreements	
[147]			Counter-cross		≤ 17.0%	
[139]	Conjugate heat and mass transfer method	Flat-plate membrane	Cross	Finite volume	≤ 4.0%	Pros: Accurate; Suitable for heat and mass transfer analysis Cons: Exhaustive iteration; Less efficiency
[83]			Cross		≤ 8.0%	
[148]		Hollow fibre	Counter		≤ 5.0%	
[149]			Cross		≤ 7.5%	

2.7 Application of liquid desiccant dehumidification system

In recent years, most research devoted to liquid desiccant dehumidification systems to directly absorb water vapour from the moist air [150-153] has proven to be energy-efficient, healthy, and environmentally friendly, where the optimisation algorithms are also discussed in previous works [154-160]. Packed-bed columns are the most common pattern [49, 161], with desiccant solution exposed in the air, where small corrosive desiccant droplets are carried over the processed air, endangering indoor environments and occupants' wellbeing. To tackle this issue, the indirect contact pattern with permeable polymer hollow fibre [162-164] dehumidifiers (PHFD) are alternatives for heat and mass transfer, where membranes separate air and desiccant solution and the corrosions are prevented. The results showed that the solution concentration and the moisture flow rate were crucial for efficient moisture removal. Moreover, the small gap inside the hollow fibre leads to significantly enhanced energy-efficient performance. Another advantage of hollow fibre lies in its compacted structure with enhanced surface contact areas, reinforcing the heat and mass transfer capacity [163, 165]. Despite that, the advantages of lightweight, corrosion resistance, and being 2-3 times cheaper than the metal counterparts with the same thermal performance draw extensive attention [166]. The heat and mass transfer in a crossflow hollow fibre integrated liquid desiccant dehumidification and cooling system has been investigated [167, 168, 153]. Besides, many papers have studied the cross-flow hollow fibre system's performance [169, 82]. Chen et al. [162] conducted the experiment to study a polymer hollow fibre integrated with aqueous potassium formate solution under the conditions of incoming air temperature increasing from 30 ℃ to 45℃, where the moisture removal rate

improved from 0.20 g/s to 0.36 g/s (about 80.0%). In contrast, the sensible effectiveness increased from 0.54 to 0.66 (about 22.2%). Besides, when the relative humidity increased from 55% to 75% with a fixed inlet air temperature of 35 ℃, the moisture removal rate improved from 0.20 g/s to 0.28 g/s (about 40.0%), whereas the sensible effectiveness decreased from 0.54 to 0.37 (about 40.7%). Furthermore, Ou et al. [170] experimented with the heat and mass transfer performances of a liquid desiccant cooling and dehumidification system. It was figured out that the air outlet temperature and humidity in both model predictions and experimental results reduced with the increase of desiccant solution mass flow rate from 0.206 kg/s to 0.425 kg/s, indicating the rise of sensible and latent heat effectiveness ranging from 71.1% to 82.2% and 85.2% to 88.9%, respectively. Moreover, Ou et al. [170] also investigated the impact of solution inlet temperature reduction from 12.2℃ to 10℃ on dehumidification performances. The increasing rate of sensible heat effectiveness is 8.4%, with the outlet air temperature dropping from 16.73 ℃ to 13.93 ℃. The increasing rate for latent heat effectiveness is 4.3%, with the outlet air humidity dropping from 7.75 g/kg to 6.68 g/kg. Besides, the air outlet humidity decreased significantly from 6.22 g/kg to 5.24 g/kg, with the growing desiccant solution inlet concentration from 30 % to 33 %. Furthermore, solar collectors were assumed to be used for regeneration in the liquid desiccant cooling system. Fig 2-17 depicts a novel type of solar liquid desiccant cooling system with a solar C/R developed by Peng et al. [171], including three core components: solar collector/regenerator(C/R), air dehumidifier and evaporative cooler. The working fluids were circulated in two loops: an air loop and a liquid desiccant loop. The processed air was dehumidified in the dehumidifier before being

chilled with cooling water. The diluted solution exiting the dehumidifier was

heated in the heat exchanger before entering the solar collector/regenerator,

where it was heated to the regeneration temperature and regenerated. The

viability and effectiveness of direct solar desiccant regeneration via the C/R

component were studied.
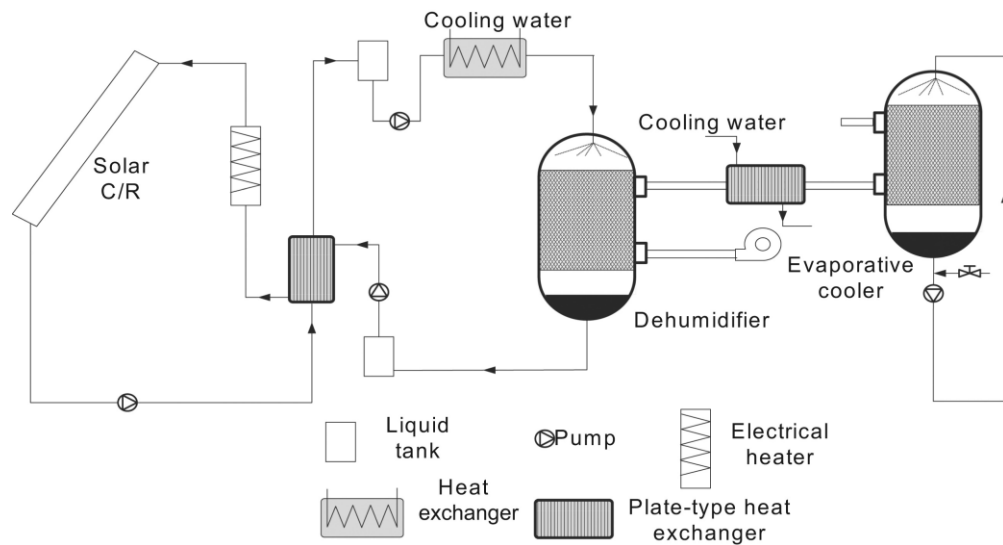
Fig 2-17 Flowchart of a solar liquid desiccant cooling system [171]

In addition to solar collectors, numerous experts combined standard vapour

compression refrigeration systems with liquid desiccant dehumidification to

create innovative air conditioning systems with separate temperature and

humidity control. For sensible cooling, the novel air conditioning system could

operate at a high COP with a high evaporation temperature. Fig 2-18 depicts the

liquid desiccant evaporation cooling air conditioning system (LDCS) developed

by Yin et al. [172]. In this system, a dehumidifier, a regenerator, and an

evaporative cooler were added. Air and low-temperature, the highly

concentrated desiccant film entered the dehumidifier, and water vapour was

transported from the air to the desiccant film. In the regenerator, a low-grade

heat source heated the diluted desiccant solution from the dehumidifier to a

higher temperature, and water vapour was transported from the desiccant solution to the air. The dehumidified air was sent via an evaporative cooler to be cooled and humidified before being delivered to the air conditioning space. The system might be powered by low-grade heat sources with temperatures between 60 ℃ and 80 ℃, such as solar energy and industrial waste heat.
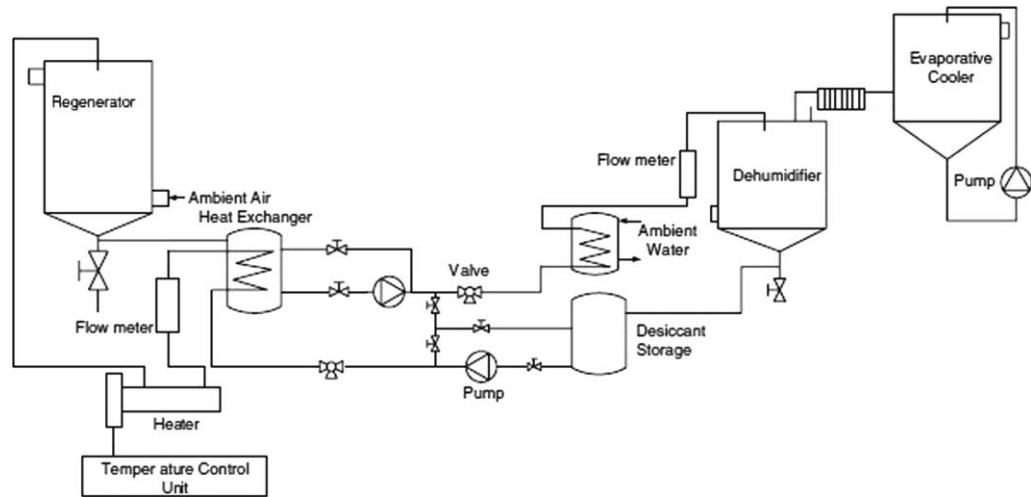
Fig 2-18 Schematic diagram of the liquid desiccant evaporation cooling air conditioning system [172]

Fig 2-19 depicts the innovative liquid desiccant air cooling system proposed by Yin et al. [173]. The new system had four units: a liquid desiccant (LiCl–H_2O) regeneration unit, an air dehumidification unit, a unit for creating chilled water through evaporative cooling, and a unit for radiant cooling and dehumidified ventilation. Utilizing solar energy, the liquid desiccant regeneration unit concentrated the diluted liquid desiccant from the dehumidifier. The air dehumidification device utilised liquid desiccant to provide extremely dry air for the evaporative cooling unit and to condition the area. Radiant cooling and ventilation with dry air could maintain a thermally comfortable environment in the conditioned space. The dehumidifier was responsible for the dry air. The

remaining dry air was directed into the evaporative cooler, which produced cooled water for the radiant ceiling panels. With high thermal performance, the chilled water temperature could be as low as 12℃.
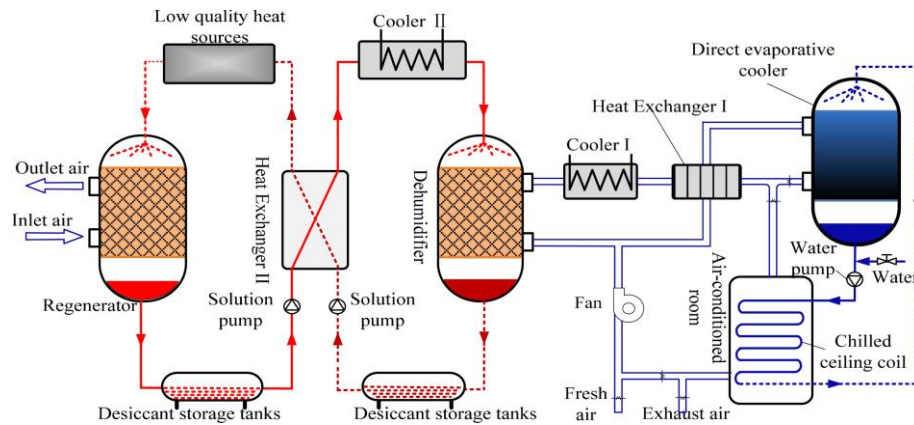
Fig 2-19 Schematic diagram of the direct evaporative cooling air conditioning system based on liquid desiccant [173]

In particular, conventional vapor-compression refrigeration and air-conditioning systems consume great energy. Numerous efforts have been made to develop energy-saving technology to improve energy efficiency. One of them is air conditioning technology based on liquid desiccant dehumidification. Grossman [174] performed a theoretical analysis on a low-grade heat-driven open desiccant cooling air conditioning system, and the results suggested that the thermal performance improved as the heat source temperature increased, with a maximum thermal COP of approximately 0.45. When simply employed for dehumidification in Haifa, Israel, the thermal COP of the system might reach around 0.8 [175]. Tang and Liu [176] examined the energy usage of conventional and liquid desiccant air conditioning systems in Shenzhen's industrial buildings. The results indicated that the COP of the conventional air-cooling system under summer outdoor design conditions was 2.94, whereas that of the liquid desiccant

air conditioning system was 5.42. All the data confirmed the energy-saving advantage of liquid desiccant air conditioning systems. A detailed review of desiccant cooling and dehumidification system application has been given in Table 2-2.

Table 2-2 Review of desiccant cooling and dehumidification system application

Ref.	Research approach	Location	Structure	Desiccant	Transient/Dynamic input air conditions	Climatic types	Performance assessment		System sizing and optimisation
							Supply air condition	System COP	
[26]	Real building	Seoul, Korea	Packed- bed	LiCl solution	Dynamic	Temperate and humid	13.9℃, 9.8 g/kg	COP$_T$=1.45 COP$_P$=0.65	N/A
[164]	Theoretical and experimental	N/A	Hollow fibre	LiCl solution	Transient	Hot and humid	21.6℃, 11.8 g/kg	COP$_T$=0.76 COP$_P$=4.2	The energy performance performs well with the heat pump's energy efficiency ratio and COP increase with the air flow rates.
[177]	Theoretical and experimental	Guangdong, China	Flat-plate membrane-based	LiCl solution	Transient	Hot and humid	16℃, 10.5 g/kg	COP$_T$=0.71	N/A
[45]	Real building	Hongkong, China	Packed- bed	N/A	Dynamic	Hot and humid	N/A	COP$_P$=4.62	Incorporating solar desiccant dehumidification has great energy-saving potential due to the higher COP.

In conclusion, most research focused on theoretical and experimental studies, however, few studies investigated the operating energy performances in real building applications. In literature [26] [44] [45], the authors have applied the desiccant cooling and dehumidification system in real buildings with dynamic input air conditions where the system's COP is calculated under complex modelling methods. Without simplified COP correlations, the calculation results are irreplicable for practical implications in other retrofit projects. Besides, it is figured out that the system COP correlations are crucial for rapid and accurate post-retrofit building energy performance prediction considering the ambient conditions, especially in combinations with different building retrofit technologies, which have been proved by [39, 46-48]. In addition, integrating the low-grade energy or renewables with the liquid desiccant dehumidification system plays a crucial role in promoting the system COP and reducing overall energy consumption.

2.8 Summary

This chapter presents a detailed literature assessment of technologies linked to the liquid desiccant dehumidification system. First, major findings from the literature review are presented:

1) Dehumidifier is the most crucial unit in a liquid desiccant dehumidification system, in which the semi-permeable membranes are used to overcome the desiccant carry-over issues of direct-contact dehumidifiers.

2) In recent years, more attention has been paid to investigating the internal cooling solutions for flat plate membrane-based heat and mass transfer, which could be divided into two types: 1) adjacent plate to the solution

channel and 2) cooling tubes inside the solution channels.

3) The regenerator is another important component of such a system, as the diluted solution produced by the dehumidifier must be re-concentrated to achieve solution recycling. Similar to dehumidifiers, regenerators can be split into direct contact and membrane-based types based on the module construction. The solution can be regenerated with low-grade energy sources such as solar thermal (TH), photovoltaic-electrodialysis (PV-ED), and photovoltaic capacitive deionization (PV-CD) (PV-CDI).

4) LiCl, CaCl2, and LiBr are the most widely used materials in which LiCl solution is the most stable liquid desiccant, featuring the lowest water vapour pressure and viscosity at the same temperature. Nevertheless, the cost of LiCl is relatively high.

5) The heat pipes are an efficient heat transfer method in improving the system performance of the liquid desiccant with high-density heat flux within compact space, which may have a significant impact on internal cooling/heating of the desiccant solution in the dehumidifier side to maintain a relatively low temperature. Among them, the most commonly used heat pipe is a straight gravitational type, which has the advantages of a simple structure and easy-to-operate.

6) There are four predominant modelling methods for the membrane-based liquid desiccant heat and mass exchanger: simplified, effectiveness NTU ($\varepsilon - NTU$), finite difference and conjugate heat and mass transfer methods. The simplified method could efficiently simulate the annual performance of a liquid desiccant system with little calculation time. The accuracy, though, is the worst. Compared to the simplified method, the

71

effectiveness NTU ($\varepsilon - NTU$) method saves time but has a broader range of applications. It provides more accuracy in modelling, and its governing equations are discretized using the finite difference method and then solved using the iterative method. The conjugate heat and mass transfer method is the most accurate, but it requires considerable iterations to solve governing equations, making it inappropriate for efficient performance prediction or annual assessment of the dehumidification system.

7) The building applications for liquid desiccant dehumidification technology can be utilised in innovative air conditioning systems, such as the liquid desiccant evaporation cooling air conditioning system and the fresh air handling unit powered by liquid desiccant and the heat pump.

Thus, based on the literature review, the novelty of this research and identified research gaps between previous studies and current study are presented:

1) Numerous experiments have been conducted to examine the performance of an internally-cooled membrane-based dehumidifier. Several numerical investigations employ conjugate heat and mass transfer methods that solve the momentum and continuity equation to produce the velocity field and the energy and mass equations to obtain the concentration and temperature distributions. These research concentrate on the fundamental heat and mass transfer mechanism of internally-cooled membrane-based plate contractors. Several studies examine the performance of liquid desiccant systems numerically by analysing the effects of multiple operational and design parameters. However, few

studies have been conducted to numerically evaluate the performance of a cross-flow internally-cooled membrane-based parallel plate liquid desiccant system by considering all relevant operational factors.

2) Although internal cooling methods are adopted by the traditionally packed tower dehumidifier, the heat and mass transfer ability do not increase significantly compared with the internal cooling methods for flat membrane dehumidifiers. Therefore, the internally-cooled flat membrane dehumidifier with higher heat transfer density and compactness should be focused on to enhance the heat and mass transfer performance. However, there is a lack of modelling of heat pipe internal cooling application in the dehumidifier, as well as comprehensive parametric analysis of the operation control with the heat pipe internal cooling method.

3) Even though many modelling studies have been carried out to investigate the impact of internal cooling on the liquid desiccant dehumidification system, most of the researches focus on the hybrid and finite difference models to achieve high accuracy with calculation iterations. A few numerical investigations have revealed the impact of cooling water temperature and flow rate on dehumidification effectiveness, however, few studies have been reported to evaluate the performance of an internally-cooled membraned-based liquid desiccant dehumidification system with heat pipe. In this study, the hybrid numerical model is established to investigate the energy performance of a heat pipe internally-cooled membraned-based liquid desiccant dehumidifier (HP-ICMLDD) with lithium chloride as the desiccant.

4) The majority of previous works have mostly analysed dehumidifiers. Few regenerator studies have concentrated on direct contact types, such as packed beds and columns. Few studies on membrane-based regenerators, particularly numerical modelling, have been undertaken. Heat and mass transfer in a membrane-based regenerator are examined numerically and experimentally with the parametric analysis in this thesis.

Chapter 3 Methods
3.1 Introduction
This chapter presents the description from the perspective of the heat pipe membrane-based liquid desiccant dehumidification (HP-ICMLDD), membrane-based regeneration, complete system, and the integrated liquid desiccant air-conditioning (ILDAC) system. Firstly, the HP-ICMLDD system comprises a membrane-based dehumidifier integrated with heat pipes and a cooling box. **Section 3.2** presents the system description and calculation methods for air and solution properties and introduces the performance evaluation indices.

Secondly, for the membrane-based regeneration system, the regenerator uses the same membrane-based heat and mass exchanger test facility built in the laboratory with no cooling box or internal cooling source involved since the primary purpose of the regenerator is to re-concentrate the weak solution coming from the dehumidifier. **Section 3.3** presents the system description and calculation methods for air and solution properties and introduces the performance evaluation indices.

The complete membrane-based flat-plate liquid desiccant dehumidification system includes a dehumidifier, a regenerator, and hot and cold water supply systems. **Section 3.4** presents the complete system description for the heat exchangers and introduces the performance evaluation indices.

For the integrated liquid desiccant air-conditioning (ILDAC) system, the modelling method for the ILDAC system is presented in **section 3.5.1**, including the air-water heat pump (AWHP) circuit, simulation parameters and conditions and the dynamic energy simulation procedure in EnergyPro. Besides, the definition and modelling of the reference building (RB) are presented in **section**

3.5.2, including RB's location, heating and cooling schedule, building material, etc. In order to analyse the energy and techno-economic performance of the ILDAC system, the flowchart of the RB's simulation method is proposed with eight steps, as described in **section 3.5.3**. Finally, the comprehensive economic performance and calculation method of the ILDAC system has been given in **section 3.5.4**.

3.2 Description of the dehumidifier

In this study, the dehumidifier comprises a heat pipe internally-cooled membrane-based liquid desiccant dehumidification system, abbreviated as the HP-ICMLDD system. An HP-ICMLDD system is designed and built to assess its energy performance through numerical study and experimental tests, principally comprising a membrane-based dehumidifier integrated with heat pipes and a cooling box. The concept and structure of the HP-ICMLDD are shown in Fig 3-1. The membrane-based dehumidifier has separate channels for the air stream and desiccant solution, where heat and moisture transfer between the air stream and desiccant solution is through the semi-permeable micro-porous hydrophobic membranes. Gravitational heat pipes are inserted in each solution channel. The desiccant solution flows downwards in the solution channels, where the solution absorbs the air moisture and heat while the liquid desiccant is impermeant through the membrane. Simultaneously, the evaporator section of the heat pipe takes heat from the desiccant solution and transfers it to the condenser section, reducing the desiccant solution temperature. A cooling box is installed on the top of the dehumidifier, and heat from the heat pipe condenser section is taken away by cold water. The structure of the HP-ICMLDD is depicted in Fig 3-1 (a), with the air and solution flow in a cross-flow

arrangement. The perspective view of the HP-ICMLDD and the detail of a single solution channel with adjacent air channels are shown in Fig 3-1 (b) and (c), respectively. In order to monitor, control and predict the heat and mass transfer process of the HP-ICMLDD system, a hybrid numerical model is established. The proposed hybrid model starts by combining the conjugate heat and mass transfer model with the nondimensionalized physical governing equations, as the heat and mass transfer coefficients are usually hard to calculate in $\varepsilon - NTU$ model. The finite difference method is used to solve the iterative computational steps for air, solution and cooling box sides.

(a)

(b)

(c)
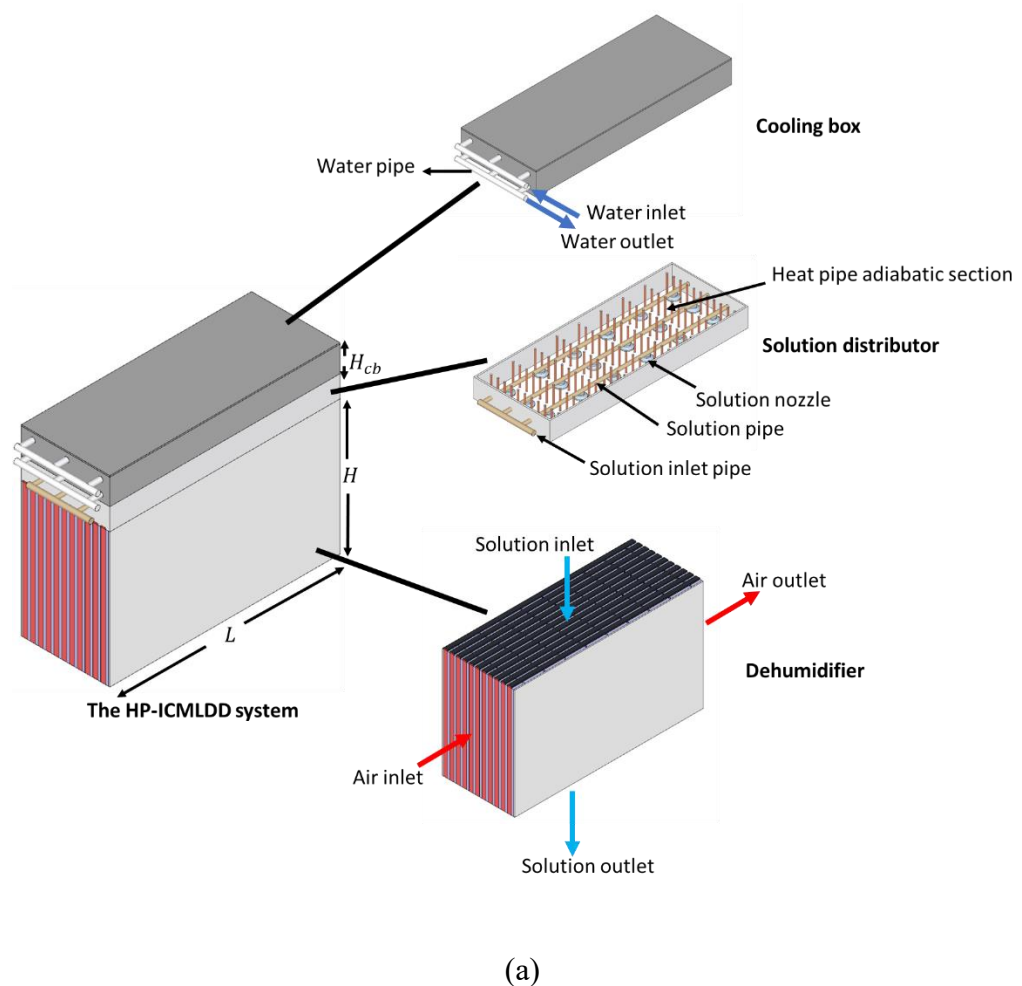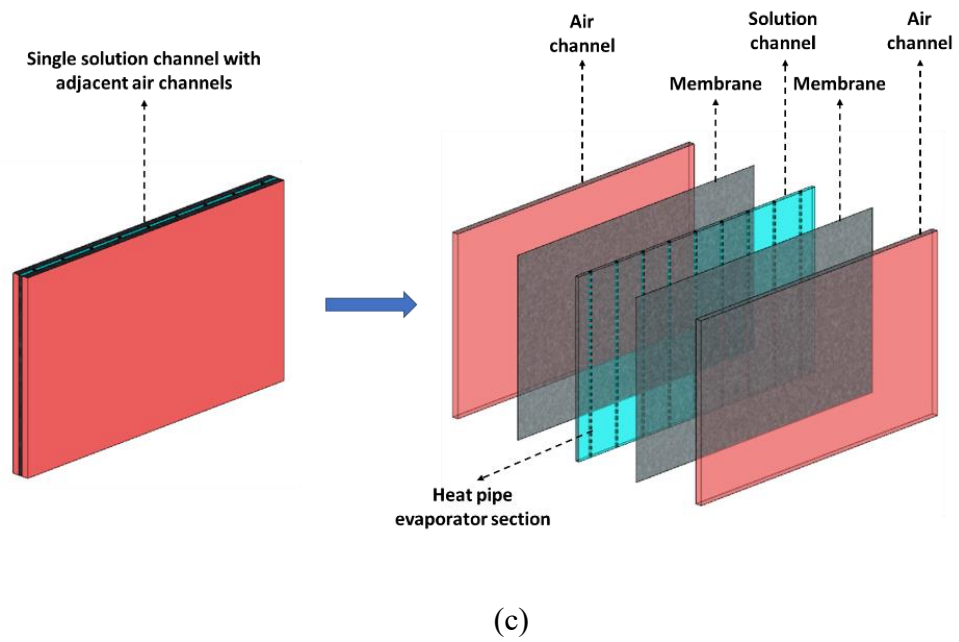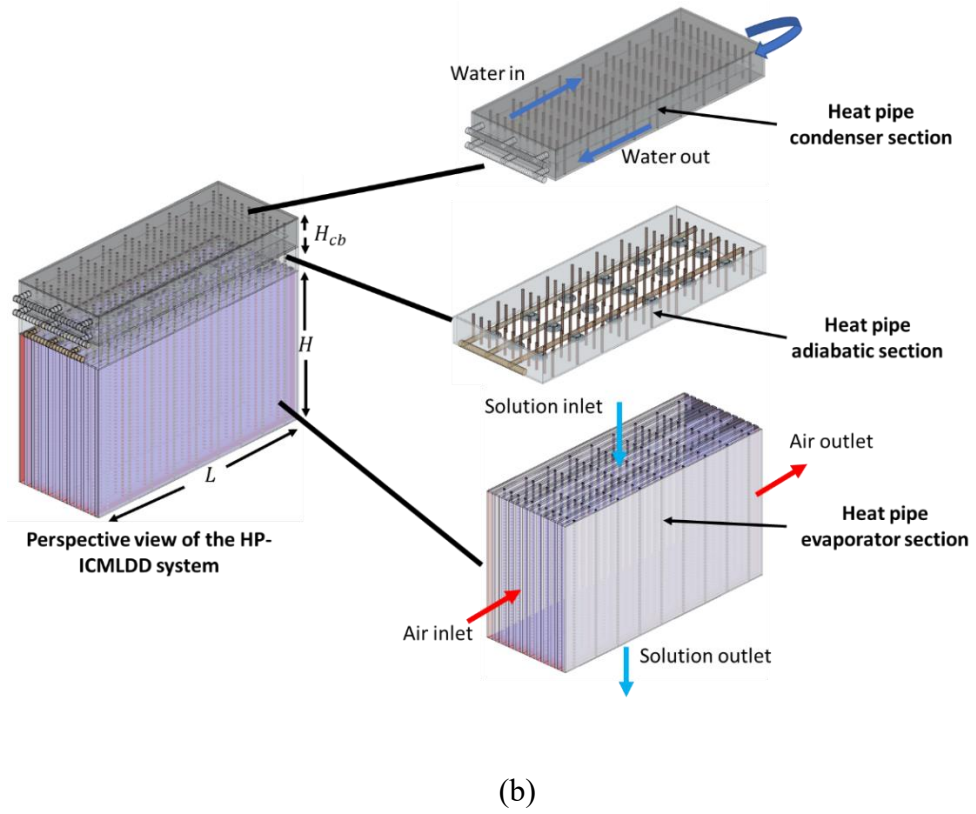
Fig 3-1 Concept and structure of the HP-ICMLDD system (a) Structure; (b)

Perspective view; (c) Single solution channel with adjacent air channels

3.2.1 Air and solution property equations

For analysis, the air humidity ratio (W_{air}) (kg/kgdryair) needs to be determined where the correlation between relative humidity (RH) (%) and absolute humidity (AH) (kg/m^3) is derived by Mander [178]:

$$AH = \frac{6.112 \times e^{\left[\frac{17.67 \times T_{air}}{T_{air}+243.5}\right] \times RH \times 2.1674}}{1000(273.15+T_{air})} \qquad (3\text{-}1)$$

Where T_{air} is air temperature (°C). Then W_{air} can be calculated by:

$$W_{air} = \frac{AH}{\rho_{air}} \qquad (3\text{-}2)$$

Where ρ_{air} is air density (kg/m^3).

W_{sol} is the solution equilibrium specific humidity (kg/kgdryair), and calculated by [179]:

$$W_{sol} = 0.62198 \frac{P_{sol}(C_{sol}, T_{sol})}{P_{atm}-P_{sol}(C_{sol}, T_{sol})} \qquad (3\text{-}3)$$

where P_{atm} is the atmospheric pressure (Pa); P_{sol} is the vapour pressure of the LiCl solution (Pa), which is a function of solution concentration C_{sol} and temperature T_{sol}, and given by [180]:

$$\log P_{sol} = KI \left[A - \frac{B}{T_{sol}-E_s}\right] + \left[C - \frac{D}{T_{sol}-E_s}\right] \qquad (3\text{-}4)$$

Where K and I are the electrolyte parameters relating to solute (LiCl); A, B, C, D and E_s are the parameters regarding the solvent (water). All the parameters are specified for the LiCl solution [180], as shown in Table 3-1.

Table 3-1 Specified parameters for LiCl solution [180]

A	B	C	D	E_s	K	I
-0.0183	3.9110	7.1523	1730	39.53	5.3703	8.2671

Moreover, A, B, C and D can be calculated as:

$$A = A_s + 3.60591 \times 10^{-4} \times I + M_s/2303 \tag{3-5}$$

$$B = B_S + 1.382982 \times I - 0.031185 \times I^2 \tag{3-6}$$

$$C = C_S - 3.99334 \times 10^{-3} \times I - 1.11614 \times 10^{-4} \times I^2 + M_s \times I \times (1 - \chi)/$$

$$2303 \tag{3-7}$$

$$D = D_S - 0.138481 \times I + 0.027511 \times I^2 - 1.79277 \times 10^{-3} \times I^3 \tag{3-8}$$

Where A_s, B_s, C_s, D_s are electrolyte parameters related to solute and solvent. For

LiCl aqueous solution, these parameters are given in Table 3-2 [180].

Table 3-2 Electrolyte parameters for LiCl solution [180]

A_s	B_s	C_s	D_s
-0.021302	-5.390915	7.192959	1730.2857

I is the ionic strength (mol/kg), which can be obtained by [180]:

$$I = \frac{1}{2}\Sigma\, b_{(i)}Z_{(i)}{}^2 \tag{3-9}$$

Where $b_{(i)}$ is the molality of electrolyte i; $Z_{(i)}$ is the valence of electrolyte i. M_s

is the molecular weight of the solvent (kg/mol). For water solvents, M_s=0.018

kg/mol. χ is another electrolyte property related to the solute as calculated by

[180]:

$$\chi = 2(v_+ + v_-)/(v_+Z_+{}^2 + v_-Z_-{}^2) \tag{3-10}$$

Where v_+ and v_- are number of models of cation and anion produced by the dissociation of one mole of the electrolyte, respectively; Z_+ and Z_- are valence of cation and anion, respectively.

Consequently, once the temperature and concentration of the solution are given, the equilibrium vapour pressure can be obtained. Then, the solution equilibrium specific humidity W_{sol} can be calculated by Eq. (3-3). In this study, LiCl is selected as the working solution for the entire system. Thus, a psychometric chart of the LiCl solution is plotted in Fig 3-2.
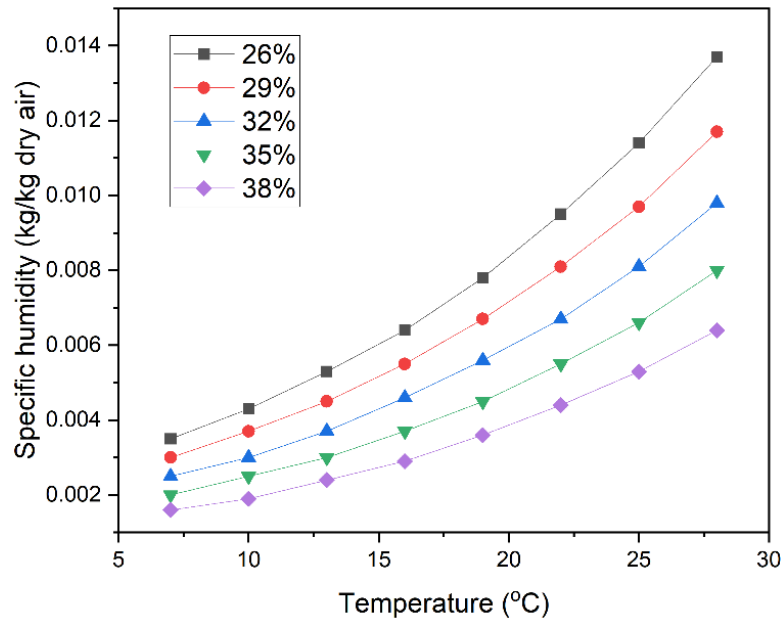
Fig 3-2 Psychometric chart of LiCl for dehumidifier

3.2.2 Performance evaluation indices

3.2.2.1 Air side effectiveness for dehumidifier

Air side effectiveness is commonly used to evaluate the dehumidification and cooling capabilities of a heat and mass exchanger [181, 182]. This study employs three effectiveness types, including sensible effectiveness (ε_{sen}), latent effectiveness (ε_{lat}), and total effectiveness (ε_{tot}). The air side sensible effectiveness (ε_{sen}) is an essential criterion for evaluating the overall heat

transfer performance of air, solution and water. It is determined as the product of the effectiveness of air and solution heat exchanger, heat pipe heat exchanger. The effectiveness of air and solution heat exchanger is the ratio of the actual sensible energy difference when the air passes through the dehumidifier $(T_{air,out} - T_{air,in})$ to the maximum possible sensible energy difference in the dehumidifier ($T_{sol,in} - T_{air,in}$) [183]. The effectiveness of heat pipe heat exchanger is the ratio of the actual sensible energy difference when water passes through the heat pipes $(T_{w,out} - T_{w,in})$ to the maximum possible sensible energy difference in the heat pipe heat exchanger $(T_{sol,in} - T_{w,in})$ [183]:

$$\varepsilon_{sen} = \frac{(\dot{m}c_p)_{air}(T_{air,in}-T_{air,out})}{(\dot{m}c_p)_{min,a-s}(T_{air,in}-T_{sol,in})} \cdot \frac{(\dot{m}c_p)_w(T_{w,out}-T_{w,in})}{(\dot{m}c_p)_{min,s-w}(T_{sol,in}-T_{w,in})} \tag{3-11}$$

where $T_{air,in}$ is the inlet air temperature of the dehumidifier (℃); $T_{air,out}$ is the outlet air temperature of the dehumidifier (℃); $T_{sol,in}$ is the inlet solution temperature (℃); $T_{w,in}$ is the inlet water temperature of the cooling box (℃); $T_{w,out}$ is the outlet water temperature of the cooling box (℃).

The air side latent effectiveness (ε_{lat}) is used to evaluate the mass transfer performance or moisture removal efficiency. Due to the water vapour partial pressure difference in the air and solution channels, the water vapour will pass through the microporous on the membrane surface and then condense in the solution channel. The latent effectiveness (ε_{lat}) is defined as the ratio of the actual air latent energy difference ($W_{air,in} - W_{air,out}$) to the maximum possible latent energy difference ($W_{air,in} - W_{sol,in}$) [183]:

$$\varepsilon_{lat} = \frac{\dot{m}_{air}h_{fg}(W_{air,in}-W_{air,out})}{\dot{m}_{min}h_{fg}(W_{air,in}-W_{sol,in})} \tag{3-12}$$

where $W_{air,in}$ and $W_{air,out}$ are the inlet and outlet air humidity ratio (kg/kgdryair), respectively; $W_{sol,in}$ is the equilibrium humidity ratio of air at the inlet condition of the desiccant solution (kg/kgdryair).

The total effectiveness (ε_{tot}) is the ratio of the enthalpy transfer rate to the maximum possible energy (enthalpy) transfer rate in the dehumidifier [183]:

$$\varepsilon_{tot} = \frac{\varepsilon_{sen} + h^* \varepsilon_{lat}}{1 + h^*}$$

$$(h^* = \frac{h_{fg}}{c_{p,air}} \frac{W_{sol,in} - W_{air,in}}{T_{sol,in} - T_{air,in}}) \tag{3-13}$$

3.2.2.2 Air side moisture removal rate (MRR)

The air side moisture removal rate (MRR) indicates the dehumidification capacity (g/s), depending on both the air absolute moisture content difference ($\omega_{air,in} - \omega_{air,out}$) and the air mass flow rate $\dot{m}_{air,in}$, which can be calculated by:

$$MRR = \dot{m}_{air} (W_{air,in} - W_{air,out}) \tag{3-14}$$

3.2.2.3 Internal cooling capacity (Q_{ic})

The internal cooling capacity (Q_{ic}) is used to assess the internal cooling performance. Under the steady condition, heat from the air side is absorbed by the solution where a part of the heat load results in the solution temperature rise, and the remaining part is removed by the cooling box water through the heat pipes. Therefore, the internal cooling capacity is calculated, representing the cooling capacity generated by the heat pipes rather than the total cooling capacity (system cooling capacity). The high internal cooling capacity means that the more absorbed heat is removed. In addition, a high internal cooling capacity also

indicates that the low solution temperature is reached to maintain efficient cooling and dehumidification performance [84].

$$Q_{ic} = C_{p,w}\dot{m}_w\left(T_{w,out} - T_{w,in}\right) \tag{3-15}$$

Where $C_{p,w}$ is the water specific heat capacity (J/kg·K); $\dot{m}_w$ is the water mass flow rate (kg/s); $T_{w,in}$ and $T_{w,out}$ are the inlet and outlet cooling box water temperatures (°C), respectively.

According to Bell's uncertainty analysis method [184], the uncertainty value of U_Y is determined by the function of U_{X_i} of each variable X_i:

$$U_Y = \sqrt{\sum_{i=1}^{N}(\frac{\partial Y}{\partial X_i})^2 U_{X_i}{}^2} \tag{3-16}$$

Based on Eq. (3-16), the absolute uncertainty of a calculated value can be derived with error bars included in the graphs for experimental results validation.

3.3 Description of the regenerator

The majority of previous literature focused on the dehumidification process, according to the literature review. However, within the liquid desiccant dehumidification system, regeneration is regarded as one of the most essential processes, as the diluted desiccant solution must be re-concentrated to achieve solution recycling. Regarding regeneration, previous research has focused on direct contact regeneration between the desiccant solution and air. The regenerator uses the same membrane-based heat and mass exchanger test facility built in the laboratory with no cooling box or internal cooling source involved since the primary purpose of the regenerator is to re-concentrate the weak solution coming from the dehumidifier. The concept and structure of the regenerator are shown in Fig 3-3. The membrane-based regenerator has separate

channels for the air stream and desiccant solution, where heat and moisture transfer between the air stream and desiccant solution is through the semi-permeable micro-porous hydrophobic membranes. The desiccant solution flows downwards in the solution channels, where the air absorbs the solution moisture and heat while the liquid desiccant is impermeant through the membrane. The structure of the regenerator is depicted in Fig 3-3 (a), with the air and solution flow in a cross-flow arrangement. The perspective view of the regenerator and detail of a single solution channel with adjacent air channels are shown in Fig 3-3 (b) and (c), respectively. The structure of the regenerator is identical to that of the dehumidifier, except that there are no internal cooling sources.

(a)

(b)

(c)
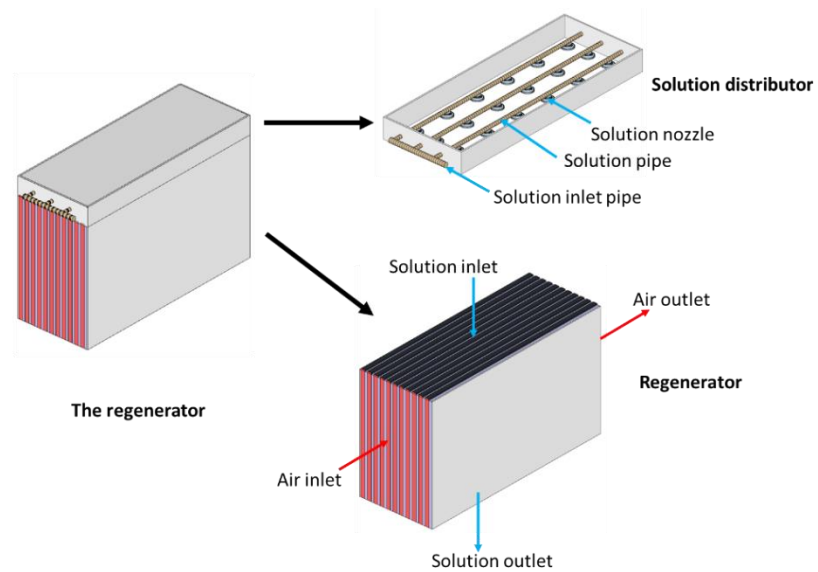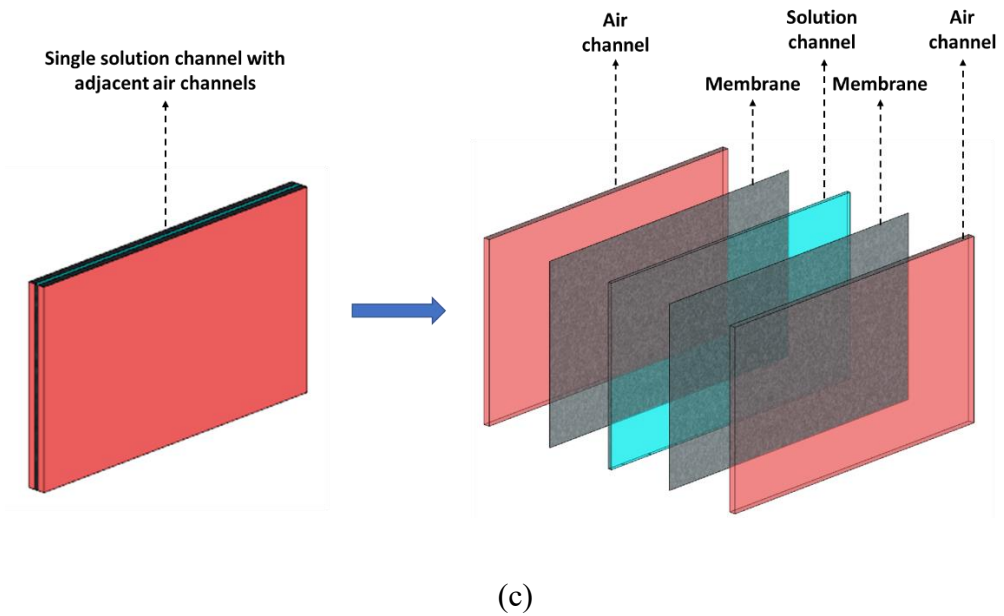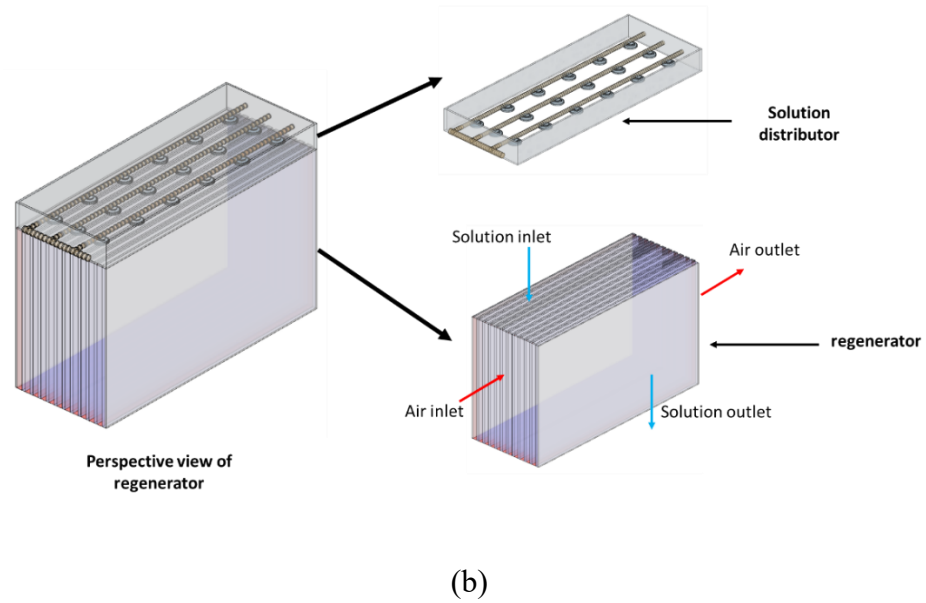
Fig 3-3 Concept and structure of the regenerator (a) Structure; (b) Perspective view; (c) Single solution channel with adjacent air channels

3.3.1 Air and solution property calculations

The calculation methods for air and solution properties have been explained in **Section 3.2.1**. It should be noticed that compared with the investigation into the dehumidifier, the solution concentration and temperature of interest for regenerator performance investigation in this chapter are different. Thus the

equilibrium specific humidity of LiCl under different conditions is calculated, and another psychometric chart of the LiCl solution is given in Fig 3-4.
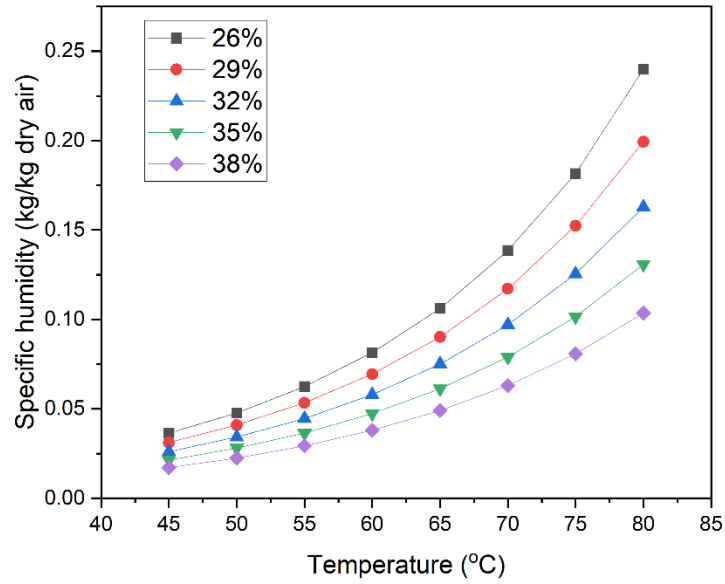
Fig 3-4 Psychometric chart of LiCl for regenerator

3.3.2 Performance evaluation indices

3.3.2.1 Solution side effectiveness for regenerator

Effectiveness is the most critical parameter used to evaluate the performance of a heat and mass exchanger. Air side effectiveness has been widely used for dehumidification performance evaluation. They are used for the dehumidifier performance evaluation in the previous section. However, in the regeneration process, where the main focus is on the desiccant solution, the air side effectiveness cannot reflect the regenerator performance correctly. Thus the solution side effectiveness for the regenerator is introduced by referring to the literature [29]:

$$\varepsilon_{sen,sol} = \frac{(\dot{m}c_p)_{sol}(T_{sol,in,reg}-T_{sol,out,reg})}{(\dot{m}c_p)_{min}(T_{sol,in,reg}-T_{air,in,reg})} \tag{3-17}$$

$$\varepsilon_{lat,sol} = \frac{\dot{m}_{desi}h_{fg}(X_{sol,in,reg}-X_{sol,out,reg})}{\dot{m}_{min}h_{fg}(W_{sol,in,reg}-W_{air,in,reg})} \tag{3-18}$$

$$\varepsilon_{tot,sol} = \frac{\varepsilon_{sen,sol} + h^* \varepsilon_{lat,sol}}{1 + h^*}$$ (3-19)

Where $\dot{m}_{desi}$ is the desiccant flow rate (kg/s), which is given by:

$$\dot{m}_{desi} = \frac{\dot{m}_{sol}}{1 + X_{sol}}$$ (3-20)

3.3.2.2 Solution side moisture flux rate (MFR)

As discussed in **section 3.2.2.2**, the moisture removal rate for the dehumidifier has been introduced to evaluate the amount of moisture being removed by the air from diluted liquid desiccant solution or the amount of moisture absorbed by concentrated solution from humid air. In this study, with the main focus on the desiccant solution, a similar index called the moisture removal rate of the regenerator (MRR_{reg}) has been defined and given as:

$$MRR_{reg} = \dot{m}_{desi}\left(X_{sol,in,reg} - X_{sol,out,reg}\right)$$ (3-21)

Then, another vital index called solution side moisture flux rate (MFR) is defined and given as:

$$MFR = \frac{MRR_{reg}}{U_m A_{mem}} = \frac{\dot{m}_{desi}\left(X_{sol,in,reg} - X_{sol,out,reg}\right)}{U_m A_{mem}}$$ (3-22)

As seen from the above equation, MFR is the ratio between the moisture removal rate of the regenerator (MRR_{reg}) and membrane overall mass transfer conductance ($U_m A_{mem}$). MFR is generally used for performance evaluation rather than MRR_{reg}, since it is independent of the size of the regenerator. It only depends on the inlet condition, making the results more general [185].

3.3.2.3 Solution temperature decrease rate (TDR)

Apart from re-concentration of the liquid desiccant solution, the lower solution temperature is preferred, where a lower solution temperature would make the

dehumidification process more effective. Thus, the index so-called solution temperature decrease rate (TDR) is applied to evaluate the sensible performance of regeneration, which is defined as:

$$TDR = \frac{T_{sol,in} - T_{sol,out}}{T_{sol,in}} \tag{3-23}$$

3.4 Description of the complete system

The previous two sections covered the performance of a single dehumidifier and a regenerator, respectively. In the majority of published works on membrane-based dehumidification systems, the supply and exhaust side exchangers are coupled to a closed-loop aqueous salt solution. In these publications, it is assumed that the heat and mass transfer rates in the supply exchanger are equivalent to those in the exhaust exchanger, i.e. no heat or moisture is added or removed from the system. However, the system can benefit significantly from an external heat or cold source, in which case a hot water loop and a cooling water loop are incorporated into the design. The heat and mass transfer rates of the dehumidifier and regenerator might not be identical. This section investigates a comprehensive membrane-based liquid desiccant dehumidification system, including a dehumidifier, a regenerator, and hot and cold water supply systems. This section includes a full parametric study on a complete membrane-based liquid desiccant system and offers meaningful information for developing and operating a liquid desiccant dehumidification air-conditioning system.

Dehumidifier, regenerator, and heat exchanger comprise most of the constructed numerical model. The structures of the dehumidifier and regenerator are comparable, except that their heat and mass transfer directions are opposite.

3.4.1 Description of heat exchangers

There are three liquid-to-liquid plate heat exchangers installed in the complete system. The concept diagram of the complete system is given in Fig 3-5. The diluted (weak) solution is initially heated by hot water in heat exchanger 1 (HX1) before entering the regenerator. Then, heat recovery occurs between the strong and weak solutions in heat exchanger 2 (HX2). The concentrated (strong) solution is cooled by tap water in heat exchanger 3 (HX3) before entering the dehumidifier. For the parallel-flow heat exchanger, the effectiveness ε is defined as the ratio of the actual heat transfer rate over the maximum possible heat transfer rate [186]:

$$\varepsilon \equiv \frac{q}{q_{max}} = \frac{c_{p,h}(T_{h,in}-T_{h,out})}{c_{min}(T_{h,in}-T_{c,in})} = \frac{c_{p,c}(T_{c,out}-T_{c,in})}{c_{min}(T_{h,in}-T_{c,in})} \tag{3-24}$$

Where $c_{p,h}$ and $c_{p,c}$ are heat capacity rates of hot and cold fluid, respectively; $T_{h,in}$, $T_{h,out}$, $T_{c,in}$ and $T_{c,out}$ are temperatures of hot and cold fluids at inlets and outlets. For HX1-HX3, their effectiveness are expressed as:

$$\varepsilon_1 = \frac{\dot{m}_{sol}c_{p,sol}(T_{sol,in,reg}-T_{sol,2})}{min(\dot{m}_{sol}c_{p,sol},\dot{m}_{hot,w}c_{p,w})(T_{hot,w,in}-T_{sol,2})} \tag{3-25}$$

$$\varepsilon_2 = \frac{\dot{m}_{sol}c_{p,sol}(T_{sol,out,reg}-T_{sol,1})}{\dot{m}_{sol}c_{p,sol}(T_{sol,out,reg}-T_{sol,out,deh})} = \frac{\dot{m}_{sol}c_{p,sol}(T_{sol,2}-T_{sol,out,deh})}{\dot{m}_{sol}c_{p,sol}(T_{sol,out,reg}-T_{sol,out,deh})} \tag{3-26}$$

$$\varepsilon_3 = \frac{\dot{m}_{sol}c_{p,sol}(T_{sol,1}-T_{sol,in,deh})}{min(\dot{m}_{sol}c_{p,sol},\dot{m}_{cooling,w}c_{p,w})(T_{sol,1}-T_{cooling,w,in})} \tag{3-27}$$

Where subscript "deh" and "reg" represent dehumidifier and regenerator, respectively; $T_{cooling,w,in}$ and $T_{hot,w,in}$ are temperatures of cooling water from tap water and hot water from the boiler at inlets (°C), respectively; $T_{sol,1}$ and $T_{sol,2}$ are temperatures of strong and weak solution after HX1 (°C). As depicted

in Fig 3-5. $\dot{m}_{cooling,w}$ and $\dot{m}_{hot,w}$ are mass flow rates of cooling and hot water (kg/s), respectively.
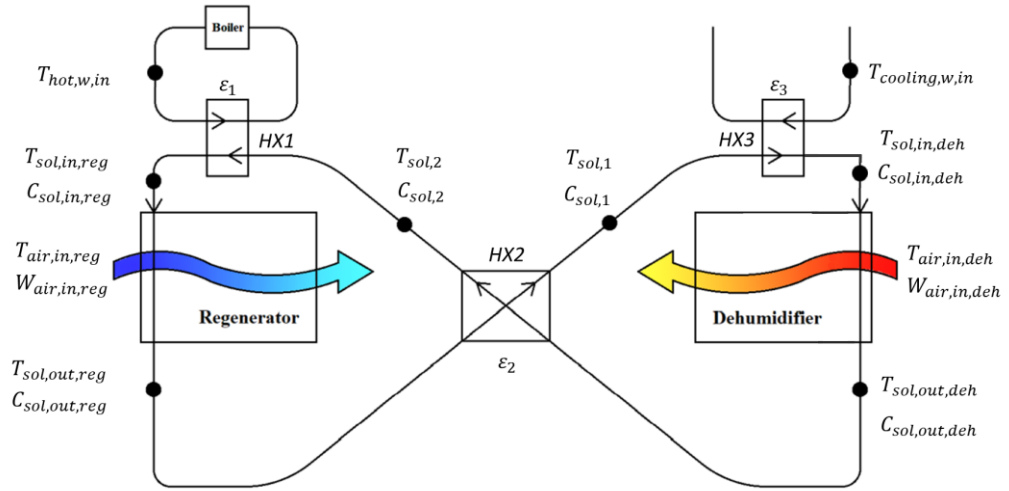
Fig 3-5 Concept diagram of the heat exchangers

3.4.2 Performance evaluation indices

3.4.2.1 Total cooling capacity (Q_{tot})

The internal cooling capacity for the heat pipe alone has been determined and analysed to evaluate how much heat has been taken by the heat pipes during the dehumidification process. However, from the complete system perspective, the most significant functions are absorbing moisture from the moist air (latent cooling) and reducing its temperature (sensible cooling). Therefore, it is crucial to evaluate and determine the dehumidifier's total cooling capacity (Q_{tot}) (kW), which is the sum of system sensible cooling (Q_c) (kW) and latent cooling capacities (Q_{deh}) (kW):

$$Q_{tot} = Q_c + Q_{deh} \tag{3-28}$$

$$Q_c = \dot{m}_{air,deh} c_{p,air} (T_{air,in,deh} - T_{air,out,deh}) \tag{3-29}$$

$$Q_{deh} = \dot{m}_{air,deh} h_{fg} (W_{air,in,deh} - W_{air,out,deh}) \tag{3-30}$$

3.4.2.2 Coefficient of Performance (COP)

To evaluate the energy efficiency of the complete system, the Coefficient of Performance (COP) is divided into three parts: the thermal COP (COP_{th}), the electrical COP (COP_{ele}) and the total COP (COP_{tot}), in which COP_{th} includes thermal energy input of the regeneration heat from the regenerator (Q_{reg}) and COP_{ele} comprises the power needed for the pumps and fans supplied by the electricity (W_{fan} and W_{pump}), with the expression:

$$If \ T_{w,in} > 18°C, \ COP_{th} =$$

$$\frac{Q_{tot}}{Q_{reg}/\eta/delivery \ efficiency + \dot{m}_w c_{p,w}(T_{w,in}-18)/\eta_w/water \ delivery \ efficiency}$$

$$If \ T_{w,in} \leq 18°C, \ COP_{th} = \frac{Q_{tot}}{Q_{reg}/\eta/delivery \ efficiency} \tag{3-31}$$

$$COP_{ele} = \frac{Q_{tot}}{Q_{ele}} = \frac{Q_{tot}}{W_{fan}+W_{pump}} \tag{3-32}$$

$$COP_{tot} = \frac{Q_{tot}}{Q_{reg}+Q_{ele}+Q_{tap}} = \frac{Q_{tot}}{Q_{reg}+W_{fan}+W_{pump}+Q_{tap}} \tag{3-33}$$

$$Q_{reg} = \dot{m}_{sol,reg}c_{p,sol}(T_{sol,out,HX1} - T_{sol,in,HX1}) \tag{3-34}$$

$$W_{fan} = \frac{W_{output,fan}}{\eta_{fan}} = \frac{Q_{fan}\Delta P_{air}}{\eta_{fan}} = \frac{\dot{m}_{air}\Delta P_{air}}{\rho_{air}\eta_{fan}} \tag{3-35}$$

$$W_{pump} = \frac{W_{output,pump}}{\eta_{pump}} = \frac{Q_{pump}\Delta P_{sol}}{\eta_{pump}} = \frac{\dot{m}_{sol}\Delta P_{sol}}{\rho_{sol}\eta_{pump}} \tag{3-36}$$

$$\Delta P_{air} = \frac{1}{2}\rho_{air}u_{air}^2(\frac{A_{deh,reg}}{A_d})^2(\frac{A_d}{A_{deh,reg}} - 1)^2 \tag{3-37}$$

$$\Delta P_{sol} = \frac{1}{2}\rho_{sol}u_{sol}^2(\frac{A_{deh,reg}}{A_d})^2(\frac{A_d}{A_{deh,reg}} - 1)^2 \tag{3-38}$$

$$f = \frac{8vL}{\pi r^4} \tag{3-39}$$

Where COP_{th} is thermal COP; When $T_{w,in} > 18°C$, the inlet cold water needs to be cooled to 18°C (explained in section 5.4.1). Therefore, the cold water cooling energy consumption is considered in the thermal COP equation. Besides, the cold water cooling energy consumption is not considered when $T_{w,in} \leq 18°C$.

COP_{ele} is electrical COP; COP_{tot} is total COP; Q_{tot} is the sum of total cooling and dehumidification capacity (kW); Q_{reg} is the regeneration heat input (kW); Q_{ele} is the total electricity consumption (kW); η is boiler efficiency, η_w is cold water efficiency and *water delivery efficiency* is heat transfer efficiency from cooler to the system; W_{fan} is fan power consumption (kW); W_{pump} is pump power consumption (kW); $T_{sol,in,HX1}$ is the solution temperature at the inlet of the HX1 (°C); $T_{sol,out,HX1}$ is the solution temperature at the outlet of the HX1 (°C); $W_{output,fan}$ is the fan power output, which is the useful power output applied to the air (kW); $W_{output,pump}$ is the pump power output, which is the useful power output applied to the solution (kW); η_{fan} is the fan efficiency; η_{pump} is the pump efficiency; Q_{fan} is the air volumetric flow rate through the fan (m³/s); Q_{pump} is the solution volumetric flow rate through the pump (m³/s); ΔP_{air} is the total pressure drop across the air (Pa); ΔP_{sol} is the total pressure drop across the solution (Pa); u_{air} is the air velocity (m/s); u_{sol} is the solution velocity (m/s); $A_{deh,reg}$ is the windward area of the dehumidifier or regenerator (m²); A_d is the cross area of the duct connected to the dehumidifier or regenerator (m²); f is the flow resistance of air, solution and water in the channel; L is the channel length (m) and r is hydraulic diameter (m).

3.5 Modelling of the integrated liquid desiccant air-conditioning system

3.5.1 Description of the ILDAC system

The HP-ICMLDD system described in previous sections could provide pre-cooled and dehumidified air. However, in order to achieve the supply air under thermal comfort conditions, this section proposes an integrated system combining the complete LDD system with the air-water heat pump (AWHP) system, where the PVT renewable technology and thermal storage system are introduced to provide the renewable heat and electricity. The concept of the integrated liquid desiccant air-conditioning (ILDAC) system is depicted in Fig 3-6.

In general, the ILDAC system consists of four circuits, including:

1. Dehumidification circuit: The HP-ICMLDD (dehumidifier), regenerator, two solution storage tanks (strong and weak solution), liquid-to-liquid heat exchanger);

2. Heat pump circuit: Evaporator, compressor, condenser and expansion valve;

3. Energy storage circuit: Hot water storage cylinder (single-coil indirect unvented water storage cylinder);

4. Renewable energy circuit: Photovoltaics-Thermal (PVT) panel.

In the air loop, the ambient hot and humid air enters the HP-ICMLDD (dehumidifier) with the outlet of pre-cooled and dehumidified air, and then further cooled by the cooling coil of the evaporator, with the cooled and dehumidified air supplied to the indoor environment. Besides, the hot return air extracted from the indoor environment enters the regenerator to concentrate the weak solution with the exhaust air at the outlets to the outdoor environment.

In the refrigerant loop, the hot and high-pressure vapour flows into the condenser, where the heat is released and absorbed by the pre-heated water from the PVT outlet. Then, the hot and high-pressure liquid refrigerant passes through the expansion valve, with cold and low-pressure liquid refrigerant entering the evaporator. By absorbing heat from the pre-cooled air (from HP-ICMLDD outlet), the cold and low-pressure liquid refrigerant is converted from liquid to vapour phase and then enters the compressor, where the cold and low-pressure vapour refrigerant will be transformed to hot and high-pressure vapour refrigerant.

In the solution loop, the weak solution from the solution tank is pumped to the liquid-to-liquid heat exchanger, where the cold and weak solution absorbs heat from hot water, with hot and weak solution passing through the regenerator. The hot and weak solution is concentrated into the cold and strong solution by releasing the moisture and heat to the return air and storing it in the solution tank. The cold and strong solution passes through the HP-ICMLDD, absorbs heat and moisture from the inlet hot and humid air, and stores in the weak solution tank.

In the water loop, the cold water outlet from the coil of the hot water storage cylinder (top side outlet) enters the PVT back panel absorbing the heat from the PV layer. Then, the pre-heated water absorbs the heat from the condenser and transfers it into hot water, and flows into the coil of the hot water storage cylinder (bottom side outlet). The hot water out from the cylinder has two branches: the first hot water flow enters the liquid-to-liquid heat exchanger in the dehumidification circuit to heat the weak solution that flows to the regenerator; the other water flow enters the indoor radiator to provide space heating.

The air loop functions as the cooling and dehumidification source, where the indoor environment is adjusted by the LDD-AWHP cascade air-conditioning process, whereas the space heating is not undertaken by it. The control strategies of the air loop during summertime and wintertime are introduced as:

1) In the summertime, the air loop is activated, where the hot and humid air from the outdoor environment enters the HP-ICMLDD at first with pre-cooled and dehumidified air flowing through the evaporator in the heat pump circuit with cooled and dehumidified air supplying to the indoor environment. Meanwhile, the return air from the indoor environment flows into the regenerator to concentrate the weak solution, with the exhausted air emitted to the outdoor environment.

2) In wintertime, the air loop is deactivated, where the dehumidification circuit does not function.

The water loop is functioning as either supplying regeneration heat in summertime or space heating in the wintertime. The control strategies of the water loop during summertime and wintertime are introduced as:

1) In the summertime, the water loop functioning as regeneration heat is activated, where the cold and weak solution is heated by the hot water coming from the water storage cylinder. Meanwhile, the water loop functioned as the space heating is deactivated.

2) In wintertime, the water loop functioning as space heating is activated, where the indoor radiator is heated by the hot water coming from the water storage cylinder. Meanwhile, the water loop functioned as the regeneration heat is deactivated.

Moreover, another advantage of this integrated system is that the PVT panels provide renewable electricity to support the heat pump compressor when solar radiation is sufficient, thereby reducing grid electricity requirements. Besides, instead of installing additional batteries and storing renewable electricity, this integrated system transforms the renewable electricity into renewable heat and stores the thermal energy by supporting renewable electricity to the heat pump compressor.
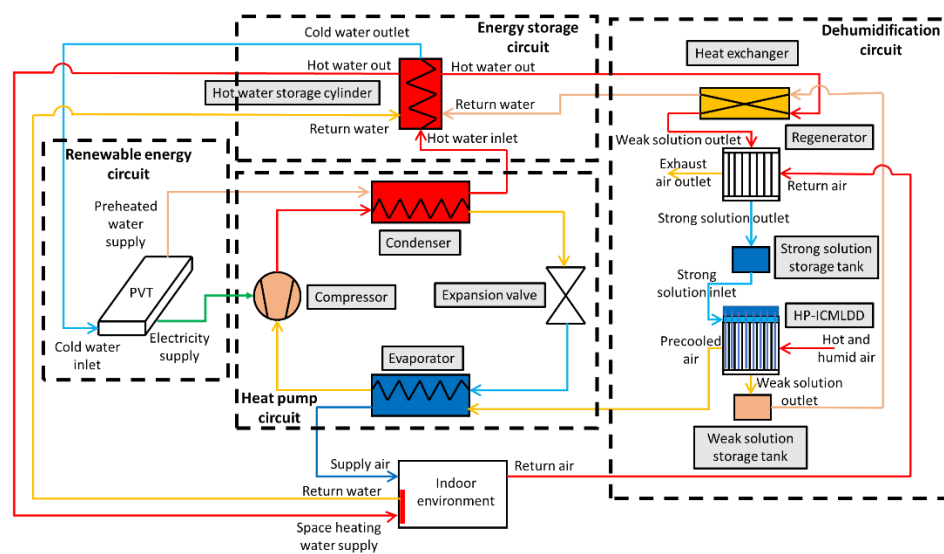
Fig 3-6 The concept of the integrated liquid desiccant air-conditioning (ILDAC) system

3.5.1.1 Air-water heat pump (AWHP) circuit

Since the ILDAC system combines the LDD with the AWHP and the LDD modelling has been described in previous sections, the AWHP modelling needs to be discussed in order to integrate the outlet air from the LDD system with the inlet air to the AWHP. Besides, the commercial AWHP specification is described under the condition of stand-alone operation with hot and humid ambient air rather than pre-cooled and dehumidified air. Therefore, the practical AWHP cooling and heating performance needs to be discussed with the dynamic

modelling method. Fig 3-7 shows the air-water heat pump circuit and main components. The ideal thermodynamic cycle consists in four processes is given as:

Between 1 or 1' and 2 (condensation of the refrigerant): the hot refrigerant gas is condensed and releases heat in the condenser (to hot water storage cylinder). During this process, the pressure is kept constant (isobaric process).

Between 2 and 3 (expansion of the refrigerant): the liquid refrigerant expands in the expansion valve, and its pressure and temperature decrease (isenthalpic process).

Between 3 and 4 or 4' (evaporation of the refrigerant): the refrigerant is heated by the extracted heat from the environment. The refrigerant is converted to vapour at constant pressure (isobaric process) during this process.

Between 4 and 1 (or 4' and 1') (compression of the refrigerant): the refrigerant gas is compressed in the compressor, which increases its pressure and temperature.
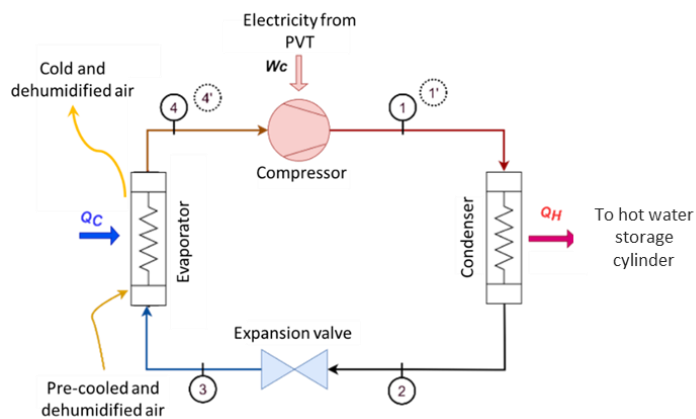
Fig 3-7 The schematic diagram of the traditional air-water heat pump circuit

For modelling the AWHP cycle, the following assumptions are considered:

No heat losses in the cycle.

The heat extraction factor (F_R from Eq. (3-197)) of the cooling coil is considered constant.

The mass flow rate of the refrigerant can be adjusted aiming to allow it to be completely evaporated in the solar panel (minimum saturated vapour) or to be at the maximum super-heated condition with a temperature equal to air temperature near the cooling coil (T'_a).

The temperature of the air near the cooling coil T'_a is considered to be constant.

The pressure after the expansion valve can be adjusted according to the supply air temperature of the HP-ICMLDD system at the outlets.

The refrigerant is always saturated liquid after the condenser (point 2).

The refrigerant used in this work is R134a, and its thermodynamic properties are obtained from [187], with the pressure-enthalpy and temperature-entropy diagrams shown in Fig 3-8, which shows the general Pressure – Enthalpy (P-H) and Temperature – Entropy (T-S) diagrams of the thermodynamic cycle.

(a)   (b)
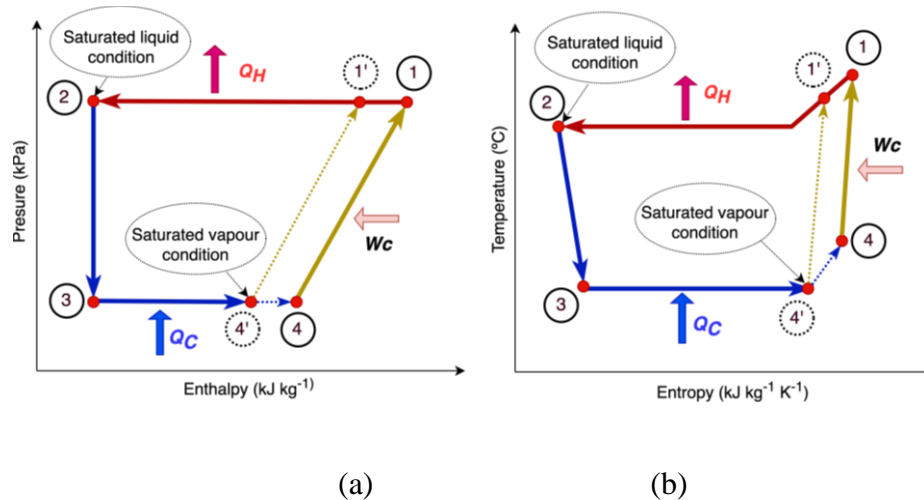
Fig 3-8 (a) Pressure - Enthalpy (P-H) and (b) Temperature – Entropy (T-S)

diagrams of the AWHP thermodynamic cycle

Based on the approaches described above, the enthalpy/energy balance in each process/component is:

Condenser

$$Q_H = \dot{m}(h_1 - h_2) \tag{3-40}$$

Expansion valve

$$h_3 = h_2 \tag{3-41}$$

Evaporator

$$Q_C = \dot{m}(h_4 - h_3) \tag{3-42}$$

Compressor

$$W_C = \dot{m}(h_1 - h_4) \tag{3-43}$$

Where h_1, h_2, h_3 and h_4 are enthalpies in points 1, 2, 3 and 4, respectively (in case of saturated vapour condition (point 4'), h_4 and h_1 are h'_4 and h'_1, respectively), $\dot{m}$ is the mass flow rate of the refrigerant, and Q_H is the heat released in the condenser (storage tank), Q_C is the heat absorbed from the cooling coil and W_C is the power consumed in the compressor.

The heat absorbed from the cooling coil can also be calculated using:

$$Q_C = F_R A[U_{overall}(T_3 - T'_a)] \tag{3-44}$$

in which F_R is the ratio between actual output power and output power when $T_p = T_3$, T_p is the temperature of the cooling coil, T_3 is the temperature of the refrigerant at the inlet of the cooling coil, A is the heat transfer area of the cooling

coil, U is the total heat transfer coefficient on the surface of the cooling coil and T'_a is the air temperature of the HP-ICMLDD system at the outlets.

The wind convection heat transfer coefficient h_{air} is calculated using [188]:

$$h_{air} = 5.7 + 3.8V \tag{3-45}$$

Where V (m/s) is the air velocity.

The overall heat transfer coefficient is given as:

$$U_{overall} = (\frac{1}{h_{air}} + \frac{\delta}{k} + \frac{1}{h_{refrigerant}})^{-1} \tag{3-46}$$

Where δ is the thickness of the coil (m); k is the thermal conductivity of the coil (W/m^{2}K) and $h_{refrigerant}$ is the heat transfer coefficient of the refrigerant (W/m^{2}K).

Depending on the mass flow rate, super-heated refrigerant conditions in the cooling coil may occur for high supply air temperature from the HP-ICMLDD system at the outlets. In these situations, the relation between the super-heated temperature and the absorbed heat from the cooling coil is described as:

$$Q_C = \dot{m}[h_{cL} + c'_p(T'_4 - T_4)] \tag{3-47}$$

Where h_{cL} is the enthalpy of evaporation of the refrigerant at a given pressure, c'_p is the heat capacity of the vapour at that pressure and T'_4 is the super-heated temperature at the outlet of the cooling coil (in this work T'_4 is imposed to be at maximum equal to T'_a, which is achieved by adjusting the mass flow).

The power consumed in the compressor can also be calculated using:

$$W_C = \dot{m}\left(\frac{P_4 v_4}{\eta_c}\left(\frac{k}{k+1}\right)\left[\left(\frac{P_1}{P_4}\right)^{\frac{k-1}{k}} - 1\right]\right) \tag{3-48}$$

Where P_4 is the pressure at point 4 (same pressure if point 4' occurs), P_1 is the pressure at point 1 (same pressure if point 1' occurs), v_4 is the specific volume of the refrigerant at point 4 (or v'_4 if the condition of point 4' occurs), η_c is the efficiency of the compressor, and k is the ratio of specific refrigerant heat.

The cooling (COP_C) and heating (COP_H) coefficient of performance of the AWHP is calculated using:

$$COP_C = \frac{h_4 - h_3}{h_1 - h_4} = \frac{Q_C}{W_C} \tag{3-49}$$

$$COP_H = \frac{h_1 - h_2}{h_1 - h_4} = \frac{Q_H}{W_C} \tag{3-50}$$

3.5.1.2 Simulation parameters and conditions
To control the inlet conditions of the refrigerant in the cooling coil, the following relations between pressure after the expansion valve and supply air temperature from the HP-ICMLDD system at the outlets are considered:

If $25°C \leq T'_a < 30°C$, $P_3 = 320$ kPa ($T'_4 = 2.5$ °C), $c'_p = 0.94$ kJ/kgK

If $30°C \leq T'_a < 35°C$, $P_3 = 400$ kPa ($T'_4 = 8.9$ °C), $c'_p = 0.95$ kJ/kgK

If $35°C \leq T'_a < 40$ °C, $P_3 = 500$ kPa ($T'_4 = 15.7$ °C), $c'_p = 0.98$ kJ/kgK

If $T'_a \geq 40$ °C, $P_3 = 600$ kPa ($T'_4 = 21.5$ °C), $c'_p = 1$ kJ/kgK

Table 3-3 shows the system geometric and thermal parameters and relevant thermodynamic properties of the R134a refrigerant.

Table 3-3 Thermal, geometric and relevant thermodynamic properties of the R134a refrigerant [187]

Parameter	Value
η_c	0.8
F_R	0.85
A (m^2)	3.2
k	1.2

All the other thermodynamic properties of the refrigerant (h, P, T, v, c_p) are obtained through interpolation data from [187].

3.5.1.3 ILDAC system dynamic energy simulation in EnergyPro

The EnergyPRO software is used to simulate the ILDAC system energy flow from the energy source to energy demand via the integrated system, as shown in Fig 3-9. The energyPro is the leading software for modelling and analysing complex energy projects with the combined supply of electricity and thermal energy (process heat, hot water and cooling), which is used for detailed technical of both existing and new energy projects in a very user-friendly interface providing the user with a clear overview of the project. The software offers a long range of technical and economic reports, including a graphical presentation of the simulated operation, which provides an overview and in-depth understanding of the dynamics of a complex energy system. To simulate the ILDAC system performance, the EnergyPro software requires inputs of:

1) Specification of the PVT panels;

2) COP correlations of the AWHP;

3) Thermal and electrical COP correlations of the complete LDD system;

4) Specification of the water cylinder;

5) Building dehumidification demand;

6) Building cooling demand;

7) Building space heating demand.

The specifications of the PVT panels (Solimpeks [189]) are given in Table 3-4. The specifications of the hot water cylinder (Telford Tempest 500 Litre Twin Coil Solar Indirect Unvented Cylinder [190]) are given in Table 3-5.
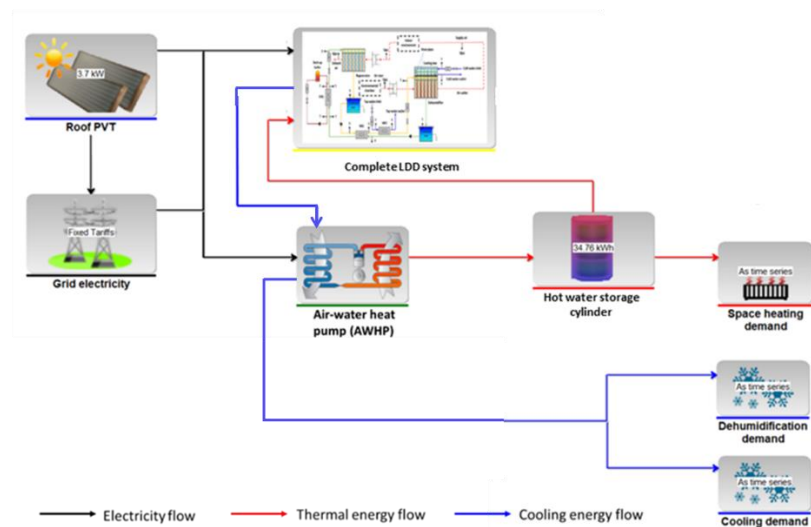
Fig 3-9 Energy flow work simulation process in EnergyPro software

Table 3-4 The specifications of the PVT panels [189]

Dimension	$1670mm \times 995mm \times 60mm$
Nominal electricity output	315 W (under STC of 1000 W/m^2 and 25 ℃)
Nominal thermal energy output	855 W (under STC of 1000 W/m^2 and 25 ℃)
Solar-to-electricity conversion efficiency	20% (under STC of 1000 W/m^2 and 25 ℃)
Solar-to-thermal conversion efficiency	47% (under STC of 1000 W/m^2 and 25 ℃)
Temperature coefficient for module efficiency	-0.5 %/℃
Nominal cell temperature	24 ℃
Temperature coefficient of Pmp	0.048 %/℃

Temperature coefficient of Voc	-0.255 %/°C
Temperature coefficient of Isc	-0.0331 %/°C

Table 3-5 The specifications of the hot water cylinder [190]

Capacity	500 L
Total heat loss (EN 12897)	69 W
Peak hot water flow	1800 L/hour
Maximum hot water temperature	80 °C
Insulation thickness	95 mm

3.5.2 Reference building and modelling

The residential building stock can be classified according to several variables, including different climate conditions, locations, construction years, building typologies and the influence of the surrounding environment. The clustering of the EU residential buildings has been discussed and classified by several projects and documents, such as the TABULA [191], the MARIE [192] and the ENTRANZE [193].

Selection of building retrofit measures, their applicability and associated energy-saving potentials are inherently dependent on building typologies (i.e. residential, commercial, etc.), operating patterns and climatic conditions [46]. This has been recognised by EPBD (European Performance Building Directive), which requires all EU member states to establish their Reference Buildings (RBs) to represent the diversification and functionalities of the national building stocks under different climatic conditions [46]. Various scientific studies have identified reference buildings within this context, representing varying

geographic and sectorial conditions for EU building stocks. Based on the source and the type of data collected, these RBs can be categorised into two types [194]:

Hypothetical or example RB: idealised buildings with assumed geometry and construction details, aiming to represent a large number of national building stocks;

Real RB: existing buildings with well-defined geometry, building fabric details, and internal energy demands that are able to facilitate characterisation of the general energy performance for substantial building stocks with similar building typologies and construction conditions.

The scientific community tends to adopt hypothetical RBs when conducting data-driven/statistical-based building energy performance analysis [195, 196] and/or urban-scale building energy planning [197] under the entire EU building stocks [198]. While real RBs are often applied for one particular building typology under the same climatic condition [199, 200], results are limited to the case study scale. Similarly, intending to create a harmonised EU building stock covering a range of building typologies, the EU-funded TABULA project [201] defined a series of "agreed parameters of a common classification", including construction year class, building size class, country, region or climate zone.

According to the literatures [202, 203], most of the previous research focused on the dehumidification technology applied in hot and humid Asian regions. However, few studies discussed the energy and techno-economic performance in Meditteranean climates in Southern European regions, such as Italy, Spain and Greece, where subtropical and humid climate dominates most of the summertime [204-207]. Especially, due to climate change, the statistics have

indicated the air temperature and relative humidity increase under the Mediterranean climate, where heatwaves and extreme weather frequently occur in summer [208].

On the basis of the ENTRANZE database [193], the share of multi-family dwellings in total residential building stock account for 60 %, 74 % and 70 % in Greece, Italy and Spain, respectively. Besides, the multi-family dwellings constructed before the 1970s have approximately 38 %, 56 % and 33 % of the multi-family building stocks in Greece, Italy and Spain, respectively, where few air-conditioning systems are installed, and the overheating issue occurred. Thus, it is significant to retrofit the multi-family terraced houses constructed before the 1970s to achieve indoor hydrothermal comfort during summertime by introducing energy-efficient cooling and dehumidification systems.

Therefore, the hypothetical RB is established in this research to analyse multi-family terraced house typology under similar subtropical humid Meditteranean climate conditions and regions with different levels of details in global costs, primary energy consumption calculations and economic parameters, which makes the comparison results more replicable.

The hypothetical RB defined in this research represents a multi-family terraced house selected within the Meditteranean subtropical and humid regions of building construction before the 1970s. Construction during this period followed regulations in force at that time for new building design, as summarised by the TABULA project [209]. The hypothetical RB established in this research case is four multi-family terraced houses with a total of 130 m^2 in each building's floor area with four people in each building, with the selected location of Methoni,

Rome and Barcelona. The building energy model was created as a baseline in IES VE [210] software to test the ILDAC system performance, with the geometry model and the 3D geometric wireframe view shown in Fig 3-10 (a) and (b). The weather file was chosen from the Ladybug website [211] in epw. Format. The 30-year average ambient weather conditions with solar radiation, ambient temperature and relative humidity are obtained from the WeatherOnline website [212], as shown in Fig 3-11. It is figured out that the high-intensity solar radiation periods are between April and September in Methoni, Rome and Barcelona, while low-intensity periods are for the rest of the months [213]. The highest ambient temperature in Methoni, Rome and Barcelona is 36.0 ℃ under the relative humidity of 80%.

(a)   (b)
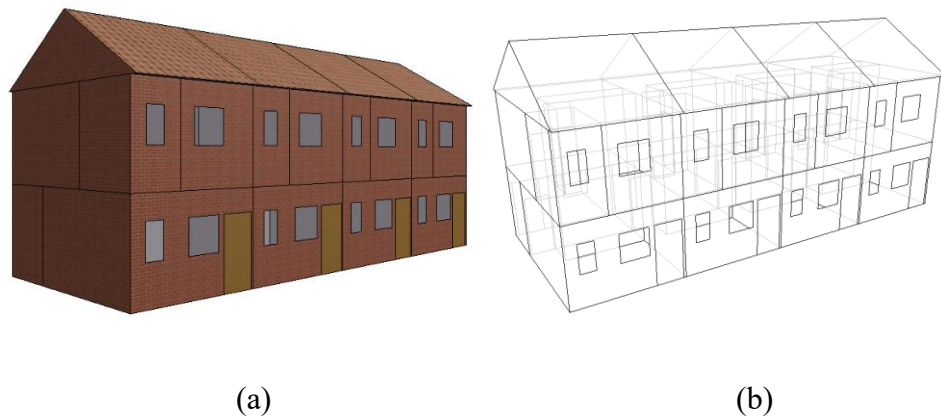
Fig 3-10 (a) The geometry model of the hypothetical RB (b) The 3D geometric wireframe view of the hypothetical RB
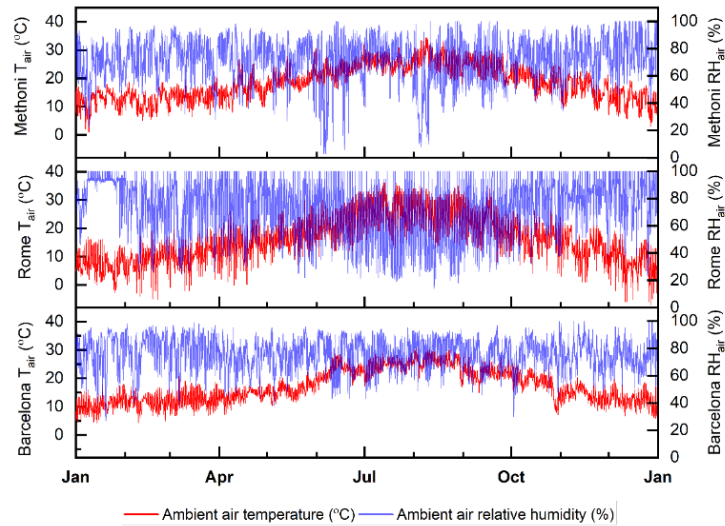
(a)
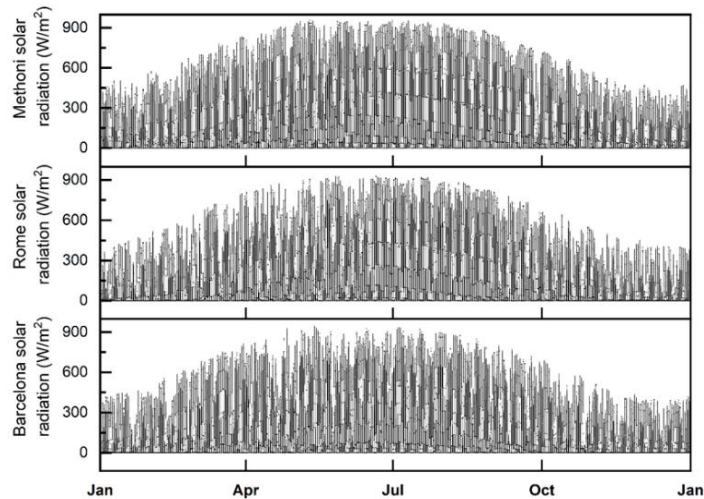
(b)

Fig 3-11 30-year average ambient weather conditions in Greece, Italy and Spain (a) air temperature and relative humidity and (b) solar radiation [212]

Furthermore, buildings constructed before the 1970s had exceeded their service life by at least 50 years [214]. This led to the construction of many multi-family terraced houses featuring brick walls with poor insulation, comprising more than 60% of their building stocks [193]. The construction type, U-value of the fabric

existing energy systems, household electrical appliances, occupancy and energy consumption in Greece, Italy and Spain can be extracted from the TABULA database [191].

According to the TABULA [191], the average energy consumption of the RBs for space heating in Greece, Italy and Spain would be about 74 kWh/m^2 to 94 kWh/m^2 per year, 135 kWh/m^2 to 154 kWh/m^2 per year and 95 kWh/m^2 to 123 kWh/m^2 per year, respectively. The building construction materials and U-value specifications of the RBs are summarized in **Appendix A.** The Air Change per Hour (ACH) for the entire RBs is assumed to be 6.7 h^{-1} under a pressure difference of 50 Pa [215]. Besides, the primary energy source of the baseline building is considered as electricity and natural gas. In addition, the space heating is driven by combi-boilers with seasonal space heating energy efficiency of 94%. Moreover, the RB's model has a continuous schedule, where all the RBs are assumed to be heated continuously to 20℃ during the heating season [215]. The initial set temperature for space cooling in Greece (May-October), Italy (June-September) and Spain (June-September) is 25℃ during the cooling season, as shown in Table 3-6 [215].

Table 3-6 Heating and cooling schedule for the RBs in Greece, Italy and Spain [215]

RB sites	Heating schedule	Cooling schedule
Greece	From 1 November to 31 March, 20 ℃ (0:00-9:00, 19:00-24:00)	From 1 May to 31 October, 25 ℃ (0:00-9:00, 19:00-24:00)

	From 1 December to 28 February, 20 ℃ (0:00-9:00, 19:00-24:00)	From 1 June to 31 September, 25℃ (0:00-9:00, 19:00-24:00)
Italy		
Spain	From 1 October to 30 April, 20 ℃ (0:00-9:00, 19:00-24:00)	From 1 June to 31 September, 25℃ (0:00-9:00, 19:00-24:00)

However, natural ventilation is applied by opening the windows to maintain indoor air quality and avoid summer overheating. 25% of windows are open from 8 am to 9 am and from 5 pm to 6 pm in the winter, while half of the windows are open from 8 am to 11 am, and all windows are open from 11 am to 5 pm, and 30% of windows open from 5 pm to 8 pm in the summer. Windows remain closed for the rest of the time. The ventilation profiles are shown in Fig 3-12.

(a)   (b)
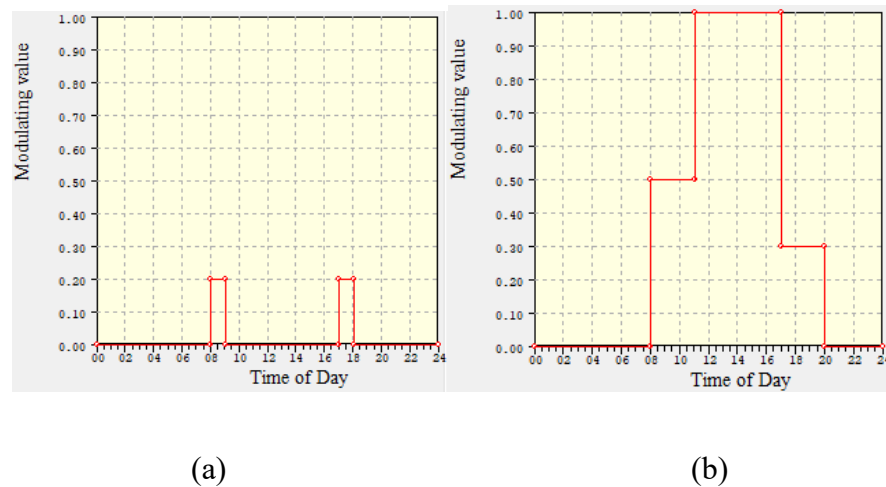
Fig 3-12 Window opening profiles in (a) winter and (b) summer

3.5.3 Building simulation method

In order to analyse the energy and techno-economic performance of the ILDAC system, the flowchart of RB's simulation method is proposed with eight steps, as shown in Fig 3-13.

Step 1: The complete LDD system COP modelling and correlation. The numerical modelling method of the complete LDD system with the correlation (Variations of COP_{th} and COP_{ele} with the inlet air temperature and relative humidity);

Step 2: The AWHP system modelling and correlation. The numerical modelling method of the AWHP system with the correlation (Variations of COP_C and COP_H with the inlet air temperature and relative humidity);

Step 3: RB establishment and modelling. The three multifamily terraced RBs are defined regarding the TABULA database with the location selected in Methoni-Greece, Rome-Italy and Barcelona-Spain under the subtropical and humid climate condition. The geometry modelling is established in IES VE software with space cooling, dehumidification and heating demand calculated;

Step 4: Retrofit technologies. The specifications of four retrofit technologies are collected and the correlations of COP_{th} and COP_{ele} with the inlet air temperature and relative humidity of the complete LDD system collected from **Step 1**, the correlations of COP_C and COP_H with the inlet air temperature and relative humidity of the AWHP system collected from **Step 2**;

Step 5: Post-retrofit building energy simulation. The ILDAC system energy simulation coding and virtualization are achieved in EnergyPro software, where the specifications and correlations of retrofit technologies (output from **Step 4**), weather files (output from **Step 3**) and space cooling, dehumidification and heating demands (output from **Step 3**) serve as the input of the EnergyPro boundary conditions (**section 3.5**);

Step 6: The ILDAC system energy performance. According to the simulation results from **Step 5**, the energy and carbon reduction rates, ILDAC and AWHP system COP, and building cooling efficiency are calculated;

Step 7: The economic modelling. The economic model will be established. The electricity, natural gas and PV export tariff are collected, serving as input. The initial investment is calculated according to the retrofit technologies in **Step 4**. The energy reduction rate from **Step 6**, the initial investment from **Step 4** and energy prices serve as the input for the lifecycle energy cost (LCEC) calculation. Besides, the bank interest rate and inflation rate in different countries are summarized in **Step 7**;

Step 8: Techno-economic and sensitivity analysis. The discount payback period (DPP), the annual return on investment (AROI) and the real rate of return (RROR) are calculated based on the input of LCEC, bank interest rate and inflation rate from **Step 7**. Moreover, the sensitivity analysis is conducted with the variations of electricity, natural gas and PV export tariff, bank interest rate and inflation rate.
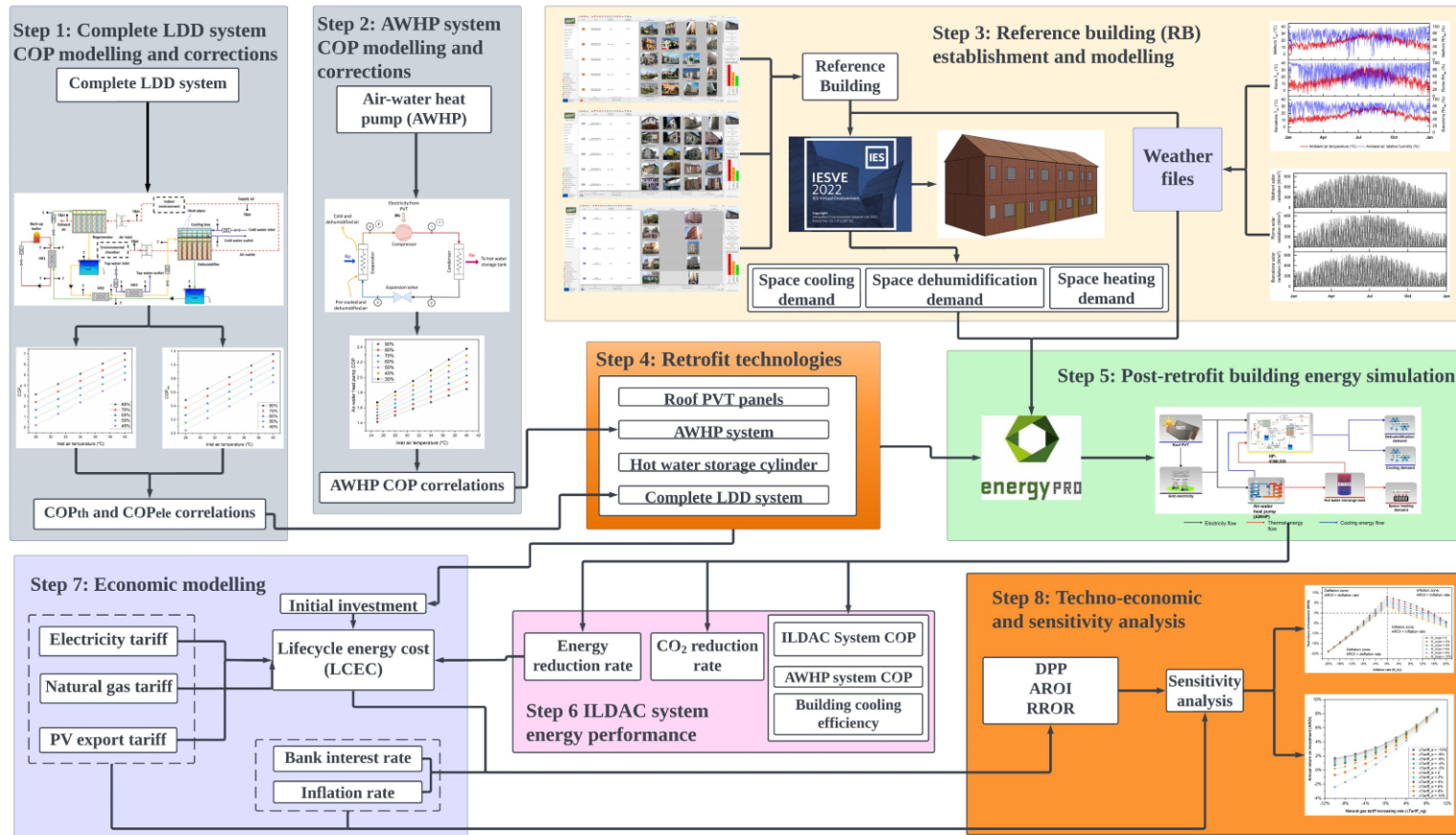
Fig 3-13 The flowchart of the RB simulation method

3.5.4 Techno-economic performance indices

The comprehensive techno-economic performance is calculated with details in this section, where two primary economic assessments are discussed: energy reduction rate (ERR), carbon reduction rate (CRR), initial investment (II), discounted payback performances (DPP), annualised return on investment (AROI) and the real rate of return (RROR). According to the Energy Performance and Building Directive (EPBD) [216], buildings before the 1970s often had a calculated remaining useful lifespan of at most 30 years, and investments in deep retrofit will extend the useful life of the building. Moreover, the cost-optimal level calculation of energy retrofit according to the regulation EU No. 244/2012 [217] is based on the global costs over a calculation period of 20 years. Therefore, the DPP, AROI and RROR consider cost-optimality for the 20-year lifecycle approach in this research.

Energy reduction rate (ERR) is proposed to determine the energy-saving potential for the ILDAC system, whose final energy consumption will be compared with that of the baseline reference building with the unit of percentage (%). ERR can be calculated as the ratio between the post-retrofit scenario's primary energy consumption and the primary energy reduction between the post-retrofit and baseline model.

$$ERR = (\sigma(0) - \sigma(i))/\sigma(0) \qquad (3\text{-}51)$$

Where, $\sigma(i)$ is the final energy consumption with the ILDAC system (kWh/m^2); $\sigma(0)$ is the RB's baseline final energy consumption (kWh/m^2).

Carbon reduction rate CRR is proposed to determine the carbon-saving potential for the ILDAC system, whose final carbon emission will be compared with that

of the baseline reference building with the unit of percentage (%). CRR can be calculated as the ratio between the post-retrofit scenario's carbon emission and the carbon reduction between the post-retrofit and baseline model.

$$CRR = (\lambda(0) - \lambda(i))/\lambda(0) \hspace{3cm} (3\text{-}52)$$

Where, $\lambda(i)$ is the final carbon emission with the ILDAC system ($kgCO_2/m^2$); $\lambda(0)$ is the baseline carbon emission ($kgCO_2/m^2$).

According to Statista, the average hourly labour cost is estimated as 28.5 €/h [218] and the installation cost as 34 €/m^2 [1]. The initial investment (II) is calculated by the sum of the capital cost of components and the labour cost for installation:

$$\phi_{II} = \phi_{capital} + \phi_{labour} \hspace{3cm} (3\text{-}53)$$

The capital cost of each technology (complete LDD, AWHP, hot water storage cylinder, roof PVT panels and the ILDAC systems) and their miscellaneous cost are given in Table 3-7.

Table 3-7 The capital cost of each technology and their miscellaneous cost

		unit	Cost per unit	Barcelona	Rome	Methoni
Complete LDD system	Core semi-permeable membrane	21kW in Barcelona; 17kW in Rome; 19kW in Methoni	€59.55/kW [219]	€ 1,250.55	€ 1,012.35	€ 1,131.45
	fan	3 in each house; 4 houses in total	€72.35 per fan [220]	€ 868.20	€ 868.20	€ 868.20

116

	solution pump	3 in each house; 4 houses in total	€238.84 per pump [221]	€ 2,866.08	€ 2,866.08	€ 2,866.08
	Liquid Heat Exchanger	3 in each house; 4 houses in total	€343.52 per heat exchanger [222]	€ 4,122.24	€ 4,122.24	€ 4,122.24
	Storage tank	3 in each house; 4 houses in total	€69 per tank [223]	€ 828.00	€ 828.00	€ 828.00
	Heat pipe	99 in each house; 4 houses in total	€9.1 per heat pipe [224]	€ 3,603.60	€ 3,603.60	€ 3,603.60
Complete LDD system total cost				€ 13,538.67	€ 13,300.47	€ 13,419.57
Air water heat pump (AWHP) system	Vaillant Arotherm Plus Air Water Heat Pump	19kW in Barcelona; 24kW in Rome; 24kW in Methoni	€880.53/kW [225]	€ 16,730.07	€ 21,132.72	€ 21,132.72
	Heat pump mounting and control accessories	1 kit of installation and control devices in each house, 4 houses in total	€334/kit [225]	€ 1,336.00	€ 1,336.00	€ 1,336.00
AWHP system total cost				€ 18,066.07	€ 22,468.72	€ 22,468.72

117

	Telford Tempest 500 Litre Twin Coil Solar Indirect Unvented Cylinder twin Immersion	500L cylinder for each house, 4 houses in total	€1538.40 for each 500L cylinder [226]	€ 6,153.60	€ 6,153.60	€ 6,153.60
Hot water storage cylinder						
Hot water storage system total cost				€ 6,153.60	€ 6,153.60	€ 6,153.60
Roof PVT panels	Solimpkes Excell PV-T Hybrid Panel	12 panels in each house; 4 houses in total	€250.00 for each PVT panel [227]	€ 12,000.00	€ 12,000.00	€ 12,000.00
	DC-AC Inverter	1 inverter for each house; 4 houses in total	€1468.98 for each inverter [228]	€ 5,875.80	€ 5,875.80	€ 5,875.80
	Scaffolding	4 houses in total	€1166.78 for each house [227]	€ 4,667.12	€ 4,667.12	€ 4,667.12
	Other accessories	4 houses in total	€2142 for each house [227]	€ 8,568.00	€ 8,568.00	€ 8,568.00
	Labour cost	3 people, 5 days	€28.5 per hour per day [218]	€ 3,420.00	€ 3,420.00	€ 3,420.00
Roof PVT panels' total cost				€ 34,530.92	€ 34,530.92	€ 34,530.92
Installation of the	accessories (pipes, controllers,	4 houses in total	€832.5 for each house [229]	€ 3,330.00	€ 3,330.00	€ 3,330.00

ILDAC system	cables, etc.)					
	Labour cost	2 people, 4 houses in total	€28.5 per hour per day [218]	€ 1,824.00	€ 1,824.00	€ 1,824.00
Total initial investment				€ 77,443.26	€ 81,607.71	€ 81,726.81

DPP is defined as variation and modification of the payback period that accounts for the time value and uses discounted cash flows when calculating the payback period with the unit of years [230]. DPP represents the economic performance of the retrofit investment to assess the rapidity of the investment payback period. To assess DPP, the cumulative discounted net present values (CNPV) are calculated first through the difference between initial investment and the cumulative annual net cash flows:

$$CNPV (t = n) = \phi_{II} - \sum_{t=1}^{n} NPV(t = n) \tag{3-54}$$

Therefore, DPP equals to 't = n' year when the CNPV (t=n) =0

$$DPP (i) = n, when\ CNPV(t = n) = 0 \tag{3-55}$$

The Net Present Value Method (NPV) is the difference between the present value of cash inflows and the present value of cash outflows over a period used in capital budgeting and investment planning to analyse an integrated retrofit's profitability. The following equation [231] is used to calculate the NPV of annual energy bill savings:

$$NPV (t) = R_d(t) \times (\phi_b(t = 0) - \phi_b(t) - \phi_{maintenance}(t)) \tag{3-56}$$

Where $\phi_{\text{maintenance}}$ is the annual maintenance cost (€), which has been given in Table 3-8. ϕ_b is the annual bill (€), which can be expressed as:

$$\phi_b(t) = \theta_{\text{grid-ele}}(t) \times p_{grid-ele}(t) + \theta_{\text{gas}}(t) \times p_{gas}(t) - \theta_{\text{exported}}(t) \times$$
$$FIT(t) + \theta_{\text{water}}(t) \times p_{water}(t) \tag{3-57}$$

Where $\theta_{\text{grid-ele}}$ is the grid electricity consumption (kWh); $p_{grid-ele}$ is the unit price of the grid electricity (€/kWh); θ_{gas} is the natural gas consumption (kWh); p_{gas} is the unit price of the natural gas (€/kWh); θ_{exported} is the PVT exported electricity to the grid (kWh); FIT is the PVT feed-in tariff (€/kWh); θ_{water} is the water consumption (m³); p_{water} is the unit price of water (€/m³);

Table 3-8 The maintenance cost and lifespan for each technology

		Annual maintenance cost (€) [232]			Lifespan
		Barcelona	Rome	Methoni	(years)
HP-ICMLDD system	Core semi-permeable membrane	N/A	N/A	N/A	10 [233]
	Fan	N/A	N/A	N/A	10 [234]
	Solution pump	N/A	N/A	N/A	15 [235]
	Liquid Heat Exchanger	N/A	N/A	N/A	15 [236]
	Storage tank	N/A	N/A	N/A	20 [237]
	Heat pipe	N/A	N/A	N/A	20 [238]
Air water heat pump	Vaillant Arotherm Plus Air Water Heat Pump	501.9	634.0	634.0	20 [239]

(AWHP) system	Heat pump mounting and control accessories	N/A	N/A	N/A	N/A
Hot water storage cylinder	Telford Tempest 500 Litre Twin Coil Solar Indirect Unvented Cylinder twin Immersion	123.1	123.1	123.1	8 [240]
Roof PVT panels	Solimpkes Excell PV-T Hybrid Panel	72.0	72.0	72.0	20 [241]
	DC-AC Inverter	N/A	N/A	N/A	10 [242]
	Scaffolding	N/A	N/A	N/A	N/A
	Other accessories	N/A	N/A	N/A	N/A
	Labour cost	N/A	N/A	N/A	N/A
Installation of the ILDAC system	accessories (pipes, controllers, cables, etc.)	99.9	99.9	99.9	N/A
	Labour cost	N/A	N/A	N/A	N/A

The discount rate $R_d(t)$ depends on the real discount rate R_r and the years (t) of the considered costs. The discount rate can be expressed as:

$$R_d\ (t) = (1/(1 + R_r))^t \qquad (3\text{-}58)$$

Where t is the number of years and R_r is the real discount rate, which is closely related to the bank interest rate R and inflation rate R_i. It can be calculated using:

$$R_r = (R - R_i)/(1 + R_i) \qquad (3\text{-}59)$$

The market values of interest rate, inflation rate and energy price with their increasing rate for Greece, Italy and Spain are shown in Table 3-9.

Table 3-9 The market values of interest rate, inflation rate and energy price with their increasing rate for Greece, Italy and Spain

	Bank interest rate R (%)	Inflation rate R_i (%)	Real discount rate R_r (%)	Electricity price increase rate (%)	Natural gas increase rate (%)	Natural gas price (€/kWh)	Electricity price (€/kWh)	PV electricity Feed-in tariff (FIT) (€/kWh)	Tap water price (€/m³)
Methoni-Greece	8.32% [243]	9.50% [244]	-1.08%	3.88% [245]	3.22% [245]	0.0897 [246]	0.3071 [247]	0.06 [248]	1.16 [249]
Rome-Italy	7.94% [243]	12.60% [244]	-4.14%	3.88% [245]	3.22% [245]	0.0986 [246]	0.3115 [247]	0.105 [250]	1.05 [249]
Barcelona-Spain	7.66% [243]	7.30% [244]	0.34%	3.88% [245]	3.22% [245]	0.0888 [246]	0.2305 [247]	0.03 [251]	2.00 [249]

Inflation erodes the purchasing power of cash and impacts borrowing costs and real economic returns on investment securities. For this reason, investors are wise to understand and calculate what is called "the real rate of return" ($RROR$), which is an investment's rate of return after adjusting for inflation. The real rate of return can be calculated by subtracting the current or expected inflation rate from the nominal annual return on investment [252].

The annualised return on investment ($AROI$) is to evaluate the profitability efficiency of the retrofit investment in the timescales of the entire building serving lifespan after retrofit, which could help decision-makers compare the

investment profitability between building retrofit and other market investments with the fixed funding ranges [253].

ROI represents the gain or loss from an investment relative to the cost, which is useful in evaluating the potential return from a stand-alone investment as it is in comparing returns from several investments when deciding whether to invest in the purchase of a business or evaluate the results of a real estate retrofit transaction [254]. It is calculated by subtracting the pre- and post-retrofit energy bills (energy bill savings), dividing them by the cost of the initial retrofit investment, and multiplying it by 100%. However, the annualised return on investment *AROI* provides an accurate solution to access the average annual *ROI*, which considers the investment profitability in one year.

The calculation formula of *RROR*, *AROI* and *ROI* are summarised as:

$$RROR = AROI - R_i \tag{3-60}$$

$$AROI = \left[(1 + ROI)^{\frac{1}{20}} - 1 \right] \times 100\% \tag{3-61}$$

$$ROI = \frac{\sum_{i=1}^{20} \left[\left(\frac{1+R_i}{1+R} \right)^t (\phi_b(t=0) - \phi_b(t) - \phi_{maintenance}(t)) \right]}{\phi_{II}} \tag{3-62}$$

Where *RROR*, *AROI* and *ROI* are based on the calculated the ILDAC system serving lifecycle after retrofit, considered as a maximum of 20 years.

3.6 Summary

Firstly, this chapter established a concept of the complete membrane-based liquid desiccant dehumidification system. By applying such a method, the innovative HP-ICMLDD system performance could be calculated, where the heat pipe internal cooling method has been first integrated into the dehumidifier

and solved. Moreover, the innovative and energy-efficient concept of the ILDAC system has been proposed by integrating the complete LDD system with the air-water heat pump (AWHP) system, where the PVT renewable technology and thermal storage system are introduced to provide renewable heat and electricity. The ILDAC system has been integrated with the reference buildings (RBs) to supply cooled and dehumidified air to the indoor environment for terraced multi-family houses in subtropical and humid climate regions. Finally, the building energy simulation method and techno-economic performance indices and calculation methods are also introduced.

Chapter 4 Experimental set-up
4.1 Introduction
This chapter presents the detailed experiment set-up of the HP-ICMLDD (dehumidifier), the regenerator and the complete membrane-based liquid desiccant system. Besides, there are no specific experiment procedures for the ILDAC system since the system is based on the simulation of the reference building and energy simulation software (IES VE and EnergyPro), and the main objective of this integrated system is to investigate the applications of the integrated liquid desiccant in different Meditteranean climate conditions. **Sections 4.1-4.3** present the laboratory test rig for the HP-ICMLDD, the regeneration and complete liquid desiccant dehumidification systems and all the related configurations of the test rigs, including the physical properties of the membrane, the air, desiccant solution and water transportation properties, the specifications of the experimental equipment and the primary measurement instruments with their corresponding accuracies.

4.2 The experiment of the dehumidifier
In order to assess the performance of a heat pipe membrane-based liquid desiccant dehumidification (HP-ICMLDD) system, a laboratory test rig is constructed to evaluate the system performance in various air, solution, and cold water states, with the schematic diagram, test rig and its lateral view shown in Fig 4-1, Fig 4-2 and Fig 4-3. The test rig principally comprises a membrane-based dehumidifier integrated with heat pipes and a cooling box unit, a membrane-based regenerator, two solution tanks, three pumps, three liquid-to-liquid heat exchangers (HX) and a boiler. An environmental chamber provides hot and humid air to the dehumidifier to simulate outdoor weather conditions. Simultaneously, the indoor return air is used to regenerate the desiccant solution

in the regenerator. The air flow rates are controlled by adjusting the axial fan rotation speeds (Ebm-Papst Mlfingen GmbH & Co. KG). The dimension of membrane-based units for the dehumidifier and regenerator is 410mm (L) × 230mm (W) × 210mm (H) with 11 air channels and 11 solution channels, where 9 gravitational heat pipes are installed in each solution channel of the dehumidifier in an aligned arrangement.

The dehumidifier and regenerator are originally designed in literature [255] at the Marmont lab in the University of Nottingham in the UK, where many previous research [256, 150, 257, 258] have proved the stability and well dehumidification performance. Therefore, in this research, the same dimension, structure and membrane materials (semi-permeable hydrophobic AY Tech ePTFE Lam membrane [219]) are used for experiment design and test. In theory, the more heat pipes indicates more heat transfer area and better solution cooling performance. However, to ensure the uniformity of heat pipe heat transfer in each solution channel, 11 rows of heat pipes are inserted into 11 solution channels. Besides, due to limited space of the cooling box, only 9 heat pipes can be arranged with same distance in each row inside each solution channels. Therefore, in this research, there are 99 heat pipes altogether inserted in 11 solution channels with 9 heat pipes in each channel. In addition, commercial copper heat pipes with water serving as the working fluid are used with operating temperature from 0 ℃ to 250 ℃ and low cost.

The dehumidifier, regenerator, storage tanks, cooling box, heat pipe adiabatic section, and pipeworks are all well-insulated to reduce the environmental influence. Especially each air channel is sealed with water-proof sealant at the top and bottom to avoid condensed water leakage. Therefore, the condensed

water is absorbed by the desiccant solution if there is condensation in the air channel.

The specifications of the HP-ICMLDD system and the physical properties of the membrane are given in Table 4-1. The regenerator has the same structure as the dehumidifier. Three gauze layers are paved on the top surface of the dehumidifier and regenerator units to ensure even solution distribution. As long as the desirable inlet conditions for the dehumidifier are met, the system runs repeatedly until it achieves a steady state, at which point the measured data will be collected. Lithium Chloride (LiCl) aqueous solution is used as the desiccant in the HP-ICMLDD system. The solution and water flows are circulated in the system by three identical pumps (15W centrifugal magnetic-driven pump with a flow rate range of up to 10L/min), and their flow rates are measured by two liquid flow indicators. The air, desiccant solution and water transportation properties are given in Table 4-2. A series of K-type thermocouples are used to get the desiccant solution and water temperatures. A Testo anemometer is adopted to obtain the air velocity. The humidity and temperature sensors are installed at the inlet and outlet of the dehumidifier to obtain the air temperature and relative humidity. All probes are connected to a DT80 data logger. The specifications of the experimental equipment are listed in Table 4-3.

The calibration procedure of the K-type thermocouples, the humidity sensors and the anemometer is described below:

- The K-type thermocouples connected to the DT-80 data logger are inserted into ice-water mixture to test if the temperature is 0°C. In this experiment, the accuracy of thermocouples is $\pm$ 0.75%.

- The EK-H4 temperature and humidity sensor are calibrated inside the environmental chmaber using different temperature and relative humidity. In this experiment, the accuracy of temperature and humidity of EK-H4 sensor is 3% and 2%, respectively.

- The Testo anemometer has been calibrated in regular maintenance by lab technician once a year.

- To calibrate the flow meter, place a small portion of process fluid in a test meter and weigh it for a precise amount of time while it flows 60 seconds. Then, use a calibrated scale to obtain an accurate measurement of the weight of test fluid. After the test period is completed, divert the test fluid into a discharge container. Obtain the flow rate of the fluid by dividing its volumetric weight by the test duration. Compare the calculated flow rate to the flow rate of the flow meter and adjust it to the measured flow rate. In this experiment, the accuracy for Parker series flow meter is 2% and 5%, respectively.

The EK-H4 is used to measure the air temperature and relative humidity where the entire cross-sectional area of duct is divided into 3 concentric circles with the same area. Then, the sensor is inserted into the duct where the measurement point is 10 cm away from the surface. Next, 9 points in total on 3 concentric circles are measured and the average value of them is taken.

The Testo anemometer is used to measure the inlet air velocity where the entire cross-sectional area of duct is divided into 3 concentric circles with the same area. Then, the sensor is inserted into the duct where the measurement point is 10 cm away from the surface. Next, 9 points in total on 3 concentric circles are measured and the average value of them is taken.

The locations, numbers and functions of the K-type thermocouples are listed below and shown in Fig 4-1. The average value of each type of test is calculated from the original recorded data.

1) To test the solution tempearture of the strong solution tank: 6 K-type thermocouples in total are inserted into the tank from the wall side in two columns; 3 thermocouples in each column with 10 cm distance; 10 cm distance between two columns; the sensor probes are 10 cm away from the wall side.

2) To test the solution tempearture of the weak solution tank: 6 K-type thermocouples in total are inserted into the tank from the wall side in two columns; 3 thermocouples in each column with 10 cm distance; 10 cm distance between two columns; the sensor probes are 10 cm away from the wall side.

3) To test the solution tempearture of the inlet condition of the dehumidifier: 3 K-type thermocouples in total are inserted into the solution pipe from the wall side with 2 cm distance between each thermocouple; 2 cm distance away from the solution inlet for the first probe and each thermocouple is inserted at the center of the pipe.

4) To test the solution tempearture of the inlet condition of the regenerator: 3 K-type thermocouples in total are inserted into the solution pipe from the wall side with 2 cm distance between each thermocouple; 2 cm distance away from the solution inlet for the first probe and each thermocouple is inserted at the center of the pipe.

5) To test the tempearture of the inlet tap water: 3 K-type thermocouples in total are inserted into the water pipe from the wall side with 2 cm distance

between each thermocouple; 2 cm distance away from the cooling box inlet for the first probe and each thermocouple is inserted at the center of the pipe.

6) To test the tempearture of the outlet tap water: 3 K-type thermocouples in total are inserted into the water pipe from the wall side with 2 cm distance between each thermocouple; 2 cm distance away from the cooling box outlet for the first probe and each thermocouple is inserted at the center of the pipe.

7) To test the tempearture of the cold water inlet and outlet from the HX3: 3 K-type thermocouples in total are inserted into the cold water inlet from the wall side with 2 cm distance between each thermocouple; 2 cm distance away from the HX3 inlet for the first probe and each thermocouple is inserted at the center of the pipe. Besides, 3 K-type thermocouples in total are inserted into the cold water outlet from the wall side with 2 cm distance between each thermocouple; 2 cm distance away from the HX3 outlet for the first probe and each thermocouple is inserted at the center of the pipe.

8) To test the tempearture of the inlet and outlet boiler water: 3 K-type thermocouples in total are inserted into the hot water pipe from the wall side with 2 cm distance between each thermocouple; 2 cm distance away from the HX1 inlet for the first probe and each thermocouple is inserted at the center of the pipe. 3 K-type thermocouples in total are inserted into the hot water pipe from the wall side with 2 cm distance between each thermocouple; 2 cm distance away from the HX1 outlet for the first probe and each thermocouple is inserted at the center of the pipe.

9) To test the weak solution tempearture of the inlet and outlet from HX1: 3 K-type thermocouples in total are inserted into the solution pipe from the wall side with 2 cm distance between each thermocouple; 2 cm distance away from the HX1 inlet for the first probe and each thermocouple is inserted at the center of the pipe. 3 K-type thermocouples in total are inserted into the solution pipe from the wall side with 2 cm distance between each thermocouple; 2 cm distance away from the HX1 outlet for the first probe and each thermocouple is inserted at the center of the pipe.

10) To test the strong solution tempearture of the inlet and outlet from HX2: 3 K-type thermocouples in total are inserted into the solution pipe from the wall side with 2 cm distance between each thermocouple; 2 cm distance away from the HX2 inlet for the first probe and each thermocouple is inserted at the center of the pipe. 3 K-type thermocouples in total are inserted into the solution pipe from the wall side with 2 cm distance between each thermocouple; 2 cm distance away from the HX2 outlet for the first probe and each thermocouple is inserted at the center of the pipe.

11) To test the weak solution tempearture of the inlet to HX2: 3 K-type thermocouples in total are inserted into the solution pipe from the wall side with 2 cm distance between each thermocouple; 2 cm distance away from the HX2 inlet for the first probe and each thermocouple is inserted at the center of the pipe.

To ensure the reliability and accuracy of experimental tests, variables including 1) inlet cold water temperature, 2) inlet cold water flow rate, 3) inlet air

temperature, 4) inlet air relative humidity, 5) inlet air flow rate, 6) inlet solution temperature, 7) solution concentration and 8) solution flow rate have been tested with 3 repeated tests for each variable and the average values are taken for analysis.

The primary measurement instruments with corresponding accuracies are presented in Table 4-4. The LiCl desiccant solution concentration (C_{sol}) is calculated by the function of the solution density and its temperature in Melinder's work [259]:

$$C_{sol} = -253.148 + 0.04438563996T_{sol} + 0.000162666247T_{sol}^2 +$$
$$0.331709855T_{sol}^3 - 0.000079370267\rho_{sol} \qquad (4\text{-}1)$$

where T_{sol} is the solution temperature (°C); ρ_{sol} is the solution density (kg/m³) measured by a Brannan hydrometer. Notably, the equation is suitable to be used with the solution temperature and density ranging from -40 °C to 40 °C and 1004 kg/m³ to 1450 kg/m³. Besides, the solution concentration ranges from 2.0 % to 42.4 %.

Moreover, the desiccant volumetric flow rate is measured by a Parker liquid flow meter calibrated with water at 20 °C. The correction correlation is used to ensure accurate readings from the installed flow meter and is expressed by [260]:

$$v_{sol} = v_W \sqrt{\frac{(m_{float} - V_{float}\rho_{sol})\rho_W}{(m_{float} - V_{float}\rho_W)\rho_{sol}}} \qquad (4\text{-}2)$$

where v_{sol} and v_W are the volumetric flow rates of desiccant solution and water (L/min), respectively. ρ_{sol} and ρ_W are the solution and water densities (kg/m³), respectively. m_{float} and V_{float} are the flow meter float weight (kg) and volume

(m³), respectively. As for the flow meter used in this study, the float weight

(m_{float}) is 2.1×10^{-3}kg and volume (V_{float}) is 0.25×10^{-6}m³.
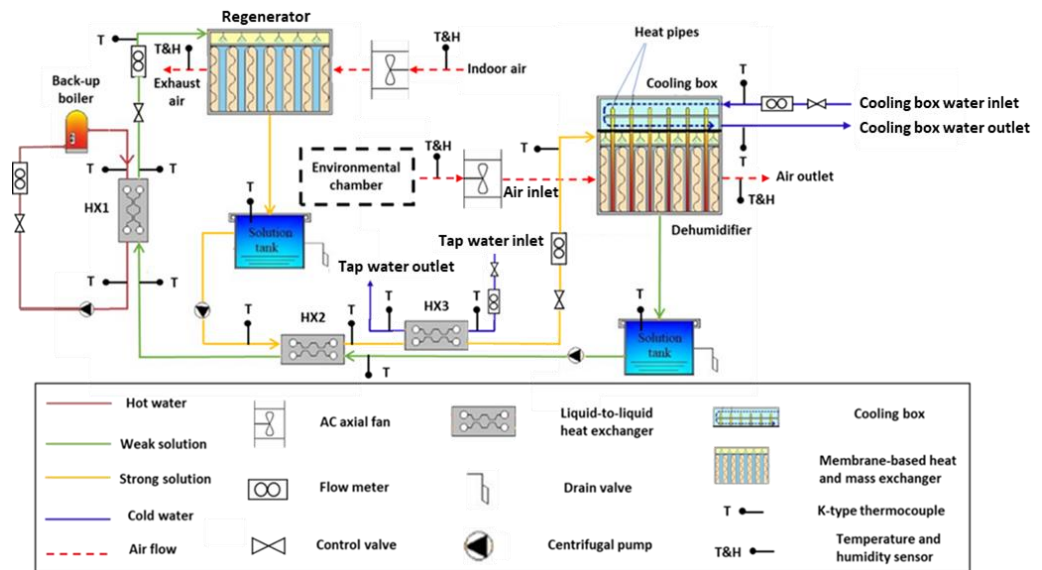
Fig 4-1 Schematic diagram of the HP-ICMLDD system
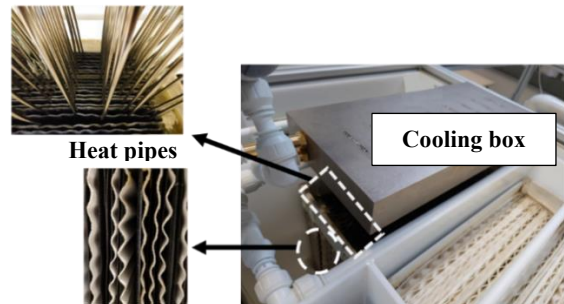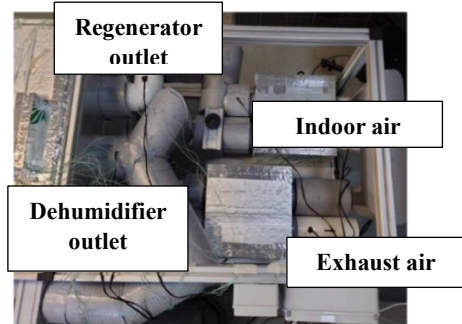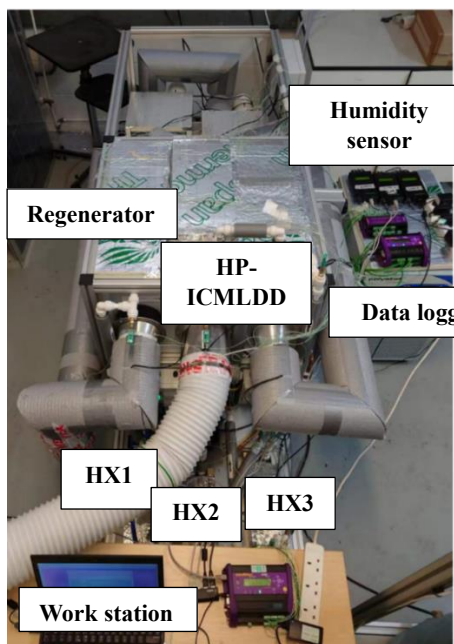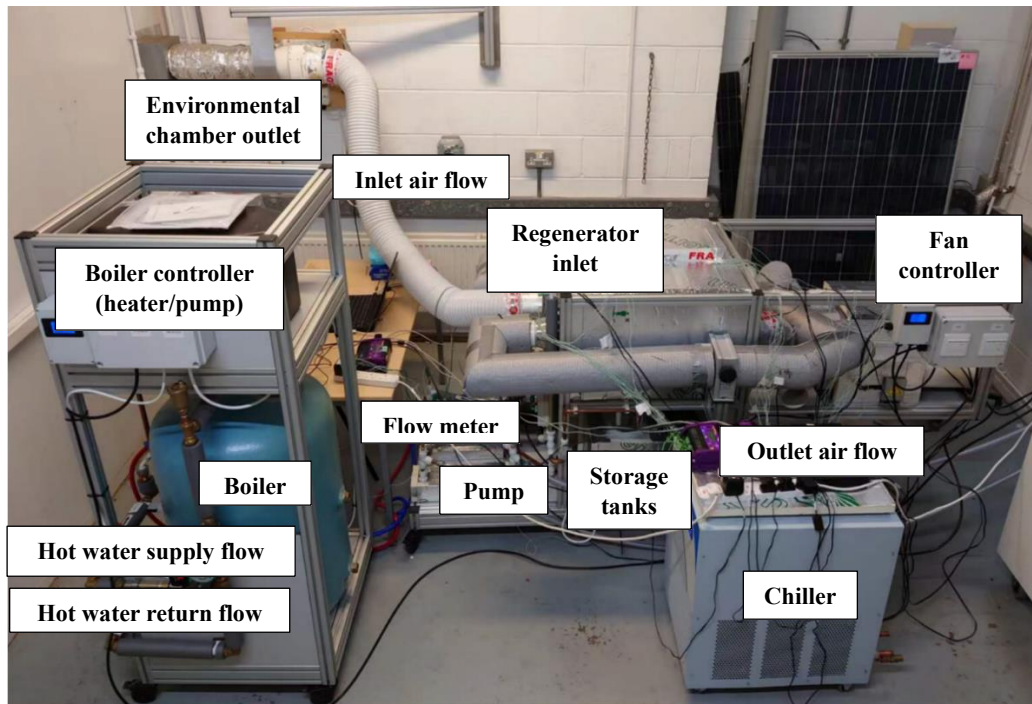
Fig 4-2 Test rig of the HP-ICMLDD system
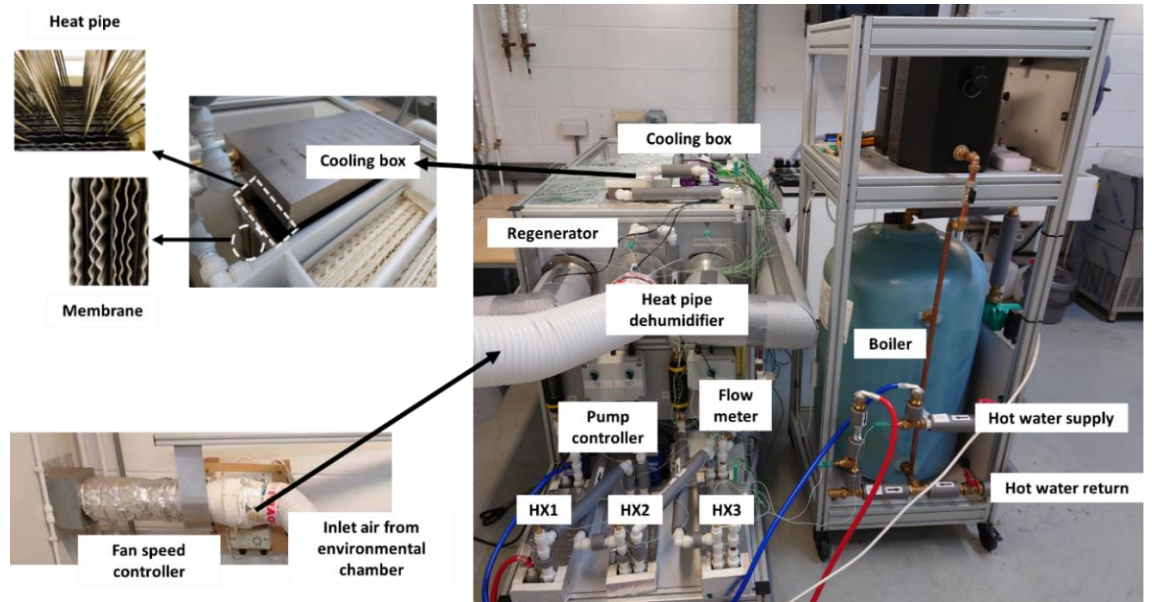
Fig 4-3 Lateral view of the HP-ICMLDD system

Table 4-1 Specifications of the HP-ICMLDD system and physical properties of the membrane

Symbol	Definition	Value
L_{deh} (m)	Dehumidifier length	0.41
W_{deh} (m)	Dehumidifier width	0.23
H_{deh} (m)	Dehumidifier height	0.21
$d_{h,sol}$ (m)	The hydraulic diameter of the solution channel	0.73×10^{-2}
$d_{h,air}$ (m)	The hydraulic diameter of the air channel	1.5×10^{-2}
$d_{h,w}$ (m)	The hydraulic diameter of the water channel	2.1×10^{-2}
d_{air} (m)	Air channel thickness	0.0077
d_{sol} (m)	Solution channel thickness	0.0043
k_{mem} (W/m·K)	Membrane thermal conductivity	0.3
$k_{m,mem}$ (kg/m·s)	Membrane mass transfer conductivity	3.87×10^{-6}
δ_{mem} (m)	Membrane thickness	1.05×10^{-4}
$L_{hp,e}$ (m)	Heat pipe evaporator section length	0.18
$L_{hp,c}$ (m)	Heat pipe condenser section length	0.04

Symbol	Definition	Value
$L_{hp,a}$ (m)	Heat pipe adiabatic section length	0.034
W_{cb} (m)	Cooling box width	0.195
H_{cb} (m)	Cooling box height	0.05
L_{cb} (m)	Cooling box length	0.41

Table 4-2 Air, solution and water transportation properties

Symbol	Definition	Value
h_{fg} (kJ/kg)	Water condensation heat	2450
$C_{p,air}$ (J/kg·K)	Air specific heat capacity	1020
$C_{p,sol}$ (J/kg·K)	Solution specific heat capacity	3200
$C_{p,w}$ (J/kg·K)	Water specific heat capacity	4186
ρ_{air} (kg/m³)	Air density	1.127 - 1.204 Temperature varies from 40 ℃ to 20℃
ρ_{sol} (kg/m³)	Solution density	1120 - 1200 Temperature varies from 70 ℃ to 10℃
ρ_w (kg/m³)	Water density	997 Temperature at 20 ℃

Table 4-3 Specifications of experimental instruments

Instruments	Properties	Manufacturer

Centrifugal magnetic-driven pump	Power	15 W	Xylem
	Maximum frequency	50 Hz	
	Maximum speed	2600 r/min	
	Maximum capacity	10 L/min	
AC axial fan	Power	45 W	Ebm-papst Mlfingen GmbH & Co. KG
	Nominal speed	2800/min	
Boiler	Capacity	12.87 kW	RM cylinders
	Supply temperature range	50 – 70 ℃	
	Water storage	117 L	
	Circulating pump	68 W	
	Hot water flow rate	0 - 5 L/min	
Liquid-to-liquid exchanger	Designed temperatures	-35 ℃ to 170 ℃	Xylem
	Maximum flow rate	81900 L/min	
	Maximum heat transfer area	1858 m^2	
	Designed pressure	Up to 30 bar	
Chiller	Designed temperatures	-10 ℃ to 30 ℃	Polystat
	Cooling capacity at 20 ℃	2000 W	
	Reservoir volume	18.9 L	

Table 4-4 Specifications of measurement instruments with associated accuracies

Measurement devices	Parameter	Measurement range	Accuracy
RS K-type thermocouple probe	Liquid temperature	0-1100 ℃	±0.75%
Sensirion EK-H4 humidity sensor	Temperature and humidity	-40-125 ℃	±3%
		0-100 % RH	±2%
Testo anemometer 405	Air velocity	0-10 m/s	±5%
Brannan hydrometer 200 Series	Solution density	1.0-1.4 g/m^3	±2%

Parker liquid flow indicator	Water flow rate	1-22 L/min	±2%
Parker Easiflow Series flowmeter	Solution flow rate	1-15 L/min	±5%
Data logger DT-80 Series 2	N/A	Data acquisition	±0.15%

4.3 The experiment of the regenerator

Experimental tests are carried out using the same membrane-based heat and mass exchanger test facility without the heat pipe structure built in the laboratory, as introduced in **section 4.1**. The regenerator and its membrane have identical physical properties to the dehumidifier, which are already given in Table 4-1. The weak desiccant solution temperature is controlled by a hot water supply system with the supply water temperature range of 20°C to 80°C. The hot water flow rate is controlled and measured by a liquid flow indicator (Parker FM 26 122 212 0.5-4.5 L/min). All measurement devices and their accuracies have been listed in Table 3-4. Uncertainty analysis has been conducted for all experimental data by applying Bell's uncertainty analysis method, as explained in **section 3.2.5,** to estimate uncertainties for experimental data.

To ensure the reliability and accuracy of experimental tests, variables including 1) inlet air temperature, 2) inlet air relative humidity, 3) inlet air flow rate, 4) inlet solution temperature, 5) solution concentration and 6) solution flow rate of the regenerator have been tested with 3 repeated tests for each variable and the average values are taken for analysis.

4.4 The experiment of the complete LDD system

The schematic diagram for the complete liquid desiccant dehumidification system is set up in the laboratory, as illustrated in Fig 4-1. As can be seen, the complete system consists of one air dehumidifier, one solution regenerator, two solution tanks, three liquid-to-liquid heat exchangers, and one hot and one cold water supply unit. Before entering the dehumidifier, a strong solution is cooled with cold water, which reduces the air's temperature and humidity ratio. The indoor environment is supplied with the dehumidifier's output air. The air from the indoor environment is returned to the regenerator, where it is humidified and heated before being eventually expelled to the outdoors. Before entering the regenerator, the diluted solution is heated with hot water. A solution heat exchanger (HX2) is used to recover heat between the diluted and re-concentrated solutions. There are two solution tanks used for collection. Regarding experimental set-up, air flow rates through the dehumidifier and regenerator are controlled by two variable speed fans and measured by a Testo thermos-anemometer (0-10m⁄s) with an accuracy of ±5%. The solution is circulated by two 15W centrifugal magnetically driven pumps, and its flow rates in the dehumidifier and regenerator are adjusted by two liquid flow indicators (1-15L/min) with an accuracy of ±5% to make sure the system runs at the steady condition. The solution concentration is obtained by measuring its density using a Brannan hydrometer with an accuracy of ±2%. The hot water is provided by an electrical boiler with a temperature range of 20°C to 80°C, and the cold water is from the main supply pipe with a temperature of 14 °C. Temperatures of the solution and water are measured by K-type thermocouples (0-1100°C) with an accuracy of ±0.75%. The air relative humidity is measured by Sensiron Evaluation KIT (0-100 %) with an accuracy of ±3%. All sensors are connected

to a data logger (DT500) with an accuracy of ±0.15% for data acquisition. Besides, the energy consumption of fans and pumps is monitored by the energy meter (MECHEER 2900W). The physical and transport properties of the dehumidifier (the HP-ICMLDD system) and regenerator are listed in Table 4-5.
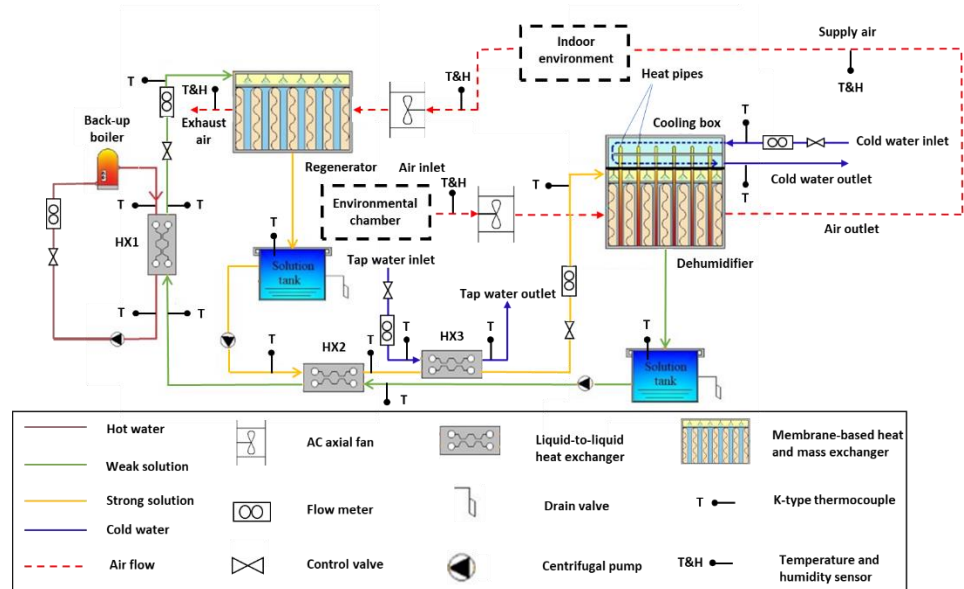
Fig 4-1 Schematic diagram of a complete liquid desiccant dehumidification system

Table 4-5 Specifications and physical properties of the dehumidifier and regenerator

Symbol	Definition	Value
L_{deh} (m)	Dehumidifier length	0.41
L_{reg} (m)	Regenerator length	0.41
W_{deh} (m)	Dehumidifier width	0.23
W_{reg} (m)	Regenerator width	0.23
H_{deh} (m)	Dehumidifier height	0.21
H_{reg} (m)	Regenerator height	0.21
$d_{h,sol}$ (m)	The hydraulic diameter of the solution channel	0.73×10^{-2}

$d_{h,air}$ (m)	The hydraulic diameter of the air channel	1.5×10^{-2}
$d_{h,w}$ (m)	The hydraulic diameter of the water channel	2.1×10^{-2}
d_{air} (m)	Air channel thickness	0.0077
d_{sol} (m)	Solution channel thickness	0.0043
k_{mem} (W/m·K)	Membrane thermal conductivity	0.3
$k_{m,mem}$ (kg/m·s)	Membrane mass transfer conductivity	3.87×10^{-6}
δ_{mem} (m)	Membrane thickness	1.05×10^{-4}
$L_{hp,e}$ (m)	Heat pipe evaporator section length	0.18
$L_{hp,c}$ (m)	Heat pipe condenser section length	0.04
$L_{hp,a}$ (m)	Heat pipe adiabatic section length	0.034
W_{cb} (m)	Cooling box width	0.195
H_{cb} (m)	Cooling box height	0.05
L_{cb} (m)	Cooling box length	0.41

4.5 Summary

This chapter illustrates the detailed experiments of the HP-ICMLDD, the regenerator and the complete membrane-based liquid desiccant system. **Section 4.1**-**4.3** present the laboratory test rig for the HP-ICMLDD, the regeneration and complete liquid desiccant systems and all the related configurations of the test rigs, including the physical properties of the membrane, the air, desiccant solution and water transportation properties, the specifications of the experimental equipment and the primary measurement instruments with their corresponding accuracies, which provide imperative guidance for the detailed investigation and parametric analysis of the HP-ICMLDD, regeneration and the complete liquid desiccant dehumidification systems in the following chapter.

Chapter 5 Experimental investigation of the dehumidifier, regenerator and complete liquid desiccant system

5.1 Introduction

Based on the literature review and the experimental set-up, this chapter focuses on the parametric analysis and performance evaluations of the heat pipe membrane-based liquid desiccant dehumidification (HP-ICMLDD), membrane-based regeneration and the complete membrane-based liquid desiccant dehumidification which are structured in the following sections:

Section 5.2 presents the influences of the main parameters of the HP-ICMLDD system (i.e. cold water properties in **section 5.2.1**: inlet cold water temperature $T_{w,in}$, inlet cold water mass flow rate $\dot{m}_{w,in}$; inlet air properties in **section 5.2.2**: inlet air temperature $T_{air,in}$, inlet air relative humidity $RH_{air,in}$ and inlet air mass flow rate $\dot{m}_{air,in}$; inlet solution properties in **section 5.2.3**: inlet solution temperature $T_{sol,in}$, solution concentration C_{sol}, solution mass flow rate $\dot{m}_{sol}$ on the air side sensible (ε_{sen}), latent (ε_{lat}) and total effectiveness (ε_{tot}), the moisture removal rate (MRR), and the internal cooling capacity (Q_{ic}).

Section 5.3 presents the influences of the main parameters of the membrane-based regeneration system (i.e. inlet air properties in **section 5.3.1**: inlet air temperature $T_{air,in,reg}$, inlet air relative humidity $RH_{air,in,reg}$ and inlet air mass flow rate $\dot{m}_{air,in,reg}$; inlet solution properties in **section 5.3.2**: inlet solution temperature $T_{sol,in,reg}$, solution concentration C_{sol} and solution mass flow rate $\dot{m}_{sol,reg}$ on the solution side sensible ($\varepsilon_{sen,sol}$), latent ($\varepsilon_{lat,sol}$) and total effectiveness ($\varepsilon_{tot,sol}$), the moisture flux rate (MFR) and the solution temperature decrease rate (TDR).

Section 5.4 presents the performance evaluations for the complete liquid

desiccant dehumidification system through 1) system optimal operating conditions for the dehumidifier and regenerator in order to assess the energy performance of the complete system (in **section 5.4.1**); 2) the relationship and correlations between the supply temperature $T_{air,out}$ and relative humidity $RH_{air,out}$ at the outlet of the dehumidifier under different inlet air temperature $T_{air,in}$ and relative humidity $RH_{air,in}$ of the dehumidifier (in **section 5.4.2**) and 3) the relationship and correlations between the inlet air relative humidity $RH_{air,in}$ and the sensible cooling capacity Q_c, latent dehumidification capacity Q_{deh}, system total cooling capacity Q_{tot}, thermal COP COP_{th}, electrical COP COP_{ele} and system total COP COP_{tot} under different inlet air temperature $T_{air,in}$ of the dehumidifier (in **section 5.4.3**). Besides, the original data processing examples have been provided in **Appendix B**.

This chapter provides a comprehensive parametric study on the membrane-based liquid desiccant dehumidifier performance, which supplies valuable data for the optimum design of the dehumidification and air-conditioning systems in practice and the applications of the integrated liquid desiccant air-conditioning system in residential buildings, which will be introduced in **Chapter 6**.

5.2 Dehumidifier performance
5.2.1 Effects of cold water

5.2.1.1 Effects of inlet cold water temperature
In order to assess the impact of the cooling box water inlet temperature, a series of tests are carried out under the same operating conditions as stated previously, except for the inlet water temperature. As shown in Fig 5-1, the ε_{sen}, ε_{lat} and ε_{tot} drop by 14.6%, 2.8% and 4.1% from 0.3293 to 0.2813, 0.7615 to 0.7405 and 0.6610 to 0.6337, respectively, when the cooling box water inlet temperature

($T_{w,in}$) rises from 10°C to 19°C. This is due to the fact that the solution absorbed heat from air-solution heat transfer and moisture condensation heat is removed by the heat pipe's internal cooling effect in the solution channels. Besides, the lower inlet water temperature, the superior internal cooling capability. Moreover, the MRR and Q_{ic} also decrease from 0.403g/s to 0.353g/s and 632.3W to 401.6W, respectively, as shown in Fig 5-2. This is attributed to that the solution equilibrium vapour pressure is increased with the solution temperature increase, where the heat pipe's internal cooling capacity is reduced. Moreover, although the $T_{w,in}$ reached 10 °C minimally in the experiment, no solution crystallization is observed since the cold water indirectly removes the solution heat gain via the heat pipe heat transfer to maintain the solution temperature. Therefore, it is proved that reducing the cold water temperature of the cooling box could considerably lower the desiccant solution temperature, thereby improving the dehumidifier performance.
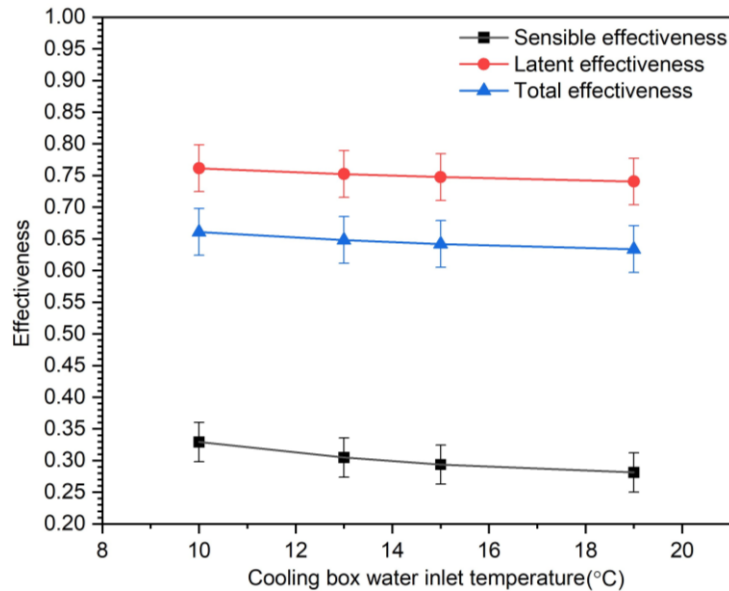
Fig 5-1 Effects of $T_{w,in}$ on ε_{sen}, ε_{lat} and ε_{tot} ($T_{air,in}$=30 °C, $RH_{air,in}$=80 %, $\dot{m}_{air,in}$=1.91 kg/min, C_{sol}=32 %, $T_{sol,in}$=18 °C, $\dot{m}_{sol}$=3 L/min, $\dot{m}_{w,in}$=3
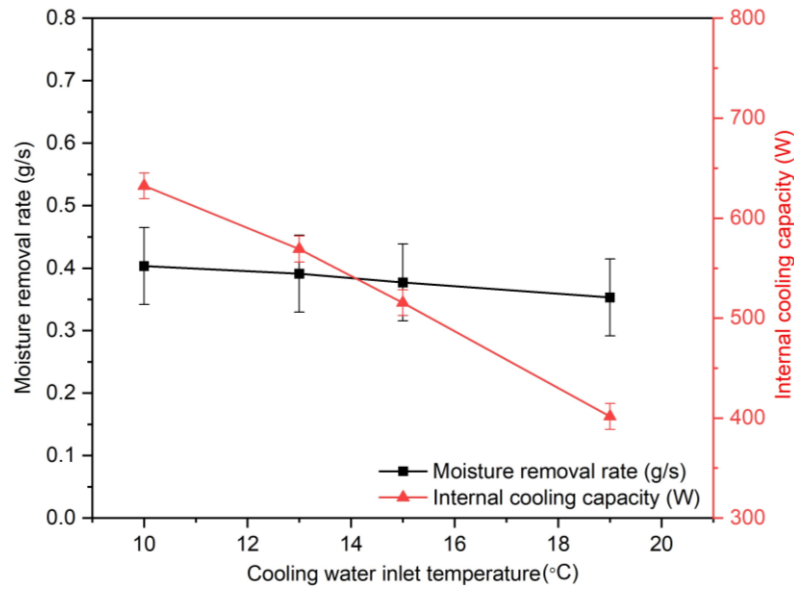
L/min).

Fig 5-2 Effects of $T_{w,in}$ on MRR and Q_{ic} ($T_{air,in}$=30 °C, $RH_{air,in}$=80 %,

$\dot{m}_{air,in}$=1.91 kg/min, C_{sol}=32 %, $T_{sol,in}$=18 °C, $\dot{m}_{sol}$= 3 L/min, $\dot{m}_{w,in}$=3

L/min).

5.2.1.2 Effects of cold water flow rate

The variations of the ε_{sen}, ε_{lat} and ε_{tot} with the cooling box water flow rate

($\dot{m}_{w,in}$) are shown in Fig 5-3, under the above-mentioned operating conditions

with $T_{w,in}$ of 10°C. The ε_{sen}, ε_{lat} and ε_{tot} increase by 19.6%, 5.0% and 6.6%

from 0.3051 to 0.3650, 0.7442 to 0.7813 and 0.6421 to 0.6845, respectively,

when the water flow rate changes from 1L/min to 5L/min. Increasing the water

flow rate through the heat pipe condenser section enhances the convection heat

transfer coefficient, leading to high heat removal ability and a relatively low

temperature in the heat pipe evaporator section. Consequently, raising the water

flow rate produces a more significant temperature difference between the air and

solution channels. At the same time, the MRR and Q_{ic} also increase drastically

from 0.33g/s to 0.42g/s and 324W to 711W respectively, as shown in Fig 5-4.

145

Thus, it is evident that the dehumidification and cooling performance can be drastically improved by increasing the cold water flow rate in the cooling box.
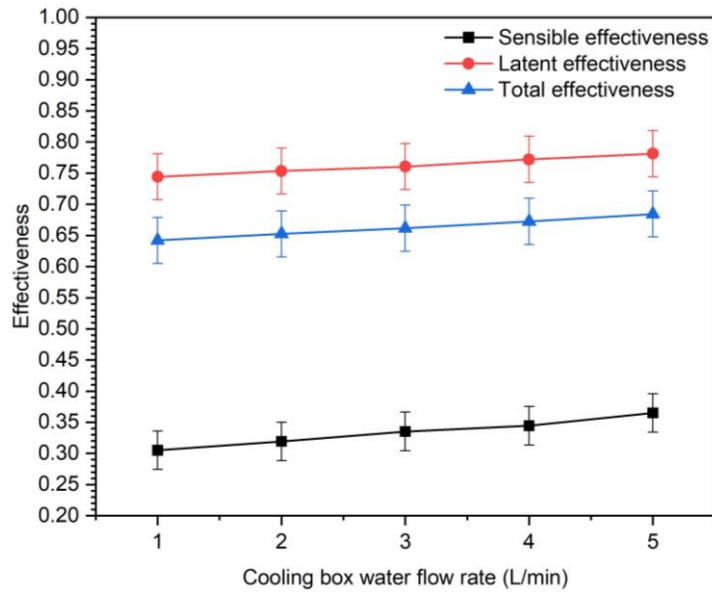
Fig 5-3 Effects of cooling box water flow rate ($\dot{m}_{w,in}$) on ε_{sen}, ε_{lat} and ε_{tot}
($T_{air,in}$=30 ℃, $RH_{air,in}$=80 %, $\dot{m}_{air,in}$=1.91 kg/min, C_{sol}=32 %, $T_{sol,in}$=18 ℃, $\dot{m}_{sol}$=3 L/min, $T_{w,in}$=10 ℃).
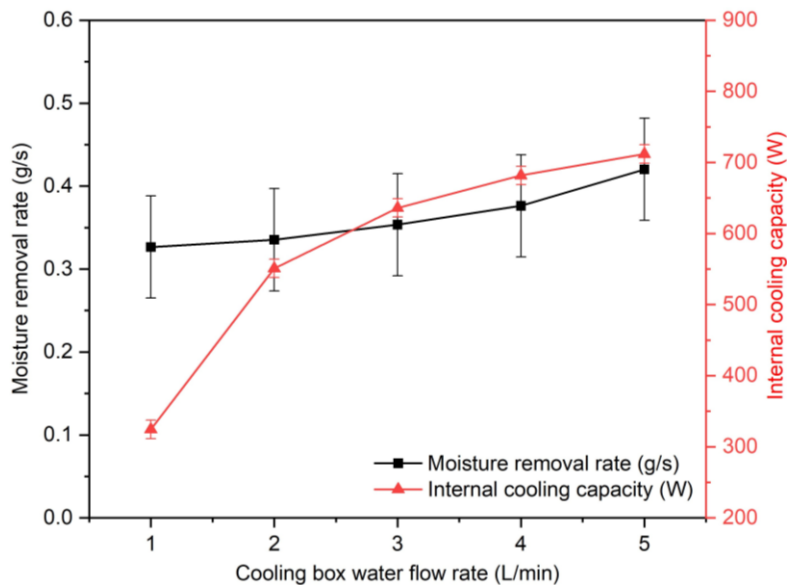
Fig 5-4 Effects of cooling box water flow rate ($\dot{m}_{w,in}$) on MRR and Q_{ic}
($T_{air,in}$=30 ℃, $RH_{air,in}$=80 %, $\dot{m}_{air,in}$=1.91 kg/min, C_{sol}=32 %, $T_{sol,in}$=18 ℃, $\dot{m}_{sol}$=3 L/min, $T_{w,in}$=10 ℃).

5.2.2 Effects of inlet air condition
5.2.2.1 Effects of inlet air temperature

The variations of the ε_{sen}, ε_{lat} and ε_{tot} with inlet air temperature ($T_{air,in}$) are illustrated in Fig 5-5. The ε_{lat} decreases slightly by 2.7 % from 0.7633 to 0.7426 under $RH_{air,in}$=80 % when $T_{air,in}$ increases from 28 °C to 36 °C. This is caused by the increased moisture resistance, and the air becomes more humid as the absolute humidity increases when the air temperature rises with the same relative humidity, which is also associated with membrane water permeability [75]. Besides, based on Eq. (3-12), the increasing air temperature leads to larger differences of $W_{air,in} - W_{sol,in}$ (Denominator: $W_{air,in} - W_{sol,in}$) when keeping the $RH_{air,in}$ constant. However, with the increased moisture resistance, the mass transfer potential is reduced, leading to a lower increasing rate of $W_{air,in} - W_{air,out}$ (Numerator: $W_{air,in} - W_{air,out}$).

The ε_{sen} gradually rises with the $T_{air,in}$ and peaks at 34 °C. This is because increasing air temperature while keeping constant air relative humidity enlarges the temperature difference between the air and solution, thereby enhancing the heat transfer potential [76]. Based on Eq. (3-11), the increased $T_{air,in}$ leads to larger differences of $T_{air,in} - T_{sol,in}$ (Denominator: $T_{air,in} - T_{sol,in}$), indicating higher heat transfer potential. Besides, a significant increase in heat transfer potential promotes the difference of $T_{air,in} - T_{air,out}$ (Numerator: $T_{air,in} - T_{air,out}$). However, the increment of heat transfer potential tends to be slower to reach its peak with progressively higher $T_{air,in}$. In addition, more condensation heat will be absorbed by the solution to increase the solution temperature indirectly. Gradually, the impact of condensation heat dominates the solution temperature increase when the heat transfer potential increases to its limit, which

is found to be $T_{air,in}$ =34 °C, with heat pipe internal cooling effect. Therefore, the increasing rate of $T_{air,in} - T_{air,out}$ is weakened after $T_{air,in}$ =34 °C, resulting in the slight decrease in ε_{sen}. To summarize, the ε_{sen} increases when the increase of heat transfer potential dominates the temperature difference between the air and solution, whereas the ε_{sen} decreases when the increase of condensation heat dominates the temperature difference between the air and solution.

The influences of inlet air temperature on the MRR and Q_{ic} are indicated in Fig 5-6, the MRR increases from 0.31g/s to 0.52g/s when the $T_{air,in}$ changes from 28°C to 36°C, this is because the air absolute humidity rises with the inlet air temperature increase under the same relative humidity. Besides, the increased air absolute humidity will enhance the mass transfer potential, leading to the increase of $W_{air,in} - W_{air,out}$. However, the slightly reduced latent effectiveness is attributed to that the increasing rate of $W_{air,in} - W_{air,out}$ (Numerator: $W_{air,in} - W_{air,out}$) is lower than that of the denominator ($W_{air,in} - W_{sol,in}$) since the increasingly moisture resistance. Moreover, according to Eq. (3-12), the difference between the inlet and outlet air absolute moisture content ($W_{air,in} - W_{air,out}$) increases as previously discussed. Moreover, the Q_{ic} is enhanced from 597W to 744W because of the high temperature difference between the air and solution.
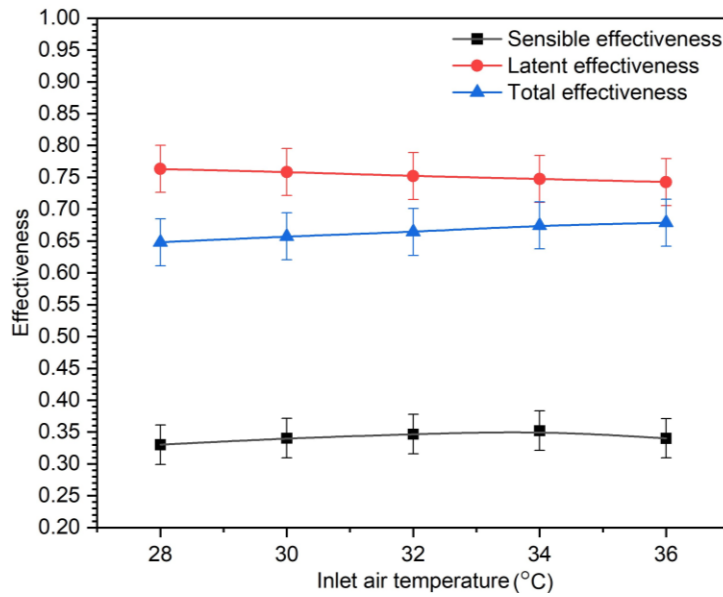
Fig 5-5 Effects of inlet air temperature ($T_{air,in}$) on ε_{sen}, ε_{lat} and ε_{tot}

($RH_{air,in}$=80 %, $\dot{m}_{air,in}$=1.91 kg/min, C_{sol}=32 %, $T_{sol,in}$=18 ℃, $\dot{m}_{sol}$=3 L/min, $\dot{m}_{w,in}$=3 L/min, $T_{w,in}$=10 ℃).

Fig 5-6 Effects of inlet air temperature ($T_{air,in}$) on MRR and Q_{ic} ($RH_{air,in}$=80 %, $\dot{m}_{air,in}$=1.91 kg/min, C_{sol}=32 %, $T_{sol,in}$=18 °C, $\dot{m}_{sol}$=3 L/min, $\dot{m}_{w,in}$=3 L/min, $T_{w,in}$=10 ℃).

5.2.2.2 Effects of inlet air relative humidity

The effects of inlet air relative humidity ($RH_{air,in}$) on ε_{sen}, ε_{lat} and ε_{tot} are

149

reflected in Fig 5-7, the $RH_{air,in}$ is changed while maintaining the $T_{air,in}$ at 30 °C, $\dot{m}_{air,in}$ at 1.91kg/min, C_{sol} at 32 %, $T_{sol,in}$ at 18 °C, $\dot{m}_{sol}$ at 3L/min, $\dot{m}_{w,in}$ at 3L/min and $T_{w,in}$ at 10 °C. The ε_{sen} declines by 2.4% from 0.3473 to 0.3391 when the $RH_{air,in}$ rises from 60% to 85%. Under the constant $T_{air,in}$, more moisture content is absorbed by the desiccant solution, resulting in more condensation heat release when the inlet air relative humidity increases. Based on Eq. (3-11), the increasing condensation heat leads to the solution temperature increase and the temperature difference reduction between air and solution, which further reduces the heat transfer potential and the numerator $T_{air,in} - T_{air,out}$. Moreover, the denominator $T_{air,in} - T_{sol,in}$ remains constant.

On the contrary, the ε_{lat} escalates by 25.6% from 0.6248 to 0.7849 due to the increment of water vapour partial pressure difference between the air and solution [261]. However, the solution temperature increase caused by more condensation heat leads to increased solution equilibrium vapour pressure, slightly weakening the mass transfer potential. Therefore, the increasing rate of the ε_{lat} is gradually declined. Besides, the ε_{tot} rises by 21.6% from 0.5603 to 0.6812. The variations of MRR and Q_{ic} with $RH_{air,in}$ are shown in Fig 5-8. The MRR increases from 0.30g/s to 0.37g/s when the $RH_{air,in}$ changes from 60% to 85%. Moreover, the Q_{ic} increases from 572W to 645W because of the increased temperature difference between the solution and heat pipe evaporation section, resulting from the rising moisture condensation heat.
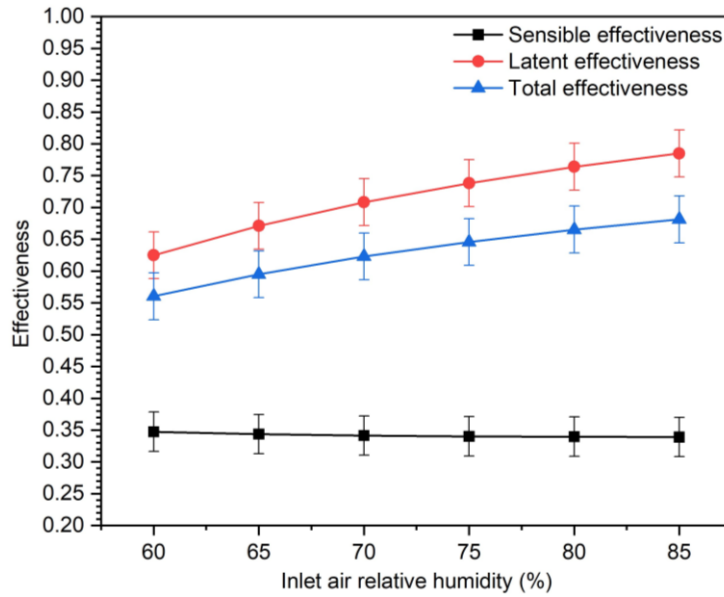
Fig 5-7 Effects of inlet air relative humidity ($RH_{air,in}$) on ε_{sen}, ε_{lat} and ε_{tot}

($T_{air,in}$=30 °C, $\dot{m}_{air,in}$=1.91 kg/min, C_{sol}=32 %, $T_{sol,in}$=18 °C, $\dot{m}_{sol}$=3 L/min, $\dot{m}_{w,in}$=3 L/min, $T_{w,in}$=10 °C).
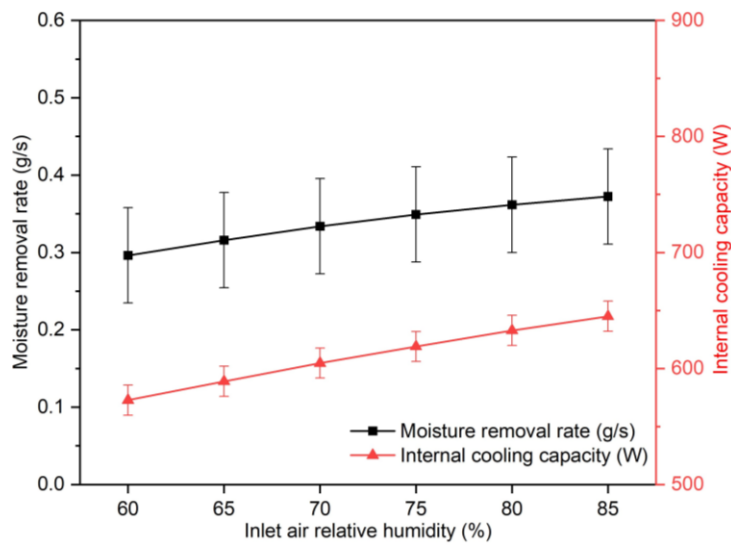
Fig 5-8 Effects of inlet air relative humidity ($RH_{air,in}$) on MRR and Q_{ic}

($T_{air,in}$=30 °C, $\dot{m}_{air,in}$=1.91 kg/min, C_{sol}=32 %, $T_{sol,in}$=18 °C, $\dot{m}_{sol}$=3 L/min, $\dot{m}_{w,in}$=3 L/min, $T_{w,in}$=10 °C).

5.2.2.3 Effects of air flow rate

The impacts of air flow rate ($\dot{m}_{air,in}$) on ε_{sen}, ε_{lat} and ε_{tot} are shown in Fig 5-9

under $T_{air,in}=30\,°C$, $RH_{air,in}=80\%$, $C_{sol}=26\%$, $T_{sol,in}=18\,°C$, $\dot{m}_{sol}=3L/min$, $\dot{m}_{w,in}=3L/min$ and $T_{w,in}=10°C$. It is found that the ε_{lat} decreases by 5.8% from 0.7962 to 0.7501 when the $\dot{m}_{air,in}$ from 0.38kg/min to 2.29kg/min. Moreover, the ε_{sen} and ε_{tot} decrease by 40.7% and 10.7% from 0.4337 to 0.2574 and 0.7119 to 0.6354, respectively. This is attributed to the air short contact time with the membrane at the high air flow rate, leading to the decreased moisture content difference at the air inlets and outlets. The ε_{lat} is proportional to the moisture content difference at the air inlets and outlets, as indicated in Eq. (3-12). The MRR increases significantly from 0.06g/s to 0.42g/s when the $\dot{m}_{air,in}$ changes from 0.38kg/min to 2.29kg/min, as indicated in Fig 5-10. According to Eq. (3-14), the MRR is proportional to air flow rate and moisture content difference, thereby resulting in a substantial increase. Similarly, the Q_{ic} enlarges from 600W to 637W due to the high air temperature in the air channel, increasing the temperature difference between the air and solution channels.
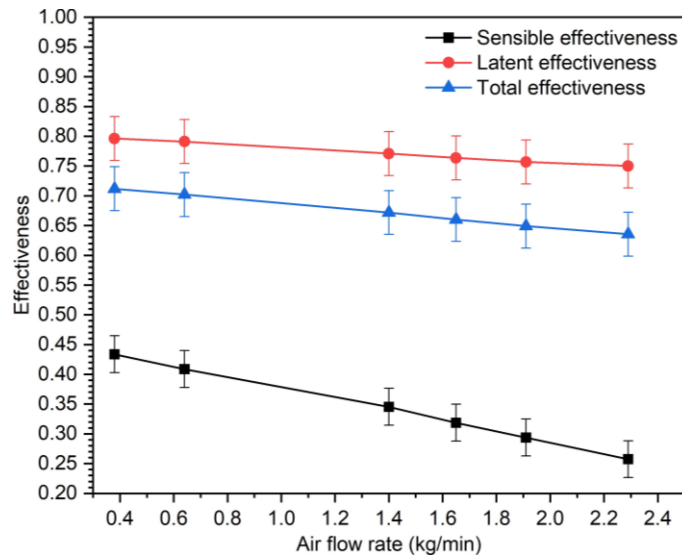
Fig 5-9 Effects of air flow rate ($\dot{m}_{air,in}$) on ε_{sen}, ε_{lat} and ε_{tot} ($T_{air,in}=30\,°C$, $RH_{air,in}=80\,\%$, $C_{sol}=32\,\%$, $T_{sol,in}=18\,°C$, $\dot{m}_{sol}=3\,L/min$, $\dot{m}_{w,in}=3\,L/min$, $T_{w,in}=10\,°C$).
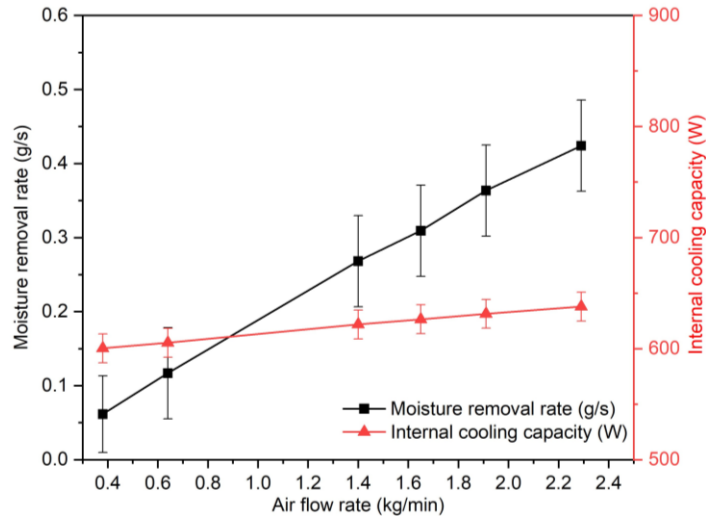
Fig 5-10 Effects of air flow rate ($\dot{m}_{air,in}$) on MRR and Q_{ic} ($T_{air,in}$=30 ℃,

$RH_{air,in}$=80 %, C_{sol}=32 %, $T_{sol,in}$=18 ℃, $\dot{m}_{sol}$=3 L/min, $\dot{m}_{w,in}$=3 L/min,

$T_{w,in}$=10 ℃).

5.2.3 Effects of solution properties
5.2.3.1 Effects of inlet solution temperature
The solution temperature ($T_{sol,in}$) has apparent influences on the system cooling

and dehumidification performance since it is relevant to the surface vapour

pressure of the solution. The effects of $T_{sol,in}$ on the ε_{sen}, ε_{lat} and ε_{tot} are

reflected in Fig 5-11 under $T_{air,in}$=30℃, $RH_{air,in}$=80%, $\dot{m}_{air,in}$=1.91kg/min,

C_{sol}=32%, $\dot{m}_{sol}$=3L/min, $\dot{m}_{w,in}$=3L/min and $T_{w,in}$=10℃. It can be seen that all

the effectiveness decline with the solution temperature. The decreased

temperature difference between the air and solution also leads to a decrease in

the heat transfer potential, resulting from the decline in the ε_{sen}. The decrease of

the ε_{lat} is because the increasing vapour partial pressure on the solution side

restricts the system's dehumidification potential, which is also stated in the

literature [140].

However, the effect of $T_{sol,in}$ on ε_{sen} is significantly greater than its effect on

ε_{lat}. For example, the ε_{sen} decreases by 21.7% from 0.3347 to 0.2620 as the $T_{sol,in}$ rises from 14 °C to 21 °C, whereas the ε_{lat} is only reduced by 5.2 % from 0.7834 to 0.7429. According to Eq. (3-11), lower inlet solution temperature leads to a higher temperature difference between air and solution, which improves the heat transfer potential. In addition, the impact of condensation heat is negligible compared with the increase in heat transfer potential. However, with high inlet solution temperature, the temperature difference between air and solution is comparably small, and the heat transfer potential is weakened, where the impact of condensation heat is more prioritized. Based on Eq. (3-12), the lower inlet solution temperature will increase the mass transfer potential and further lead to more moisture absorbed by the solution. Meanwhile, more condensation heat diminishes the dehumidification performance.

Owing to the reduced latent effectiveness, the MRR also declines from 0.43g/s to 0.33g/s, as shown in Fig 5-12. Moreover, the Q_{ic} has a noticeable improvement from 620W to 653W as the heat pipes are heated by the high temperature solution. This leads to the high temperature difference between the heat pipe condenser section and the cold water in the cooling box.
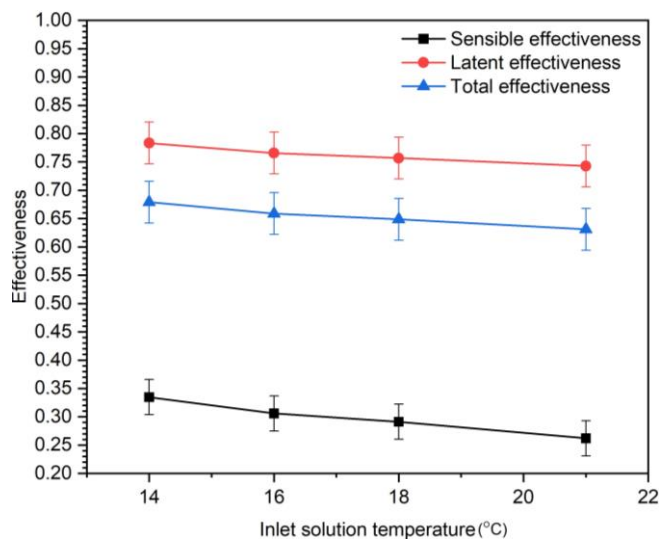
Fig 5-11 Effects of inlet solution temperature ($T_{sol,in}$) on ε_{sen}, ε_{lat} and ε_{tot}

$(T_{air,in}$=30 °C, $RH_{air,in}$=80 %, $\dot{m}_{air,in}$=1.91 kg/min, C_{sol}=32 %, $\dot{m}_{sol}$=3 L/min, $\dot{m}_{w,in}$=3 L/min, $T_{w,in}$=10 °C).
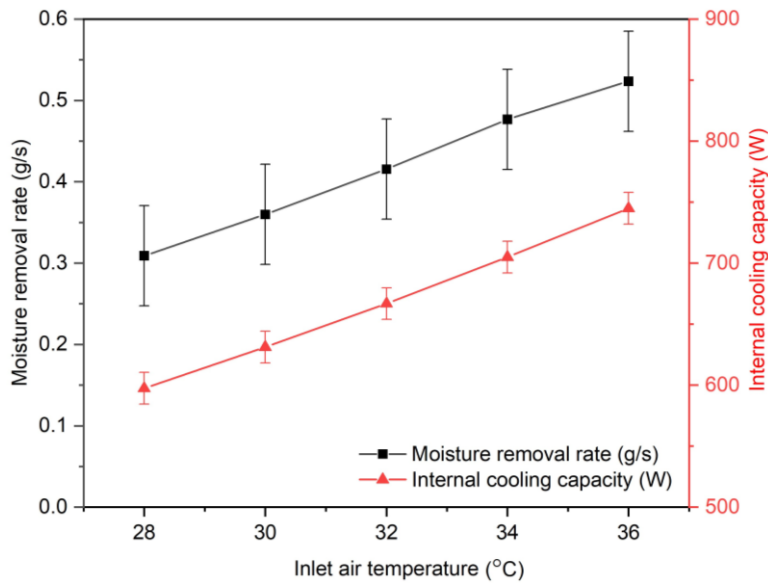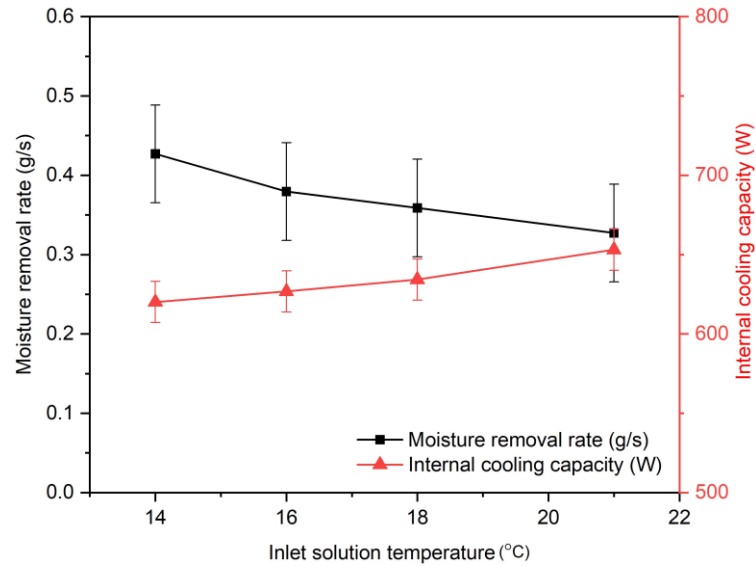

Fig 5-12 Effects of inlet solution temperature ($T_{sol,in}$) on MRR and Q_{ic}

$(T_{air,in}$=30 °C, $RH_{air,in}$=80 %, $\dot{m}_{air,in}$=1.91 kg/min, C_{sol}=32 %, $\dot{m}_{sol}$=3 L/min, $\dot{m}_{w,in}$=3 L/min, $T_{w,in}$=10 °C)

5.2.3.2 Effects of solution concentration

The performance of the system's cooling and dehumidification is significantly influenced by the solution concentration (C_{sol}), with a higher solution concentration producing better dehumidification results, as depicted in Fig 5-13 and Fig 5-14. Under the examined circumstance ($T_{air,in}$=30°C, $RH_{air,in}$=80%, $\dot{m}_{air,in}$ =1.91kg/min, $T_{sol,in}$ =18 °C , $\dot{m}_{sol}$ =3L/min, $\dot{m}_{w,in}$ =3L/min and $T_{w,in}$=10°C), the ε_{sen} decreases by 13.0% from 0.3635 to 0.3162 when the C_{sol} varies from 26% to 38%, while the ε_{lat} and ε_{tot} rise by 20.3% and 15.7% from 0.6981 to 0.8395 and 0.6203 to 0.7178, respectively. The decline of the ε_{sen} is owing to the increased condensation heat with more moisture absorbed. In addition, the higher C_{sol} has a lower solution surface vapour pressure to improve the solution absorption ability, which results in the ε_{lat} increase. It is noteworthy

155

from Error! Reference source not found. that high concentration solution will a lso improve both MRR and Q_{ic}. Due to the significant difference in vapour pressure between the air and solution at a high solution concentration, the MRR increases from 0.21g/s to 0.48g/s as the C_{sol} increases from 26% to 38%. Moreover, with more moisture absorbed by the solution, the increased moisture condensation heat is removed by the heat pipes, resulting in Q_{ic} increasing from 542W to 721W as well. Besides, the maximum concentration for this study is 38%, and it is possible to increase the concentration above this maximum value for better dehumidification performance. However, higher solution concentration may lead to the desiccant crystallisation issue on the membrane surface, thereby decreasing the system performance [25].
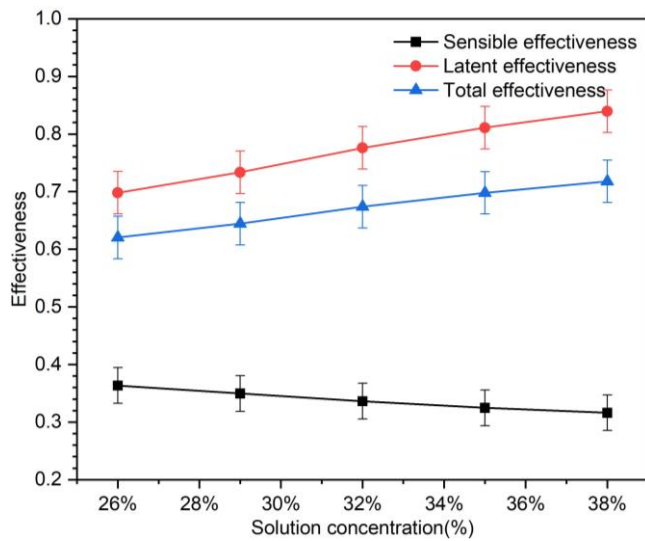
Fig 5-13 Effects of solution concentration (C_{sol}) on ε_{sen}, ε_{lat} and ε_{tot} ($T_{air,in}$=30 ℃, $RH_{air,in}$=80 %, $\dot{m}_{air,in}$=1.91 kg/min, $T_{sol,in}$=18 ℃, $\dot{m}_{sol}$=3 L/min, $\dot{m}_{w,in}$=3 L/min, $T_{w,in}$=10 ℃).
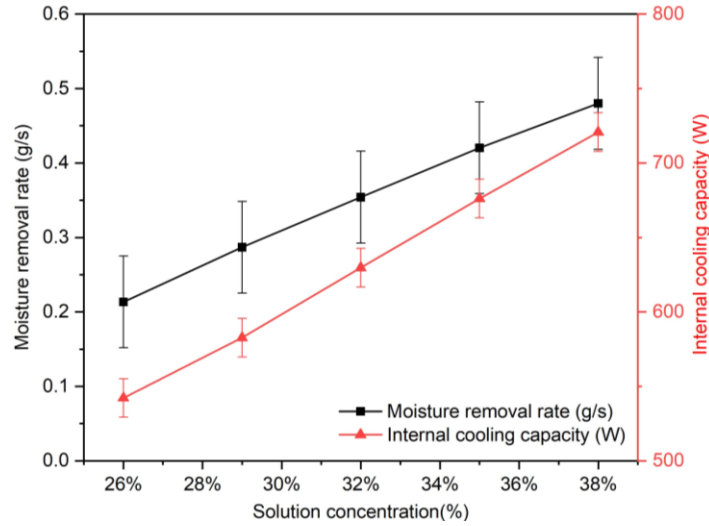
Fig 5-14 Effects of solution concentration (C_{sol}) on MRR and Q_{ic} ($T_{air,in}$=30

°C, $RH_{air,in}$=80 %, $\dot{m}_{air,in}$=1.91 kg/min, $T_{sol,in}$=18 °C, $\dot{m}_{sol}$=3 L/min, $\dot{m}_{w,in}$=3

L/min, $T_{w,in}$=10 °C)

5.2.3.3 Effects of solution flow rate

The variations of the ε_{sen}, ε_{lat} and ε_{tot} and MRR, as well as the Q_{ic} with the

$\dot{m}_{sol}$ are shown in Fig 5-15 and Fig 5-16, while maintaining $T_{air,in}$=30℃,

$RH_{air,in}$=80%, $\dot{m}_{air,in}$=1.91kg/min, C_{sol}=32%, $T_{sol,in}$=18℃, $\dot{m}_{w,in}$=3L/min

and $T_{w,in}$=10℃. The ε_{sen} increases substantially by 45.3% from 0.2687 to

0.3904 when the $\dot{m}_{sol}$ rises from 1L/min to 5L/min. It is due to that a higher

solution flow rate leads to a lower solution temperature, and correspondingly a

lower air temperature at outlets, thus increasing the sensible effectiveness. The

ε_{lat} also raises with the $\dot{m}_{sol}$, where the ε_{lat} improves by 4.5 % from 0.7427 to

0.7763 since low solution temperature and its equilibrium vapour pressure will

be obtained as the solution flow rate rises, resulting in higher mass transfer

potential [262]. Therefore, the ε_{tot} increases by 8.6% from 0.6325 to 0.6866. It

can be seen that the MRR increases from 0.35g/s to 0.45g/s as well. It is also

noted that the Q_{ic} enhances from 542W to 706W because of the raised heat

157

transfer between the solution and heat pipe evaporator section.
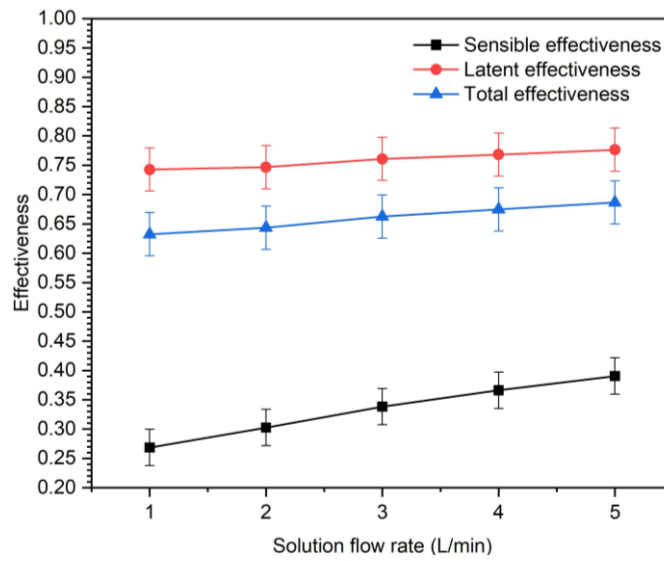
Fig 5-15 Effects of solution flow rate ($\dot{m}_{sol}$) on ε_{sen}, ε_{lat} and ε_{tot} ($T_{air,in}$=30 °C, $RH_{air,in}$=80 %, $\dot{m}_{air,in}$=1.91 kg/min, C_{sol}=32 %, $T_{sol,in}$=18 °C, $\dot{m}_{w,in}$=3 L/min, $T_{w,in}$=10 °C)
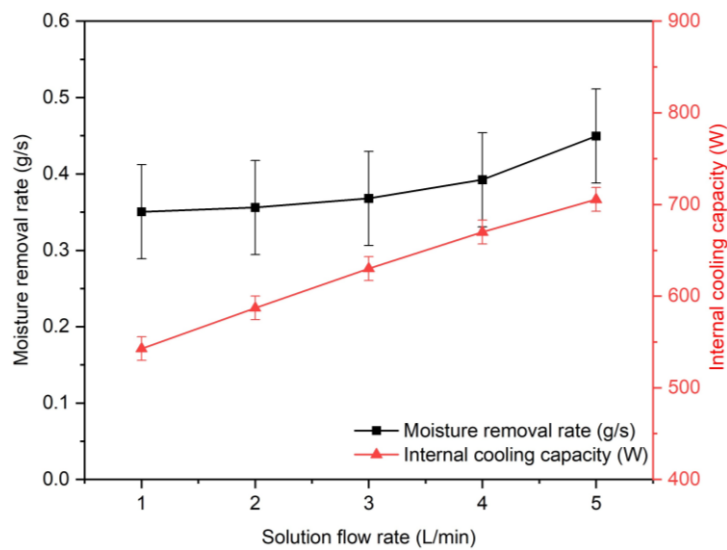
Fig 5-16 Effects of solution flow rate ($\dot{m}_{sol}$) on MRR and Q_{ic} ($T_{air,in}$=30 °C, $RH_{air,in}$=80 %, $\dot{m}_{air,in}$=1.91 kg/min, C_{sol}=32 %, $T_{sol,in}$=18 °C, $\dot{m}_{w,in}$=3 L/min, $T_{w,in}$=10 °C)

5.3 Regenerator performance
5.3.1 Effects of inlet air condition
5.3.1.1 Effects of inlet air temperature of regenerator

The variations of solution side effectiveness, TDR and MFR with inlet air temperature ($T_{air,in,reg}$), are illustrated in Fig 5-17 and Fig 5-18. All effectiveness hardly vary with $T_{air,in,reg}$ in the temperature range of 24℃ to 32℃ under $RH_{air,in,reg}$=40%, and only change by 4.4%, 2.9% and 3.2% for the sensible, latent and total effectiveness, respectively. For the latent heat transfer, air vapour pressure is only governed by the air humidity ratio $W_{air,in}$, and the change in air temperature alone would have a negligible effect on air vapour pressure. Consequently, the mass transfer potential between the air and solution would remain unchanged. The latent effectiveness and MFR rise marginally with $T_{air,in,reg}$. Literature [263] explains where significant sensible heat transfer would occur between air and solution when the solution temperature exceeds the air temperature. The decrease in air vapour pressure brought about by the cooling of the solution upon contact with air would inhibit regeneration. There would be less sensible heat transfer from the solution to the air if the air entering the system was at a higher temperature. As a result, the vapour pressure difference between the air and solution sides can be maintained at a high level, and the latent heat transfer can still be marginally improved. On the other hand, the high $T_{air,in,reg}$ would reduce the temperature difference between the air and solution, thereby diminishing the potential for sensible heat transfer. As a result, the sensible effectiveness and TDR are marginally diminished. Therefore, the effect of air inlet temperature on regeneration performance can be disregarded and adjusting $T_{air,in,reg}$ has no discernible effect.
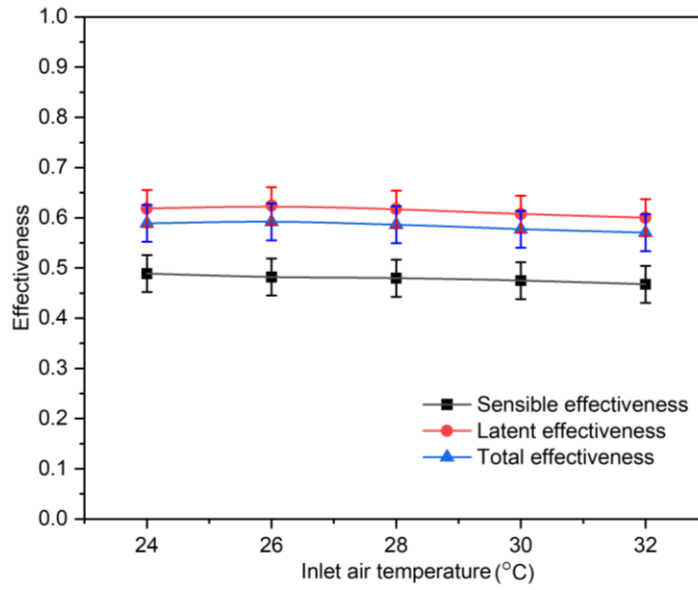
Fig 5-17 Effects of inlet air temperature ($T_{air,in,reg}$) on $\varepsilon_{sen,sol}$, $\varepsilon_{lat,sol}$ and $\varepsilon_{tot,sol}$ ($RH_{air,in,reg}$=40 %, $\dot{m}_{air,reg}$=1.91 kg/min, C_{sol}=32 %, $T_{sol,in,reg}$=60 ℃, $\dot{m}_{sol,reg}$=2 L/min)
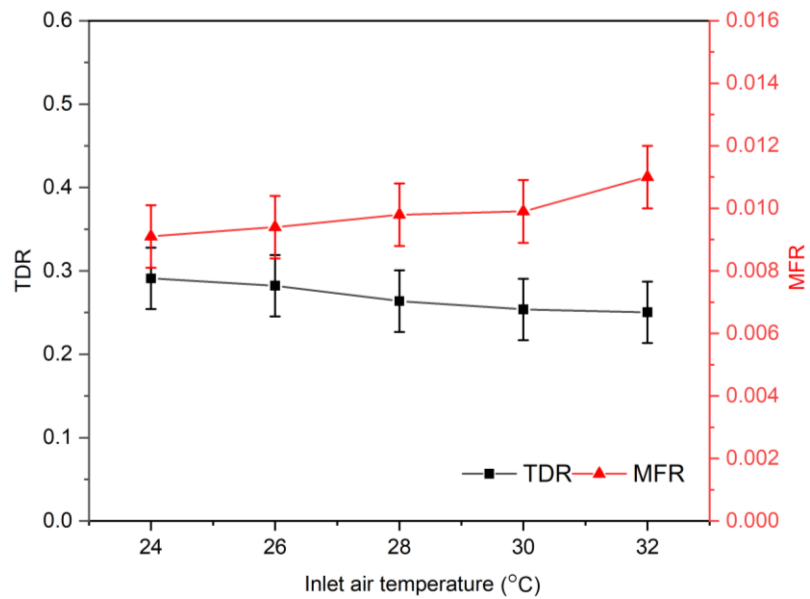
Fig 5-18 Effects of inlet air temperature ($T_{air,in,reg}$) on TDR and MFR ($RH_{air,in,reg}$=40 %, $\dot{m}_{air,reg}$=1.91 kg/min, C_{sol}=32 %, $T_{sol,in,reg}$=60 ℃, $\dot{m}_{sol,reg}$=2 L/min)

5.3.1.2 Effects of inlet air relative humidity of regenerator

The effects of inlet air relative humidity ($RH_{air,in,reg}$) on $\varepsilon_{sen,sol}$, $\varepsilon_{lat,sol}$, $\varepsilon_{tot,sol}$, TDR and MFR are reflected in Fig 5-19 and Fig 5-20. The $RH_{air,in,reg}$ is changed while maintaining the $T_{air,in,reg}$ at 28 ℃, $\dot{m}_{air,reg}$ at 1.91kg/min, C_{sol} at 32 %, $T_{sol,in,reg}$ at 60 ℃, $\dot{m}_{sol,reg}$ at 2L/min at 10 ℃. The $\varepsilon_{sen,sol}$ increases by 2.4% from 0.4723 to 0.4836 when the $RH_{air,in,reg}$ rises from 30% to 50%. The $\varepsilon_{lat,sol}$ escalates by 2.3% from 0.6058 to 0.6197 due to the decrease in water vapour partial pressure difference between the air and solution [261]. Based on Eq. (3-22), the mass transfer potential is reduced significantly with the considerable reduction of the vapour pressure difference between the air and solution sides. As a result, MFR is decreased gradually, as displayed in Error! R eference source not found.. Regarding the sensible heat transfer, it is slightly influenced by reduced heat absorption during the evaporation process when the mass transfer is weakened. Thus, the solution temperature at the outlet would increase to a small extent, resulting in the decrease of TDR.
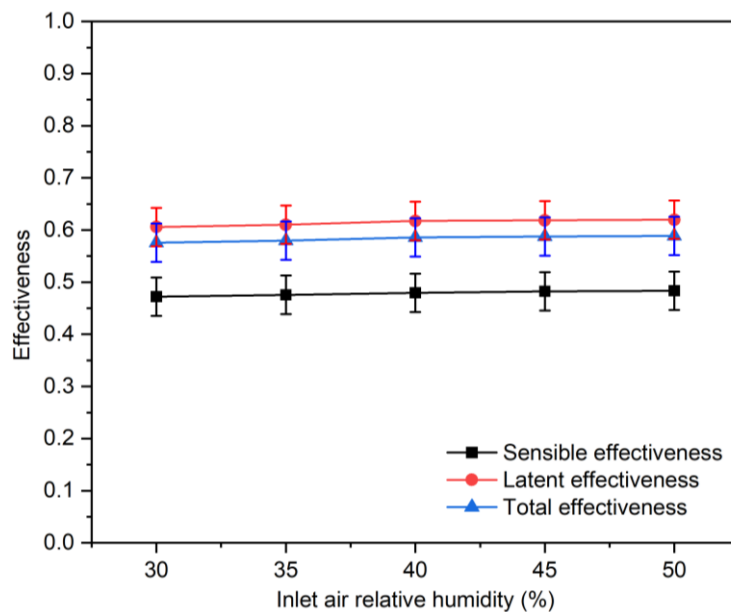
Fig 5-19 Effects of inlet air relative humidity ($RH_{air,in,reg}$) on $\varepsilon_{sen,sol}$, $\varepsilon_{lat,sol}$ and $\varepsilon_{tot,sol}$ ($T_{air,in,reg}$=28 °C, $\dot{m}_{air,reg}$=1.91 kg/min, C_{sol}=32 %, $T_{sol,in,reg}$=60 °C, $\dot{m}_{sol,reg}$=2 L/min)
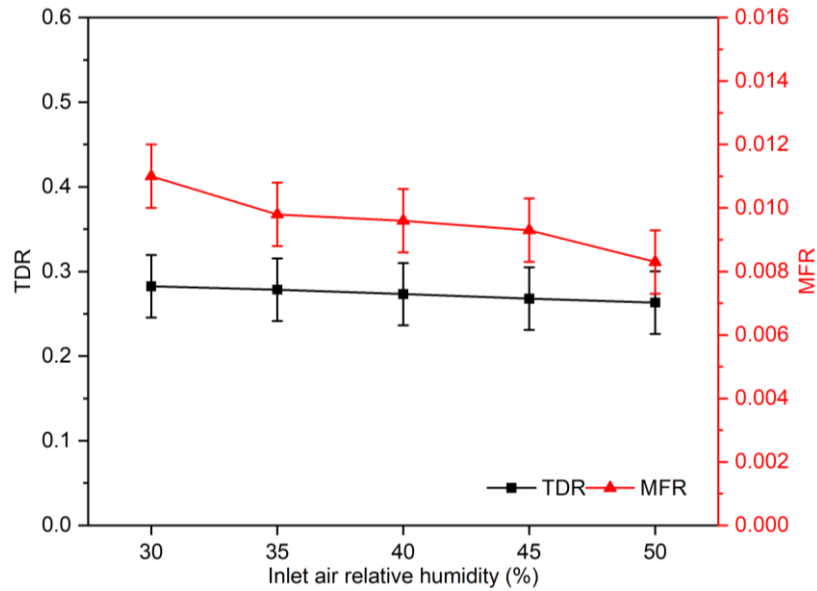
Fig 5-20 Effects of inlet air relative humidity ($RH_{air,in,reg}$) on TDR and MFR ($T_{air,in,reg}$=28 °C, $\dot{m}_{air,reg}$=1.91 kg/min, C_{sol}=32 %, $T_{sol,in,reg}$=60 °C, $\dot{m}_{sol,reg}$=2 L/min)

5.3.1.3 Effects of air flow rate of regenerator

The impacts of air flow rate ($\dot{m}_{air,in,reg}$) on $\varepsilon_{sen,sol}$, $\varepsilon_{lat,sol}$ and $\varepsilon_{tot,sol}$ are reflected in Fig 5-21 under $T_{air,in,reg}$=28 °C, $RH_{air,in,reg}$=40%, C_{sol}=32%, $T_{sol,in,reg}$=60°C and $\dot{m}_{sol,reg}$=2L/min. It is found that the $\varepsilon_{lat,sol}$ decreases by 45.9% from 0.6528 to 0.3532 when the $\dot{m}_{air,in}$ from 0.64kg/min to 2.29kg/min. Moreover, the $\varepsilon_{sen,sol}$ and $\varepsilon_{tot,sol}$ decrease by 34.6% and 43.9% from 0.4892 to 0.3198 and 0.6157 to 0.3456, respectively. The $\varepsilon_{lat,sol}$ is proportional to the moisture content difference at the air inlets and outlets of the regenerator, as indicated in Eq. (3-18). Apart from the solution side effectiveness, the solution side TDR and MFR have also been applied for regeneration performance

evaluation. The variations of TDR and MFR with $\dot{m}_{air,in,reg}$ are shown in Fig 5-22. As seen from the figure, TDR decreases from 0.2849 to 0.1772 when the $\dot{m}_{air,reg}$ from 0.64kg/min to 2.29kg/min, indicating that the solution cooling effect deteriorates through the process. The MFR increases significantly from 0.0081g/s to 0.0222g/s when the $\dot{m}_{air,reg}$ changes from 0.38kg/min to 2.29kg/min. According to Eq. (3-22), the MFR is proportional to air flow rate and moisture content difference at the regenerator side, thereby resulting in a considerable increase.
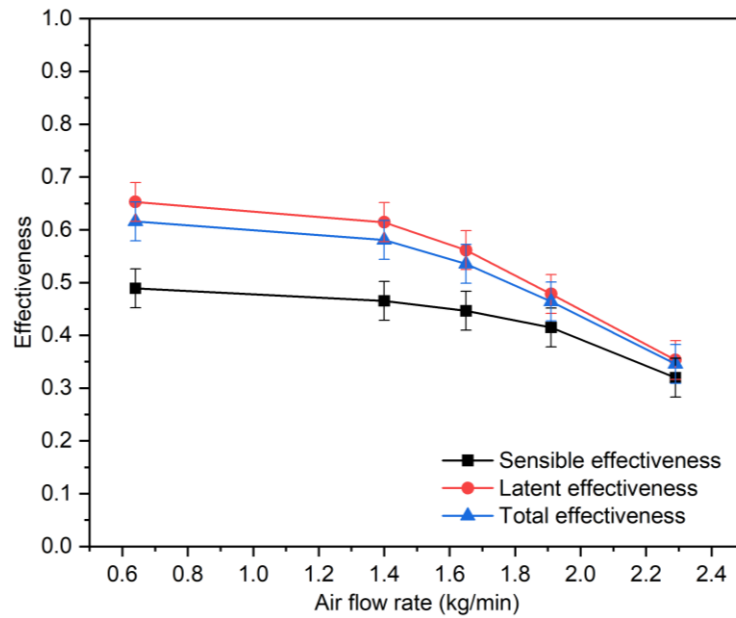
Fig 5-21 Effects of air flow rate ($\dot{m}_{air,reg}$) on $\varepsilon_{sen,sol}$, $\varepsilon_{lat,sol}$ and $\varepsilon_{tot,sol}$

($T_{air,in,reg}$=28 ℃, $RH_{air,in,reg}$=40 %, C_{sol}=32 %, $T_{sol,in,reg}$=60 ℃, $\dot{m}_{sol,reg}$=2 L/min)
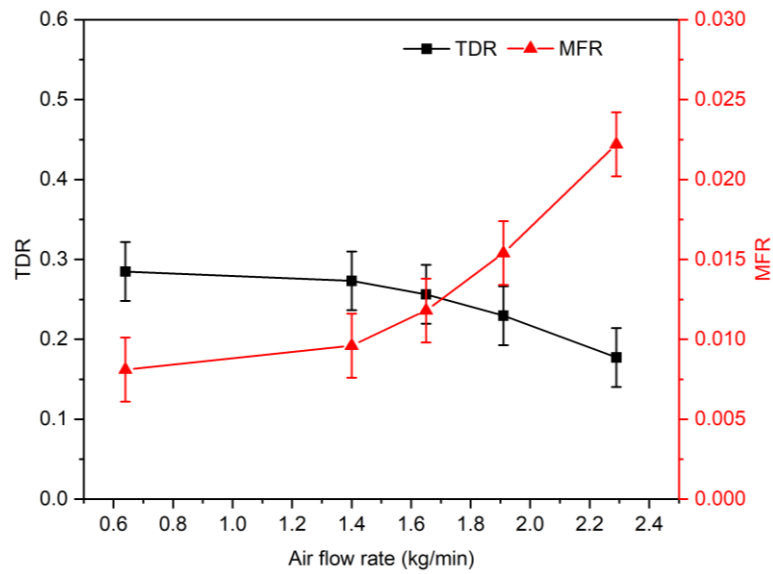
Fig 5-22 Effects of air flow rate ($\dot{m}_{air,reg}$) on TDR and MFR ($T_{air,in,reg}$=28 ℃, $RH_{air,in,reg}$=40 %, C_{sol}=32 %, $T_{sol,in,reg}$=60 ℃, $\dot{m}_{sol,reg}$=2 L/min)

5.3.2 Effects of solution properties
5.3.2.1 Effects of inlet solution temperature

The inlet solution temperature of the regenerator ($T_{sol,in,reg}$) has apparent influences on the system regenerator performance since it is relevant to the surface vapour pressure of the solution. The effects of $T_{sol,in,reg}$ on the $\varepsilon_{sen,sol}$, $\varepsilon_{lat,sol}$ and $\varepsilon_{tot,sol}$ are reflected in Fig 5-23 under $T_{air,in,reg}$ =28 ℃, $RH_{air,in,reg}$ =40%, $\dot{m}_{air,reg}$ =1.91kg/min, C_{sol} =32% and $\dot{m}_{reg}$ =2L/min, respectively. It can be seen that all the effectiveness decline with the inlet solution temperature of the regenerator. Compared to the latent and total effectiveness, the solution side sensible effectiveness is insensitive to $T_{sol,in,reg}$. Apart from the deterioration of all solution side effectiveness with increasing $T_{sol,in,reg}$, the higher $T_{sol,in,reg}$, the higher solution equilibrium humidity ratio and vapour pressure. Regarding the definition of the solution side sensible effectiveness in Eq. (3-17), the absolute value of the denominator in the equation

164

increases with $T_{sol,in,reg}$, thus the sensible effectiveness is reduced gradually. Furthermore, the increase of $T_{sol,in,reg}$ under the same C_{sol} could lead to a high solution equilibrium humidity ratio. According to the definition of the solution side latent effectiveness in Eq. (3-18), the absolute value of the denominator in the equation increases with $T_{sol,in,reg}$, resulting in a decrease in the latent effectiveness. Besides, both heat and mass transfer potentials are strengthened, which have been reflected in Fig 5-24, where TDR and MFR are improved with $T_{sol,in,reg}$.
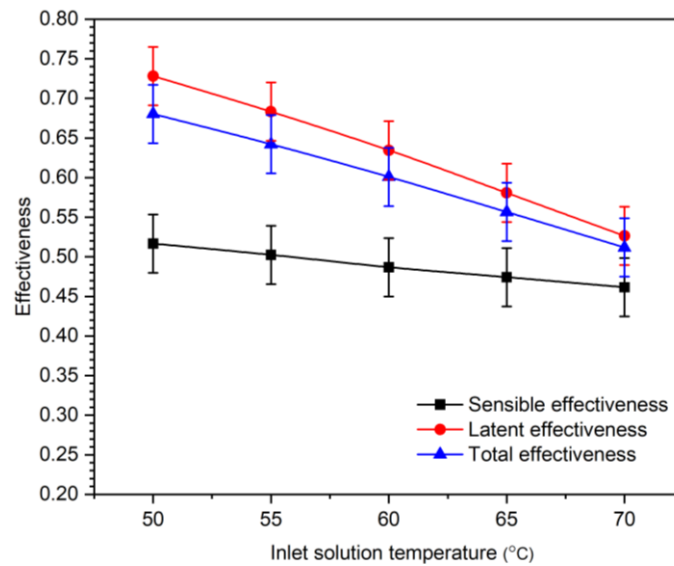

Fig 5-23 Effects of inlet solution temperature ($T_{sol,in,reg}$) on $\varepsilon_{sen,sol}$, $\varepsilon_{lat,sol}$ and $\varepsilon_{tot,sol}$ ($T_{air,in,reg}$=28 °C, $RH_{air,in,reg}$=40 %, $\dot{m}_{air,reg}$=1.91 kg/min, C_{sol}=32 %, $\dot{m}_{sol,reg}$=2 L/min)
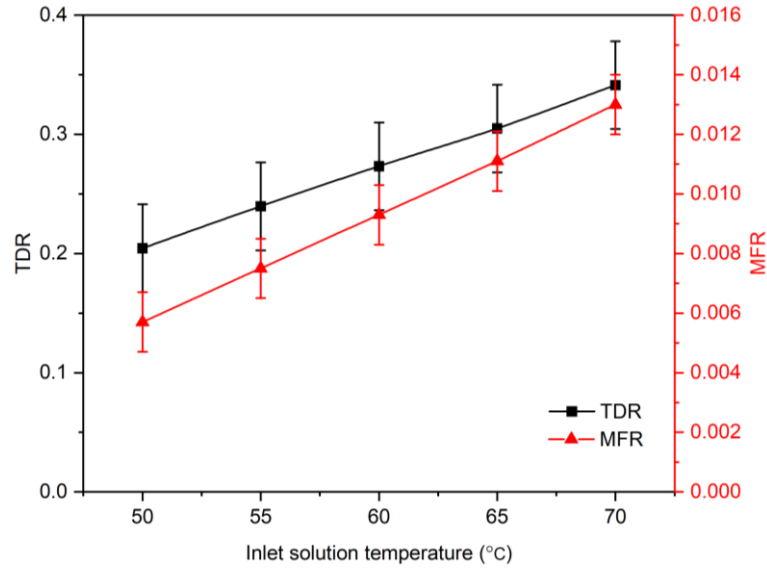
Fig 5-24 Effects of inlet solution temperature ($T_{sol,in,reg}$) on TDR and

MFR($T_{air,in,reg}$=28 °C, $RH_{air,in,reg}$=40 %, $\dot{m}_{air,reg}$=1.91 kg/min, C_{sol}=32 %,

$\dot{m}_{sol,reg}$=2 L/min)

5.3.2.2 Effects of solution concentration

Similar to the dehumidifier, the solution concentration (C_{sol}) also influences the

regeneration performance since it is directly related to surface vapour pressure

as well, with a higher solution concentration producing better dehumidification

results. Variations of the solution side effectiveness, TDR and MFR with C_{sol}

are depicted in Fig 5-25 and Fig 5-26. Under the examined circumstance

($T_{air,in,reg}$=28 °C, $RH_{air,in,reg}$=40 %, $\dot{m}_{air,reg}$=1.91 kg/min, $T_{sol,in,reg}$=60 °C,

$\dot{m}_{sol,reg}$=2 L/min), the ε_{sen} increases by 24.6% from 0.4329 to 0.5394 when the

C_{sol} varies from 26% to 38%, while the ε_{lat} and ε_{tot} rise by 23.2% and 23.5%

from 0.5690 to 0.7011 and 0.5381 to 0.6644, respectively. Based on Eq. (3-17),

increasing the solution concentration would decrease the solution equilibrium

humidity ratio, and then both the solution inlet mass fraction $X_{sol,in}$ and

equilibrium humidity ratio $W_{sol,in}$ in Eq. (3-3) are decreased. These offset

effects interact with each other, and the solution side latent effectiveness increases. Nevertheless, the decrease of the solution vapour pressure would reduce the mass transfer potential, leading to the decrease in MFR. In the meantime, the reduction of the mass transfer would decrease the heat absorption during the evaporation process in the solution channel, leading to an increase in $T_{sol,out,reg}$ and TDR. Besides, to explain the increase of the solution side sensible effectiveness, based on Eq. (3-17), increase $T_{sol,out,reg}$ would decrease the absolute value of the total heat transfer, which is the first term in the numerator. Meanwhile, the second term in the numerator also deteriorates, representing the latent transfer. Consequently, the solution side's sensible effectiveness increases by the offset effect mentioned above.
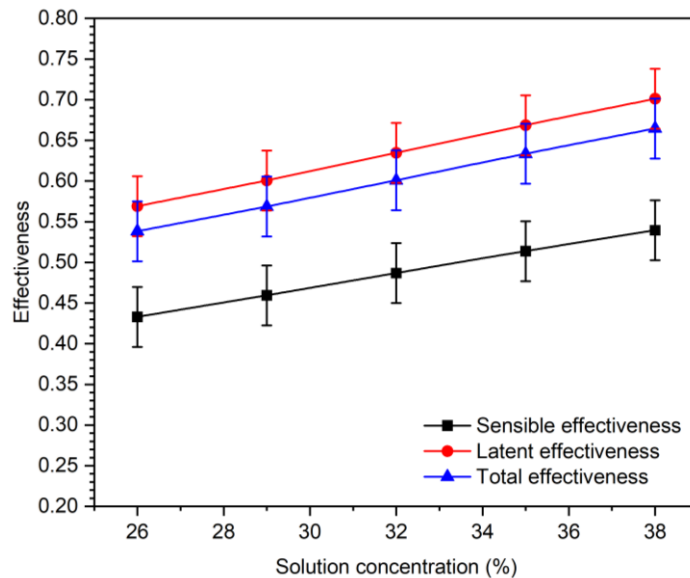
Fig 5-25 Effects of solution concentration (C_{sol}) on $\varepsilon_{sen,sol}$, $\varepsilon_{lat,sol}$ and $\varepsilon_{tot,sol}$ ($T_{air,in,reg}$=28 ℃, $RH_{air,in,reg}$=40 %, $\dot{m}_{air,reg}$=1.91 kg/min, $T_{sol,in,reg}$=60 ℃, $\dot{m}_{sol,reg}$=2 L/min)
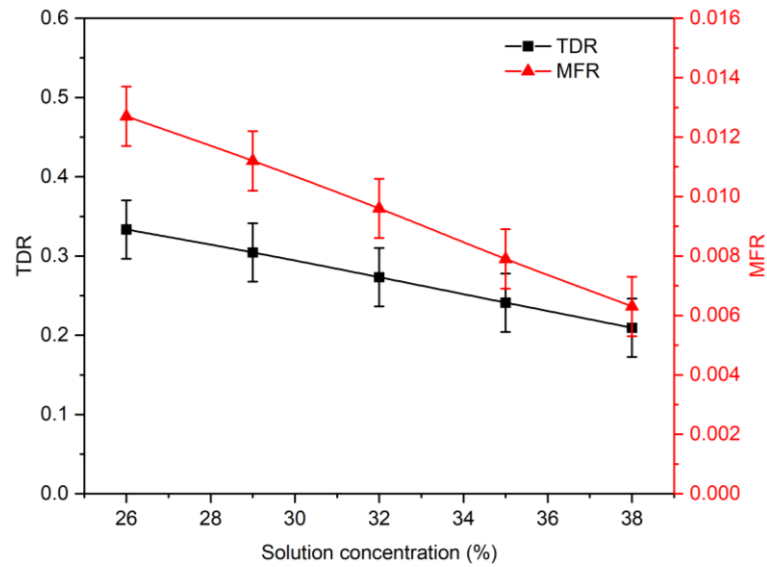
Fig 5-26 Effects of solution concentration (C_{sol}) on TDR and MFR

($T_{air,in,reg}$=28 °C, $RH_{air,in,reg}$=40 %, $\dot{m}_{air,reg}$=1.91 kg/min, $T_{sol,in,reg}$=60 °C,

$\dot{m}_{sol,reg}$=2 L/min)

5.3.2.3 Effects of solution flow rate

The variations of the $\varepsilon_{sen,sol}$, $\varepsilon_{lat,sol}$ and $\varepsilon_{tot,sol}$ and MFR, as well as the TDR

with the $\dot{m}_{sol,reg}$ are shown in Fig 5-27 and Fig 5-28, while maintaining

$T_{air,in,reg}$ =28 °C , $RH_{air,in,reg}$ =40 %, $\dot{m}_{air,reg}$ =1.91 kg/min, C_{sol} =32 %,

$T_{sol,in,reg}$ =60 °C. The $\varepsilon_{sen,sol}$ increases substantially from 0.1867 to 0.5598

when the $\dot{m}_{sol,reg}$ rises from 0.5 L/min to 3.5 L/min. The $\varepsilon_{lat,sol}$ increases

substantially from 0.2679 to 0.7562 when the $\dot{m}_{sol,reg}$ rises from 0.5 L/min to

3.5 L/min. Besides, the $\varepsilon_{tot,sol}$ increases substantially from 0.2495 to 0.7117

when the $\dot{m}_{sol,reg}$ rises from 0.5 L/min to 3.5 L/min. This is because a high

solution flow rate leads to a low solution temperature, and correspondingly a low

outlet air temperature, thus increasing the sensible effectiveness. The latent

effectiveness also increases with the solution flow rate since high mass transfer

capacity and heat transfer coefficient will be obtained as the solution flow rate

increases [262]. It can be seen from Error! Reference source not found. that the

MFR increases from 0.004g/s to 0.0114g/s as well. This is mainly because that

increasing the solution mass flow rate would raise the desiccant mass flow rate

as well, thereby improving the MFR. It is also noted that the TDR enhances from

122W to 312W since the heat capacity rate of the solution becomes higher with

the solution flow rate, causing less temperature reduction of the desiccant

solution during the phase change process [92], representing the solution outlet

temperature is increased, and TDR is reduced.
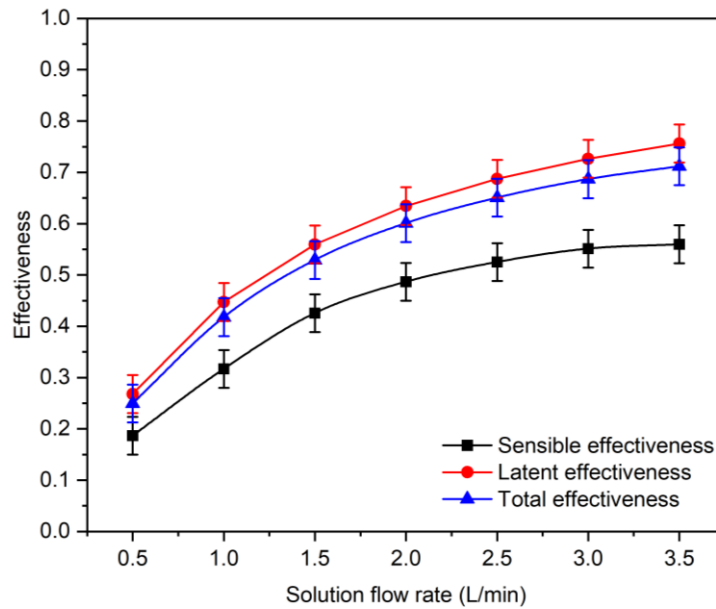
Fig 5-27 Effects of solution flow rate ($\dot{m}_{sol,reg}$) on $\varepsilon_{sen,sol}$, $\varepsilon_{lat,sol}$ and $\varepsilon_{tot,sol}$

($T_{air,in,reg}$=28 °C, $RH_{air,in,reg}$=40 %, $\dot{m}_{air,reg}$=1.91 kg/min, C_{sol}=32 %,
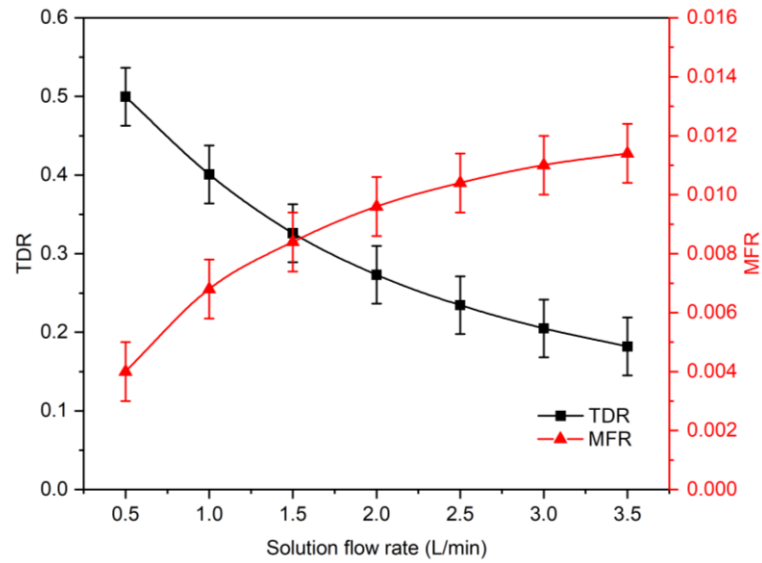
$T_{sol,in,reg}$=60 °C)

Fig 5-28 Effects of solution flow rate ($\dot{m}_{sol,reg}$) on TDR and MFR

($T_{air,in,reg}$=28 °C, $RH_{air,in,reg}$=40 %, $\dot{m}_{air,reg}$=1.91 kg/min, C_{sol}=32 %,

$T_{sol,in,reg}$=60 °C)

5.4 Complete LDD system performance

5.4.1 System optimal operating conditions

This section will determine the system's optimal operation strategy according to

the parametric analysis in order to optimize the thermal and energy efficiency of

the complete LDD system. The system variable parameters mainly include 1)

solution inlet temperature of the dehumidifier, 2) solution concentration of the

dehumidifier, 3) inlet water mass flow rate of the cooling box unit, 4) inlet water

temperature of the cooling box unit and 5) boiler temperature, where the

optimisation strategy follows three principles as listed below:

- To maximise the whole system's cooling and dehumidification efficiency
  by balancing the air-cooling demand;

- To reduce the system complexity, additional cooling sources, fan and
  pump consumption;

170

- To reduce the system operation cost by avoiding extremely high solution concentration;

- To avoid regeneration heat increase significantly.

In order to determine the system's optimal operating conditions, the complete system operating performance under different inlet variables is presented in Fig 5-29. As seen in Fig 5-29 (a), although reducing the cold water temperature can significantly improve the dehumidifier's effectiveness, additional cooling sources are required to cool down the cold water, thereby reducing higher cooling energy consumption. Compared with the cold water temperature drop, improving the inlet cold water mass flow rate of the cooling box unit becomes an alternative to enhance the total effectiveness. In practice, additional cooling systems will also increase the cost and complexity of the complete system and additional cooling energy consumption. According to the literature [264], the range of housing tap water temperature is between 16℃ and 20℃, with an average temperature of 18℃ in most Mediterranean regions during summertime. Meanwhile, it is figured out that the total effectiveness does not have an obvious change once exceeding the inlet cold water temperature of 18℃, however, it is sensitive to the increase of inlet water mass flow rate. According to the analysis of the critical value of cold water mass flow rate, it is found that selecting the optimal cold water mass flow rate of 0.017 kg/s could effectively improve the total effectiveness and avoid massive pump energy consumption and water cost. It is observed from Fig 5-29 (b) that increasing the solution concentration of the dehumidifier will increase the total effectiveness. Besides, it is figured out that the total effectiveness considerably increases before C_{sol} reaches 32% and slowly afterwards. Nevertheless, extremely high C_{sol} will increase the system

171

operation cost and crystallization risk. Therefore, $C_{sol} = 32\%$ is selected as the optimal solution concentration for the dehumidification system. Moreover, it is discovered that reducing the inlet solution temperature of the dehumidifier will increase the total effectiveness before it reaches 18 ℃. To avoid additional cooling energy consumption, tap water is used to lower the inlet solution temperature to 18 ℃.

It is observed from Fig 5-29 (c) that reducing the inlet solution temperature of the regenerator could enlarge the sensible, latent and total effectiveness of the regenerator. However, the lower the inlet solution temperature, the lower MFR. In practice, most regeneration heat will be supplied by renewables instead of traditional boilers, where most renewable technologies could provide hot water temperatures of 55-60 °C, such as solar collectors, PV/T, etc. Therefore, the regeneration temperature of 55 ℃ is selected to balance the regenerator's effectiveness and regeneration heat capacity and reduce the regeneration thermal energy consumption.

It should be noted that the above-mentioned optimal operating conditions are for the tested system and could be generalised in the future. The system optimisation serves as the guidance for selection of optimal operating conditions and is used for the complete system COP performance and building application in Chapter 6.
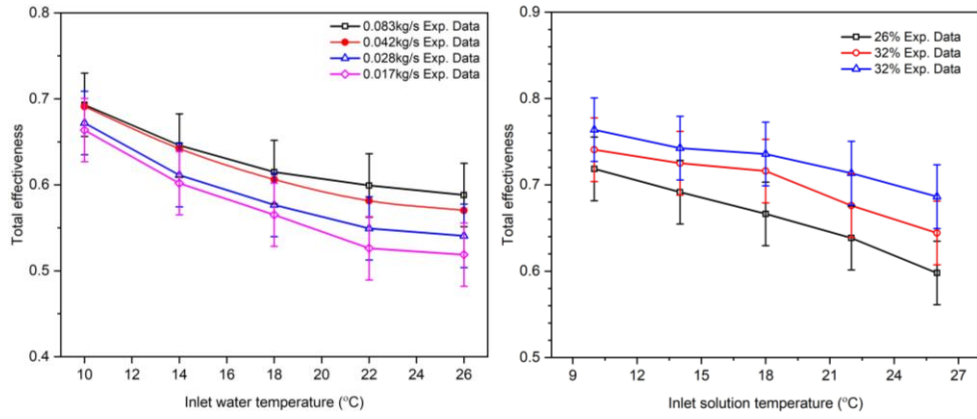
(a)

(b)
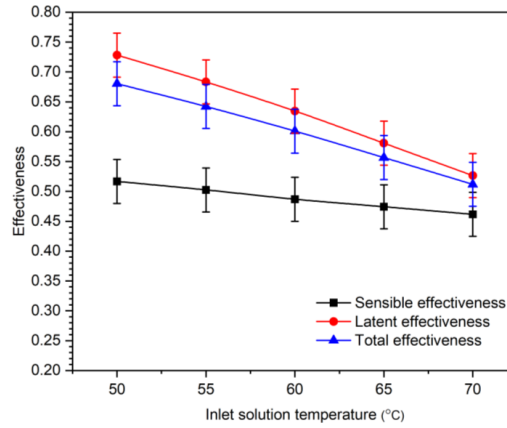
(c)

Fig 5-29 Complete system operating performance under different inlet variables: (a) $T_{w,in}$ and $\dot{m}_w$ variations with ε_{tot} of the cooling box unit; (b) $T_{sol,in}$ and C_{sol} variations with ε_{tot} of the dehumidifier and (c) Variation of $T_{sol,in,reg}$ with $\varepsilon_{sen,sol}$, $\varepsilon_{lat,sol}$ and $\varepsilon_{tot,sol}$ of the regenerator

5.4.2 Outlet air temperature and relative humidity

The variations of supply air temperature $T_{air,out,deh}$ and relative humidity $RH_{air,out,deh}$ with the inlet air relative humidity $RH_{air,in,deh}$ under different inlet air temperature $T_{air,in,deh}$ as well as the 3D diagram are shown in Fig 5-30 and Fig 5-31, respectively. It is figured out that the $T_{air,out,deh}$ decreases from 33.6 °C when $T_{air,in,deh} = 40°C$ and $RH_{air,in,deh} = 80\%$ to 26.7 °C when

$T_{air,in,deh} = 28°C$ and $RH_{air,in,deh} = 40\%$. Besides, under the same $RH_{air,in,deh}$, the $T_{air,out,deh}$ drops with the decreasing $T_{air,in,deh}$. Meanwhile, under the same $T_{air,in,deh}$, the $T_{air,out,deh}$ has a similar trend where it decreases with the lower $RH_{air,in,deh}$. Thus, increasing both the $T_{air,in,deh}$ and $RH_{air,in,deh}$ have the same influences on the increasing $T_{air,out,deh}$. Moreover, it is found that the decrease of the $T_{air,out,deh}$ is evident when the $RH_{air,in,deh}$ is at a relatively low level, and the temperature difference between the air at the inlet and outlet is smaller when the $RH_{air,in,deh}$ is at a relatively high level. This is due to the fact that more air moisture needs to be removed at higher inlet air temperature and relative humidity.

It is figured out that the $RH_{air,out,deh}$ varies between 46.7% to 53.4% when $T_{air,in,deh}$ and $RH_{air,in,deh}$ range from 28°C - 40°C and 40% - 80%, respectively. The highest $RH_{air,out,deh}$ of 53.4% occurs when $T_{air,in,deh} = 28°C$ and $RH_{air,in,deh} = 80\%$, while the lowest $RH_{air,out,deh}$ of 46.7% when $T_{air,in,deh} = 40°C$ and $RH_{air,in,deh} = 40\%$. Under the same $T_{air,in,deh}$, the $RH_{air,out,deh}$ decreases with the drop of $RH_{air,in,deh}$, since less humidity removal is required. Although under the same $RH_{air,in,deh}$, the $RH_{air,out,deh}$ rises with the drop of $T_{air,in,deh}$, the $RH_{air,out,deh}$ only has a slight increase. For instance, the $RH_{air,out,deh}$ rises from 50.5% to 53.4%, with the $T_{air,in,deh}$ drops from 40°C to 28°C under $RH_{air,in,deh} = 80\%$. Under the same $RH_{air,in,deh}$, the decrease of the $T_{air,in,deh}$ represents an obvious decline in absolute humidity. Therefore, humidity removal is less required with the lower $T_{air,in,deh}$.

Based on Fig 5-30 and Fig 5-31, the correlations are derived using the linear regression method:

$$T_{air,out,deh} = \left(-0.0001 \times RH_{air,in,deh}^2 + 0.0098 \times RH_{air,in,deh} + 0.0809\right) \times$$

$$T_{air,in,deh} + \left(0.0041 \times RH_{air,in,deh}^2 - 0.3258 \times RH_{air,in,deh} + 24.448\right)$$

$$(5\text{-}1)$$

$$RH_{air,out,deh} = \left(0.0002 \times RH_{air,in,deh}^2 - 0.022 \times RH_{air,in,deh} + 0.2375\right) \times$$

$$T_{air,in,deh} + \left(-0.0041 \times RH_{air,in,deh}^2 + 0.5077 \times RH_{air,in,deh} + 45.862\right)$$

$$(5\text{-}2)$$
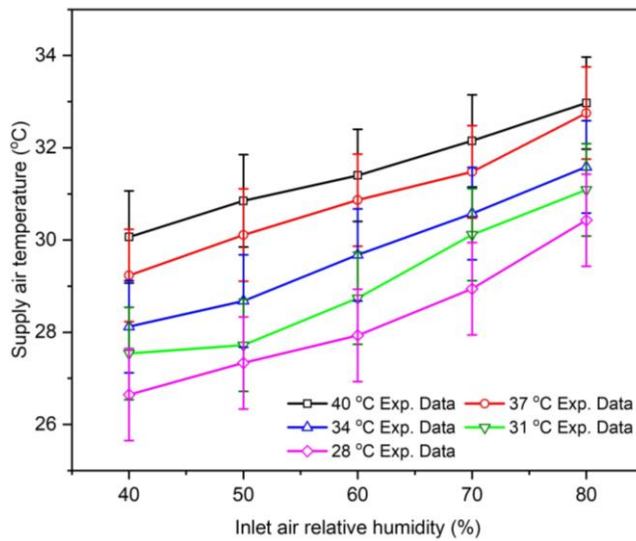
Fig 5-30 Variations of $T_{air,out,deh}$ with $RH_{air,in,deh}$ under different $T_{air,in,deh}$
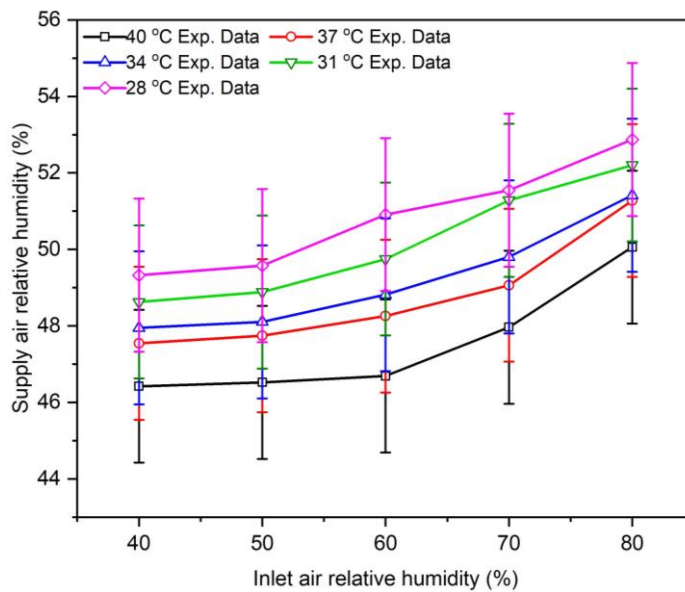
Fig 5-31 Variations of $RH_{air,out,deh}$ with $RH_{air,in,deh}$ under different $T_{air,in,deh}$

5.4.3 Complete system cooling capacity and COP

The variations of sensible cooling capacity Q_c, latent dehumidification capacity Q_{deh} and total cooling capacity Q_{tot} with the inlet air relative humidity $RH_{air,in,deh}$ under different inlet air temperature $T_{air,in,deh}$ are shown in Fig 5-32, Fig 5-33 and Fig 5-34, respectively. It is figured out that the Q_c decreases from 138.0 W when $T_{air,in,deh} = 40°C$ and $RH_{air,in,deh} = 80\%$ to 27.3 W when $T_{air,in,deh} = 28°C$ and $RH_{air,in,deh} = 40\%$. The Q_{deh} decreases from 885.8 W when $T_{air,in,deh} = 40°C$ and $RH_{air,in,deh} = 80\%$ to -68.4 W when $T_{air,in,deh} = 28°C$ and $RH_{air,in,deh} = 40\%$. The Q_{tot} decreases from 1023.7 W when $T_{air,in,deh} = 40°C$ and $RH_{air,in,deh} = 80\%$ to -41.1 W when $T_{air,in,deh} = 28°C$ and $RH_{air,in,deh} = 40\%$. Especially, it is figured out that the Q_{tot} is negative only when $T_{air,in,deh} = 28°C$ and $RH_{air,in,deh} = 40\%$ since the complete LDD system mainly aims at air dehumidification and sole pre-cooling. Therefore, the Q_{tot} is negative when the Q_c and Q_{deh} are 27.3 W and -68.4 W under $T_{air,in,deh} = 28°C$ and $RH_{air,in,deh} = 40\%$.
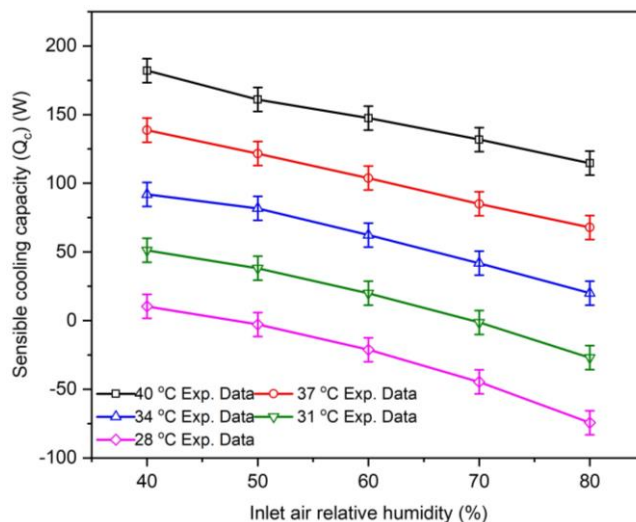
Fig 5-32 Variations of Q_c with $RH_{air,in,deh}$ under different $T_{air,in,deh}$
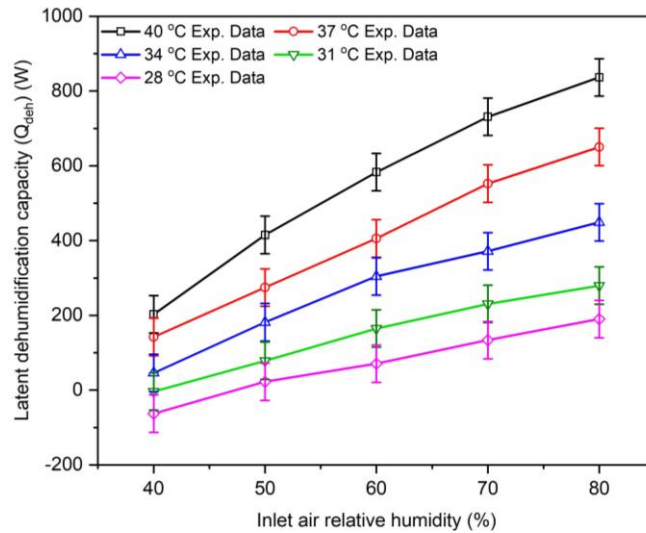
Fig 5-33 Variations of Q_{deh} with $RH_{air,in,deh}$ under different $T_{air,in,deh}$
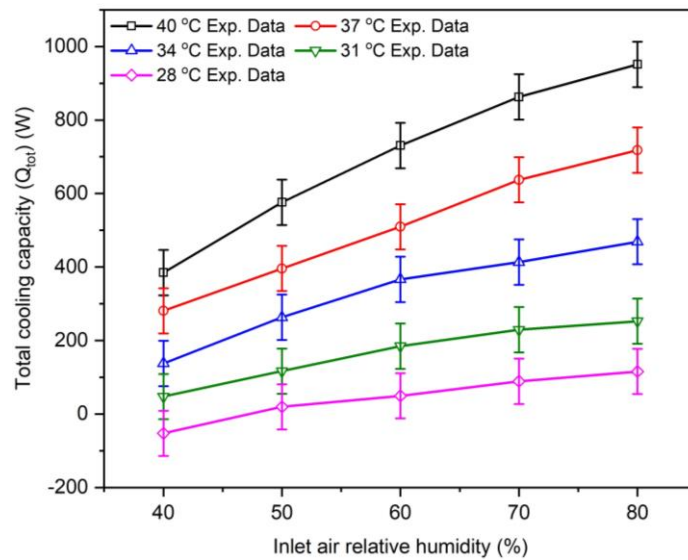
Fig 5-34 Variations of Q_{tot} with $RH_{air,in,deh}$ under different $T_{air,in,deh}$

The variations of thermal COP (COP_{th}), electrical COP (COP_{ele}) and total COP (COP_{tot}) with the inlet air relative humidity $RH_{air,in,deh}$ under different inlet air temperature $T_{air,in,deh}$ are shown in Fig 5-35, Fig 5-36 and Fig 5-37, respectively. It is figured out that the COP_{th} decreases from 1.157 when $T_{air,in,deh} = 40°C$ and $RH_{air,in,deh} = 80\%$ to 0.045 when $T_{air,in,deh} = 28°C$ and $RH_{air,in,deh} = 40\%$. The COP_{ele} decreases from 7.068 when $T_{air,in,deh} =$

40°C and $RH_{air,in,deh} = 80\%$ to 0.198 when $T_{air,in,deh} = 28°C$ and

$RH_{air,in,deh} = 40\%$. The COP_{tot} decreases from 0.983 when $T_{air,in,deh} = 40°C$

and $RH_{air,in,deh} = 80\%$ to 0.030 W when $T_{air,in,deh} = 28°C$ and $RH_{air,in,deh} =$

40%. In general, it is figured out that the COP_{th}, COP_{ele} and COP_{tot} rise with

the increase of both the $T_{air,in,deh}$ and $RH_{air,in,deh}$.

The correlations are derived using the linear regression method:

$$COP_{ele} = \left(-9 \times 10^{-4} \times RH_{air,in,deh} + 0.3988\right) \times T_{air,in,deh} + (0.0989 \times$$

$$RH_{air,in,deh} - 13.916) \tag{5-3}$$

$$COP_{th} = \left(-7 \times 10^{-5} \times RH_{air,in,deh} + 0.0615\right) \times T_{air,in,deh} + (0.013 \times$$

$$RH_{air,in,deh} - 2.1186) \tag{5-4}$$

$$COP_{tot} = \left(-7 \times 10^{-5} \times RH_{air,in,deh} + 0.0532\right) \times T_{air,in,deh} + (0.0115 \times$$

$$RH_{air,in,deh} - 1.841) \tag{5-5}$$
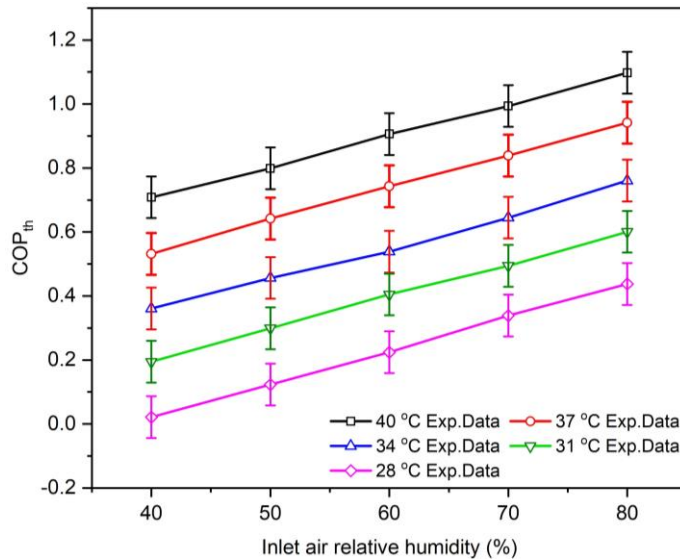
Fig 5-35 Variations of COP_{th} with $RH_{air,in,deh}$ under different $T_{air,in,deh}$
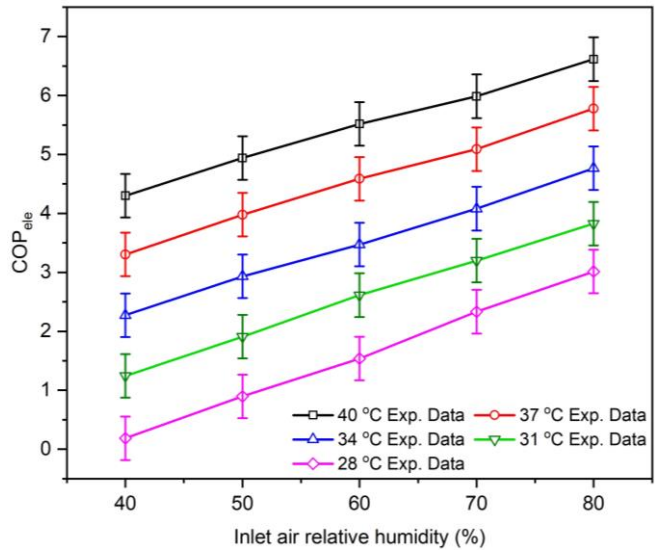
Fig 5-36 Variations of COP_{ele} with $RH_{air,in,deh}$ under different $T_{air,in,deh}$
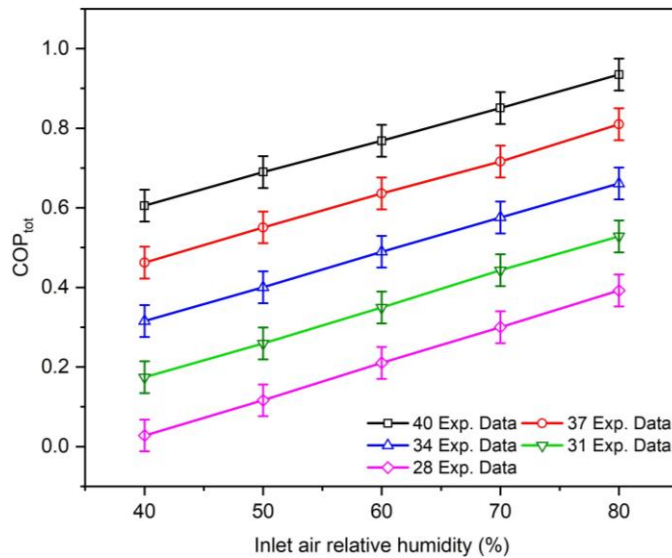
Fig 5-37 Variations of COP_{tot} with $RH_{air,in,deh}$ under different $T_{air,in,deh}$

5.5 Summary

From the above-mentioned analysis of experimental data on the performance of the heat pipe internally-cooled liquid desiccant dehumidification (HP-ICMLDD), membrane-based regeneration and the complete membrane-based liquid desiccant dehumidification systems, the following conclusions can be drawn as:

1. The dehumidification (HP-ICMLDD) system (**section 5.2**):

- The dehumidification performance is significantly impacted by the internal cooling of the heat pipe, where reducing the cold water temperature of the cooling box could considerably lower the desiccant solution temperature, thereby improving the dehumidifier performance, however, decreasing water temperature will not significantly improve the sensible effectiveness when the water temperature is higher than 22°C;

- The dehumidification and cooling performance can be drastically improved by increasing the cold water flow rate in the cooling box;

- All effectiveness are sensitive to solution concentration C_{sol} increment only with a higher inlet solution temperature $T_{sol,in}$, whereas inlet solution temperature drop plays a more significant role;

2. The membrane-based regeneration system (**section 5.3**):

- The solution side's sensible effectiveness is insensitive to inlet solution temperature at the regenerator when the solution concentration is high, while latent effectiveness is sensible to inlet solution temperature when the solution concentration is low. Thus, it implies that the regenerator benefits from the high solution temperature due to enhanced re-concentration and cooling effects.

3. The complete LDD system (**section 5.4**):

- In order to optimize the thermal and energy efficiency of the complete system, the system's optimal operating conditions have been determined based on the performance analysis of the dehumidifier and regenerator. For the dehumidifier, the optimal inlet cold water temperature, mass flow rate, solution temperature and solution concentration are determined as

18°C, 0.017 kg/s, 18°C and 32%, respectively; For the regenerator, the optimal solution temperature is determined as 55°C.

- The decrease of the $T_{air,out,deh}$ is evident when the $RH_{air,in,deh}$ is at a relatively low level, and the temperature difference between the air at the inlet and outlet is smaller when the $RH_{air,in,deh}$ is at a relatively high level.

- Although under the same $RH_{air,in,deh}$, the $RH_{air,out,deh}$ rises with the drop of $T_{air,in,deh}$, the $RH_{air,out,deh}$ only has a slight increase.

- The correlations of $T_{air,out,deh}$ and $RH_{air,out,deh}$ with the $T_{air,in,deh}$ and $RH_{air,in,deh}$ are derived as below:

$$T_{air,out,deh} = \left(-0.0001 \times RH_{air,in,deh}{}^2 + 0.0098 \times RH_{air,in,deh} + 0.0809\right) \times$$

$$T_{air,in,deh} + \left(0.0041 \times RH_{air,in,deh}{}^2 - 0.3258 \times RH_{air,in,deh} + 24.448\right)$$

$$RH_{air,out,deh} = \left(0.0002 \times RH_{air,in,deh}{}^2 - 0.022 \times RH_{air,in,deh} + 0.2375\right) \times$$

$$T_{air,in,deh} + \left(-0.0041 \times RH_{air,in,deh}{}^2 + 0.5077 \times RH_{air,in,deh} + 45.862\right)$$

- The COP_{th}, COP_{ele} and COP_{tot} rise with the increase of both the $T_{air,in,deh}$ and $RH_{air,in,deh}$.

- The correlations of COP_{th}, COP_{ele} and COP_{tot} with the $T_{air,in,deh}$ and $RH_{air,in,deh}$ are derived as below:

$$COP_{th} = \left(-7 \times 10^{-5} \times RH_{air,in,deh} + 0.0615\right) \times T_{air,in,deh} + (0.013 \times$$

$$RH_{air,in,deh} - 2.1186)$$

$$COP_{ele} = \left(-9 \times 10^{-4} \times RH_{air,in,deh} + 0.3988\right) \times T_{air,in,deh} + (0.0989 \times$$

$$RH_{air,in,deh} - 13.916)$$

$$COP_{tot} = \left(-7 \times 10^{-5} \times RH_{air,in,deh} + 0.0532\right) \times T_{air,in,deh} + (0.0115 \times$$

$$RH_{air,in,deh} - 1.841)$$

Chapter 6 Application of integrated liquid desiccant air-conditioning system in residential buildings

6.1 Introduction

This chapter describes the applications of the integrated liquid desiccant air-conditioning (ILDAC) system for multi-family terraced houses under subtropical and humid climatic conditions in the Mediterranean regions. The reference building has been established in **section 3.5.2** as the case study to investigate the performance of the ILDAC system. The building baseline will be analysed in **section 6.2**, with its hourly and annual cooling, dehumidification and heating demand in Methoni, Rome and Barcelona. The energy performance of the ILDAC system will be discussed in **section 6.3**, compared with the complete LDD and the AWHP system. Besides, the hourly electrical and thermal COP of the complete LDD system in three locations will also be discussed. Moreover, the building energy/carbon performance of the ILDAC system will be discussed in **section 6.4**, including the COP comparison with the complete LDD and the AWHP system, as well as the electricity/thermal demand and generation. In the end, the initial investment, annual bill, discounted payback period, annual return on investment and the real rate of return of the ILDAC system regarding the economic parameters in three locations will be analysed in **section 6.5**. Moreover, the sensitivity analysis will be conducted with the variation of the inflation rate, bank interest rate, grid electricity tariff and PV electricity export tariff increasing rates.

6.2 Building baseline

According to the simulation in IES VE, the annual cooling, dehumidification, and heating demands of the baseline model in Mehtoni, Rome, and Barcelona

have been calculated, as shown in Table 6-1. The maximum cooling, dehumidification, and heating demands are 23.97 MWh in Rome, 25.79 MWh in Barcelona and 79.43 MWh in Rome, respectively. Besides, the hourly cooling, dehumidification and heating demands of the baseline model in Methoni, Rome and Barcelona are also presented in Fig 6-1. The cooling period of Methoni, Rome and Barcelona is from June to October, June to September and June to September, with the peak value of 29.78 kW, 29.25 kW and 23.08 kW, respectively. The dehumidification period of Methoni, Rome, and Barcelona is from June to September, June to September and May to September, with the peak value of 20.40 kW, 17.33 kW and 24.47 kW, respectively. The heating period of Methoni, Rome and Barcelona is from November to April, October to May and November to May, with the peak value of 38.02 kW, 48.20 kW and 35.33 kW, respectively. Moreover, the cooling, dehumidification and heating demand percentage accounted for the annual total energy consumption is shown in Fig 6-2. It is figured out that the heating demand accounts for 49.2%, 68.4% and 58.5% in Methoni, Rome and Barcelona, respectively. Besides, the cooling demand accounts for 25.3%, 20.6% and 16.8% in Methoni, Rome and Barcelona, respectively. In addition, the dehumidification demand accounts for 25.5%, 10.9% and 24.7% in Methoni, Rome and Barcelona, respectively. Based on Fig 6-2, the dehumidification demands in Methoni and Barcelona are higher than their cooling demands. However, the cooling demands exceed the dehumidification demands in Rome.

Table 6-1 The cooling, dehumidification and heating demand of the baseline model in Methoni, Rome and Barcelona

	Cooling demand (MWh)	Dehumidification demand (MWh)	Heating demand (MWh)

Methoni	23.81	24.01	46.26
Rome	23.97	12.69	79.43
Barcelona	17.55	25.79	61.1
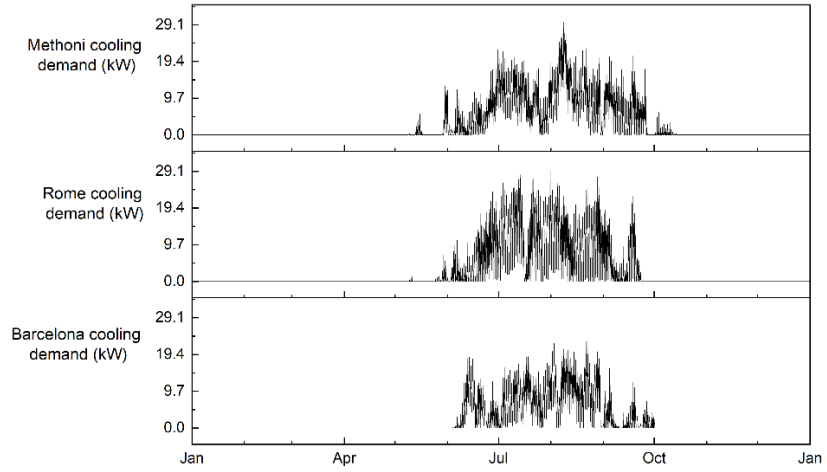
(a)
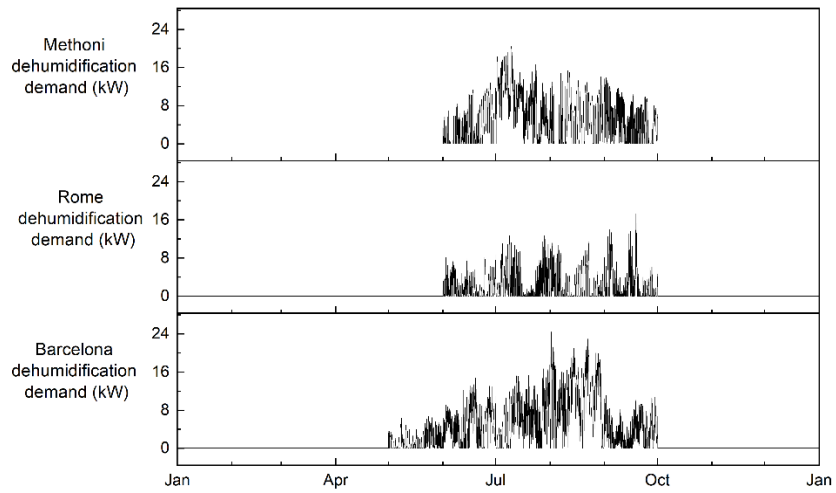
(b)
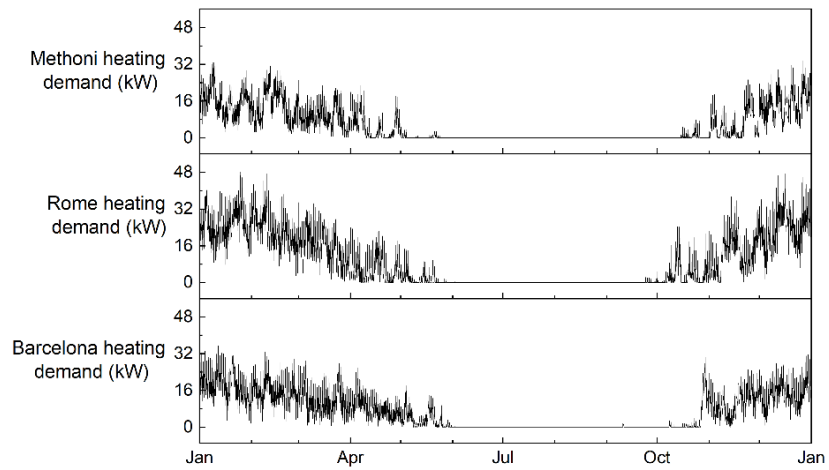
(c)

Fig 6-1 The hourly (a) cooling, (b) dehumidification and (c) heating demand of the baseline model in Methoni, Rome and Barcelona

(a) Methoni

(b) Rome
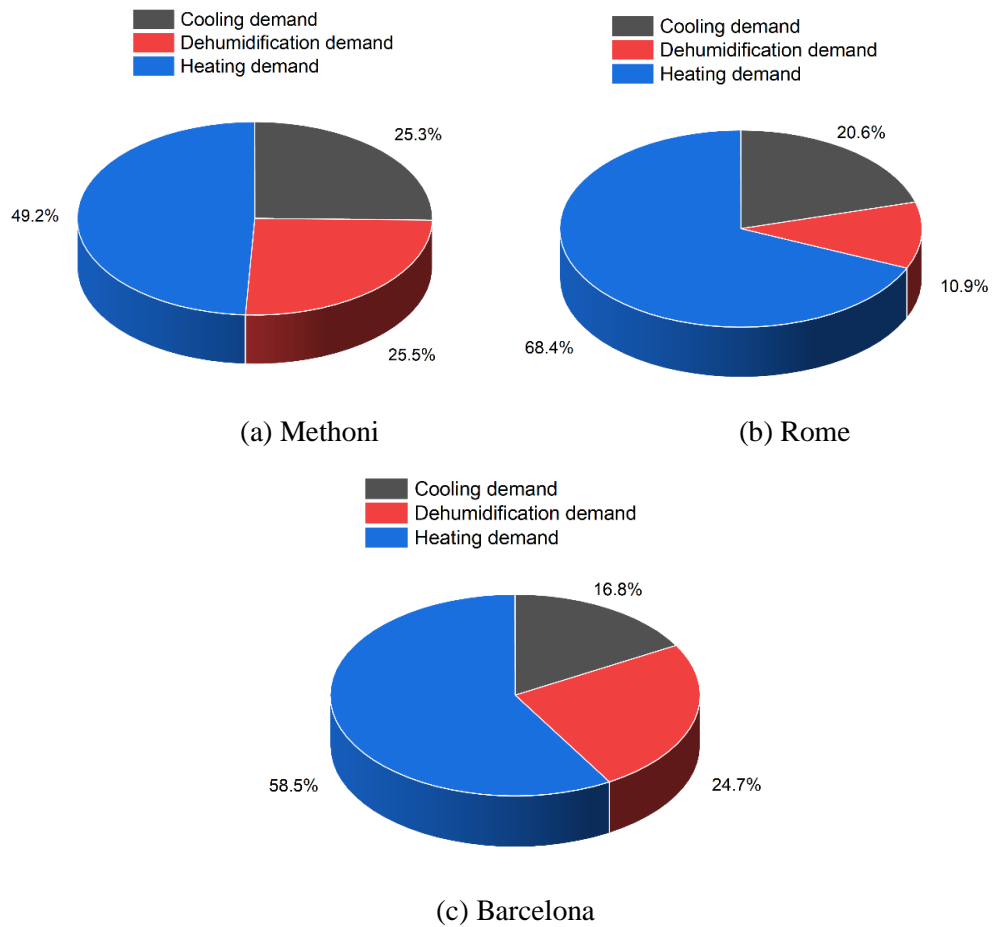
(c) Barcelona

Fig 6-2 The cooling, dehumidification and heating demand percentage of the baseline model in Methoni, Rome and Barcelona

6.3 Integrated system energy performance

Based on the simulation method, the variation of the AWHP system cooling COP with the inlet air temperature and relative humidity are calculated and shown in Fig 6-3. It is found that the cooling COP (COP_C) increases with the increasing inlet air temperature, however, higher air relative humidity could weaken its COP performance. For example, the COP_C increases from 1.76 to 2.29, with the inlet air temperature increasing from 28 ℃ to 40 ℃ under the

inlet air relative humidity of 40%. However, the COP_C declines from 2.29 to 1.94, with the inlet air relative humidity increasing from 40% to 80% when the inlet air temperature is 40 ℃. Besides, the heat released from the heat pump condenser will be utilised as the regeneration heat for the regenerator in the complete LDD system. Therefore, the variation of the AWHP system heating COP (COP_H) with the inlet air temperature and relative humidity also calculated, as shown in Fig 6-4. Furthermore, the correlation of the COP_C and COP_H with the inlet air temperature and relative humidity are derived using the linear regression method:

$$COP_C = (-0.0003 \times T_{air,in} + 0.0032) \times RH_{air,in} + (0.056 \times T_{air,in} + 0.4011) \tag{6-1}$$

$$COP_H = (-0.0003 \times T_{air,in} - 0.0012) \times RH + (0.0413 \times T_{air,in} + 2.1638) \tag{6-2}$$
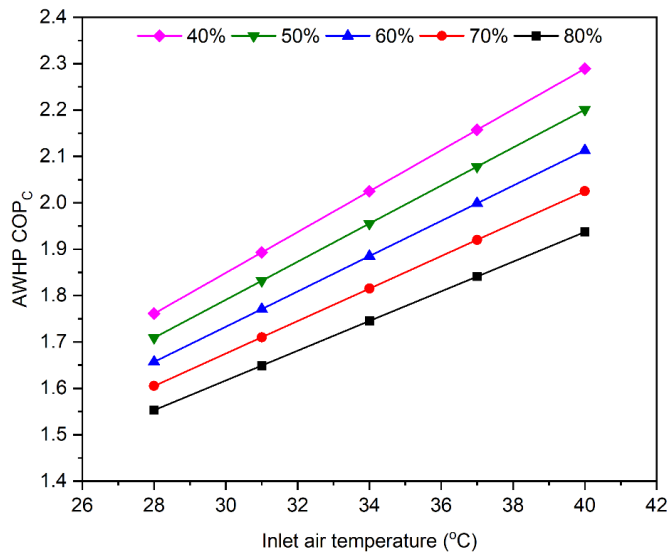
Fig 6-3 The variation of the AWHP system cooling COP with the inlet air temperature and relative humidity
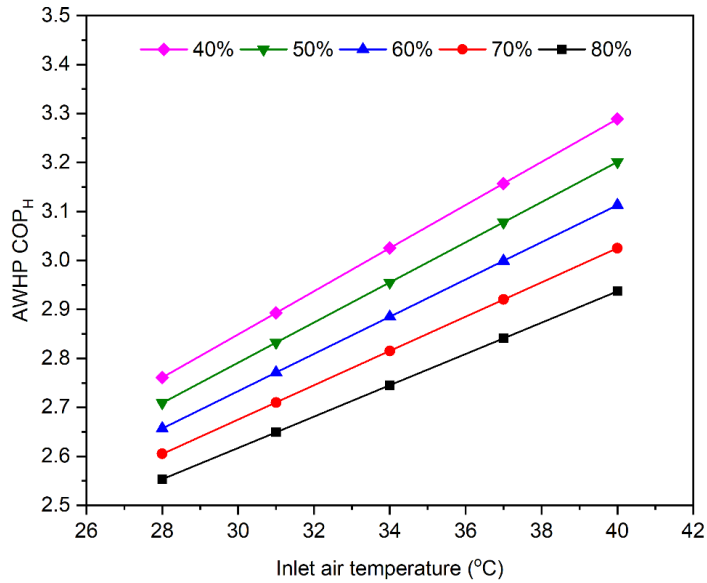
Fig 6-4 The variation of the AWHP system heating COP with the inlet air temperature and relative humidity

In addition, by integrating the AWHP, complete LDD, PVT, and hot water storage systems in EnergyPro simulation software with the derived COP correlations of AWHP and complete LDD system, the variation of the ILDAC system COP with the inlet air temperature and relative humidity is depicted in Fig 6-5. Differing from the AWHP system, the ILDAC system COP rises with the increasing inlet air relative humidity. For instance, the ILDAC system COP increases from 5.16 to 10.24 with the inlet air relative humidity increasing from 40% to 80% when the inlet air temperature is 40 ℃ due to that the air inlet relative humidity of the AWHP system is considerably reduced by the dehumidification process in the HP-ICMLDD. This is also attributed to the fact that the electricity demand of the heat pump compressor is supplied by the PVT module. Moreover, the ILDAC system COP also increases with the rise of the inlet air temperature. For example, the ILDAC system COP increases from 6.47 to 10.24 with the inlet air temperature increasing from 28 ℃ to 40 ℃ when the inlet air relative humidity is 80%.

187
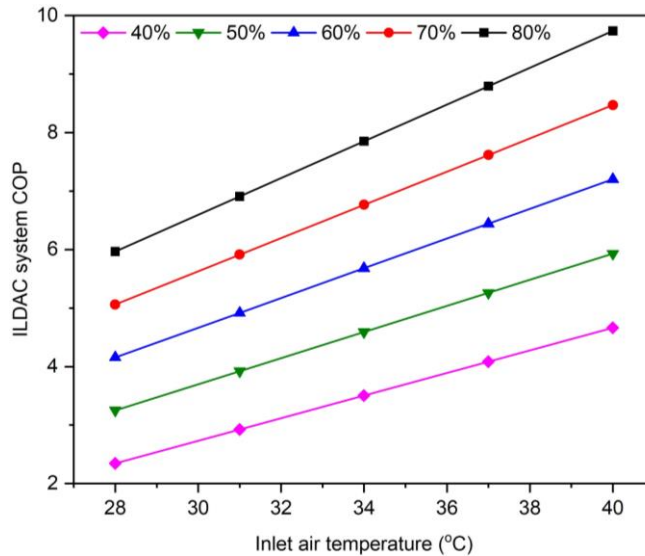
Fig 6-5 The variation of the ILDAC system COP with the inlet air temperature and relative humidity

6.4 Building energy/carbon performance

Integrating the ILDAC system with the cooling, dehumidification and heating demands of the RBs in EnergyPro simulation software, the building energy and carbon emission performances have been calculated in Table 6-2. The net electricity consumption is calculated by the differences between the ILDAC and AWHP electricity demands and the PVT electricity generation, which can also be calculated by the differences between the imported electricity from grid and exported electricity to grid. It is found that the maximum and minimum net electricity consumptions are 26.6 MWh and 16.4 MWh in Rome and Methoni, respectively. Besides, most PVT electricity generation is consumed by the ILDAC and AWHP systems with 12.3 MWh, 9.4 MWh and 17.1 MWh in Barcelona, Rome and Methoni, respectively, where the electricity is exported to the grid is 3.5 MWh, 3.4 MWh and 3.6 MWh.

Besides, the pre-retrofit energy consumption is summarized in Table 6-3 with the space heating by natural gas combi-boiler, space cooling by the AWHP

188

system and net energy consumption. By multiplying the imported grid electricity and natural gas energy consumption with the carbon emission intensity, the total carbon emission is calculated in Table 6-4, with the carbon reduction rate (CRR) calculated. It is figured out that the carbon emission is curtailed from 29.5 tCO_2 to 3.3 tCO_2 (CRR=88.8%) in Barcelona, 38.0 tCO_2 to 6.0 tCO_2 (CRR=84.3%) in Rome and 32.1 tCO_2 to 7.4 tCO_2 (CRR=76.9%) in Methoni. Moreover, by comparing the pre-retrofit net energy and post-retrofit net electricity consumption, the energy reduction rate (ERR) is calculated as 77.6%, 74.8% and 78.8% in Barcelona, Rome and Methoni.

Table 6-2 Post-retrofit building energy consumption

	The ILDAC system cooling electricity demand (MWh)	AWHP heating electricity demand (MWh)	PVT electricity generation (MWh)	PVT thermal heat generation (MWh)	Net electricity consumption (MWh)	Imported electricity from grid (MWh)	Exported electricity to grid (MWh)
Barcelona	21.5	14.1	15.8	39.7	19.8	23.3	3.5
Rome	16.6	22.8	12.8	36.6	26.6	30.0	3.4
Methoni	26.4	10.7	20.7	47.0	16.4	20.0	3.6

Table 6-3 Pre-retrofit building energy consumption

	Space heating by natural gas boiler (MWh)	Space cooling by AWHP (MWh)	Net energy consumption (MWh)
Barcelona	65.0	23.3	88.3
Rome	84.5	21.1	105.6
Methoni	49.3	28.2	77.5

Table 6-4 The pre- and post-retrofit building energy/carbon performance

	Pre-retrofit carbon emission (tCO2)	Post-retrofit carbon emission (tCO2)	Energy reduction rate (ERR)	Carbon reduction rate (CRR)
Barcelona	29.5	3.3	77.6%	88.8%
Rome	38.0	5.9	74.8%	84.3%

Methoni	32.1	7.4	78.8%	76.9%

The cooling and dehumidification demand, as well as the COP of different systems in Methoni, Rome and Barcelona are shown in Fig 6-6. With the input of the cooling and dehumidification demands in three locations obtained from IES VE simulation software, the EnergyPro is used to compare the energy efficiency applying the ILDAC (COP_{tot}), complete LDD (COP_{tot}) and AWHP (COP_C) systems. It is found that the ILDAC system could achieve higher COP of 6.41, 8.14 and 7.52, which is significantly higher than both the complete LDD and AWHP systems. Moreover, by looking into the detail of the ILDAC system, the electricity demand and renewable electricity generation in three locations are illustrated in Fig 6-7. Besides, the regeneration heat demand and thermal generation by the PVT and AWHP systems are depicted in Fig 6-8.
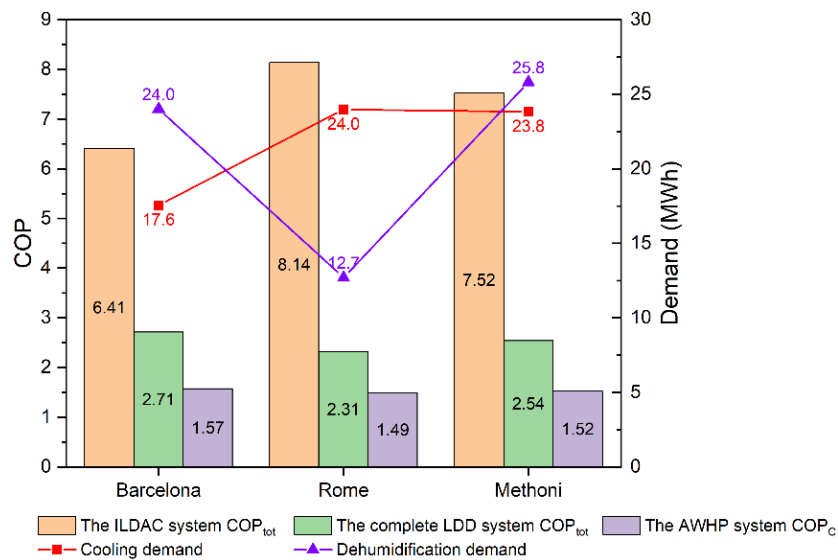
Fig 6-6 The cooling and dehumidification demand and COP of different systems in Methoni, Rome and Barcelona
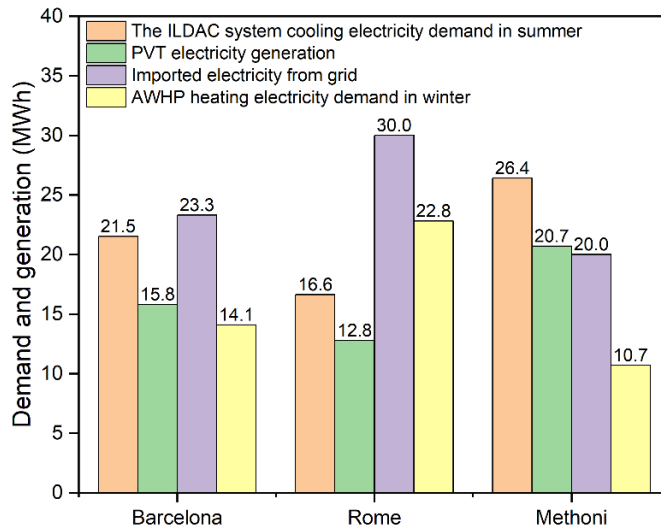
Fig 6-7 The electricity demand and generation of the ILDAC system in Methoni, Rome and Barcelona
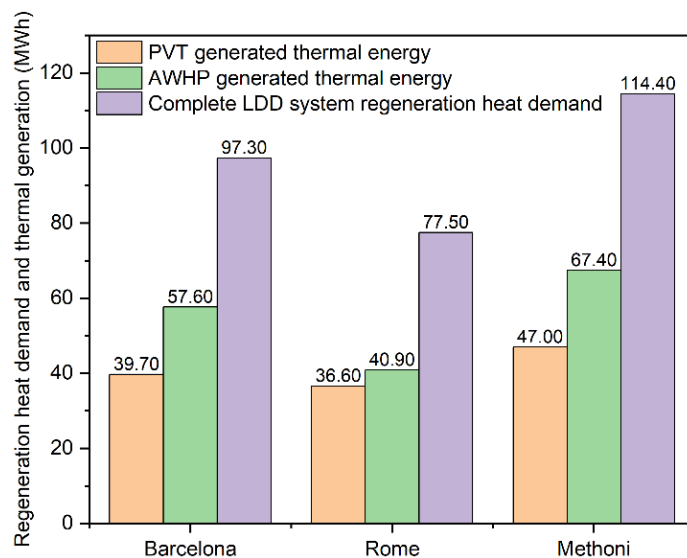
Fig 6-8 The regeneration heat demand and thermal generation of the ILDAC system in Methoni, Rome and Barcelona

6.5 Economic performance and sensitivity analysis

Based on the calculation method of the techno-economic performance mentioned in **section 3.5.4**, the DPP, AROI and RROR are calculated with the initial investment (II), pre- and post-retrofit annual bills summarized in Table 6-5. It is found that the DPP varies between 7-9 years with AROI ranging from

191

8.40% to 11.90% in Barcelona, Rome and Methoni. However, due to the high inflation rate in 2022, the RROR is different from -1.10% to 3.00%. It is also found that the only positive RROR occurs in Spain since a relatively lower inflation rate of 7.30% compared with that 12.60% and 9.50% in Italy and Greece. Moreover, the economic performance under different market standards is presented in Table 6-6. Under the EU market standard with the same bank interest and inflation rates of 6.61% and 10.60%, the DPP are 7 years, 7 years and 9 years for the RBs in Spain, Italy and Greece, respectively. Besides, the RROR for the RBs in Spain and Greece are reduced from 3.00% to 1.00% and -1.10% to -1.40%, whereas the RROR for Italy increases from -0.70% to 1.10%.

Table 6-5 Economic performance in real case scenario

	Initial investment (€)	Pre-retrofit annual bills (€)	Post-retrofit annual bills (€)	DPP (years)	AROI	RROR
Barcelona	77443.3	12999.4	6945.4	8	10.30%	3.00%
Rome	81607.7	14899.3	8988	7	11.90%	-0.70%
Methoni	81726.8	10877.9	4502	9	8.40%	-1.10%

Table 6-6 Economic performance under different market standards

	bank interest rate	inflation rate	real interest rate	DPP (years)	AROI	RROR
EU standard-Spain	6.61%	10.60%	-3.61%	7	11.60%	1.00%
EU standard-Italy	6.61%	10.60%	-3.61%	7	11.70%	1.10%
EU standard-Greece	6.61%	10.60%	-3.61%	9	9.20%	-1.40%
Spain standard-Spain	7.66%	7.30%	0.34%	8	10.30%	3.00%
Italy standard-Italy	7.94%	12.60%	-4.14%	7	11.90%	-0.70%
Greece standard-Greece	8.32%	9.50%	-1.08%	9	8.40%	-1.10%

Due to the uncertainty of the market economic performance, the sensitivity analysis is conducted to investigate the economic performance of installing the ILDAC system for RBs in three locations. All the sensitivity analysis data are

presented in **Appendix C.** Fig 6-9 illustrates the variation of grid electricity tariff increasing rate with *AROI* in Greece, Italy and Spain. It is found that the AROI slightly increases from 10.90% to 12.40% (in Spain and Italy) and 8.50% to 9.80% (in Greece), with the grid electricity tariff increasing rate increasing from -10% to 10%, indicating that the installation of the ILDAC system could relieve the pressure of increasingly living expenses with the rising grid electricity tariff on the homeowners.

Fig 6-10 illustrates the variation of bank interest rates with *AROI* in Greece, Italy and Spain. It is found that the AROI gradually decreases from 14.00% to 10.60% (in Spain and Italy) and 11.00% to 8.20% (in Greece), with the bank interest rate increasing from 0% to 10%, indicating that higher bank interest rate will deteriorate the pressure of the living expenses after installing the ILDAC system.

Fig 6-11 illustrates the variation of PV electricity export tariff increasing rate with *AROI* in Greece, Italy and Spain. It is found that the AROI is insensitive to the PV electricity export tariff increasing rate. For example, the AROI increases from 11.59% to 11.68% (in Spain), 11.59% to 11.72% (in Italy) and 9.13% to 9.18% (in Greece) with the PV electricity export tariff increasing rate escalating from -50% to 50%. This is attributed to the fact that the majority of the PVT electricity generation is consumed by the ILDAC system rather than exported to the grid.

Fig 6-12 demonstrates the variation of inflation rate with *AROI* in Greece, Italy and Spain. It is found that the AROI substantially increases from 4.20% to 14.70% (in Spain), 4.30% to 14.70% (in Italy) and 3.10% to 11.80% (in Greece), with the inflation rate increasing from -20% to 20%, indicating that the AROI is sensitive to the inflation rate, where the installation of the ILDAC system could

evidently relieve the pressure of increasingly living expenses with the rising inflation rate on the homeowners.

Fig 6-13 indicates the variation of inflation rate with $RROR$ in Greece, Italy and Spain, where it has been classified into four zones: 1) Inflation zone with AROI > inflation rate, 2) Inflation zone with AROI < inflation rate, 3) Deflation zone with AROI > inflation rate, and 4) Deflation zone with AROI < inflation rate. In general, the RROR increases at first with the reducing deflation rate and decreases with the rising inflation rate, with the maximum RROR when the inflation/deflation rate is 0. For example, the RROR for the RB in Spain increases from -15.80% to 8.50%, then decreases to -5.30% with the inflation rate from -20% to 20%. In addition, the RROR for the RB in Italy increases from -15.70% to 8.50%, then decreases to -5.30% with the inflation rate from -20% to 20%. The RROR for the RB in Greece increases from -16.90% to 6.50%, followed by a decrease to -8.20%, with the inflation rate from -20% to 20%. The results could provide guidance for selecting the proper time to invest in the ILDAC system installation when the investment is profitable. In other words, it is worth installing the ILDAC system when the calculated AROI is higher than the inflation/deflation rate (RROR>0). Moreover, it is appropriate to invest in the ILDAC system for the RBs in Spain, Italy and Greece when the inflation rates fall between -6.80% and 12.20%, -6.90% and 12.20%, and -5.40% and 8.70%, respectively.
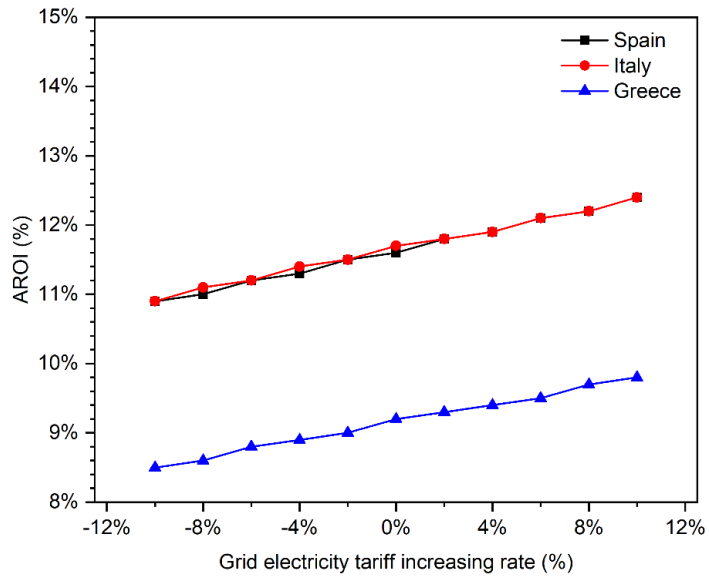
Fig 6-9 The variation of *AROI* with grid electricity tariff increasing rate in Greece, Italy and Spain
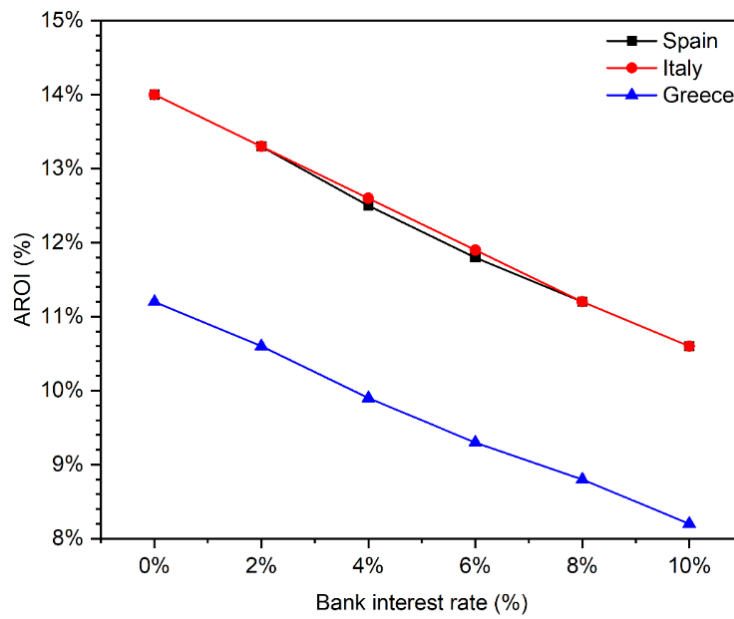
Fig 6-10 The variation of *AROI* with bank interest rate in Greece, Italy and Spain

195
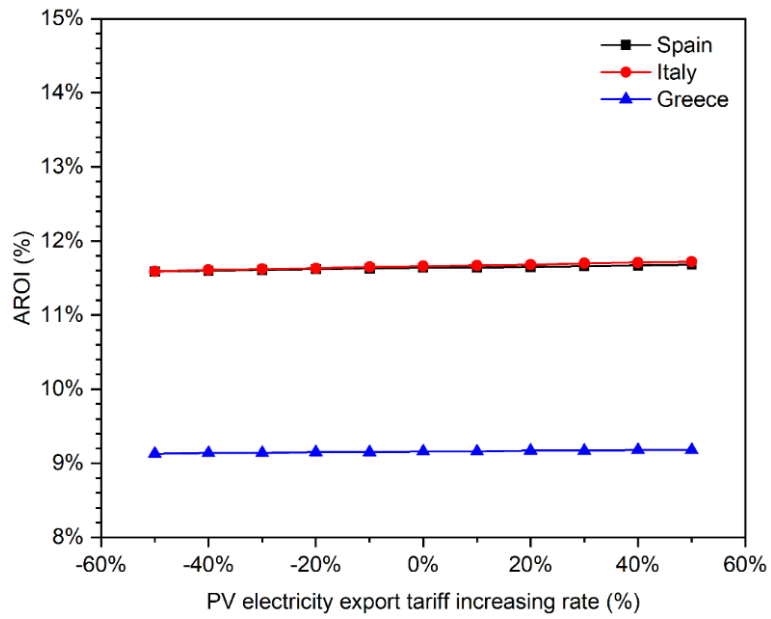
Fig 6-11 The variation of *AROI* with PV electricity export tariff increasing rate in Greece, Italy and Spain
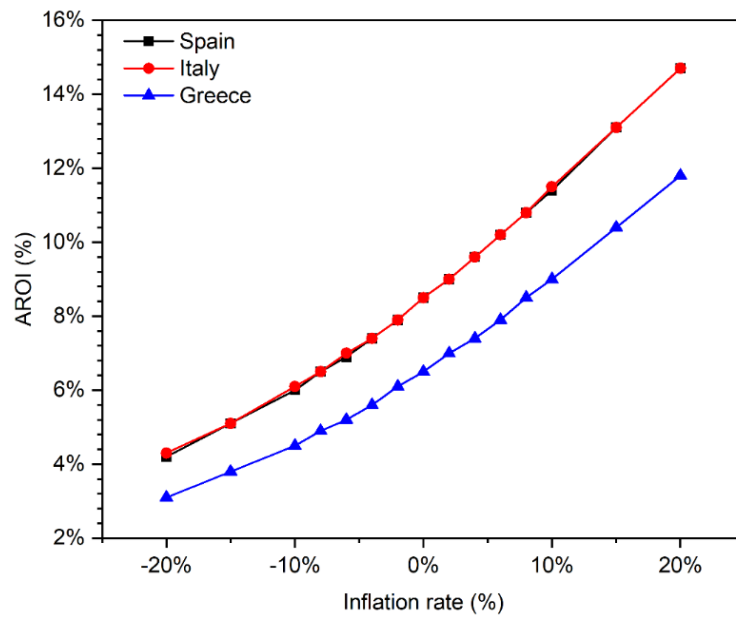
Fig 6-12 The variation of *AROI* with inflation rate in Greece, Italy and Spain

196
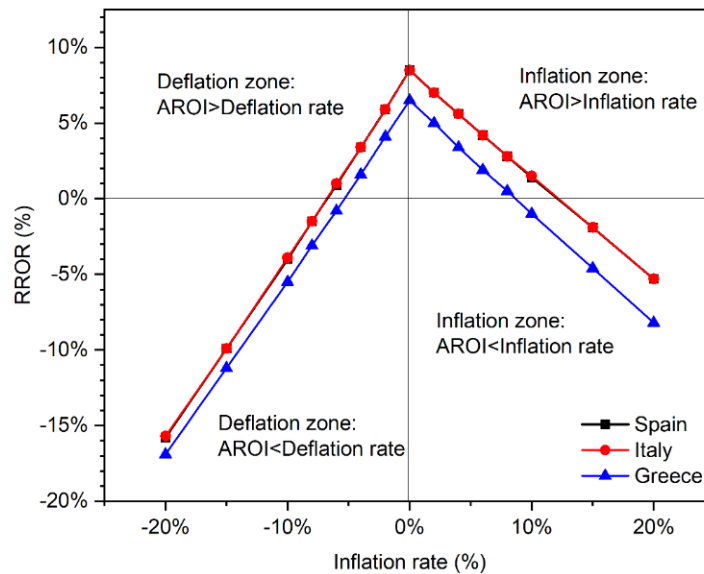
Fig 6-13 The variation of $RROR$ with inflation rate in Greece, Italy and Spain

6.6 Summary

This chapter describes the energy, carbon and economic performances of the integrated liquid desiccant air-conditioning (ILDAC) system for multi-family terraced houses under the subtropical and humid climatic conditions in the Mediterranean regions. According to the simulation in IES VE, the annual cooling, dehumidification, and heating demands of the baseline model in Mehtoni, Rome, and Barcelona have been calculated. It is figured out that the heating demand accounts for 49.2%, 68.4% and 58.5% in Methoni, Rome and Barcelona, respectively. Besides, the cooling demand accounts for 25.3%, 20.6% and 16.8% in Methoni, Rome and Barcelona, respectively. In addition, the dehumidification demand accounts for 25.5%, 10.9% and 24.7% in Methoni, Rome and Barcelona, respectively. Moreover, the dehumidification demands in Methoni and Barcelona are higher than their cooling demands. However, the cooling demands exceed the dehumidification demands in Rome. In addition, by integrating the AWHP, complete LDD, PVT, and hot water storage systems in EnergyPro simulation software with the derived COP correlations of AWHP and

complete LDD system, the variation of the ILDAC system COP with the inlet air temperature and relative humidity have been presented in this chapter. Differing from the AWHP system, the ILDAC system COP rises with the increasing inlet air relative humidity. It is also figured out that the carbon reduction rate of the RBs is 88.8%, 84.3% and 76.9% in Barcelona, Rome and Methoni. Moreover, by comparing the pre-retrofit net energy and post-retrofit net electricity consumption of the RBs, the energy reduction rate is calculated as 77.6%, 74.8% and 78.8% in Barcelona, Rome and Methoni. Furthermore, the ILDAC system could achieve higher COP of 6.41, 8.14 and 7.52, which is significantly higher than both the complete LDD and AWHP systems. For the economic analysis, it is found that the DPP varies between 7-9 years, with AROI ranging from 8.40% to 11.90% in Barcelona, Rome and Methoni. However, due to the high inflation rate in 2022, the RROR is different from -1.10% to 3.00%. Due to the market uncertainty, the sensitivity analysis is conducted and concluded as:

1. The installation of the ILDAC system could relieve the pressure of increasingly living expenses with the rising grid electricity tariff on the homeowners;

2. The higher bank interest rate will deteriorate the pressure on the living expenses after installing the ILDAC system;

3. The AROI is insensitive to the PV electricity export tariff increasing rate, which is attributed to the fact that the majority of the PVT electricity generation is consumed by the ILDAC system rather than exported to grid;

4. The AROI is sensitive to the inflation rate, where the installation of the ILDAC system could evidently relieve the pressure of increasingly living

expenses with the rising inflation rate on the homeowners;

Finally, the RROR increases at first with the reducing deflation rate and decreases with the rising inflation rate, with the maximum RROR when the inflation/deflation rate is 0. In other words, it is recommended to install the ILDAC system when the calculated AROI is higher than the inflation/deflation rate (RROR>0). Moreover, it is appropriate to invest in the ILDAC system for the RBs in Spain, Italy and Greece when the inflation rates fall between -6.80% and 12.20%, -6.90% and 12.20%, and -5.40% and 8.70%, respectively.

Chapter 7 Conclusions and future work

The primary objective of this thesis is to develop and assess a novel membrane-based liquid desiccant dehumidification system consisting of two primary units: the heat pipe internally-cooled membrane-based liquid desiccant dehumidifier (the HP-ICMLDD) and membrane-based regenerator. In addition to these two units, the complete LDD system and the integrated liquid desiccant dehumidification air conditioning system have been explored. On the basis of experimental results, this thesis has analysed the design concept of the membrane-based liquid desiccant dehumidification system, thus making a significant contribution to the field of desiccant dehumidification technology. To produce a coherent conclusion of the thesis, the main findings are categorized into five parts (the research gaps, the heat pipe membrane-based liquid desiccant dehumidification system, the membrane-based regeneration system, the complete liquid desiccant dehumidification system and the integrated liquid desiccant air-conditioning system), and the recommendations for future work have been proposed accordingly.

7.1 Main conclusions

The preceding six chapters have sought to analyse and evaluate the performance of the HP-ICMLDD system, the membrane-based regeneration system, the complete liquid desiccant dehumidification system and the integrated liquid desiccant air-conditioning system through the experiments in order to bridge the research gaps mentioned in **Chapter 2**. Thus, the main findings of this thesis are presented in five parts in this section:

1. **The research gaps**:

i. Although several studies examine the performance of liquid desiccant

systems numerically by analysing the effects of multiple operational and design parameters, few studies have been conducted to experimentally evaluate the performance of a cross-flow internally-cooled membrane-based parallel plate liquid desiccant system by considering all relevant operational factors;

ii. There is a lack of experiments of heat pipe internal cooling in the dehumidifier. The comprehensive parametric analysis of the operation control with the heat pipe internal cooling method should be conducted since the internally-cooled flat membrane dehumidifier has higher heat transfer density and compact size;

iii. Even though many modelling studies have been carried out to investigate the impact of internal cooling on the liquid desiccant dehumidification system, most of the researches focus on the hybrid and finite difference models to achieve high accuracy with calculation iterations. Few studies have been reported to evaluate the performance of an internally-cooled membraned-based liquid desiccant dehumidification system with heat pipe;

2. **The HP-ICMLDD system**:

i. The dehumidifier performance is significantly impacted by the internal cooling of the heat pipe, where reducing the cold water temperature of the cooling box could considerably lower the desiccant solution temperature, thereby improving the dehumidifier performance;

ii. The dehumidification and cooling performance can be drastically improved by increasing the cold water flow rate in the cooling box;

iii. All effectiveness are sensitive to solution concentration only with a high

inlet solution temperature, whereas inlet solution temperature drop plays a more significant role;

3. **The membrane-based regeneration system**:

i. The solution side's sensible effectiveness is insensitive to inlet solution temperature at the regenerator when the solution concentration is high, while latent effectiveness is sensible to inlet solution temperature when the solution concentration is low. Therefore, it is concluded that the regenerator benefits from the high solution temperature due to the enhanced re-concentration effect;

4. **The complete liquid desiccant dehumidification (LDD) system**:

i. The optimal operating conditions for the complete LDD system have been determined based on the performance analyses of the dehumidifier and regenerator: For the dehumidifier, the optimal inlet cold water temperature, mass flow rate, solution temperature, solution concentration are 18°C, 0.017 kg/s, 18°C, 32%, respectively; For the regenerator, the optimal solution temperature is 55°C. It should be noted that the above-mentioned optimal operating conditions are for the tested system and could be generalised in the future. The system optimisation serves as the guidance for selection of optimal operating conditions.

ii. The decrease in the air temperature at the dehumidifier's outlet is evident when the air relative humidity at the dehumidifier's outlet is at a relatively low level, and the temperature difference between the air at the inlet and outlet is smaller when the air relative humidity at the dehumidifier's outlet is at a relatively high level;

iii. Although the air relative humidity at the dehumidifier's inlet is the same,

the outlet air relative humidity rises with the decrease of the inlet air temperature;

iv. All the thermal, electrical and total COP rise with the air temperature and relative humidity at the dehumidifier's inlet;

v. The correlations of the thermal, electrical, total COP, air temperature and relative humidity at the dehumidifier's outlet with the inlet air conditions have been developed using the linear regression method.

5. **The integrated liquid desiccant air-conditioning (ILDAC) system**:

i. The ILDAC system COP rises with the increasing inlet air temperature and relative humidity;

ii. By comparing the energy consumption of the residential building without and with the ILDAC system in three different locations, the building energy consumption is reduced by 77.6%, 74.8% and 78.8% in Barcelona, Rome and Methoni, and the corresponding carbon reduction rate are 88.8%, 84.3% and 76.9%;

iii. The ILDAC system could achieve higher COP of 6.41, 8.14 and 7.52 in Barcelona, Rome and Methoni, which are significantly higher than those of the complete LDD and AWHP systems;

iv. The DPP varies between 7 and 9 years, with AROI ranging from 8.40% to 11.90% in Barcelona, Rome and Methoni. However, due to the high inflation rate in 2022, the RROR ranges from -1.10% to 3.00%;

v. Installing the ILDAC system could relieve the pressure of increasing living expenses with the rising grid electricity tariff and inflation rates on the homeowners. The AROI is insensitive to the PV electricity export tariff increasing rate;

vi. Installing the ILDAC system is recommended when the calculated AROI is higher than the inflation/deflation rate (RROR>0). Moreover, it is appropriate to invest in the ILDAC system in Spain, Italy and Greece when the inflation rates fall between -6.80% and 12.20%, -6.90% and 12.20%, and -5.40% and 8.70%, respectively.

7.2 Recommendations for future work

Based on the major findings as presented in the previous section, recommendations for the future work of the heat pipe membrane-based liquid desiccant dehumidification system are presented as follows:

1) In **Chapter 5**, the effects of various operational factors, such as solution and air properties, on dehumidifier and regenerator performance are explored. However, the influence of utilising different membrane materials has not yet been studied due to the constraints on research time and funding. Numerous sophisticated materials have been created in recent years, and using different types of membrane materials can result in considerable differences in system performance. Future research would concentrate on the detailed heat and mass transfer mechanism through a more complex structure of advanced membrane materials;

2) For a better understanding of the system, velocity and pressure profiles should be estimated in the future by creating more sophisticated Naiver-Stokes equations and applying CFD to their solutions.

3) Due to testing rig building time constraints, only data at inlets and outlets are used to validate the numerical model. Despite the fact that the entire temperature and concentration fields are attained through numerical modelling, they are not thoroughly validated by experimental experiments. Thus, future research will

examine the construction of dehumidifiers and regenerators with improved structural designs, allowing sensors to be put within solution and air channels to improve data accuracy.

4) The energy, carbon and economic performances need to be further discussed under different climate conditions, building types, construction years, and control strategies in order to achieve comprehensive guidance for engineering applications;

5) The validation and correlation of the reference building model simulation results should be conducted in real building applications, which could benefit the future optimization of the integrated liquid desiccant air-conditioning system.

References

1. Kouloumpi, B.A.I., *Implementing the cost-optimal methodology in EU countries*, in *Lessons learned from three case studies*. 2013, The Buildings Performance Institute Europe (BPIE).

2. Isaac, M. and van Vuuren, D.P., *Modeling global residential sector energy demand for heating and air conditioning in the context of climate change.* Energy Policy, 2009. **37**(2): p. 507-521.

3. Chiara Delmastro, T.A., Kevin Lane, Yannick Monschauer. *IEA tracking report: Cooling*. November 2021 [cited 2022 02/04/2022]; Available from: https://www.iea.org/reports/cooling.

4. European, C., Joint Research, C., Tchung-Ming, S., Mantzos, L., Wiesenthal, T., Matei, N., and Rozsai, M., *JRC-IDEES : Integrated Database of the European Energy Sector : methodological note*. 2017: Publications Office.

5. Bokor, B., Kajtár, L., and Eryener, D., *Nocturnal Radiation: New Opportunity in Building Cooling.* Energy Procedia, 2017. **112**: p. 118-125.

6. Pezzutto, S., De Felice, M., Fazeli, R., Kranzl, L., and Zambotti, S. *Status Quo of the Air-Conditioning Market in Europe: Assessment of the Building Stock*. Energies, 2017. **10**, DOI: 10.3390/en10091253.

7. Andreou, A., Barrett, J., Taylor, P.G., Brockway, P.E., and Wadud, Z., *Decomposing the drivers of residential space cooling energy consumption in EU-28 countries using a panel data approach.* Energy and Built Environment, 2020. **1**(4): p. 432-442.

8. Izquierdo, M., Moreno-Rodríguez, A., González-Gil, A., and García-Hernando, N., *Air conditioning in the region of Madrid, Spain: An approach to electricity consumption, economics and CO2 emissions.* Energy, 2011. **36**(3): p. 1630-1639.

9. Filippín, C., *Energy Efficiency in Buildings*. 2007. p. pp. 223-245.

10. Kjellström, E., Nikulin, G., Strandberg, G., Christensen, O.B., Jacob, D., Keuler, K., Lenderink, G., van Meijgaard, E., Schär, C., Somot, S., Sørland, S.L., Teichmann, C., and Vautard, R., *European climate change at global mean temperature increases of 1.5 and 2 °C above pre-industrial conditions as simulated by the EURO-CORDEX regional climate models.* Earth Syst. Dynam., 2018. **9**(2): p. 459-478.

11. Kneiske, T.M. and Braun, M., *Flexibility potentials of a combined use of heat storages and batteries in PV-CHP hybrid systems.* Energy Procedia, 2017. **135**: p. 482-495.

12. Qu, K., Barreto, G., Iten, M., Wang, Y., and Riffat, S., *Energy and thermal performance of optimised hollow fibre liquid desiccant cooling and dehumidification systems in mediterranean regions: Modelling, validation and case study.* Energy, 2023. **263**: p. 125852.

13. Dong, C., Lu, L., and Wen, T., *Investigating dehumidification performance of solar-assisted liquid desiccant dehumidifiers considering different surface properties.* Energy, 2018. **164**: p. 978-994.

14. Luo, Y., Chen, Y., Yang, H., and Wang, Y., *Study on an internally-cooled liquid desiccant dehumidifier with CFD model.* Applied Energy, 2017. **194**: p. 399-409.

15. Aziz, A.A., Sumiyoshi, D., and Akashi, Y., *Low cost humidity controlled air-conditioning system for building energy savings in tropical climate.* Journal of Building Engineering, 2017. **11**: p. 9-16.

16.   Fu, Y., O'Neill, Z., Wen, J., Pertzborn, A., and Bushby, S.T., *Utilizing commercial heating, ventilating, and air conditioning systems to provide grid services: A review.* Applied Energy, 2021: p. 118133.

17.   Zhuang, C., Wang, S., and Shan, K., *Adaptive full-range decoupled ventilation strategy and air-conditioning systems for cleanrooms and buildings requiring strict humidity control and their performance evaluation.* Energy, 2019. **168**: p. 883-896.

18.   Huang, X., Li, K., Xie, Y., Liu, B., Liu, J., Liu, Z., and Mou, L., *A novel multistage constant compressor speed control strategy of electric vehicle air conditioning system based on genetic algorithm.* Energy, 2022. **241**: p. 122903.

19.   Lundgren-Kownacki, K., Hornyanszky, E.D., Chu, T.A., Olsson, J.A., and Becker, P., *Challenges of using air conditioning in an increasingly hot climate.* International Journal of Biometeorology, 2018. **62**(3): p. 401-412.

20.   Feng, Z., Zhou, X., Xu, S., Ding, J., and Cao, S.-J., *Impacts of humidification process on indoor thermal comfort and air quality using portable ultrasonic humidifier.* Building and Environment, 2018. **133**: p. 62-72.

21.   Cao, S.-J. and Meyers, J., *Influence of turbulent boundary conditions on RANS simulations of pollutant dispersion in mechanically ventilated enclosures with transitional slot Reynolds number.* Building and Environment, 2013. **59**: p. 397-407.

22.   *The effects of indoor air quality on performance and productivity.* Indoor Air, 2004. **14**(s7): p. 92-101.

23.   Low, E., Huang, S.-M., Yang, M., Show, P.L., and Law, C.L., *Design of cascade analysis for renewable and waste heat recovery in a solar thermal regeneration unit of a liquid desiccant dehumidification system.* Energy, 2021. **235**: p. 121284.

24.   Bhowmik, M., Rath, S., Jayson Varela, R., Muthukumar, P., Anandalakshmi, R., and Saito, K., *Performance assessment of integrated liquid desiccant dehumidification with vapor-compression system for energy-efficient air conditioning applications.* Applied Thermal Engineering, 2022. **216**: p. 119118.

25.   Cho, H.-J., Cheon, S.-Y., and Jeong, J.-W., *Experimental analysis of dehumidification performance of counter and cross-flow liquid desiccant dehumidifiers.* Applied Thermal Engineering, 2019. **150**: p. 210-223.

26.   Park, J.-Y., Dong, H.-W., Cho, H.-J., and Jeong, J.-W., *Energy benefit of a cascade liquid desiccant dehumidification in a desiccant and evaporative cooling-assisted building air-conditioning system.* Applied Thermal Engineering, 2019. **147**: p. 291-301.

27.   Liu, J., Zhang, T., Liu, X., and Jiang, J., *Experimental analysis of an internally-cooled/heated liquid desiccant dehumidifier/regenerator made of thermally conductive plastic.* Energy and Buildings, 2015. **99**: p. 75-86.

28.   Qi, R., Lu, L., and Yang, H., *Development of simplified prediction model for internally cooled/heated liquid desiccant dehumidification system.* Energy and Buildings, 2013. **59**: p. 133-142.

29.   Ghadiri Moghaddam, D., Besant, R.W., and Simonson, C.J., *Solution-side effectiveness for a liquid-to-air membrane energy exchanger used as a dehumidifier/regenerator.* Applied Energy, 2014. **113**: p. 872-882.

30.   Liu, J., Liu, X., and Zhang, T., *Comparison of internally cooled and adiabatic liquid desiccant dehumidification-regeneration system.* Building and Environment, 2019. **163**: p. 106313.

31.   Abdel-Salam, M.R.H., Besant, R.W., and Simonson, C.J., *Performance testing of a novel 3-fluid liquid-to-air membrane energy exchanger (3-fluid LAMEE)*

under desiccant solution regeneration operating conditions. International Journal of Heat and Mass Transfer, 2016. **95**: p. 773-786.

32.   Woods, J. and Kozubal, E., *A desiccant-enhanced evaporative air conditioner: Numerical model and experiments.* Energy Conversion and Management, 2013. **65**: p. 208-220.

33.   Huang, S.-M., Yang, M., Hu, B., Tao, S., Qin, F., Weng, W., Wenhao, W., and Liu, J., *Performance analysis of an internally-cooled plate membrane liquid desiccant dehumidifier (IMLDD): An analytical solution approach.* International Journal of Heat and Mass Transfer, 2018. **119**: p. 577-585.

34.   Huang, S.-M., Yang, M., Hong, Y., and Ye, W.-B., *Performance correlations of an adjacently internally-cooled membrane contactor applied for liquid desiccant air dehumidification.* Applied Thermal Engineering, 2018. **129**: p. 1660-1669.

35.   Das, R.S. and Jain, S., *Performance characteristics of cross-flow membrane contactors for liquid desiccant systems.* Applied Energy, 2015. **141**: p. 1-11.

36.   Alan, S.W.L., Islam, M.R., and Chua, K.J., *A Theoretical Model on Internally Cooled Liquid Desiccant Dehumidification and Cooling Processes.* Energy Procedia, 2017. **142**: p. 1009-1014.

37.   Islam, M.R., Alan, S.W.L., and Chua, K.J., *Studying the heat and mass transfer process of liquid desiccant for dehumidification and cooling.* Applied Energy, 2018. **221**: p. 334-347.

38.   Wen, T. and Lu, L., *Numerical and experimental study on internally cooled liquid desiccant dehumidification concerning film shrinkage shape and vapor condensation.* International Journal of Thermal Sciences, 2019. **136**: p. 316-327.

39.   Barreto, G., Qu, K., Wang, Y., Iten, M., and Riffat, S., *An innovative window heat recovery (WHR) system with heat pipe technology: Analytical, CFD, experimental analysis and building retrofit performance.* Energy Reports, 2022. **8**: p. 3289-3305.

40.   Calautit, J.K., Chaudhry, H.N., Hughes, B.R., and Ghani, S.A., *Comparison between evaporative cooling and a heat pipe assisted thermal loop for a commercial wind tower in hot and dry climatic conditions.* Applied Energy, 2013. **101**: p. 740-755.

41.   Shen, S., Cai, W., Wang, X., Wu, Q., and Yon, H., *Hybrid model for heat recovery heat pipe system in Liquid Desiccant Dehumidification System.* Applied Energy, 2016. **182**: p. 383-393.

42.   Srimuang, W. and Amatachaya, P., *A review of the applications of heat pipe heat exchangers for heat recovery.* Renewable and Sustainable Energy Reviews, 2012. **16**(6): p. 4303-4315.

43.   Cooper, J.T., *Heat Pipe Impact on Dehumidification, Indoor Air Quality and Energy Savings.* 1996.

44.   Keniar, K., Ghali, K., and Ghaddar, N., *Study of solar regenerated membrane desiccant system to control humidity and decrease energy consumption in office spaces.* Applied Energy, 2014. **138**.

45.   Li, Y., Lu, L., and Yang, H., *Energy and economic performance analysis of an open cycle solar desiccant dehumidification air-conditioning system for application in Hong Kong.* Solar Energy, 2010. **84**(12): p. 2085-2095.

46.   Wang, Y., Qu, K., Chen, X., Gan, G., and Riffat, S., *An innovative retrofit Motivation-Objective-Criteria (MOC) approach integrating homeowners' engagement to unlocking low-energy retrofit in residential buildings.* Energy and Buildings, 2022. **259**: p. 111834.

47.   Wang, Y., Qu, K., Chen, X., Zhang, X., and Riffat, S., *Holistic electrification vs deep energy retrofits for optimal decarbonisation pathways of UK dwellings: A case study of the 1940s' British post-war masonry house.* Energy, 2022. **241**: p. 122935.

48.   Wang, Y., Qu, K., Chen, X., Zhang, X., and Riffat, S., *A novel Energy-Flow based Ensemble Calibration model for rapid and accurate energy-economic performance prediction of deep energy retrofit in single-family houses.* Energy Conversion and Management, 2022. **258**: p. 115507.

49.   Huang, S.-M. and Zhang, L.-Z., *Researches and trends in membrane-based liquid desiccant air dehumidification.* Renewable and Sustainable Energy Reviews, 2013. **28**: p. 425-440.

50.   Jain, S. and Bansal, P.K., *Performance analysis of liquid desiccant dehumidification systems.* International Journal of Refrigeration, 2007. **30**(5): p. 861-872.

51.   Chung, T.-W. and Wu, H., *Comparison between Spray Towers with and without Fin Coils for Air Dehumidification Using Triethylene Glycol Solutions and Development of the Mass-Transfer Correlations.* Industrial & Engineering Chemistry Research, 2000. **39**(6): p. 2076-2084.

52.   Scalabrin, G. and Scaltriti, G., *A Liquid Sorption-Desorption System for Air Conditioning With Heat at Lower Temperature.* Journal of Solar Energy Engineering, 1990. **112**(2): p. 70-75.

53.   Zurigat, Y.H., Abu-Arabi, M.K., and Abdul-Wahab, S.A., *Air dehumidification by triethylene glycol desiccant in a packed column.* Energy Conversion and Management, 2004. **45**(1): p. 141-155.

54.   Babakhani, D. and Soleymani, M., *An analytical solution for air dehumidification by liquid desiccant in a packed column.* International Communications in Heat and Mass Transfer, 2009. **36**(9): p. 969-977.

55.   Factor, H.M. and Grossman, G., *A packed bed dehumidifier/regenerator for solar air conditioning with liquid desiccants.* Solar Energy, 1980. **24**(6): p. 541-550.

56.   Patnaik, S., Lenz, T.G., and Löf, G.O.G., *Performance studies for an experimental solar open-cycle liquid desiccant air dehumidification system.* Solar Energy, 1990. **44**(3): p. 123-135.

57.   Elsarrag, E., *Performance study on a structured packed liquid desiccant regenerator.* Solar Energy, 2006. **80**(12): p. 1624-1631.

58.   Pietruschka, D., Eicker, U., Huber, M., and Schumacher, J., *Experimental performance analysis and modelling of liquid desiccant cooling systems for air conditioning in residential buildings.* International Journal of Refrigeration, 2006. **29**(1): p. 110-124.

59.   Liu, J., Zhang, T., and Liu, X., *Model-based investigation of a heat pump driven, internally cooled liquid desiccant dehumidification system.* Building and Environment, 2018. **143**: p. 431-442.

60.   Liu, J., Liu, X., and Zhang, T., *Performance comparison of three typical types of internally-cooled liquid desiccant dehumidifiers.* Building and Environment, 2016. **103**: p. 134-145.

61.   Fang, S., Zhou, X., Rong, Y., Zhi, X., Wang, K., and Qiu, L., *Multi-stage internally-cooled membrane-based liquid desiccant dehumidifiers: Driving-force based insights into structural improvement.* International Journal of Heat and Mass Transfer, 2021. **171**: p. 121068.

62.   Park, J.-Y., Kim, B.-J., Yoon, S.-Y., Byon, Y.-S., and Jeong, J.-W., *Experimental analysis of dehumidification performance of an evaporative cooling-assisted*

        internally cooled liquid desiccant dehumidifier. Applied Energy, 2019. **235**: p. 177-185.

63.   Liu, J., Liu, X., and Zhang, T., *Analytical solution of heat and mass transfer process in internally cooled liquid desiccant dehumidifiers using refrigerant as cooling medium.* Energy and Buildings, 2019. **190**: p. 1-14.

64.   Li, W. and Yao, Y., *Performance analysis of different flow types of internally-cooled membrane-based liquid desiccant dehumidifiers.* Energy, 2021. **228**: p. 120597.

65.   Grossman, G., *Solar cooling, dehumidification and air conditioning.*, in *Chapter in Encyclopedia of Energy*. 2004. p. 575-585.

66.   L.Z.Zhang, *Total heat recovery: heat and moisture recovery from ventilation air.* 2008, New York: Nova Science Publishers Inc.

67.   Bansal, P., Jain, S., and Moon, C., *Performance comparison of an adiabatic and an internally cooled structured packed-bed dehumidifier.* Applied Thermal Engineering, 2011. **31**(1): p. 14-19.

68.   Yin, Y., Zhang, X., Wang, G., and Luo, L., *Experimental study on a new internally cooled/heated dehumidifier/regenerator of liquid desiccant systems.* International Journal of Refrigeration, 2008. **31**(5): p. 857-866.

69.   Kessling, W., Laevemann, E., and Kapfhammer, C., *ENERGY STORAGE FOR DESICCANT COOLING SYSTEMS COMPONENT DEVELOPMENT.* Solar Energy, 1998. **64**(4): p. 209-221.

70.   Yoon, J.-I., Phan, T.-T., Moon, C.-G., and Bansal, P., *Numerical study on heat and mass transfer characteristic of plate absorber.* Applied Thermal Engineering, 2005. **25**(14): p. 2219-2235.

71.   Zhang, T., Liu, X., Jiang, J., Chang, X., and Jiang, Y., *Experimental analysis of an internally-cooled liquid desiccant dehumidifier.* Building and Environment, 2013. **63**: p. 1-10.

72.   Zhang, L.-Z., *An Analytical Solution to Heat and Mass Transfer in Hollow Fiber Membrane Contactors for Liquid Desiccant Air Dehumidification.* Journal of Heat Transfer, 2011. **133**: p. 092001.

73.   Zhang, L.-Z., Huang, S.-M., Chi, J.-H., and Pei, L.-X., *Conjugate heat and mass transfer in a hollow fiber membrane module for liquid desiccant air dehumidification: A free surface model approach.* International Journal of Heat and Mass Transfer, 2012. **55**(13): p. 3789-3799.

74.   Zhang, L.-Z., *Heat and mass transfer in a cross-flow membrane-based enthalpy exchanger under naturally formed boundary conditions.* International Journal of Heat and Mass Transfer, 2007. **50**(1): p. 151-162.

75.   Niu, J.L. and Zhang, L.Z., *Membrane-based Enthalpy Exchanger: material considerations and clarification of moisture resistance.* Journal of Membrane Science, 2001. **189**(2): p. 179-191.

76.   Abdel-Salam, A.H., Ge, G., and Simonson, C.J., *Performance analysis of a membrane liquid desiccant air-conditioning system.* Energy and Buildings, 2013. **62**: p. 559-569.

77.   Fan, H., Simonson, C.J., Besant, R.W., and Shang, W., *Performance of a Run-Around System for HVAC Heat and Moisture Transfer Applications Using Cross-Flow Plate Exchangers Coupled with Aqueous Lithium Bromide.* Hvac&r Research, 2006. **12**(2): p. 313-336.

78.   Min, J. and Su, M., *Performance analysis of a membrane-based enthalpy exchanger: Effects of the membrane properties on the exchanger performance.* Journal of Membrane Science, 2010. **348**(1): p. 376-382.

79.   Namvar, R., Pyra, D., Ge, G., Simonson, C.J., and Besant, R.W., *+Transient characteristics of a liquid-to-air membrane energy exchanger (LAMEE)*

experimental data with correlations. International Journal of Heat and Mass Transfer, 2012. **55**(23): p. 6682-6694.

80. Huang, S.-M., Yang, M., and Yang, X., *Performance analysis of a quasi-counter flow parallel-plate membrane contactor used for liquid desiccant air dehumidification.* Applied Thermal Engineering, 2014. **63**(1): p. 323-332.

81. Mansourizadeh, A. and Ismail, A.F., *Hollow fiber gas–liquid membrane contactors for acid gas capture: A review.* Journal of Hazardous Materials, 2009. **171**(1): p. 38-53.

82. Zhang, L.-Z., Huang, S.-M., and Pei, L.-X., *Conjugate heat and mass transfer in a cross-flow hollow fiber membrane contactor for liquid desiccant air dehumidification.* International Journal of Heat and Mass Transfer, 2012. **55**: p. 8061–8072.

83. Huang, S.-M., Zhong, Z., and Yang, M., *Conjugate heat and mass transfer in an internally-cooled membrane-based liquid desiccant dehumidifier (IMLDD).* Journal of Membrane Science, 2016. **508**: p. 73-83.

84. Yang, Y., Yan, J., Zhou, X., Xiao, L., and Huang, S.-M., *Transient performance study of an internally-cooled plate membrane liquid desiccant air dehumidification system.* International Journal of Refrigeration, 2021. **131**: p. 87-100.

85. Saman, W.Y. and Alizadeh, S., *An experimental study of a cross-flow type plate heat exchanger for dehumidification/cooling.* Solar Energy, 2002. **73**(1): p. 59-71.

86. Huang, S.-M., Qiu, D., Weihao, H., Yang, M., and Xiao, H., *Laminar flow and heat transfer in a quasi-counter flow parallel-plate membrane channel in the solution side with cooling tubes.* International Journal of Heat and Mass Transfer, 2017. **105**.

87. Abdel-Salam, M.R.H., Besant, R.W., and Simonson, C.J., *Design and testing of a novel 3-fluid liquid-to-air membrane energy exchanger (3-fluid LAMEE).* International Journal of Heat and Mass Transfer, 2016. **92**: p. 312-329.

88. Qiu, D., Wu, Z., Huang, S.-M., Ye, W.-B., Chen, X., Luo, J., and Yang, M., *Laminar flow and heat transfer in an internally-cooled hexagonal parallel-plate membrane channel (IHPMC).* Applied Thermal Engineering, 2017. **124**: p. 767-780.

89. Zhang, L.-Z., *Heat and mass transfer in a quasi-counter flow membrane-based total heat exchanger.* International Journal of Heat and Mass Transfer, 2010. **53**(23): p. 5478-5486.

90. Nada, S.A., *Air cooling-dehumidification/desiccant regeneration processes by a falling liquid desiccant film on finned-tubes for different flow arrangements.* International Journal of Thermal Sciences, 2017. **113**: p. 10-19.

91. Kim, M.-H., Park, J.-Y., and Jeong, J.-W., *Simplified model for packed-bed tower regenerator in a liquid desiccant system.* Applied Thermal Engineering, 2015. **89**: p. 717-726.

92. Yang, Z., Lin, B., Zhang, K., and Lian, Z., *Experimental study on mass transfer performances of the ultrasonic atomization liquid desiccant dehumidification system.* Energy and Buildings, 2015. **93**: p. 126-136.

93. Duong, H.C., Hai, F.I., Al-Jubainawi, A., Ma, Z., He, T., and Nghiem, L.D., *Liquid desiccant lithium chloride regeneration by membrane distillation for air conditioning.* Separation and Purification Technology, 2017. **177**: p. 121-128.

94. Rafique, M.M., Gandhidasan, P., and Bahaidarah, H.M.S., *Liquid desiccant materials and dehumidifiers – A review.* Renewable and Sustainable Energy Reviews, 2016. **56**: p. 179-195.

95. Wen, T., Lu, L., Li, M., and Zhong, H., *Comparative study of the regeneration characteristics of LiCl and a new mixed liquid desiccant solution.* Energy, 2018. **163**: p. 992-1005.

96. Chen, Y., Zhang, X., and Yin, Y., *Experimental and theoretical analysis of liquid desiccant dehumidification process based on an advanced hybrid air-conditioning system.* Applied Thermal Engineering, 2016. **98**: p. 387-399.

97. *Open-Cycle Absorption Cooling Using Packed-Bed Absorbent Reconcentration.* 1980: United States.

98. Lazzarin, R.M., Gasparella, A., and Longo, G.A., *Chemical dehumidification by liquid desiccants: theory and experiment.* International Journal of Refrigeration, 1999. **22**(4): p. 334-347.

99. Liu, X.H., Yi, X.Q., and Jiang, Y., *Mass transfer performance comparison of two commonly used liquid desiccants: LiBr and LiCl aqueous solutions.* Energy Conversion and Management, 2011. **52**(1): p. 180-190.

100. Conde, M.R., *Properties of aqueous solutions of lithium and calcium chlorides: formulations for use in air conditioning equipment design.* International Journal of Thermal Sciences, 2004. **43**(4): p. 367-382.

101. Koronaki, I.P., Christodoulaki, R.I., Papaefthimiou, V.D., and Rogdakis, E.D., *Thermodynamic analysis of a counter flow adiabatic dehumidifier with different liquid desiccant materials.* Applied Thermal Engineering, 2013. **50**(1): p. 361-373.

102. Dai, Y.J. and Zhang, H.F., *Numerical simulation and theoretical analysis of heat and mass transfer in a cross flow liquid desiccant air dehumidifier packed with honeycomb paper.* Energy Conversion and Management, 2004. **45**(9): p. 1343-1356.

103. Lowenstein, A., *Review of Liquid Desiccant Technology for HVAC Applications.* Hvac&r Research, 2008. **14**: p. 819-839.

104. Elmer, T., Worall, M., Wu, S., and Riffat, S., *An experimental study of a novel integrated desiccant air conditioning system for building applications.* Energy and Buildings, 2016. **111**: p. 434-445.

105. Luo, Y., Shao, S., Qin, F., Tian, C., and Yang, H., *Investigation on feasibility of ionic liquids used in solar liquid desiccant air conditioning system.* Solar Energy, 2012. **86**: p. 2718–2724.

106. Al-Farayedhi, A.A., Gandhidasan, P., and Al-Mutairi, M.A., *Evaluation of heat and mass transfer coefficients in a gauze-type structured packing air dehumidifier operating with liquid desiccant.* International Journal of Refrigeration, 2002. **25**(3): p. 330-339.

107. Ertas, A., Anderson, E.E., and Kiris, I., *Properties of a new liquid desiccant solution—Lithium chloride and calcium chloride mixture.* Solar Energy, 1992. **49**(3): p. 205-212.

108. 84-2013, A.A.S., *Method of Test for Air-to-Air Heat/energy Exchangers.* 2017, American Society of Heating, Refrigerating, and Air-Conditioning Engineers: Atlanta.

109. Zhao, X., Li, X., and Zhang, X., *Selection of optimal mixed liquid desiccants and performance analysis of the liquid desiccant cooling system.* Applied Thermal Engineering, 2016. **94**: p. 622-634.

110. Zhang, X.-R., Zhang, L.-Z., Liu, H.-M., and Pei, L.-X., *One-step fabrication and analysis of an asymmetric cellulose acetate membrane for heat and moisture recovery.* Journal of Membrane Science, 2011. **366**(1): p. 158-165.

111. Zhang, L.-Z., Wang, Y.-Y., Wang, C.-L., and Xiang, H., *Synthesis and characterization of a PVA/LiCl blend membrane for air dehumidification.* Journal of Membrane Science, 2008. **308**(1): p. 198-206.

112. Zhang, L.-Z., *Progress on heat and moisture recovery with membranes: From fundamentals to engineering applications.* Energy Conversion and Management, 2012. **63**: p. 173-195.

113. Jansen AE, F.P., *Method for gas absorption across a membrane*. 1998.

114. Gabelman, A. and Hwang, S.-T., *Hollow fiber membrane contactors.* Journal of Membrane Science, 1999. **159**(1): p. 61-106.

115. Zhang, L.-Z., *Numerical study of heat and mass transfer in an enthalpy exchanger with a hydrophobic-hydrophilic composite membrane core.* Numerical Heat Transfer, Part A: Applications, 2007. **51**(7): p. 697-714.

116. Pathak, S.K., Kumar, R., Goel, V., Pandey, A.K., and Tyagi, V.V., *Recent advancements in thermal performance of nano-fluids charged heat pipes used for thermal management applications: A comprehensive review.* Applied Thermal Engineering, 2022. **216**: p. 119023.

117. Sudhan, A.L.S., Solomon, A.B., and Sunder, S., *Heat transport limitations and performance enhancement of anodized grooved heat pipes charged with ammonia under gravity and anti-gravity condition.* Applied Thermal Engineering, 2022. **200**: p. 117633.

118. Zhang, Z., Wang, Y., Yao, W., Gao, F., and Shou, C., *Effect of thermo-physical parameters on heat transfer characteristics of the wall implanted with heat pipes.* Applied Thermal Engineering, 2022. **210**: p. 118375.

119. Ayel, V., Slobodeniuk, M., Bertossi, R., Romestant, C., and Bertin, Y., *Flat plate pulsating heat pipes: A review on the thermohydraulic principles, thermal performances and open issues.* Applied Thermal Engineering, 2021. **197**: p. 117200.

120. Rouaze, G., Marcinichen, J.B., Cataldo, F., Aubin, P., and Thome, J.R., *Simulation and experimental validation of pulsating heat pipes.* Applied Thermal Engineering, 2021. **196**: p. 117271.

121. Mroue, H., Ramos, J.B., Wrobel, L.C., and Jouhara, H., *Experimental and numerical investigation of an air-to-water heat pipe-based heat exchanger.* Applied Thermal Engineering, 2015. **78**: p. 339-350.

122. Gilani, N., Doustani Hendijani, A., and Shirmohammadi, R., *Developing of a novel water-efficient configuration for shower cooling tower integrated with the liquid desiccant cooling system.* Applied Thermal Engineering, 2019. **154**: p. 180-195.

123. Liu, J., Liu, X., and Zhang, T., *Performance comparison and exergy analysis of different flow types in internally-cooled liquid desiccant dehumidifiers (ICDs).* Applied Thermal Engineering, 2018. **142**: p. 278-291.

124. Zhao, Y.n., Yan, T., and Liang, J., *Experimental Investigation on Thermal Characteristics of Long Distance Loop Heat Pipes.* Journal of Thermal Science, 2022. **31**(3): p. 741-750.

125. Abd El-Baky, M.A. and Mohamed, M.M., *Heat pipe heat exchanger for heat recovery in air conditioning.* Applied Thermal Engineering, 2007. **27**(4): p. 795-801.

126. Xiao Ping, W., Johnson, P., and Akbarzadeh, A., *Application of heat pipe heat exchangers to humidity control in air-conditioning systems.* Applied Thermal Engineering, 1997. **17**(6): p. 561-568.

127. Yau, Y.H., *Application of a heat pipe heat exchanger to dehumidification enhancement in a HVAC system for tropical climates—a baseline performance characteristics study.* International Journal of Thermal Sciences, 2007. **46**(2): p. 164-171.

128. Pesaran, A.A., Parent, Y.O., Meckler, M., and Novosel, D. *Evaluation of a liquid-desiccant-enhanced heat-pipe air preconditioner*. 1994. United States.

129.   Ou, X., Cai, W., He, X., and Wu, Y., *Dynamic model development of heat and mass transfer for a novel desiccant regeneration system in liquid desiccant dehumidification system.* Applied Thermal Engineering, 2018. **145**: p. 375-385.

130.   Shen, S., Cai, W., Wang, X., Wu, Q., and Yon, H., *Investigation of liquid desiccant regenerator with heat recovery heat pipe system.* Energy and Buildings, 2017. **146**: p. 353-363.

131.   Liu, X.H., Qu, K.Y., and Jiang, Y., *Empirical correlations to predict the performance of the dehumidifier using liquid desiccant in heat and mass transfer.* Renewable Energy, 2006. **31**(10): p. 1627-1639.

132.   Liu, X.-H., Jiang, Y., and Qu, K.-Y., *Analytical solution of combined heat and mass transfer performance in a cross-flow packed bed liquid desiccant air dehumidifier.* International Journal of Heat and Mass Transfer, 2008. **51**(17): p. 4563-4572.

133.   *ASHRAE Transactions*, in *Development of a generalized model for performance evaluation of packed-type liquid sorbent dehumidifiers and regenerators*. 1992, Khan, A.Y. and H.D. Ball.

134.   Stevens, D.I., Braun, J.E., and Klein, S.A., *An effectiveness model of liquid-desiccant system heat/mass exchangers.* Solar Energy, 1989. **42**(6): p. 449-455.

135.   Ge, G., Ghadiri Moghaddam, D., Namvar, R., Simonson, C.J., and Besant, R.W., *Analytical model based performance evaluation, sizing and coupling flow optimization of liquid desiccant run-around membrane energy exchanger systems.* Energy and Buildings, 2013. **62**: p. 248-257.

136.   Liu, X.H., Jiang, Y., and Qu, K.Y., *Heat and mass transfer model of cross flow liquid desiccant air dehumidifier/regenerator.* Energy Conversion and Management, 2007. **48**(2): p. 546-554.

137.   Zhang, Y., Zhang, H., Yang, H., Chen, Y., and Leung, C.W., *Counter-crossflow indirect evaporative cooling-assisted liquid desiccant dehumidifier: Model development and parameter analysis.* Applied Thermal Engineering, 2022. **217**: p. 119231.

138.   Ghadiri Moghaddam, D., Oghabi, A., Ge, G., Besant, R.W., and Simonson, C.J., *Numerical model of a small-scale liquid-to-air membrane energy exchanger: Parametric study of membrane resistance and air side convective heat transfer coefficient.* Applied Thermal Engineering, 2013. **61**(2): p. 245-258.

139.   Huang, S.-M., Zhang, L.-Z., Tang, K., and Pei, L.-X., *Fluid flow and heat mass transfer in membrane parallel-plates channels used for liquid desiccant air dehumidification.* International Journal of Heat and Mass Transfer, 2012. **55**(9): p. 2571-2580.

140.   Liu, X.H., Chang, X.M., Xia, J.J., and Jiang, Y., *Performance analysis on the internally cooled dehumidifier using liquid desiccant.* Building and Environment, 2009. **44**(2): p. 299-308.

141.   Huang, S.-M., Zhang, L.-Z., and Yang, M., *Conjugate heat and mass transfer in membrane parallel-plates ducts for liquid desiccant air dehumidification: Effects of the developing entrances.* Journal of Membrane Science, 2013. **437**: p. 82-89.

142.   Chen, X.Y., Li, Z., Jiang, Y., and Qu, K.Y., *Analytical solution of adiabatic heat and mass transfer process in packed-type liquid desiccant equipment and its application.* Solar Energy, 2006. **80**(11): p. 1509-1516.

143.   Chengqin, R., Yi, J., and Yianpin, Z., *Simplified analysis of coupled heat and mass transfer processes in packed bed liquid desiccant-air contact system.* Solar Energy, 2006. **80**(1): p. 121-131.

144.   M. Sadasivam, A.R.B., *Effectiveness-NTU method for design of packed bed liquid desiccant dehumidifiers.* 1992. **70**(A6): p. 572-577.

145.   L. Z. Zhang, J.L.N., *Effectiveness Correlations for Heat and Moisture Transfer Processes in an Enthalpy Exchanger With Membrane Cores.* J. Heat Transfer, 2002. **124**(5): p. 922-929.

146.   P. Gandhidasan, M.R.U., C. F. Kettleborough, *Analysis of Heat and Mass Transfer Between a Desiccant-Air System in a Packed Towe.* J. Sol. Energy Eng, 1987. **109**(2): p. 89-93.

147.   Namvar, R., Ge, G., Simonson, C.J., and Besant, R.W., *Transient heat and moisture transfer characteristics of a liquid-to-air membrane energy exchanger (LAMEE) model verification and extrapolation.* International Journal of Heat and Mass Transfer, 2013. **66**: p. 757-771.

148.   Huang, S.-M., Yang, M., Zhong, W.-F., and Xu, Y., *Conjugate transport phenomena in a counter flow hollow fiber membrane tube bank: Effects of the fiber-to-fiber interactions.* Journal of Membrane Science, 2013. **442**: p. 8-17.

149.   Huang, S.-M., Zhang, L.-Z., and Pei, L.-X., *Transport Phenomena in a Cross-Flow Hollow Fibre Membrane Bundle Used for Liquid Desiccant Air Dehumidification.* Indoor and Built Environment, 2012. **22**(3): p. 559-574.

150.   Bai, H., Zhu, J., Chen, Z., Chu, J., and Liu, Y., *Performance evaluation of a membrane-based flat-plate heat and mass exchanger used for liquid desiccant regeneration.* Applied Thermal Engineering, 2018. **139**: p. 569-584.

151.   Dai, Y.J., Wang, R.Z., Zhang, H.F., and Yu, J.D., *Use of liquid desiccant cooling to improve the performance of vapor compression air conditioning.* Applied Thermal Engineering, 2001. **21**(12): p. 1185-1202.

152.   Kinsara, A.A., Elsayed, M.M., and Al-Rabghi, O.M., *Proposed energy-efficient air-conditioning system using liquid desiccant.* Applied Thermal Engineering, 1996. **16**(10): p. 791-806.

153.   Zhang, N., Chen, X., Su, Y., Zheng, H., Ramadan, O., Zhang, X., Chen, H., and Riffat, S., *Numerical investigations and performance comparisons of a novel cross-flow hollow fiber integrated liquid desiccant dehumidification system.* Energy, 2019. **182**: p. 1115-1131.

154.   Akbary, P., Ghiasi, M., Pourkheranjani, M.R.R., Alipour, H., and Ghadimi, N., *Extracting Appropriate Nodal Marginal Prices for All Types of Committed Reserve.* Computational Economics, 2019. **53**(1): p. 1-26.

155.   Cai, W., Mohammaditab, R., Fathi, G., Wakil, K., Ebadi, A.G., and Ghadimi, N., *Optimal bidding and offering strategies of compressed air energy storage: A hybrid robust-stochastic approach.* Renewable Energy, 2019. **143**: p. 1-8.

156.   Liu, J., Chen, C., Liu, Z., Jermsittiparsert, K., and Ghadimi, N., *An IGDT-based risk-involved optimal bidding strategy for hydrogen storage-based intelligent parking lot of electric vehicles.* Journal of Energy Storage, 2020. **27**: p. 101057.

157.   Mehrpooya, M., Ghadimi, N., Marefati, M., and Ghorbanian, S.A., *Numerical investigation of a new combined energy system includes parabolic dish solar collector, Stirling engine and thermoelectric device.* International Journal of Energy Research, 2021. **45**(11): p. 16436-16455.

158.   Mir, M., Shafieezadeh, M., Heidari, M.A., and Ghadimi, N., *Application of hybrid forecast engine based intelligent algorithm and feature selection for wind signal prediction.* Evolving Systems, 2020. **11**(4): p. 559-573.

159.   Mirzapour, F., Lakzaei, M., Varamini, G., Teimourian, M., and Ghadimi, N., *A new prediction model of battery and wind-solar output in hybrid power*

system. Journal of Ambient Intelligence and Humanized Computing, 2019. **10**(1): p. 77-87.

160. Yang, Z., Ghadamyari, M., Khorramdel, H., Seyed Alizadeh, S.M., Pirouzi, S., Milani, M., Banihashemi, F., and Ghadimi, N., *Robust multi-objective optimal design of islanded hybrid system with renewable and diesel sources/stationary and mobile energy storage systems.* Renewable and Sustainable Energy Reviews, 2021. **148**: p. 111295.

161. Liu, X.H., Jiang, Y., and Yi, X.Q., *Effect of regeneration mode on the performance of liquid desiccant packed bed regenerator.* Renewable Energy, 2009. **34**(1): p. 209-216.

162. Chen, X., Su, Y., Aydin, D., Bai, H., Jarimi, H., Zhang, X., and Riffat, S., *Experimental investigation of a polymer hollow fibre integrated liquid desiccant dehumidification system with aqueous potassium formate solution.* Applied Thermal Engineering, 2018. **142**: p. 632-643.

163. Chen, X., Zhang, N., Su, Y., Aydin, D., Zheng, H., Bai, H., Georgakis, A., Jarimi, H., and Riffat, S., *Performance analysis and design implementation of a novel polymer hollow fiber liquid desiccant dehumidifier with aqueous potassium formate.* Thermal Science and Engineering Progress, 2019. **13**: p. 100366.

164. Zhang, L.-Z. and Zhang, N., *A heat pump driven and hollow fiber membrane-based liquid desiccant air dehumidification system: Modeling and experimental validation.* Energy, 2014. **65**: p. 441-451.

165. Das, R.S. and Jain, S., *Experimental performance of indirect air–liquid membrane contactors for liquid desiccant cooling systems.* Energy, 2013. **57**: p. 319-325.

166. Bourouni, K., Martin, R., Tadrist, L., and Chaibi, M.T., *Heat transfer and evaporation in geothermal desalination units.* Applied Energy, 1999. **64**(1): p. 129-147.

167. Bai, H., Zhu, J., Chen, Z., and Chu, J., *State-of-art in modelling methods of membrane-based liquid desiccant heat and mass exchanger: A comprehensive review.* International Journal of Heat and Mass Transfer, 2018. **125**: p. 445-470.

168. Oh, S.J., Ng, K.C., Chun, W., and Chua, K.J.E., *Evaluation of a dehumidifier with adsorbent coated heat exchangers for tropical climate operations.* Energy, 2017. **137**: p. 441-448.

169. Ouyang, Y.-W. and Zhang, L.-Z., *Conjugate heat and mass transfer in a skewed flow hollow fiber membrane bank used for liquid desiccant air dehumidification.* International Journal of Heat and Mass Transfer, 2016. **93**: p. 23-40.

170. Ou, X., Cai, W., He, X., and Zhai, D., *Experimental investigations on heat and mass transfer performances of a liquid desiccant cooling and dehumidification system.* Applied Energy, 2018. **220**: p. 164-175.

171. Peng, D. and Zhang, X., *Modeling and simulation of solar collector/regenerator for liquid desiccant cooling systems.* Energy, 2011. **36**(5): p. 2543-2550.

172. Yin, Y., Zhang, X., and Chen, Z., *Experimental study on dehumidifier and regenerator of liquid desiccant cooling air conditioning system.* Building and Environment, 2007. **42**(7): p. 2505-2511.

173. S.Q., L., *Experimental study of a kind of direct evaporative cooling air conditioning system based on liquid desiccant*, in *China: Southeast University.* 2012.

174. Grossman, G., *Solar-powered systems for cooling, dehumidification and air-conditioning.* Solar Energy, 2002. **72**(1): p. 53-62.

175. Gommed, K. and Grossman, G., *Experimental investigation of a liquid desiccant system for solar cooling and dehumidification.* Solar Energy, 2007. **81**(1): p. 131-138.

176. Y.D. Tang, X.H.L., *Energy consumption analysis of liquid desiccant air conditioning system for industrial buildings.* Hvac&Research, 2010. **40**(4): p. 131-135.

177. Tu, M., Ren, C.-Q., Tang, G.-F., and Zhao, Z.-S., *Performance comparison between two novel configurations of liquid desiccant air-conditioning system.* Building and Environment, 2010. **45**(12): p. 2808-2816.

178. P.Mander. *How to convert relative humidity* 2012 [cited 2022 28th October]; Available from: https://carnotcycle.wordpress.com/2012/08/04/how-to-convert-relative-humidity-to-absolute-humidity/.

179. Chen, X., Su, Y., Aydin, D., Ding, Y., Zhang, S., Reay, D., and Riffat, S., *A novel evaporative cooling system with a polymer hollow fibre spindle.* Applied Thermal Engineering, 2018. **132**: p. 665-675.

180. Cisternas, L.A. and Lam, E.J., *An analytic correlation for the vapour pressure of aqueous and non-aqueous solutions of single and mixed electrolytes. Part II. Application and extension.* Fluid Phase Equilibria, 1991. **62**(1): p. 11-27.

181. Abdul-Wahab, S.A., Zurigat, Y.H., and Abu-Arabi, M.K., *Predictions of moisture removal rate and dehumidification effectiveness for structured liquid desiccant air dehumidifier.* Energy, 2004. **29**(1): p. 19-34.

182. Bassuoni, M.M., *An experimental study of structured packing dehumidifier/regenerator operating with liquid desiccant.* Energy, 2011. **36**(5): p. 2628-2638.

183. Simonson, C.J. and Besant, R.W., *Energy wheel effectiveness: part I—development of dimensionless groups.* International Journal of Heat and Mass Transfer, 1999. **42**(12): p. 2161-2170.

184. Bell, S., *Measurement Good Practice Guide No. 11 (Issue 2)*, in *A Beginner's Guide to Uncertainty of Measurement*. Centre for Basic, Thermal and Length Metrology, National Physical Laboratory.

185. Ge, G., Ghadiri Moghaddam, D., Abdel-Salam, A.H., Besant, R.W., and Simonson, C.J., *Comparison of experimental data and a model for heat and mass transfer performance of a liquid-to-air membrane energy exchanger (LAMEE) when used for air dehumidification and salt solution regeneration.* International Journal of Heat and Mass Transfer, 2014. **68**: p. 119-131.

186. Berk, Z., *Heat and Mass Transfer, Basic Principles*. 2009. p. 69-113.

187. WebBook, N.C. *Thermodynamic Properties of R134a TetraFlouroEthane - CF3CH2F*. 2008; Available from: https://www.ohio.edu/mechanical/thermo/property_tables/R134a/.

188. John A. Duffie, W.A.B., *Solar Engineering of Thermal Processes,*. Fourth Edition ed.

189. *Excell PV-T Hybrid Panel*. [cited 2023 02/21]; TECHNICAL SPECIFICATIONS]. Available from: https://solimpeks.com/en/product/volther-excell/.

190. *Telford Tempest 500 Litre Twin Coil Solar Indirect Unvented Cylinder twin Immersion*. [cited 2023 02/21]; Available from: https://www.cylinders2go.co.uk/shop/renewable-energy/telford-tempest-500-litre-twin-coil-solar-indirect-unvented-cylinder-twin-immersion/?gclid=CjwKCAiAhKycBhAQEiwAgf19ep2MyGm_yJyZDvAIODW2SeypXNAG1WBc9ao2zHf_0LBX-3xOM6vVmRoCra0QAvD_BwE.

191. *TABULA WebTool*. [cited 2022 28 May]; Available from: https://webtool.building-typology.eu/#bm.

192.   *Build a new Energy Renovation Strategy around the Mediterranean*. 2022 [cited 2023 02/21]; Available from: https://www.marie-medstrategic.eu/.

193.   Union, T.E. *Policies to ENforce the TRAnsition to Nearly ZEro Energy buildings in the EU-27*. [cited 2023 02/21]; Available from: https://www.entranze.eu/.

194.   Corgnati, S.P., Fabrizio, E., Filippi, M., and Monetti, V., *Reference buildings for cost optimal analysis: Method of definition and application.* Applied Energy, 2013. **102**: p. 983-993.

195.   Capozzoli, A., Piscitelli, M., Neri, F., Grassi, D., and Serale, G., *A novel methodology for energy performance benchmarking of buildings by means of Linear Mixed Effect Model: The case of space and DHW heating of out-patient Healthcare Centres.* Applied Energy, 2016. **171**: p. 592-607.

196.   Wang, W., Hong, T., Xu, X., Chen, J., Liu, Z., and Xu, N., *Forecasting district-scale energy dynamics through integrating building network and long short-term memory learning algorithm.* Applied Energy, 2019. **248**: p. 217-230.

197.   Kazas, G., Fabrizio, E., and Perino, M., *Energy demand profile generation with detailed time resolution at an urban district scale: A reference building approach and case study.* Applied Energy, 2017. **193**: p. 243-262.

198.   Petersdorff, C., Boermans, T., and Harnisch, J., *Mitigation of CO2 Emissions from the EU-15 Building Stock. Beyond the EU Directive on the Energy Performance of Buildings (9 pp).* Environmental science and pollution research international, 2006. **13**: p. 350-8.

199.   Cody, B., Loeschnig, W., and Eberl, A., *Operating energy demand of various residential building typologies in different European climates.* Smart and Sustainable Built Environment, 2018. **7**(3/4): p. 226-250.

200.   Zangheri, P., Armani, R., Pietrobon, M., and Pagliano, L., *Identification of cost-optimal and NZEB refurbishment levels for representative climates and building typologies across Europe.* Energy Efficiency, 2018. **11**(2): p. 337-369.

201.   Loga T, D.N., editors, *Use of building typologies for energy performance assessment of national building stocks. Existent experiences in European countries and common approach*, s. Edition, Editor. 2012, Darmstadt (Germany): Institut Wohnen und Umwelt GmbH.

202.   Enteria, N. and Mizutani, K., *The role of the thermally activated desiccant cooling technologies in the issue of energy and environment.* Renewable and Sustainable Energy Reviews, 2011. **15**(4): p. 2095-2122.

203.   Zhao, B., Yong, W.F., and Chung, T.-S., *Haze particles removal and thermally induced membrane dehumidification system.* Separation and Purification Technology, 2017. **185**: p. 24-32.

204.   Bilardo, M., Ferrara, M., and Fabrizio, E., *The role of solar cooling for nearly zero energy multifamily buildings: Performance analysis across different climates.* Renewable Energy, 2022. **194**: p. 1343-1353.

205.   Ozbalta, T.G., Yildiz, Y., Bayram, I., and Yilmaz, O.C., *Energy performance analysis of a historical building using cost-optimal assessment.* Energy and Buildings, 2021. **250**: p. 111301.

206.   Panagiotidou, M., Aye, L., and Rismanchi, B., *Optimisation of multi-residential building retrofit, cost-optimal and net-zero emission targets.* Energy and Buildings, 2021. **252**: p. 111385.

207.   Reda, F., Arcuri, N., Loiacono, P., and Mazzeo, D., *Energy assessment of solar technologies coupled with a ground source heat pump system for residential energy supply in Southern European climates.* Energy, 2015. **91**: p. 294-305.

208.   Ozarisoy, B. and Altan, H., *Bridging the energy performance gap of social housing stock in south-eastern Mediterranean Europe: Climate change and mitigation.* Energy and Buildings, 2022. **258**: p. 111687.

209. Vincenzo Corrado, I.B., Stefano Paolo Corgnatii. *National scientific report on the TABULA activities in Italy*. 2012 [cited 2021 5th Feb].

210. *IES Virtual environment.* 03/01/2021.

211. *Weather Data Download - Madrid 082210 (IWEC)*. 2020 [cited 2020 11 Dec]; Available from: https://energyplus.net/weather-location/europe_wmo_region_6/ESP//ESP_Madrid.082210_IWEC.

212. WeatherOnline. *Nottingham/Watnall (117m)*. Available from: https://www.weatheronline.co.uk/weather/maps/city?LANG=en&CEL=C&SI=mph&MAPS=over&CONT=ukuk&LAND=MID&REGION=0003&WMO=03354&UP=0&R=0&LEVEL=150&NOREGION=0.

213. Burnett, D., Barbour, E., and Harrison, G., *The UK solar energy resource and the impact of climate change.* Renewable Energy, 2014. **71**: p. 333–343.

214. Marteinsson, B., *SERVICE LIFE ESTIMATION IN THE DESIGN OF BUILDINGS A DEVELOPMENT OF THE FACTOR METHOD* in *Department of Technology and Built* April 2005, University of Gävle Sweden.

215. Wang, Y., Hirvonen, J., Qu, K., Jokisalo, J., and Kosonen, R., *The Impact of Energy Renovation on Continuously and Intermittently Heated Residential Buildings in Southern Europe.* Buildings, 2022. **12**: p. 1316.

216. Geissler, S., *(CT3) Existing Buildings Status in 2020*. OIB Austrian Institute of Construction Engineering: Austria.

217. Union, O.J.o.t.E., *COMMISSION DELEGATED REGULATION (EU) No 244/2012*, in *supplementing Directive 2010/31/EU of the European Parliament and of the Council on the energy performance of buildings by establishing a comparative methodology framework for calculating cost-optimal levels of minimum energy performance requirements for buildings and building elements*. 16 January 2012.

218. Clark, D. *Average hourly labor cost in selected European countries in 2020* May 4, 2021; Available from: https://www.statista.com/statistics/1211601/hourly-labor-cost-in-europe/.

219. Ge, G., Abdel-Salam, M.R.H., Besant, R.W., and Simonson, C.J., *Research and applications of liquid-to-air membrane energy exchangers in building HVAC systems at University of Saskatchewan: A review.* Renewable and Sustainable Energy Reviews, 2013. **26**: p. 464-479.

220. RS. *Sunon A2175 Series Axial Fan, 230 V ac, AC Operation, 344.9m³/h, 26W, 171 x 151 x 51mm*. RS Stock No.111-8336; Available from: https://uk.rs-online.com/web/p/axial-fans/1118336?cm_mmc=UK-PLA-DS3A-_-google-_-CSS_UK_EN_HVAC_%26_Fans_%26_Thermal_Management_Whoop-_-Axial+Fans_Whoop+(2)-_-1118336&matchtype=&pla-299783215840&cq_src=google_ads&cq_cmp=9771206788&cq_term=&cq_plac=&cq_net=g&cq_plt=gp&gclid=CjwKCAiAs8acBhA1EiwAgRFdw9ayKGi5XBZKkjxcZj8aHSnNajbH3OfS0u7it_6ZHysBP8r6GgvvrBoCoSQQAvD_BwE&gclsrc=aw.ds.

221. RS. *Xylem Flojet Diaphragm Air Operated Positive Displacement Pump, 19L/min, 8.27 bar*. RS Stock No.667-9116; Available from: https://uk.rs-online.com/web/p/positive-displacement-pumps/6679116.

222. RS. *Liquid Heat Exchanger, 214.5 x 80.7 x 24.1mm RS Stock No.144-9309*. Mfr. Part No. LN569500010009 Brand: Xylem; Available from: https://uk.rs-online.com/web/p/plate-heat-exchangers/1449309.

223. LTD, T.C.E. *50 LTR WATER STORAGE TANK*. Available from: https://www.trafalgarcleaningequipment.co.uk/50-ltr-water-storage-tank?gclid=CjwKCAiAs8acBhA1EiwAgRFdwwj-

Fn1vkQqNlQGKHrshBfuTtRpgyBxaKNLSmVUc6bszW5C0VVl6IBoCoCUQAvD_BwE.

224. RS. *Heat Pipe, Heat Pipe, 4 x 200mm*. RS Stock No.867-0913 [cited 2023 27/02]; Available from: https://uk.rs-online.com/web/p/heatsinks/8670913?cm_mmc=UK-PLA-DS3A-_-google-_-CSS_UK_EN_HVAC_%26_Fans_%26_Thermal_Management_Whoop-_-Heatsinks_Whoop+(2)-_-8670913&matchtype=&pla-341385076941&cq_src=google_ads&cq_cmp=9771206788&cq_term=&cq_plac=&cq_net=g&cq_plt=gp&gclid=CjwKCAiAs8acBhA1EiwAgRFdwzgBNQrTEAnJMAKvLMV2WvMhbCgL-H_eCMSiSiL7cKC4d7NzXJuOqBoCzQkQAvD_BwE&gclsrc=aw.ds.

225. PlumbNation. *Vaillant Arotherm Plus 5kW Air Source Heat Pump*. [cited 2023 27/02]; Available from: https://www.plumbnation.co.uk/site/vaillant-arotherm-plus-5kw-air-source-heat-pump/.

226. CYLINDERS2GO. Telford Tempest 500 Litre Twin Coil Solar Indirect Unvented Cylinder twin Immersion [cited 2023 27/02]; Available from: https://www.cylinders2go.co.uk/shop/renewable-energy/telford-tempest-500-litre-twin-coil-solar-indirect-unvented-cylinder-twin-immersion/?gclid=CjwKCAiAhKycBhAQEiwAgf19ep2MyGm_yJyZDvAIODW2SeypXNAG1WBc9ao2zHf_0LBX-3xOM6vVmRoCra0QAvD_BwE.

227. SOLIMPEKS. *Excell PV-T Hybrid Panel*. [cited 2023 27/02]; Available from: https://solimpeks.com/en/product/volther-excell/.

228. *Solis Energy Storage 5kW Hybrid 5G Inverter with DC switch*. Code: SOL-5K-RHI-48ES-5G-DC [cited 2023 27/02]; Available from: https://www.theoffgridengineer.co.uk/inverters-c132/grid-tied-storage-inverters-c160/solis-energy-storage-5kw-hybrid-5g-inverter-with-dc-switch-p487/s617?utm_source=google&utm_medium=cpc&utm_term=solis-energy-storage-5kw-hybrid-5g-inverter-with-dc-switch-sol-5k-rhi-48es-5g-dc&utm_campaign=product%2Blisting%2Bads&cid=GBP&glCurrency=GBP&glCountry=GB&gclid=CjwKCAiAs8acBhA1EiwAgRFdw57vVWgosUapnDu8jjawii3PI0Cd1cLdRWncmnAisTpLMuNI39ohaBoCZ50QAvD_BwE.

229. LTD, A. *Ventilation and Fabrication Specialists*. [cited 2023 27/02]; Available from: https://www.airmovefabs.co.uk/.

230. Khayatian, F., Sarto, L., and Dall'O, G., *Building energy retrofit index for policy making and decision support at regional and national scales.* Applied Energy, 2017. **206**: p. 1062-1075.

231. *Hourly labour costs*. Estimated labour costs, 2019 2019 31 March 2020]; Available from: https://ec.europa.eu/eurostat/statistics-explained/index.php/Hourly_labour_costs.

232. Chen, X., Qu, K., Calautit, J., Ekambaram, A., Lu, W., Fox, C., Gan, G., and Riffat, S., *Multi-criteria assessment approach for a residential building retrofit in Norway.* Energy and Buildings, 2020. **215**: p. 109668.

233. Senán-Salinas, J., Landaburu-Aguirre, J., Contreras-Martinez, J., and García-Calvo, E., *Life Cycle Assessment application for emerging membrane recycling technologies: From reverse osmosis into forward osmosis.* Resources, Conservation and Recycling, 2022. **179**: p. 106075.

234. Lloyd, P. *When should you replace a ceiling fan?* Nov 21, 2014 [cited 2023 27/02]; Appliance life spans are widely published. Exhaust and ceiling fans are estimated to typically last for a maximum of 10 years while air conditioners last for 8 to 15 years. These estimations are of course dependent on the quality of the fan you have and the frequency of its usage.]. Available from: https://www.henleyfan.com/replace-ceiling-

fan/#:~:text=Appliance%20life%20spans%20are%20widely,the%20frequency%20of%20its%20usage.

235.   Hydraulic Institute, E., and the US Department of Energy's Office of Industrial Technologies (OIT). , *PUMPLIFECYCLECOSTS: A GUIDETO LCC ANALYSISFORPUMPINGSYSTEMS EXECUTIVESUMMARY*

236.   Griffith Energy Service, I. *HOW LONG WILL A FURNACE LAST? THAT DEPENDS ON HOW YOU TREAT IT*. Dec 19, 2013 [cited 2023 27/02]; These exchangers can last as long as 30 or 40 years, much longer than the steel exchangers most manufacturers build today. Modern stainless or aluminized steel heat exchangers typically have a life span of 15 to 25 years.]. Available from: https://www.griffithenergyservices.com/articles/how-long-will-a-furnace-last-that-depends-on-how-you-treat-it#:~:text=These%20exchangers%20can%20last%20as,of%2015%20to%2025%20years.

237.   flexiliner, T. *How Long Can a Water Storage Tank Last?* Aug 29, 2022 [cited 2023 27/02]; In general, a plastic water tank should serve you for up to 20 years. Metal water tanks are quite strong and durable, as you would expect, and have a life expectancy of more than 30 years.]. Available from: https://www.flexi-liner.com/2022/08/29/how-long-can-a-water-storage-tank-last/#:~:text=In%20general%2C%20a%20plastic%20water,of%20more%20than%2030%20years.

238.   celsia. *Heat Pipe Design Guide*. [cited 2023 27/02]; Available from: https://celsiainc.com/heat-sink-blog/heat-pipe-design-guide/#:~:text=Heat%20pipes%20have%20been%20extensively,freeze%2Dthaw%20cycles%20without%20damage.

239.   energy, e. *How long does a Heat Pump last ?* [cited 2023 27/02]; Heat pumps are long-lasting. In the past, their average life expectancy was around 15 years, but thanks to several technological developments, modern units currently last around 20-25 years before they need replacing.]. Available from: https://www.evergreenenergy.co.uk/heat-pump-guides/how-long-do-heat-pumps-last/#:~:text=How%20long%20does%20a%20Heat,years%20before%20they%20need%20replacing.

240.   SOLUTIONS, H.W. *How Do I Know If My Hot Water Cylinder Needs Replacing?* Sat Feb 13, 2021 [cited 2023 27/02]; Available from: https://hotwatersolutions.nz/how-do-i-know-if-my-hot-water-cylinder-needs-replacing-2/#:~:text=Most%20hot%20water%20cylinders%20have,15%20depending%20on%20it's%20quality.

241.   SUNRUN. *How Long Do Solar Panels Really Last?* Jan 10, 2018 [cited 2023 27/02]; Solar panels, also known as photovoltaic or PV panels, are made to last more than 25 years. In fact, many solar panels installed as early as the 1980s are still working at expected capacity. Not only are solar panels remarkably reliable, solar panel longevity has increased dramatically over the last 20 years.]. Available from: https://www.sunrun.com/go-solar-center/solar-articles/how-long-do-solar-panels-really-last#:~:text=Solar%20panels%2C%20also%20known%20as,still%20working%20at%20expected%20capacity.&text=Not%20only%20are%20solar%20panels,over%20the%20last%2020%20years.

242.   Kunz, N. *Solar PV Inverter Replacement Costs and Considerations*. [cited 2023 27/02]; Solar PV inverter replacement costs vary considerably from one inverter to the other. Generally speaking, the cost of replacing a solar power

inverter can range anywhere from £500 to a couple thousand pounds, depending on the solar PV inverter your solar panels currently run on and the type you choose to go with.]. Available from: https://www.greenmatch.co.uk/blog/2018/11/solar-pv-inverter-replacement-cost-uk.

243.   statistics, e.a. *Bank interest rates - Loans*. [cited 2023 27/02]; Available from: https://www.euro-area-statistics.org/bank-interest-rates-loans?cr=eur&lg=en&page=0&charts=M..B.A2B.F.R.A.2250.EUR.N+M..B.A2B.I.R.A.2250.EUR.N+M..B.A2B.J.R.A.2250.EUR.N&template=1.

244.   statistics, e.a. *Inflation rates - Index of consumer prices*. [cited 2023 27/02]; Available from: https://www.euro-area-statistics.org/inflation-rates?cr=eur&lg=en.

245.   Eurostat. *Electricity and gas prices in the first half of 2022*. 31-10-2022 [cited 2023 27/02]; In the first half of 2022, average household electricity prices in the EU increased sharply compared with the same period in 2021, from €22.0 per 100 kWh to reach €25.3 per 100 kWh. Average gas prices also increased compared with the same period in 2021 from €6.4 per 100 kWh to €8.6 per 100 kWh in the first half of 2022.]. Available from: https://ec.europa.eu/eurostat/web/products-eurostat-news/-/ddn-20221031-1#:~:text=In%20the%20first%20half%20of%202022%2C%20average%20household%20electricity%20prices,%E2%82%AC25.3%20per%20100%20kWh.

246.   Statistics, E. *Natural gas price statistics*. [cited 2023 27/02]; This article highlights the development of natural gas prices for household and non-household consumers within the European Union (EU); it also includes prices data from Liechtenstein, North Macedonia, Serbia, Türkiye, Bosnia and Herzegovina, Moldova, Georgia and Ukraine, when available.]. Available from: https://ec.europa.eu/eurostat/statistics-explained/index.php?title=Natural_gas_price_statistics.

247.   Statistics, E. *Electricity price statistics*. [cited 2023 27/02]; The price of energy in the EU depends on a range of different supply and demand conditions, including the geopolitical situation, the national energy mix, import diversification, network costs, environmental protection costs, severe weather conditions, or levels of excise and taxation.]. Available from: https://ec.europa.eu/eurostat/statistics-explained/index.php?title=Electricity_price_statistics.

248.   TSAGAS, P.m.-I. *PV sweeps Greece's 350 MW tender with country record €0.03297/kWh tariff*. MAY 28, 2021 [cited 2023 27/02]; Greece held its latest round of solar and wind power auctions this week. Overall, 350 MW of PV was allocated while wind power projects failed to win any capacity.]. Available from: https://www.pv-magazine.com/2021/05/28/pv-sweeps-greeces-350-mw-tender-with-record-e0-03297-kwh-tariff/.

249.   *Water news Europe*. 19 March 2021; Available from: https://www.waternewseurope.com/water-prices-compared-in-36-eu-cities/.

250.   DENTONS, *Italy: The 2019-2020 incentives regime for renewable energy plants*. Dentons Europe Studio Legale Tributario.

251.   Wolfendale, E.V.H.-J. *Solar energy in Spain: Can you sell electricity back to the grid?* [cited 2023 27/02]; Available from: https://www.ecovidahomes.com/blog/can-you-sell-electricity-back-to-the-grid-in-spain/.

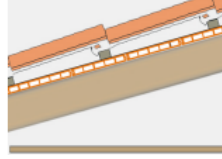252.   BANG, N. *Real Rate of Return: Meaning, Formula & Importance*. [cited 2023 02/21]; Available from: https://www.nirmalbang.com/knowledge-

center/real-rate-of-return.html#:~:text=Real%20rate%20of%20return%20is,calculation%20is%20the%20real%20rate.
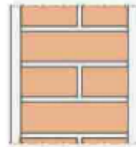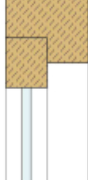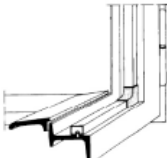
253. *Annual Return*. February 19, 2023 [cited 2023 02/21]; Available from: https://corporatefinanceinstitute.com/resources/capital-markets/annual-return/.

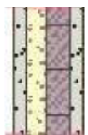254. *Return on Investment (ROI)*. [cited 2023 02/21]; Available from: https://mailchimp.com/en-gb/marketing-glossary/roi/#:~:text=on%20Investment%20(ROI)-,Return%20on%20Investment%20(ROI),be%200.9%2C%20or%2090%25.

255. Chen, Z., Zhu, J., Bai, H., Yan, Y., and Zhang, L., *Experimental study of a membrane-based dehumidification cooling system.* Applied Thermal Engineering, 2017. **115**: p. 1315-1321.

256. Bai, H., Zhu, J., Chen, Z., and Chu, J., *Parametric analysis of a cross-flow membrane-based parallel-plate liquid desiccant dehumidification system: Numerical and experimental data.* Energy and Buildings, 2017. **158**.

257. Bai, H., Zhu, J., Chen, Z., Ma, L., Wang, R., and Li, T., *Performance testing of a cross-flow membrane-based liquid desiccant dehumidification system.* Applied Thermal Engineering, 2017. **119**: p. 119-131.

258. Bai, H., Zhu, J., Chu, J., Chen, X., Cui, Y., and Yan, Y., *Influences of the mixed LiCl-CaCl2 liquid desiccant solution on a membrane-based dehumidification system: Parametric analysis and mixing ratio selection.* Energy and Buildings, 2019. **183**: p. 592-606.

259. Melinder, Å., *Thermophysical Properties of Aqueous Solutions Used as Secondary Working Fluids*, in *Division of Applied Thermodynamics and Refrigeration*. 2007, Royal Institute of Technology: Stockholm.

260. Liu, S., *A Novel Heat Recovery/Desiccant Cooling System Thesis by.* 2008.

261. Bui, D.T., Vivekh, P., Islam, M.R., and Chua, K.J., *Studying the characteristics and energy performance of a composite hollow membrane for air dehumidification.* Applied Energy, 2022. **306**: p. 118161.

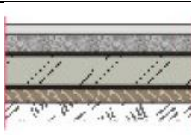262. Liu, J., Liu, X., and Zhang, T., *Corrigendum to Analytical solution of heat and mass transfer process in internally cooled liquid desiccant dehumidifiers using refrigerant as cooling medium.* Energy and Buildings, 2020. **210**: p. 109786.

263. Yang, Z., Zhang, K., Hwang, Y., and Lian, Z., *Performance investigation on the ultrasonic atomization liquid desiccant regeneration system.* Applied Energy, 2016. **171**: p. 12-25.

264. Agudelo-Vera, C., Avvedimento, S., Boxall, J., Creaco, E., de Kater, H., Di Nardo, A., Djukic, A., Douterelo, I., Fish, K.E., Iglesias Rey, P.L., Jacimovic, N., Jacobs, H.E., Kapelan, Z., Martinez Solano, J., Montoya Pachongo, C., Piller, O., Quintiliani, C., Ručka, J., Tuhovčák, L., and Blokker, M. *Drinking Water Temperature around the Globe: Understanding, Policies, Challenges and Opportunities*. Water, 2020. **12**, DOI: 10.3390/w12041049.

Appendices

Appendix A Building construction materials and specifications

Fig A-1 Building constructions and U-value of multi-family terraced houses before the 1970s

		Greece	Italy	Spain
Roof	surface area	80.0 m²	62.1 m²	52.5 m²
	type of construction	Conventional pitched roof	Pitched roof with hollow bricks and steel beam	Ventilated pitched roof wooden frame and suspended ceiling
	picture			
	U-value	3.05 W/(m²K)	1.42 W/(m²K)	4.17 W/(m²K)
Wall	surface area	90.0 m²	69.2 m²	90.0 m²
	type of construction	Brickwork 10cm - Plastered on both sides- 3cm insulation	Solid brick masonry (25 cm)	masonry of coating bricks
	picture			
	U-value	0.95 W/(m²K)	2.01 W/(m²K)	2.56 W/(m²K)
Floor	surface area	88.0m²	62.1 m²	52.5 m²
	type of construction	Slab on grade	The concrete floor on the soil	flooring on the ground
	picture			

	U-value	3.10 W/(m^{2}K)	2.00 W/(m^{2}K)	0.85 W/(m^{2}K)
Window	surface area	6.5 m^2	14.1 m^2	16.8 m^2
	type of construction	Double-glazed (6mm), wooden frame	Single glass, wood frame	metal frame, single-glazed, no thermal break
	picture			
	U-value	3.10 W/(m^{2}K)	4.90 W/(m^{2}K)	4.59 W/(m^{2}K)

Appendix B Original data and processing examples

1. Example of data processing

	Test 1	Test 2	Test 3	Average
$T_{air,in}$	30.46°C	29.87°C	29.65°C	30°C
$RH_{air,in}$	79%	77%	83%	80%
$\dot{m}_{air,in}$	1.94 kg/min	1.89 kg/min	1.90 kg/min	1.91 kg/min
C_{sol}	34%	32%	30%	32 %
$T_{sol,in}$	17.56°C	18.3°C	18.18°C	18 °C
$T_{w,in}$	15.41°C	14.73°C	14.89°C	15 °C
$T_{air,out}$	26.43°C	25.79°C	26.18°C	26.13 °C,
$RH_{air,out}$	48%	47%	43%	46 %
$T_{w,out}$	17.32°C	17.53°C	17.55°C	17.47 °C,

Average inlet condition: $T_{air,in}$=30 °C, $RH_{air,in}$=80 %, $\dot{m}_{air,in}$=1.91 kg/min, C_{sol}=32 %, $T_{sol,in}$=18 °C, $\dot{m}_{sol}$=3 L/min, $\dot{m}_{w,in}$=3 L/min, $T_{w,in}$=15 °C,

Average outlet condition: $T_{air,out}$=26.13 °C, $RH_{air,out}$=46 %, $T_{w,out}$=17.47 °C,

Final indicators:

1) $\varepsilon_{sen} = \dfrac{(\dot{m}c_p)_{air}(T_{air,in}-T_{air,out})}{(\dot{m}c_p)_{min,a-s}(T_{air,in}-T_{sol,in})} \cdot \dfrac{(\dot{m}c_p)_{w}(T_{w,out}-T_{w,in})}{(\dot{m}c_p)_{min,s-w}(T_{sol,in}-T_{w,in})}$

$c_{p,air} = 1020$ J/kgK, $c_{p,w}$ =4186 J/kgK, $c_{p,sol}$ =3200 J/kgK, $\rho_{sol} = 1180$ g/L, $\rho_w = 997$ kg/m³, $\rho_{air} = 1.164$ kg/m³

$\because (\dot{m}c_p)_{air} = 32.5 \, W/K$

$(\dot{m}c_p)_{sol} = 188.8 \, W/K$

$(\dot{m}c_p)_{w} = 208.7 \, W/K$

$\therefore (\dot{m}c_p)_{min,a-s} = 32.5 \, W/K, (\dot{m}c_p)_{min,s-w} = 188.8 \, W/K$

$\therefore \varepsilon_{sen} = \dfrac{32.5 \times (30-26.13)}{32.5 \times (30-18)} \times \dfrac{208.7 \times (17.47-15)}{188.8 \times (18-15)} = 0.2935$

2) $\varepsilon_{lat} = \dfrac{\dot{m}_{air}h_{fg}(W_{air,in}-W_{air,out})}{\dot{m}_{min,a-s}h_{fg}(W_{air,in}-W_{sol,in})}$

$h_{fg} = 2450 \, kJ/kg$

$\dot{m}_{min,a-s} = 1.91 \dfrac{\text{kg}}{\text{min}} = 0.0318 \text{ kg/s}$

$W_{air,in} = 0.02157 \, kg/kg$

$W_{air,out} = 0.0097 \, kg/kg$

$W_{sol,in} = 0.0055 \, kg/kg$

$\varepsilon_{lat} = \dfrac{0.0318 \times 2450 \times (0.02157-0.0097)}{0.0318 \times 2450 \times (0.02157-0.0055)} = 0.7386$

3) $\varepsilon_{tot} = \frac{\varepsilon_{sen} + h^* \varepsilon_{lat}}{1 + h^*}$

$h^* = \frac{h_{fg}}{c_{p,air}} \frac{W_{sol,in} - W_{air,in}}{T_{sol,in} - T_{air,in}} = \frac{2450}{1.020} \times \frac{0.0055 - 0.02157}{18 - 30} = 3.21$

$\varepsilon_{tot} = \frac{0.2935 + 3.21 \times 0.7386}{1 + 3.21} = 0.6329$

4) $MRR = \dot{m}_{air} (W_{air,in} - W_{air,out})$

$MRR = 0.0318 \times (0.02157 - 0.0097) \times 10^{-3} = 0.377 g/s$

5) $Q_{ic} = C_{p,w} \dot{m}_w (T_{w,out} - T_{w,in})$

$Q_{ic} = 4186 \times 0.04985 \times (17.47 - 15) = 515.42W$

6) $Q_c = \dot{m}_{air,deh} c_{p,air} (T_{air,in,deh} - T_{air,out,deh})$

$Q_c = 0.0318 \times 1020 \times (30 - 26.13) = 125W$

7) $Q_{deh} = \dot{m}_{air,deh} h_{fg} (W_{air,in,deh} - W_{air,out,deh})$

$Q_{deh} = 0.0318 \times 2450 \times 1000 \times (0.02157 - 0.0097) = 924.79W$

8) $Q_{tot} = Q_c + Q_{deh}$

$Q_{tot} = 125 + 924.79 = 1050.32W$

If $T_{w,in} > 18°C$, $COP_{th} =$

$$\frac{Q_{tot}}{Q_{reg}/\eta/delivery\ efficiency + \dot{m}_w c_{p,w}(T_{w,in} - 18)/\eta_w/water\ delivery\ efficiency}$$

If $T_{w,in} \leq 18°C$, $COP_{th} = \frac{Q_{tot}}{Q_{reg}/\eta/delivery\ efficiency}$

$Q_{reg} = \dot{m}_{sol,reg} c_{p,sol} (T_{sol,out,HX1} - T_{sol,in,HX1}) = 0.059 \times 3200 \times (54.92 - 40.80) = 2665.86W$

9) $COP_{th} = \frac{Q_{tot}}{Q_{reg}/\eta/delivery\ efficiency} = \frac{1050.32}{\frac{2665.86}{0.92}/0.90} = 0.326$

10) $COP_{ele} = \frac{Q_{tot}}{Q_{ele}} = \frac{Q_{tot}}{W_{fan} + W_{pump}}$

$COP_{ele} = \frac{1050.32}{270 + 90} = 2.92$

11) $COP_{tot} = \dfrac{Q_{tot}}{Q_{reg/\eta/delivery\,efficiency}+Q_{ele}+Q_{tap}} =$

$$\dfrac{Q_{tot}}{Q_{reg/\eta/delivery\,efficiency}+W_{fan}+W_{pump}+Q_{tap}}$$

$$COP_{tot} = \dfrac{1050.32}{\frac{2665.86}{0.92}/0.9+270+90+0} = 0.293$$

2. Example of uncertainty calculations

According to Bell's uncertainty analysis method [184], the uncertainty value of U_Y is determined by the function of U_{X_i} of each variable X_i:

$$U_Y = \sqrt{\sum_{i=1}^{N}\left(\dfrac{\partial Y}{\partial X_i}\right)^2 U_{X_i}^2}$$

Measurement devices	Parameter	Measurement range	Accuracy
RS K-type thermocouple probe	Liquid temperature	0-1100 ℃	±0.75%
Sensirion EK-H4 humidity sensor	Temperature and humidity	-40-125 ℃	±3%
		0-100 % RH	±2%
Testo anemometer 405	Air velocity	0-10 m/s	±5%
Brannan hydrometer 200 Series	Solution density	1.0-1.4 g/m³	±2%
Parker liquid flow indicator	Water flow rate	1-22 L/min	±2%
Parker Easiflow Series flowmeter	Solution flow rate	1-15 L/min	±5%
Data logger DT-80 Series 2	N/A	Data acquisition	±0.15%

Sensible effectiveness:

Uncertainty value of

$$U_Y = \sqrt{\begin{array}{c}(0.75\%)^2 + 2 \times (0.75\%)^2 + \\ (5\%)^2 + 2 \times (5\%)^2 + (5\%)^2 + 2 \times (3\%)^2 + 0.15\%^2\end{array}} =$$

±0.1094

Latent effectiveness:

$$\text{Uncertainty value of } U_Y = \sqrt{\begin{array}{c}(5\%)^2 + (5\%)^2 + 2 \times (2\%)^2 \\ +(0.75\%)^2 + 0.15\%^2\end{array}} = \pm0.0765$$

Total effectiveness:

Uncertainty value of $U_Y =$

$$\sqrt{\begin{array}{c}(0.75\%)^2 + 2 \times (0.75\%)^2 + \\ (5\%)^2 + 2 \times (5\%)^2 + (5\%)^2 + 2 \times (3\%)^2 + 2 \times (2\%)^2 + 0.15\%^2\end{array}} = \pm0.1130$$

MRR:

$$\text{Uncertainty value of } U_Y = \sqrt{(5\%)^2 + 2 \times (2\%)^2} = \pm0.0574$$

Qic:

$$\text{Uncertainty value of } U_Y = \sqrt{(5\%)^2 + 2 \times (0.75\%)^2 + 0.15\%^2} = \pm0.0511$$

Qc:

$$\text{Uncertainty value of } U_Y = \sqrt{(5\%)^2 + 2 \times (3\%)^2} = \pm0.0656$$

Qdeh:

$$\text{Uncertainty value of } U_Y = \sqrt{(5\%)^2 + 2 \times (2\%)^2} = \pm0.0574$$

Qtot:

$$\text{Uncertainty value of } U_Y = \sqrt{(5\%)^2 + 2 \times (3\%)^2 + 2 \times (2\%)^2} = \pm0.0714$$

COPth:

$$\text{Uncertainty value of } U_Y = \sqrt{\begin{array}{c}(5\%)^2 + 2 \times (3\%)^2 + 2 \times (2\%)^2 + (5\%)^2 + \\ 2 \times (0.75\%)^2 + 0.15\%^2 + (5\%)^2 + 2 \times (0.75\%)^2\end{array}} =$$

±0.1016

COPele:

$$\text{Uncertainty value of } U_Y = \sqrt{(5\%)^2 + 2 \times (3\%)^2 + 2 \times (2\%)^2} = \pm0.0714$$

COPtot:

$$\text{Uncertainty value of} U_Y = \sqrt{\begin{array}{c}(5\%)^2 + 2 \times (3\%)^2 + 2 \times (2\%)^2 + (5\%)^2 + \\ 2 \times (0.75\%)^2 + 0.15\%^2 + (5\%)^2 + 2 \times (0.75\%)^2\end{array}} =$$

±0.1016

3. Examples of original data records

1) Inlet cold water temperature ($\dot{m}_{sol}$=3 L/min, $\dot{m}_{w,in}$=3 L/min, $C_{sol} = 32\%$)

	Test 1	Test 2	Test 3	Average
$T_{air,in}$	30.46°C	29.87°C	29.65°C	30°C
$RH_{air,in}$	79%	77%	83%	80%
$\dot{m}_{air,in}$	1.94 kg/min	1.89 kg/min	1.90 kg/min	1.91 kg/min
$T_{sol,in}$	17.56°C	18.3°C	18.18°C	18 °C
$T_{w,in}$	15.41°C	14.73°C	14.89°C	15 °C
$T_{air,out}$	26.43°C	25.79°C	26.18°C	26.13 °C,
$RH_{air,out}$	48%	47%	43%	46 %
$T_{w,out}$	17.32°C	17.53°C	17.55°C	17.47 °C,

2) Cold water flow rate ($\dot{m}_{sol}$=3 L/min, $\dot{m}_{w,in}$=4 L/min, $C_{sol} = 32\%$)

	Test 1	Test 2	Test 3	Average
$T_{air,in}$	30.47°C	29.89°C	29.64°C	30°C
$RH_{air,in}$	82%	81%	77%	80%
$\dot{m}_{air,in}$	1.89 kg/min	1.93 kg/min	1.91 kg/min	1.91 kg/min
$T_{sol,in}$	18.13°C	17.94°C	17.93°C	18 °C
$T_{w,in}$	15.34°C	14.93°C	14.73°C	15 °C
$T_{air,out}$	25.84°C	25.88°C	26.19°C	25.97 °C,
$RH_{air,out}$	45%	43%	44%	44 %
$T_{w,out}$	17.64°C	17.56°C	17.66°C	17.62 °C,

3) Inlet air temperature ($\dot{m}_{sol}$=3 L/min, $\dot{m}_{w,in}$=3 L/min, $C_{sol} = 32\%$)

	Test 1	Test 2	Test 3	Average
$T_{air,in}$	32.31°C	31.91°C	31.78°C	32°C
$RH_{air,in}$	81%	80%	79%	80%
$\dot{m}_{air,in}$	1.94 kg/min	1.88 kg/min	1.91 kg/min	1.91 kg/min
$T_{sol,in}$	18.19°C	17.93°C	17.88°C	18 °C
$T_{w,in}$	15.14°C	14.97°C	14.89°C	15 °C
$T_{air,out}$	28.13°C	28.06°C	28.02°C	28.07 °C,
$RH_{air,out}$	46%	48%	47%	47 %
$T_{w,out}$	17.65°C	17.59°C	17.77°C	17.67 °C,

4) Inlet air relative humidity ($\dot{m}_{sol}$=3 L/min, $\dot{m}_{w,in}$=3 L/min, $C_{sol} = 32\%$)

	Test 1	Test 2	Test 3	Average
$T_{air,in}$	30.11°C	29.95°C	29.94°C	30°C
$RH_{air,in}$	71%	71%	68%	70%
$\dot{m}_{air,in}$	1.94 kg/min	1.87 kg/min	1.92 kg/min	1.91 kg/min
$T_{sol,in}$	18.07°C	18.04°C	17.89°C	18 °C
$T_{w,in}$	15.12°C	14.96°C	14.92°C	15 °C
$T_{air,out}$	26.18°C	26.09°C	26.18°C	26.15 °C,
$RH_{air,out}$	38%	39%	37%	38 %
$T_{w,out}$	17.22°C	17.29°C	17.24°C	17.25 °C,

5) Air flow rate ($\dot{m}_{sol}$=3 L/min, $\dot{m}_{w,in}$=3 L/min, $C_{sol} = 32\%$)

	Test 1	Test 2	Test 3	Average
$T_{air,in}$	29.91°C	29.98°C	30.11°C	30°C

$RH_{air,in}$	79%	80%	81%	80%
$\dot{m}_{air,in}$	1.6 kg/min	1.64 kg/min	1.62 kg/min	1.62 kg/min
$T_{sol,in}$	18.11°C	17.99°C	17.9°C	18 °C
$T_{w,in}$	15.06°C	15.03°C	14.91°C	15 °C
$T_{air,out}$	25.51°C	25.45°C	25.39°C	25.45 °C,
$RH_{air,out}$	42%	41%	43%	42 %
$T_{w,out}$	17.77°C	17.83°C	17.68°C	17.76 °C,

6) Inlet solution temperature ($\dot{m}_{sol}$=3 L/min, $\dot{m}_{w,in}$=3 L/min, $C_{sol} =$ 32%)

	Test 1	Test 2	Test 3	Average
$T_{air,in}$	29.94°C	30.09°C	29.97°C	30°C
$RH_{air,in}$	81%	81%	78%	80%
$\dot{m}_{air,in}$	1.88 kg/min	1.93 kg/min	1.92 kg/min	1.91 kg/min
$T_{sol,in}$	16.07°C	15.94°C	15.99°C	16 °C
$T_{w,in}$	15.07°C	14.97°C	14.96°C	15 °C
$T_{air,out}$	25.81°C	25.97°C	25.83°C	25.87 °C,
$RH_{air,out}$	43%	42%	44%	43 %
$T_{w,out}$	17.66°C	17.62°C	17.55°C	17.61 °C,

7) Solution concentration ($\dot{m}_{sol}$=3 L/min, $\dot{m}_{w,in}$=3 L/min, $C_{sol} = 29\%$)

	Test 1	Test 2	Test 3	Average
$T_{air,in}$	30.13°C	30.09°C	29.78°C	30°C
$RH_{air,in}$	79%	79%	82%	80%
$\dot{m}_{air,in}$	1.93 kg/min	1.95 kg/min	1.85 kg/min	1.91 kg/min
$T_{sol,in}$	18.06°C	17.93°C	18.01°C	18 °C
$T_{w,in}$	15.07°C	15.02°C	14.91°C	15 °C
$T_{air,out}$	25.34°C	25.42°C	25.29°C	25.35 °C,
$RH_{air,out}$	51%	50%	49%	50 %
$T_{w,out}$	17.11°C	17.08°C	17.23°C	17.14 °C,

8) Solution flow rate ($\dot{m}_{sol}$=2 L/min, $\dot{m}_{w,in}$=3 L/min, $C_{sol} = 32\%$)

	Test 1	Test 2	Test 3	Average
$T_{air,in}$	30.14°C	29.89°C	29.97°C	30°C
$RH_{air,in}$	80%	82%	78%	80%
$\dot{m}_{air,in}$	1.92 kg/min	1.85 kg/min	1.96 kg/min	1.91 kg/min
$T_{sol,in}$	18.03°C	18.05°C	17.92°C	18 °C
$T_{w,in}$	15.07°C	14.95°C	14.98°C	15 °C
$T_{air,out}$	26.56°C	26.52°C	26.69°C	26.59 °C,
$RH_{air,out}$	49%	51%	47%	49 %
$T_{w,out}$	17.29°C	17.21°C	17.25°C	17.25 °C,

Appendix C Sensitivity analysis data

Table C-1 The variation of *AROI* with grid electricity tariff increasing rate in Greece, Italy and Spain

Grid electricity tariff increasing rate (%)	AROI		
	Spain	Italy	Greece
-10%	10.90%	10.90%	8.50%
-8%	11.00%	11.10%	8.60%
-6%	11.20%	11.20%	8.80%
-4%	11.30%	11.40%	8.90%
-2%	11.50%	11.50%	9.00%
0%	11.60%	11.70%	9.20%
2%	11.80%	11.80%	9.30%
4%	11.90%	11.90%	9.40%
6%	12.10%	12.10%	9.50%
8%	12.20%	12.20%	9.70%
10%	12.40%	12.40%	9.80%

Table C-2 The variation of *AROI* with bank interest rates in Greece, Italy and Spain

Bank interest rate (%)	AROI		
	Spain	Italy	Greece
0%	14%	14%	11%
2%	13.30%	13.30%	10.60%
4%	12.50%	12.60%	9.90%
6%	11.80%	11.90%	9.30%
8%	11.20%	11.20%	8.80%
10%	10.60%	10.60%	8.20%

Table C-3 The variation of *AROI* with PV electricity export tariff increasing rate

in Greece, Italy and Spain

PV electricity export tariff increasing rate (%)	AROI		
	Spain	Italy	Greece
-50%	11.59%	11.59%	9.13%
-40%	11.60%	11.61%	9.14%
-30%	11.61%	11.62%	9.14%
-20%	11.62%	11.63%	9.15%
-10%	11.63%	11.65%	9.15%
0%	11.64%	11.66%	9.16%
10%	11.64%	11.67%	9.16%
20%	11.65%	11.68%	9.17%
30%	11.66%	11.70%	9.17%
40%	11.67%	11.71%	9.18%
50%	11.68%	11.72%	9.18%

Table C-4 The variation of *AROI* with inflation rate in Greece, Italy and Spain

Inflation rate (%)	AROI		
	Spain	Italy	Greece
-20%	4.20%	4.30%	3.10%
-15%	5.10%	5.10%	3.80%
-10%	6.00%	6.10%	4.50%
-8%	6.50%	6.50%	4.90%
-6%	6.90%	7.00%	5.20%
-4%	7.40%	7.40%	5.60%
-2%	7.90%	7.90%	6.10%
0%	8.50%	8.50%	6.50%
2%	9.00%	9.00%	7.00%
4%	9.60%	9.60%	7.40%

6%	10.20%	10.20%	7.90%
8%	10.80%	10.80%	8.50%
10%	11.40%	11.50%	9.00%
15%	13.10%	13.10%	10.40%
20%	14.70%	14.70%	11.80%

Table C-5 The variation of *RROR* with inflation rate in Greece, Italy and Spain

Inflation rate	RROR		
(%)	Spain	Italy	Greece
-20%	-15.80%	-15.70%	-16.90%
-15%	-9.90%	-9.90%	-11.20%
-10%	-4.00%	-3.90%	-5.50%
-8%	-1.50%	-1.50%	-3.10%
-6%	0.90%	1.00%	-0.80%
-4%	3.40%	3.40%	1.60%
-2%	5.90%	5.90%	4.10%
0%	8.50%	8.50%	6.50%
2%	7.00%	7.00%	5.00%
4%	5.60%	5.60%	3.40%
6%	4.20%	4.20%	1.90%
8%	2.80%	2.80%	0.50%
10%	1.40%	1.50%	-1.00%
15%	-1.90%	-1.90%	-4.60%
20%	-5.30%	-5.30%	-8.20%